

NO-A178 103

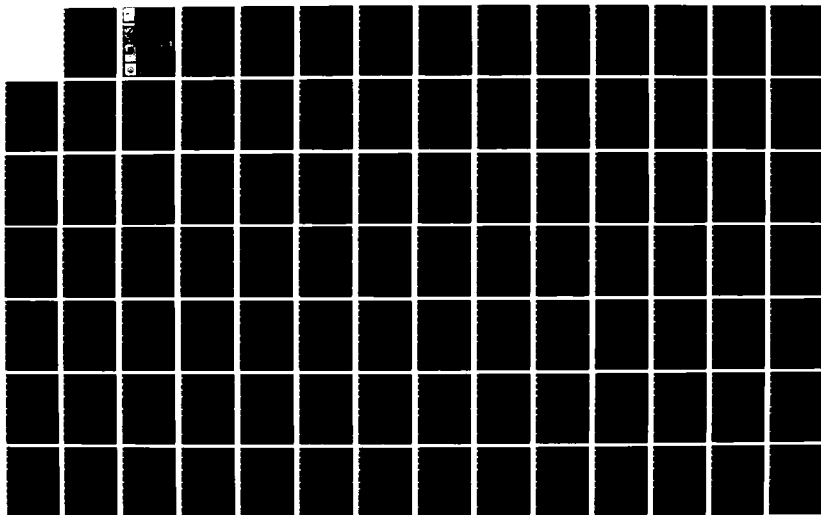
A NUMERICAL INVESTIGATION OF HURRICANE INDUCED WATER  
LEVEL FLUCTUATIONS I. (U) COASTAL ENGINEERING RESEARCH  
CENTER VICKSBURG MS R A SCHMAITZ JUN 86 CERC-MP-86-12

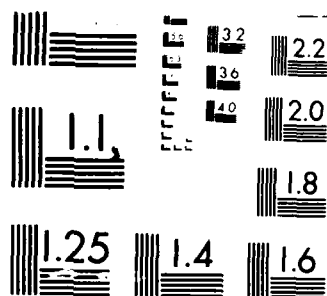
1/3

UNCLASSIFIED

F/G 8/8

NL





MICROCOPY RESOLUTION TEST CHART  
NATIONAL BUREAU OF STANDARDS-1963-A

2

MISCELLANEOUS PAPER CERC-86-12-1



US Army Corps  
of Engineers

AD-A178 103

# A NUMERICAL INVESTIGATION OF HURRICANE INDUCED WATER LEVEL FLUCTUATIONS IN LAKE OKEECHOBEE:

Report 1.

FORECASTING AND DESIGN

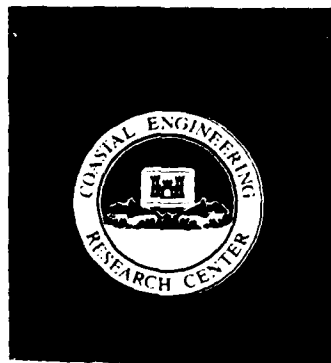
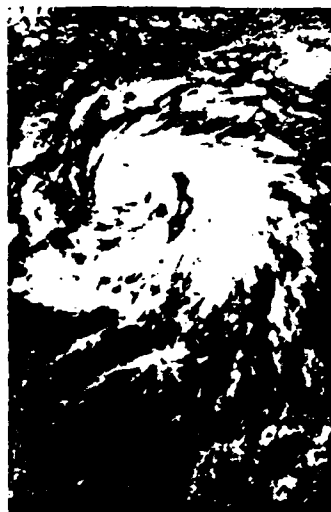
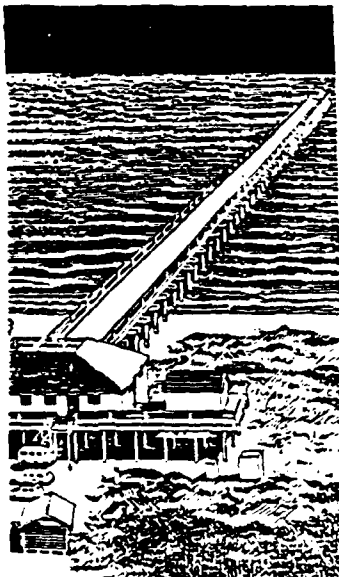
by

Richard A. Schmalz, Jr.

Coastal Engineering Research Center

DEPARTMENT OF THE ARMY

Waterways Experiment Station, Corps of Engineers  
PO Box 631, Vicksburg, Mississippi 39180-0631



OTIC FILE COPY

DTIC  
ELECTE  
MAR 18 1987  
S D



June 1986

Report 1 of a Series

Approved For Public Release; Distribution Unlimited

Prepared for US Army Engineer District, Jacksonville  
Jacksonville, Florida 32232-0019

87 3 18 028

Destroy this report when no longer needed. Do not return  
it to the originator.

The findings in this report are not to be construed as an official  
Department of the Army position unless so designated  
by other authorized documents.

The contents of this report are not to be used for  
advertising, publication, or promotional purposes.  
Citation of trade names does not constitute an  
official endorsement or approval of the use of  
such commercial products.



Unclassified  
SECURITY CLASSIFICATION OF THIS PAGE

41-178-100

REPORT DOCUMENTATION PAGE				Form Approved OMB No. 0704-0188 Exp. Date Jun 30 1986	
1a REPORT SECURITY CLASSIFICATION Unclassified			1b RESTRICTIVE MARKINGS		
2a SECURITY CLASSIFICATION AUTHORITY			3 DISTRIBUTION/AVAILABILITY OF REPORT Approved for public release; distribution unlimited		
2b DECLASSIFICATION/DOWNGRADING SCHEDULE					
4 PERFORMING ORGANIZATION REPORT NUMBER(S) Miscellaneous Paper CERC-86-12			5 MONITORING ORGANIZATION REPORT NUMBER(S)		
6a NAME OF PERFORMING ORGANIZATION USAEWES, Coastal Engineering Research Center		6b OFFICE SYMBOL (If applicable) WESCV	7a NAME OF MONITORING ORGANIZATION		
6c ADDRESS (City, State, and ZIP Code) PO Box 631 Vicksburg, MS 39180-0631			7b ADDRESS (City, State, and ZIP Code)		
8a NAME OF FUNDING/SPONSORING ORGANIZATION USAE District, Jacksonville		8b OFFICE SYMBOL (If applicable)	9 PROCUREMENT INSTRUMENT IDENTIFICATION NUMBER		
8c ADDRESS (City, State, and ZIP Code) PO Box 4970 Jacksonville, FL 32232-0019			10. SOURCE OF FUNDING NUMBERS		
			PROGRAM ELEMENT NO.	PROJECT NO.	TASK NO.
			WORK UNIT ACCESSION NO.		
11 TITLE (Include Security Classification) A Numerical Investigation of Hurricane Induced Water Level Fluctuations in Lake Okeechobee Report 1, Forecasting and Design.					
12 PERSONAL AUTHOR(S) Schmalz, Richard A., Jr.					
13a TYPE OF REPORT Report 1 of a Series		13b TIME COVERED FROM _____ TO _____		14 DATE OF REPORT (Year, Month, Day)	
				15 PAGE COUNT 135	
16 SUPPLEMENTARY NOTATION Available from National Technical Information Service, 5285 Port Royal Road, Springfield, VA 22161. Appendices A-G are contained in a second volume.					
17 COSATI CODES			18 SUBJECT TERMS (Continue on reverse if necessary and identify by block number)		
FIELD	GROUP	SUB-GROUP	Joint probability method Storm surge		
			Lake Okeechobee		
			Tropical storms		
19 ABSTRACT (Continue on reverse if necessary and identify by block number) <p>Hurricane induced water level fluctuations in Lake Okeechobee are investigated in this report, which constitutes the first report of a two report series. using a combined hurricane and hydrodynamic modelling package complete with graphics. Both the design and forecasting of hurricane induced water levels are considered. Within the design concept, both the traditional design hurricane and more recent joint probability methods are incorporated. The development of the complete joint probability approach is the subject of the second report of the two report series. The hurricane submodel contains both direct parametric and planetary boundary layer options. The hydrodynamic submodel consists of an alternating direction implicit finite difference solution of the classical long-wave shallow water equations as well as an empirical short wave description including wave runup and overtopping. The hydrodynamic submodel also accommodates user specified levee breach conditions.</p> <p style="text-align: right;">(Continued)</p>					
20 DISTRIBUTION/AVAILABILITY OF ABSTRACT <input checked="" type="checkbox"/> UNCLASSIFIED/UNLIMITED <input type="checkbox"/> SAME AS RPT <input type="checkbox"/> DTIC USERS			21 ABSTRACT SECURITY CLASSIFICATION Unclassified		
22a NAME OF RESPONSIBLE INDIVIDUAL			22b TELEPHONE (Include Area Code)		22c OFFICE SYMBOL

DD FORM 1473, 84 MAR

83 APR edition may be used until exhausted  
All other editions are obsolete

SECURITY CLASSIFICATION OF THIS PAGE  
Unclassified

Unclassified

SECURITY CLASSIFICATION OF THIS PAGE

19. ABSTRACT (Continued).

PART I provides a brief introduction. PART II outlines the hurricane submodel theoretical development and numerical implementation. The theoretical development of the long and short wave equations is presented in PART III. Detailed numerical implementation of the hydrodynamic relations is given in PART IV. A seiche calibration and verification of the bottom friction mechanics in the hydrodynamics are developed independent from surface wind stress effects in PART V. In PART VI, the wind stress in the hydrodynamics and hurricane model is calibrated using the August 1949 hurricane. Both the planetary boundary layer and standard project hurricane windfield formulations are considered. In PART VII, the October 1950 hurricane is used to further substantiate the hydrodynamics employing the standard project hurricane approach. In PART VIII, Hurricane David is simulated with the present levee configuration again using the standard project hurricane approach.

In PART IX, design hurricane conditions are developed. A representative levee breach is simulated under probable maximum hurricane conditions to demonstrate the model's capability to predict flooding potential. In PART X, major study results are collected, conclusions drawn, and technology transfer efforts itemized.

Appendices A and B contain supporting tables and plates, respectively. Appendices C-G contain code listings and documentation. All appendices are in a separate volume.

Unclassified

SECURITY CLASSIFICATION OF THIS PAGE

## PREFACE

A numerical investigation of hurricane induced water level fluctuations in Lake Okeechobee, Florida, is conducted from both forecasting and design perspectives. The report presents the development and application of a combined hurricane and hydrodynamic modeling system complete with graphics. The hydrodynamic model contains both long and short wave components.

Project administration and funding were provided by the US Army Engineer District, Jacksonville.

The numerical investigation was conducted at the US Army Engineer Waterways Experiment Station (WES) in the Coastal Engineering Research Center (CERC) from June 1982 through June 1985 under the general supervision of Drs. R. W. Whalin and L. E. Link, former Chief and Assistant Chief, respectively, and Dr. J. R. Houston, former Chief, Research Division (RD), and now Chief, CERC. This report was prepared by Dr. R. A. Schmalz, Jr., RD.

The author would like to acknowledge the contributions of Mr. David L. Leenknecht for providing the short wave modeling concepts, as well as providing preliminary versions of the graphics system to be used in the Coastal Modeling Package, Mr. Charles C. Curren for work done in the design storm software, and Mr. Mark D. Prater for providing results of his work on wind stress and drag coefficients. In addition, the following Jacksonville District personnel are acknowledged for greatly assisting in this project. Mr. Joseph E. Gurule, served as project manager and was instrumental in formulating the overall study approach in conjunction with the technology transfer process. Mr. Kaiser Edmand developed levee alignment, toe and crest elevations, and side slopes as well as digitizing the global grid. Mr. Kline Bentley provided water level and wind records for seiches in August 1964 and 1968 as well as for Hurricane David.

Commander and Director of WES during publication of this report was COL Dwayne G. Lee, CE. Technical Director was Dr. Robert W. Whalin.

# CONTENTS

	<u>Page</u>
PREFACE . . . . .	1
PART I: INTRODUCTION . . . . .	4
PART II: HURRICANE MODEL THEORY AND NUMERICAL IMPLEMENTATION . . . .	6
Overview . . . . .	6
Direct Parametric Approach . . . . .	6
Planetary Boundary Layer Approach Theoretical Considerations . .	17
Planetary Boundary Layer Approach Numerical Approximation . . . .	34
Numerical Structure of the Generalized Hurricane Submodel . . . .	47
Generalized Hurricane Submodel Interpolation (Grid) Concepts . .	50
Joint Probability Method Storm Track Geometry . . . . .	55
PART III: HYDRODYNAMIC MODEL: THEORETICAL DEVELOPMENT . . . . .	61
Long-Wave Equations . . . . .	85
Short-Wave Equations . . . . .	87
PART IV: HYDRODYNAMIC MODEL: NUMERICAL IMPLEMENTATION . . . . .	98
Long Wave Equations . . . . .	98
Development of the Numerical Implementation of the Short Wave Equations . . . . .	162
PART V: SEICHE CALIBRATION AND VERIFICATION OF THE LONG WAVE MODEL . . . . .	166
Global Grid Development . . . . .	166
Seiche Phenomena . . . . .	169
PART VI: AUGUST 1949 HURRICANE . . . . .	177
General Storm Characteristics . . . . .	177
Hurricane Sub-Model Simulation Results . . . . .	177
PBL Hydrodynamic Sub-Model Simulation Results . . . . .	181
SPH Hydrodynamic Sub-Model Simulation Results . . . . .	183
Comparison of PBL and SPH Hydrodynamic Simulation Results . . . .	183
PART VII: OCTOBER 1950 HURRICANE . . . . .	185
General Storm Characteristics . . . . .	185
SPH Hurricane Sub-Model Simulation Results . . . . .	185
SPH Hydrodynamic Sub-Model Simulation Results . . . . .	187
PART VIII: SEPTEMBER 1979 HURRICANE . . . . .	189
General Storm Characteristics . . . . .	189
SPH Hurricane Sub-Model Simulation Results . . . . .	189
SPH Hydrodynamic Sub-Model Simulation Results . . . . .	192

	<u>Page</u>
PART IX: DESIGN HURRICANES . . . . .	193
General Outline . . . . .	193
Development of Design Hurricane Parameters . . . . .	193
Development of a Standard Project Hurricane . . . . .	210
Standard Project Hurricane Initial Hydrodynamic Simulation Results . . . . .	210
Standard Project Hurricane Additional Hydrodynamic Simulations . . . . .	211
Development of a Probable Maximum Hurricane . . . . .	211
Probable Maximum Hurricane Initial Hydrodynamic Simulation Results . . . . .	212
Probable Maximum Hurricane Levee Breaching Hydrodynamic Simulation . . . . .	213
Joint Probability Method Considerations . . . . .	213
 PART X: STUDY RESULTS AND CONCLUSIONS . . . . .	215
REFERENCES . . . . .	219
APPENDIX A: TABLES* . . . . .	A1
APPENDIX B: PLATES . . . . .	B1
APPENDIX C: PROGRAM DRAG LISTING . . . . .	C1
APPENDIX D: SUBROUTINE TILT DOCUMENTATION . . . . .	D1
APPENDIX E: PROGRAM DESIGN . . . . .	E1
APPENDIX F: SUBROUTINE TERM . . . . .	F1
APPENDIX G: ABBREVIATED MODELING SYSTEM DOCUMENTATION AND USERS GUIDE . . . . .	G1

Accession For	
NTIS CRA&I	M
DTIC TAB	[ ]
Unannounced	[ ]
Justification	
By	
Distribution /	
Availability Codes	
Availability of Special	
A-1	



\* Appendices A-G are contained in a separate volume.

## PART I: INTRODUCTION

1. This report investigates hurricane induced water level fluctuations in Lake Okeechobee. In response to a letter dated 21 August 1981 from SAJ and additional telephone conversations, a meeting was held on 13 October at WES with SAJ and SAD personnel to outline the scope of the numerical investigation. Based upon results of the meeting, WES proposed on 4 December to develop a combined hurricane and hydrodynamic modeling package to be employed in both a design and forecasting mode. Within the design mode, both the traditional design hurricane and more recent joint probability methods were to be incorporated. The hurricane submodel was to contain both a direct parametric and planetary boundary layer option. The hydrodynamic submodel was to contain a short wave description including wave runup and overtopping. Upon further review by SAD and SAJ, the project scope was extended to consider extreme hurricane design conditions for purposes of dam safety and emergency action planning.

2. The above components of the study are presented in this report through the following structure. Part II outlines the hurricane model theoretical development and numerical implementation. Both direct parametric and planetary boundary layer approaches are developed in a generalized hurricane model. The theoretical development of the long and short wave equations are presented in Part III. Detailed numerical implementation of the hydrodynamics is the thrust of Part IV. The seiche calibration and verification of the bottom friction mechanics in the hydrodynamics is developed in Part V independent from the surface wind stress. In Part VI, the wind stress in the hydrodynamics and hurricane model are calibrated using the August 1949 hurricane. Both the planetary boundary layer and standard project hurricane windfield formulations are considered. In Part VII, the October 1950 hurricane is used to further substantiate the hydrodynamics by employing the standard project hurricane approach. In Part VIII, Hurricane David is simulated with the present levee configuration again using the standard project hurricane approach. In Part IX, the development of design hurricanes for Lake Okeechobee is presented. In addition, the results for a representative breach for a probable maximum hurricane are presented to demonstrate the model's capability to predict flooding potential. Joint probability method design considerations are developed in paragraphs 275-277 in conjunction with the second report in this

series. In Part X, results are summarized and a set of conclusions drawn. Directions of future work by the District are indicated in the context of technology transfer throughout the report.

Appendicies A and B contain supporting tables and plates, respectively. Appendicies C-G contain computer code listings and documentation. All appendicies appear in a separate volume.

## PART II: HURRICANE MODEL THEORY AND NUMERICAL IMPLEMENTATION

### Overview

3. Traditionally, the US Army Corps of Engineers has employed parametric approaches in determining wind and pressure fields. A Standard Project Hurricane (SPH) methodology or direct parametric approach has evolved from the work of Graham and Nunn [1] and been most recently updated by Schwerdt et al. [2]. Recent research has focused on numerical modeling of atmospheric circulation through parameterization of the planetary boundary layer, the so-called PBL approach. The theoretical development and numerical structure of these two approaches is presented initially in turn below. The numerical implementation employed in a generalized hurricane model is presented next followed by a discussion on general g 1 interpolation and joint probability method storm geometry sections.

### Direct Parametric Approach

4. Within this methodology design hurricane conditions have been developed by considering the general characteristics of previous severe hurricanes in light of improved knowledge of the hurricane phenomena in general. Reid [3] implemented the 1972 SPH methodology [4] on a digital computer. The program developed allowed the user to specify a design hurricane through input of non-time varying hurricane parameters (central pressure depression, radius to maximum winds, maximum wind speed, storm track, storm forward speed, and azimuth of maximum winds). Alternatively, by time varying the above parameters as well as specifying an effective radius to maximum winds, observed hurricane windfields could effectively be matched. As such the SPH methodology under the second option is descriptive and not predictive and therefore is not suitable in its current state for predicting windfields for hypothetical hurricanes to be considered in a joint probability method format for design.

5. Perhaps, the most widely used parametric hurricane windfield model is the Tetra Tech Model (TTM) [5] as employed for the coastal flood insurance program of the Federal Emergency Management Agency. Within this model, the user specifies central pressure depression, radius to maximum winds, forward



speed and direction and landfall point. The following variables are considered calibration parameters:

- a.  $\beta$ , Incurvature angle ( $^\circ$ )
- b.  $V_F$ , Far field wind speed (kts)
- c.  $c$ , Reduction factor (maximum gradient to 10 m over water wind speed) (-)

6. Both the SPH and TTM are structured similarly. A radial profile of windspeed is specified along the radial of maximum winds. An asymmetry factor is specified as an azimuthal relationship to modify windspeed in the left and right halves of the storm. A constant inflow or incurvature angle is specified to define the wind direction field.

7. In order to develop the parametric descriptions the following topics are presented in turn below:

- a. Cyclostrophic and gradient windfield determination
- b. Determination of the  $k$  coefficient
- c. Ten-meter, 10-minute overwater winds

Asymmetry Factor (A)

Asymmetry Angle ( $\beta$ )

General Windfield Specification

#### Cyclostrophic and Gradient Windfield Determination

8. Consider the equations of steady horizontal motion written in polar coordinates as follows:

$$v_r \frac{\partial v_r}{\partial r} + v_\theta \frac{\partial v_r}{r \partial \theta} - \frac{v_\theta^2}{r} = f v_\theta - \frac{1}{\rho} \frac{\partial P}{\partial r} \quad (a) \quad (2.1.1)$$

$$v_r \frac{\partial v_\theta}{\partial r} + v_\theta \frac{\partial v_\theta}{r \partial \theta} + \frac{v_r v_\theta}{r} = -f v_r - \frac{1}{\rho} \frac{\partial P}{r \partial \theta} \quad (b)$$

where  $v_r$ ,  $v_\theta$  represent the radial and tangential velocity components.

9. Consider the Hydromet pressure distribution developed by Schloemer [6] as valid in a hurricane.

$$\frac{P - P_o}{P_w - P_o} = e^{-R/r} = \frac{\Delta p(r)}{\Delta p_{\max}} = e^{-R/r} \quad (2.1.2)$$

where

$P$  = sea-level pressure at distance  $r$  from the hurricane center

$P_w$  = asymptotic pressure (29.92 in Hg)

$R$  = storm radius

$P_o$  = central pressure (in Hg)

This pressure distribution has concentric isobars with their centers at  $r = 0$ . Thus  $\partial P / \partial \theta = 0$ . If we assume that the velocity distribution has circular symmetry for the case of a stationary hurricane, then  $\partial v_r / \partial \theta$ ,  $\partial v_\theta / \partial \theta = 0$ . If  $v_r = 0$ , the second equation is satisfied. Replacing  $v_\theta$  with  $c$  the first equation becomes:

$$\underbrace{\frac{c^2}{r}}_{C_e} + \underbrace{fc}_{C_o} - \underbrace{\frac{1}{\rho} \frac{\partial P}{\partial r}}_P = 0 \quad (2.1.3)$$

This equation represents a balance between centrifugal ( $C_e$ ), Coriolis ( $C_o$ ), and pressure gradient force ( $P$ ).

10. If the curvature effects dominate the Coriolis effects, the following equation is obtained for the cyclostrophic wind,  $V_c$ :

$$\frac{V_c^2}{r} = \frac{1}{\rho} \frac{\partial P}{\partial r} \quad (2.1.4)$$

If both effects are important,  $c$ , represents the gradient wind. Thus one obtains the following relation between the cyclostrophic and gradient winds:

$$\frac{c^2}{r} + fc = \frac{V_c^2}{r} \quad (2.1.5)$$

or

$$V_c^2 - c^2 = rfc$$

$$(V_c + c)(V_c - c) = rfc$$

$$V_c - c = \frac{rfc}{c + V_c}$$

11. The assumption is made that the difference between  $V_c$  and  $c$  is small compared with the quantities themselves. Therefore

$$c = V_c - \frac{rf}{2} \quad (2.1.6)$$

for (2.1.2) and (2.1.4)

$$\rho \frac{V_c^2}{r} = \frac{(P_w - P_o) R e^{-R/r}}{r^2}$$

or

$$V_c^2 = \frac{(P_w - P_o) R e^{-R/r}}{\rho r}$$

For  $V_{cx}$ ,  $r = R$ ; e.g., the maximum cyclostrophic wind occurs at  $r = R$ :

$$V_{cx} = \sqrt{\frac{P_w - P_o}{\rho e}} = K(P_w - P_o)^{1/2} \quad (2.1.7)$$

where  $K = (\rho e)^{-1/2}$

Returning to Equation (2.1.6) we obtain the following relationship for the maximum gradient windspeed,  $V_{gx}$ :

$$V_{gx} = K(P_w - P_o)^{1/2} - \frac{Rf}{2} \quad (2.1.8)$$

#### Determination of the K coefficient

12. The magnitude of the maximum gradient wind is dependent not only on the pressure difference, but also on the air density at  $R$ , which has been included in  $K$ . The numerical value of  $K$  depends upon the units used. For wind speed in miles per hour and pressure in inches of mercury, Graham and Nunn [1] used  $K = 73$  based upon an air density at  $68^\circ\text{F}$  and a pressure of 29.53 inches. Schwerdt et al. [2] have assumed the latitudinal variation of

K is based on the variation of the 0.99 probability level sea-surface temperature for the PMH and the 0.75 probability level for the SPH. The assumption is made that the air temperature is equal to the sea surface temperature. The difference in K at 24°N and 45°N is about 4% and 5% for the SPH and PMH, respectively.

#### Ten-meter, 10-minute overwater winds

13. Observed maximum 10-m, 10-min winds ( $V_x$ ) over open water in hurricanes of above average intensity have been found to vary from 75-100% of  $V_{gx}$  by Myers [7]. This maximum point will lie on a circle of radius R. In general,

$$V_x = F(V_{gx}) + A \quad (2.3.1)$$

where

$V_x$  = maximum 10-m, 10-min overwater wind speed

F = reduction factor to convert from maximum gradient wind speed to 10-m, 10-min overwater wind speed

(F = .9 for the SPH

F = .95 for the PMH)

$V_{gx}$  = maximum gradient wind speed defined in (2.1.8)

A = asymmetry factor resulting from the forward speed (T) of the hurricane

For a stationary hurricane, the asymmetry factor, A, is zero.  $V_x$  for a stationary hurricane we designate as  $V_{xs}$ . Knowing  $V_{xs}$ , we can use relative wind profile information to determine 10-m, 10-min overwater winds at any distance from the hurricane center.

#### Asymmetry Factor (A)

14. For a moving hurricane, the asymmetry factor is non-zero. The general equation for A being:

$$A = yT^x \cos \beta \quad (2.3.2)$$

where  $y$  and  $x$  are two empirical constants dependent upon units,  $T$  is the forward speed, and  $\theta$  is the angle between track direction ( $\theta$ ) and the surface wind direction ( $\theta_a$ ), measured counter-clockwise from  $\theta$ . Graham and Nunn, [2] used  $y = .5$  and  $x = 1$  when the windspeed was expressed in knots. Schwerdt et al. [2] suggested  $y = 1.5$  and  $x = .63$  as more representative constants. In Table II-1 below the maximum asymmetry added is contrasted.

Table II-1: Maximum Asymmetry In Wind Speed

<u>Forward Speed (kts)</u>	<u>Graham and Nunn</u>	<u>Schwerdt et al.</u>
6	3	4.6
20	10	10.0
50	25	17.6

#### Asymmetry Angle ( $\theta$ )

15. The asymmetry angle is determined as shown in Figure II-1 below. As may be noted, it is directly dependent upon the inflow angle,  $\theta_1$ , defined as the angle between the true wind direction at a point and the tangent to a circle about the storm center passing through the point.

16. In reality,  $\theta_1$ , varies with radial distance,  $r$ , outward from the storm and with angle with respect to the storm direction. Nunez and Gray [9] define the front quadrant as being centered around the track direction ( $\theta$ ) and note the boundary layer's inflow angle magnitude decreases from quadrant to quadrant in the following order: right, front, back, left.

17. In the SPH model, neither the variation in inflow angle with respect to orientation about the storm direction nor the radial variation are considered. In the first SPH study by Graham and Nunn [1], a value of  $20^\circ$  from the hurricane center to the radius of maximum winds ( $R$ ), a transition from  $20$ - $25^\circ$  between  $R$  and  $1.2R$ , and  $25^\circ$  beyond  $1.2R$  was advocated. Later studies [8, 4] varied this. Although  $25^\circ$  was used for  $1.2R$  and beyond,

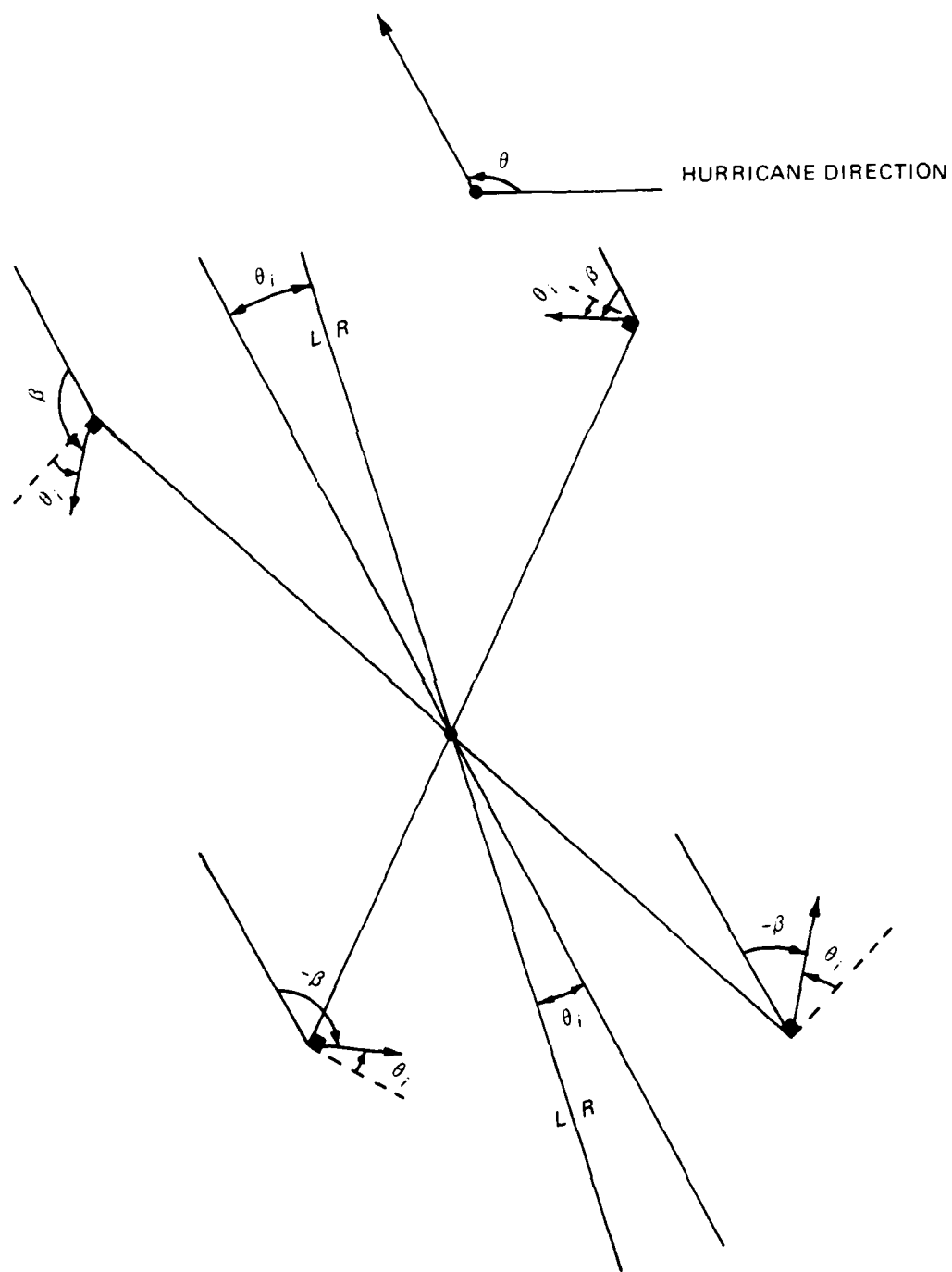


Figure II-1. Angular Variation of Asymmetry angle,  $\beta$ , for a Fixed Radial Distance,  $r$ , and Inflow Angle,  $\theta_i$ .

angles from  $0^\circ$  at the center increasingly linearly to  $10^\circ$  at  $R$  were specified. A transition from  $10^\circ$  to  $25^\circ$  was used between  $R$  and  $1.2R$ .

18. Jelesnianski [10] related inflow angle to maximum surface winds,  $R$  and pressure drop ( $P_w - P_o$ ). Nomograms can be constructed at a given latitude at prescribed distances from the hurricane center.

19. Schwerdt et al. [2] rely on the results of Jelesnianski [10] with the following assumptions:

- a. The SPH is modeled after Jelesnianski's [10] nomogram for a  $\Delta p = 2.08$  in Hg.
- b. The PMH is modeled after Jelesnianski's [10] nomogram for a  $\Delta p = 3.34$  in Hg.
- c. Maximum inflow will occur at a distance of  $3R$ .
- d. Inflow will decrease outward but remain positive from  $3R$  to the periphery of hurricane circulation.
- e. Inflow will be constant with respect to track direction orientation.
- f. Inflow will not vary with storm forward speed.
- g. Inflow will not vary with latitude.

20. These results are stated by Schwerdt et al. [2] to represent an improvement over previous inflow angle criteria from the following perspective:

- a. Curves of inflow angle versus  $R$  are now  $C_1$  continuous.
- b. Maximum inflow is no longer a constant but increases with increasing  $R$ .
- c. Maximum inflow does not extend to the periphery of the hurricane, which is in agreement with Chow [11].

#### General Windfield Specification

21. If we combine Equations (2.9) and (2.10), we may obtain a relationship for  $V_x$  in a moving hurricane in the following form:

$$V_x = F(V_{gx}) + 1.5 T^{.63} \cos \beta \quad (2.3.3)$$

(Note  $y = 1.5$  and  $x = .63$ , for  $V_x$  expressed in knots) ( $F = 9.0$  SPH)  
( $F = .95$  PMH)

22. Equation (2.3.3) may be used to describe the wind for  $r = R$  only. In other words, the equation specifies the windfield at a radial distance equal to the radius to maximum winds.

23. The following relationship is used to specify the 10-m, 10-min overwater winds at any distance ( $r$ ) from the hurricane center:

$$V = V_s + 1.5T^{.63} \cos \beta \quad (2.3.4)$$

where  $V_s$  is the windspeed in a stationary hurricane at radius  $r$ . Relative winds profiles based upon observed hurricanes are developed for  $0 < r < R$  and  $r > R$  in Chapter 13 in Schwerdt et al. [2]. It is possible to also employ the Hydromet pressure profile in Equation (2.2) to compute the profile.

24. Tetra Tech based upon work by Collins and Viehman [12] assume the following radial distribution for the maximum hurricane windspeed.

$$V_{\max}(r) = \left\{ \begin{array}{ll} \frac{\bar{V}_{\max}}{c_1 r^k} \log_{10} \frac{R}{c_2 r^m} & r > R \\ 1.5 \bar{V}_{\max} \left( \frac{r}{R} - \frac{1}{3} \right) & R \leq r < R/3 \\ 0 & R/3 \geq r \end{array} \right\} \quad (2.3.5)$$

where

$V_{\max}(r)$  = maximum windspeed at radius  $r$  (kts)

$\bar{V}_{\max}$  = maximum windspeed over all  $r$ ,  $r = R$  (kts)

$k = -.15128$

$c_1 = 3.354$

$m = 1.607$

$c_2 = 1.265 \times 10^{-3}$

25. To completely determine the windfield the location of the radial of maximum winds with respect to the storm direction must be specified. Schwerdt et al. [2] allow the radial of maximum winds to be in the interval ( $0^\circ$ ,  $180^\circ$ ) measured clockwise with respect to the track direction. In the Tetra Tech



model, [5] the locus of maximum winds at any given radial length  $r$  is a line inclined at  $(90^\circ + \alpha)$  to the direction of hurricane motion.  $\alpha$  is a user specified incurvature angle, which does not vary with radial length  $r$ .

### Angular Conventions

26. Consider the hurricane windfield setup sketched in Figure II-2 below. Note from the construction, we obtain  $\alpha + 90^\circ = \beta + \delta = \theta + \delta$ , and therefore  $\theta = \beta$ . Since the  $\cos x = \cos(-x)$ ,  $\theta$  may be measured either clockwise or counterclockwise from the radial of maximum wind.

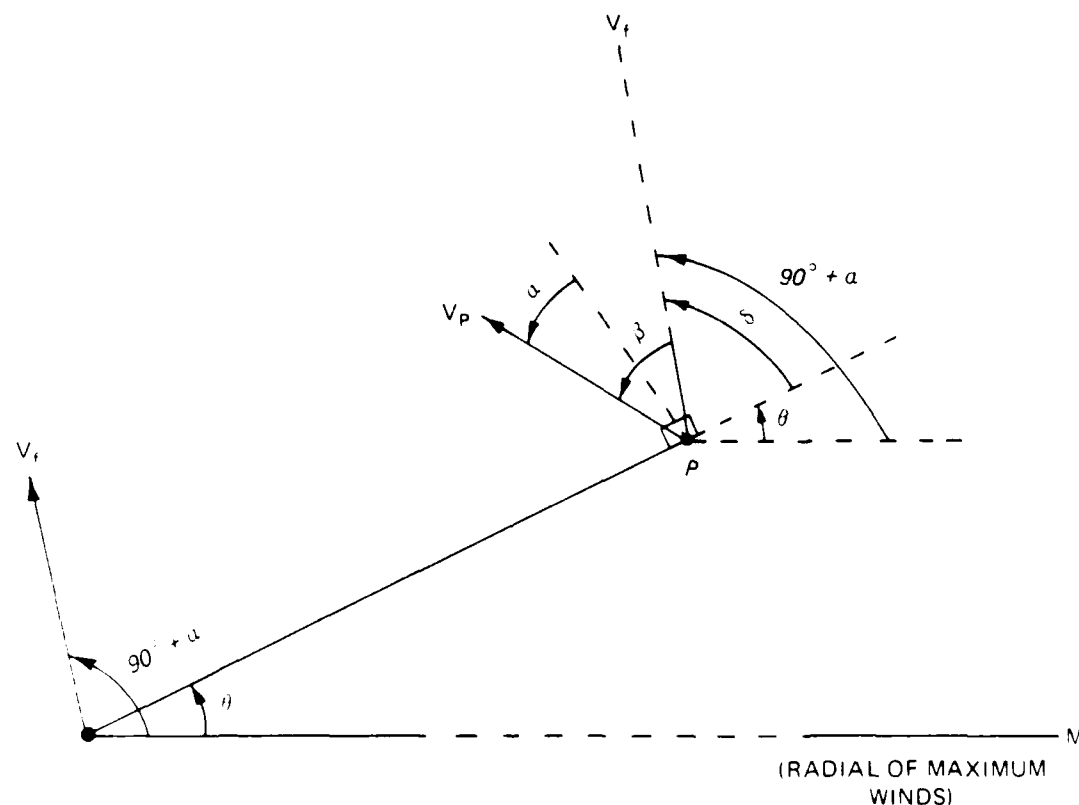


Figure II-2. Asymmetry Angle Relationships

27. In the implementation of the above procedures the following approach outlined in Figure II-3 is employed. Thus, when the maximum wind-speed is specified  $-5.V_f$  is added to convert the maximum windspeed to equivalent stationary storm case. This is necessary since the asymmetry relations

$$A_{\text{Reid}} = -.5 V_f (1 - (\cos \theta_P \cos \theta_A + \sin \theta_P \sin \theta_A))$$

$$A_s = .5 V_f \cos \theta' = .5 V_f \cos (\theta_P - \theta_A) = .5 V_f (\cos \theta_P \cos \theta_A + \sin \theta_P \sin \theta_A)$$

$$A_{\text{Reid}} = A_s - .5 V_f$$

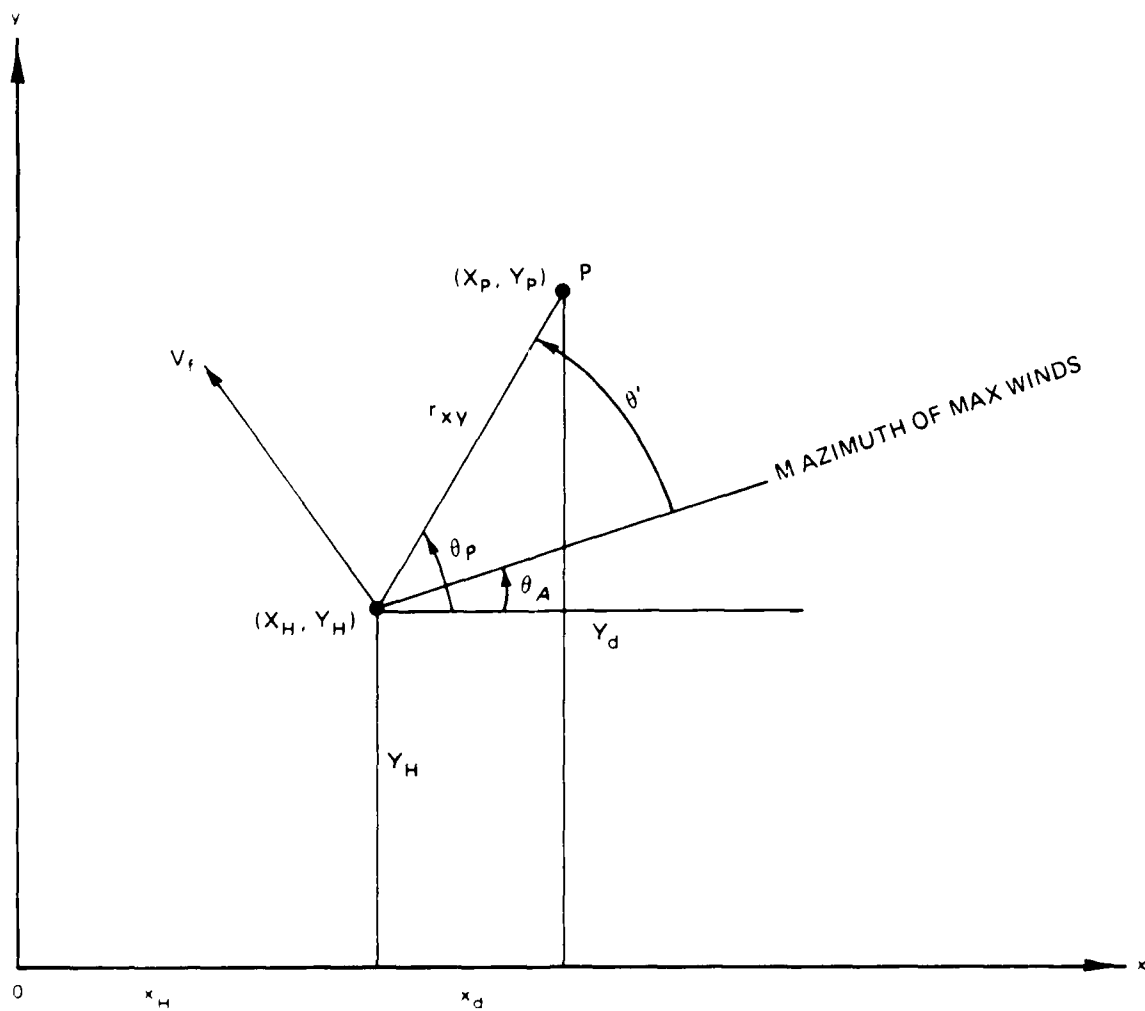


Figure II-3. SPH Model Asymmetry Relationships

are to be applied directly only to the stationary hurricane. The azimuth of maximum winds may be specified and is not equal to  $90^\circ + \alpha$ . The  $\theta$  concept is used to specify the asymmetry.

28. In the current SPH approach, the inflow angle ( $\alpha$ ) is specified as a constant. Thus the wind direction,  $\theta_w$ , equals  $\theta_p + \alpha + 90^\circ$  as shown in Figure II-4 below.

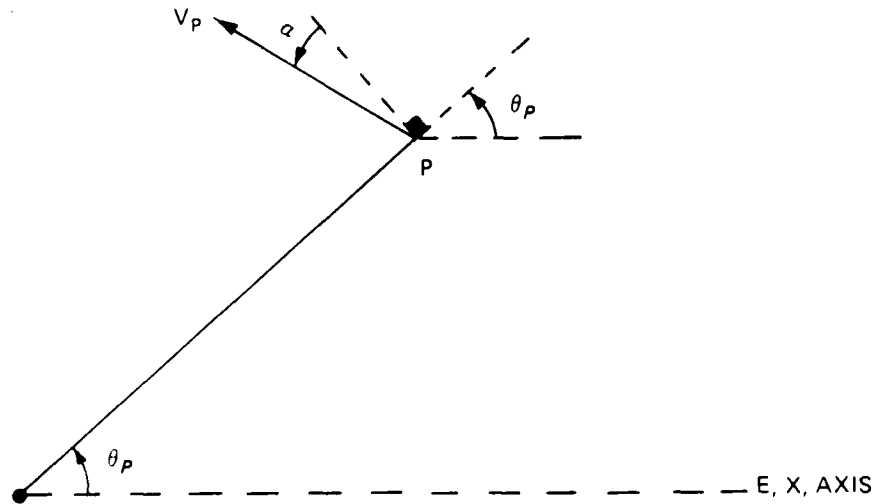


Figure II-4. Determination of Wind Direction

In component form, we have for the windspeed:

$$V_x = V_p \cos(\theta_p + \alpha + 90^\circ) = (-\sin\theta_p \cos\alpha - \sin\alpha \cos\theta_p) V_p \quad (a)$$

(2.3.6)

$$V_y = V_p \sin(\theta_p + \alpha + 90^\circ) = (-\cos\theta_p \cos\alpha - \sin\theta_p \sin\alpha) V_p \quad (b)$$

#### Planetary Boundary Layer Approach

##### General Theory

29. Chow [11] considered the following vertically averaged equation of motion in vector form with respect to coordinates fixed to the earth:

$$\frac{d\hat{w}}{dt} + f|\mathbf{k} \times \hat{w} = - \frac{1}{\rho} \nabla P + \nabla \cdot (k_H \nabla \hat{w}) - \frac{C_D}{h} |\hat{w}| \hat{w} \quad (3.1.1)$$

with

$$\frac{d}{dt} = \frac{\partial}{\partial t} + \hat{w} \cdot \nabla \quad \nabla = \frac{\partial}{\partial x} \mathbf{i} + \frac{\partial}{\partial y} \mathbf{j}$$

where

$\frac{\partial}{\partial t} \equiv$  time change local to the fixed coordinates

$\nabla \equiv$  two dimensional del operator

$\hat{w} \equiv$  vertically averaged horizontal velocity

$f \equiv$  Coriolis parameter

$\mathbf{i}, \mathbf{j}, \mathbf{k} \equiv$  unit vectors in the x, y, and z directions, respectively

$k_H \equiv$  Horizontal eddy viscosity coefficient

$C_D \equiv$  Drag coefficient

$h \equiv$  Depth of the planetary boundary layer

$P \equiv$  pressure

$\rho \equiv$  mean air density

It is assumed that the vertical advection of momentum, shear stress at the top of the boundary layer, and the turning angle are all zero.

30. The pressure  $P$  is given as the sum of  $P_c$ , the pressure field representing a tropical cyclone assumed to move at a constant velocity  $\hat{w}_c$ , and  $\bar{P}$  a large-scale pressure field of a constant gradient. The corresponding constant geostrophic flow,  $\hat{w}_g$  is given by the following equation:

$$f|\mathbf{k} \times \hat{w}_g = - \frac{1}{\rho} \nabla \bar{P} \quad (3.1.2)$$

Thus, Equation (3.1.1) may be written as follows:

$$\frac{d\hat{w}}{dt} + f|\mathbf{k} \times (\hat{w} - \hat{w}_g) = - \frac{1}{\rho} \nabla P_c + \nabla \cdot (k_H \nabla \hat{w}) - \frac{C_D}{h} |\hat{w}| \hat{w} \quad (3.1.3)$$

31. Let us now consider a moving Cartesian coordinate system (x, y) whose origin is located at the moving low center. Therefore, we may obtain:

$$\begin{aligned}\hat{w} &= w + \hat{w}_c \\ \hat{w}_g &= w_g + \hat{w}_c\end{aligned}\quad (3.1.4)$$

Substituting relations (3.1.4) into (3.1.3) we obtain:

$$\begin{aligned}\frac{d}{dt}(w + \hat{w}_c) + f|k \times (w - w_g) = \frac{1}{\rho} \nabla P_c + \nabla \cdot [k_H \nabla (w + \hat{w}_c)] \\ - \frac{C_D}{h} |w + \hat{w}_c| (w + \hat{w}_c)\end{aligned}\quad (3.1.5)$$

Noting that  $\frac{d\hat{w}_c}{dt} = 0 \Rightarrow \nabla \hat{w}_c = 0$ , we obtain the following simplification:

$$\frac{dw}{dt} + f|k \times (w - w_g) = - \frac{1}{\rho} \nabla P_c + \nabla \cdot (k_H \nabla w) - \frac{C_D}{h} |w + \hat{w}_c| (w + \hat{w}_c) \quad (3.1.6)$$

$$\text{Note: } \frac{dw}{dt} = \frac{\partial w}{\partial t} + (w + \hat{w}_c) \cdot \nabla w = \frac{\partial w}{\partial t} + \hat{w}_c \cdot \nabla w + w \cdot \nabla w = \left( \frac{\partial w}{\partial t} \right)_c + w \cdot \nabla w$$

We observe in (3.1.6) that  $w$  is the horizontal wind relative to the low center and  $(\partial w / \partial t)_c$  is the local acceleration in the moving coordinate system. Since  $\nabla P_c$  is time invariant in the moving coordinate system, the windfield may be determined as a steady state solution  $[(\partial w / \partial t)_c \rightarrow 0]$  in this system. Calculations are actually made as an initial value problem in which time marching is performed until the windfield becomes approximately steady.

32. Let us consider  $w = (u, v)$ ,  $w_g = (u_g, v_g)$ , and  $\hat{w}_c = (\hat{u}_c, \hat{v}_c)$  then Equation (3.1.6) may be written in the following component form noting:

$$-f|k \times (w - w_g) = - \begin{vmatrix} |i & |j & |k \\ 0 & 0 & f \\ (u - u_g) & (v - v_g) & 0 \end{vmatrix} = + (v - v_g) f|i - (u - u_g) f|j \quad (a)$$

(3.1.7)

$$\frac{du}{dt} = fv - P_u + H_u - F_u \quad (b)$$

$$\frac{dv}{dt} = fu - P_v + H_v - F_v \quad (c)$$

where

$$H_u = \frac{\partial}{\partial x} \left( k_H \frac{\partial u}{\partial x} \right) + \frac{\partial}{\partial y} \left( k_H \frac{\partial u}{\partial y} \right)$$

$$H_v = \frac{\partial}{\partial x} \left( k_H \frac{\partial v}{\partial x} \right) + \frac{\partial}{\partial y} \left( k_H \frac{\partial v}{\partial y} \right)$$

$$P_u = f v_g + \frac{1}{\sigma} \frac{\partial F_c}{\partial x}$$

$$P_v = -f u_g + \frac{1}{\sigma} \frac{\partial P_c}{\partial y}$$

$$F_u = \frac{C_D}{h} \left[ (u + \hat{u}_c)^2 + (v + \hat{v}_c)^2 \right]^{1/2} (u + \hat{u}_c)$$

$$F_v = \frac{C_D}{h} \left[ (u + \hat{u}_c)^2 + (v + \hat{v}_c)^2 \right]^{1/2} (v + \hat{v}_c)$$

Note that the terms  $F_u$ ,  $F_v$  depend on the wind relative to the fixed coordinates. The non-linear lateral diffusion coefficient  $k_H$  is expressed following Smagorinsky [13] as follows:

$$k_H = 2k_0^2 \left( \frac{\Delta}{2} \right)^2 |\text{Def}| \quad (3.1.8)$$

where

$$|\text{Def}| = \left( D_T^2 + D_S^2 \right)^{1/2}$$

$$D_T = \frac{\partial u}{\partial x} - \frac{\partial v}{\partial y}$$

$$D_S = \frac{\partial v}{\partial x} + \frac{\partial u}{\partial y}$$

$$k_0 = .4, \text{ von Kàrmàn's constant}$$

33. In practice the geostrophic wind components are specified relative to the fixed coordinates, thus in the expressions for  $P_u$  and  $P_v$  above:

$$u_g = u_g^f - \hat{u}_c, \quad v_g = v_g^f - \hat{v}_c$$

where

$$(u_g^f, v_g^f) = \text{the specified geostrophic wind}$$

34. Cardone [14] has considered an alternative form of Equation (3.1) in which the turning angle is non-zero. A revised parameterization of the planetary boundary layer as outlined by Arya [15] is employed to compute the drag coefficient  $C_D$  as well as the turning angle,  $\beta$ .

35. The surface drag relations may be computed with respect to the mean (vertically integrated) planetary boundary layer wind as indicated in Equation set (3.1.9) below.

$$U_{\star}^2 = C_D V_m$$

where

$$(3.1.9) \quad \begin{aligned} 1. \quad & V_m^2 = u_m^2 + v_m^2 \\ & C_D \equiv \text{drag coefficient} \\ & u_m, v_m \equiv \text{mean wind compounds along the direction and} \\ & \quad \text{perpendicular to the surface drag} \\ & U_{\star}^2 = \left( \sqrt{\frac{\tau_o}{\rho_c}} \right) \text{friction velocity} \\ 2. \quad & ku_m/U_{\star} = -(\ln \hat{z}_o + A_m) \\ & kv_m/U_{\star} = -B_m \text{ sign } f \text{ (Note sign } f, \text{ for our case, +)} \\ 3. \quad & k(\theta_{vm} - \theta_{vo})/\theta_{\star} = -(\ln \hat{z}_o + c_m) \end{aligned}$$

In 2 and 3 above  $\hat{z}_o = z_o/h$  where  $h$  is the height of the boundary layer (assumed spatially uniform) and  $z_o$  a surface roughness.

36. Arya [15] presents the following relations for  $A_m$ ,  $B_m$  and  $C_m$ :

$$\left. \begin{aligned} A_m &= \ln(-h/L) + 1.5 \\ B_m &= 1.8 \exp(.2h/L) \\ C_m &= \ln(-h/L) + 3.7 \end{aligned} \right\} \begin{aligned} &h/L \leq -2 \quad fh/V_{\star} = 1 \\ &(\text{unstable}) \end{aligned} \quad (3.1.10a)$$

$$\left. \begin{aligned} A_m &= -.96(h/L) + 2.5 \\ B_m &= .2(h/L) + 1.1 \\ C_m &= -2.0(h/L) + 4.7 \end{aligned} \right\} \begin{aligned} h/L &\geq +2 \\ (\text{stable}) \end{aligned} \quad (3.1.10b)$$

For  $-2 < h/L < 2$ , linear interpolation between unstable conditions at  $h/L = -2$  and stable conditions at  $h/L = 2$  is employed to determine  $A_m$ ,  $B_m$ , and  $C_m$ .

37. In the above,  $h$ , represents the height of the boundary layer and is considered by Cardone [14] as a constant. The Monin-Obukhov length,  $L$ , is computed as follows:

$$L = \frac{\theta_{vo} U_*^3}{Kg(\overline{\theta u_3})_o} \quad (3.1.11)$$

where

$L \equiv$  Monin-Obukhov length

$U_* \equiv$  Friction velocity

$K \equiv$  von Karman's constant

$g \equiv$  Gravity

$\theta_{vo} \equiv$  Average temperature at the surface

$(\overline{\theta u_3})_o \equiv$  Time average of the product of the temperature and vertical velocity component fluctuations at the surface

Since  $\theta_* = (\overline{\theta u_3})_o / U_*$ ,  $L = \frac{\theta_{vo} U_*^2}{K \theta_*}$ . For an unstable atmospheric condition,  $(\overline{\theta u_3})_o > 0 \rightarrow \theta_* > 0 \rightarrow L < 0$ . If we consider the parameterization involving  $\theta_*$ , the following relationship for  $L$  is obtained:

$$L = \frac{\theta_{vo} (\ln \frac{z_o}{z_m} + C_m) U_*^2}{K^2 g (\theta_{vm} - \theta_{vo})} \quad (3.1.12)$$



If  $(\ln \hat{z}_o + C_m) > 0$ , then the sign of  $L$  is determined by the sign of  $(\theta_{vm} - \theta_{vo})$ .

38. The values of  $\theta_{vo}$ ,  $\theta_{vm} - \theta_{vo}$  are specified. For a given  $V_m$  and iteration values for  $U_*$  and  $C_m$ , compute  $L$  and  $h/L$  and  $\hat{z}_o$ . The roughness length  $z_o = a/g U_*^2$ , where  $a$  is considered equal to .035. The surface corresponds to open ocean. Then determine  $A_m$ ,  $B_m$ , and  $C_m$ . Compute an iterated value of  $V_m$ ,  $V_m^u$  as follows:

$$(V_m^u)^2 = (U_*^2/k^2) \left[ (\ln \hat{z}_o + A_m)^2 + B_m^2 \right] \quad (3.1.13)$$

(Note  $V_m^u$  is determined from  $U_*$ ,  $A_m$ ,  $B_m$ , and  $C_m$ ). The procedures are iterated until  $V_m^u$  and  $V_m$  are tolerably close using the following inverse interpolation scheme. Let  $DUV_{*i} = (V_m^u)^2 - (V_m)^2$  corresponding to  $U_{*i}$ . If these two quantities are known for  $i = 1$  and  $2$ , then an updated value for  $U_*$ ,  $U_n$  is calculated with reference to the Figure II-5 below as follows.

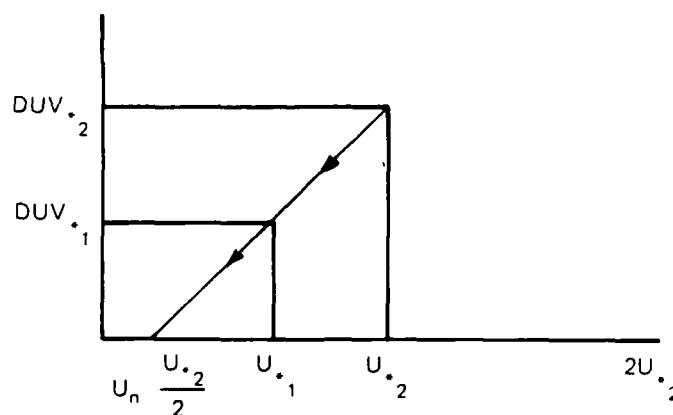


Figure II-5. Inverse Interpolation Scheme

$$\frac{U_n - U_{*2}}{0 - DUV_{*2}} = \frac{U_{*1} - U_{*2}}{DUV_{*1} - DUV_{*2}} \quad (a)$$

$$U_n - U_{*2} = \frac{-DUV_{*2} (U_{*1} - U_{*2})}{DUV_{*1} - DUV_{*2}} \quad (b)$$

$$U_n = U_{*2} - \frac{DUV_{*2} (U_{*1} - U_{*2})}{DUV_{*1} - DUV_{*2}} \quad (c)$$

(3.1.14)

$$U_n = \frac{U_{*1} (DUV_{*1} - DUV_{*2}) - DUV_{*2} (U_{*1} - U_{*2})}{DUV_{*1} - DUV_{*2}} \quad (d)$$

$$U_n = \frac{U_{*2} DUV_{*1} - DUV_{*2} U_{*1}}{DUV_{*1} - DUV_{*2}} \quad (e)$$

$U_n$  is limited with the range  $\left(\frac{U_{*2}}{2}, 2U_{*2}\right)$ . Thus in the situation shown in

Figure II-5,  $U_n = \frac{U_{*2}}{2}$ .

The drag coefficient,  $C_D$ , and turning angle,  $\beta$ , are then determined as follows:

$$C_D = \frac{K^2}{(\ln z_o + A_m)^2 + B_m^2} \quad (a)$$

(3.1.15)

$$\beta = \tan^{-1} \frac{B_m}{-(\ln \hat{z}_o + A_m)} = \tan^{-1} \frac{-V_m}{U_m}, \beta > 0 \quad (b)$$

39. Cardone [14] seeks now to modify the third term (friction term) on the right-hand side of the motion equation to account for the fact that (in the northern hemisphere) the surface wind in a hurricane is turned inward with respect to mean wind over the boundary layer.

40. In the parameterization of the planetary boundary layer employed above, a coordinate system whose x-axis is aligned in the direction of the surface wind is employed. In this system,  $V_m < 0$  as indicated in Figure II-6.

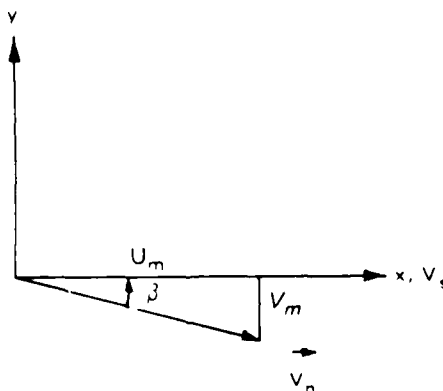


Figure II-6. Planetary Boundary Layer Parameterization Coordinate System

In Equation (3.6), a Cartesian coordinate system whose y-axis is aligned in the direction of North and whose origin moves with the center of the storm is employed. The situation is shown in Figure II-7 for an arbitrary field point in this system.

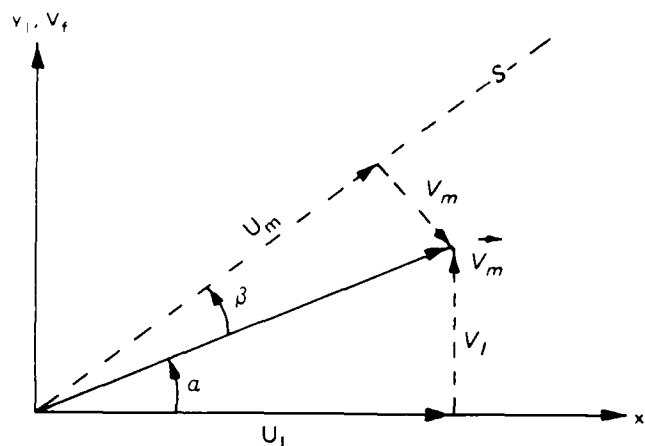


Figure II-7. Planetary Boundary Layer Computational Coordinate System

41. In order to characterize the conditions at the surface,  $\vec{V}_m$  is rotated through  $\beta$  to obtain  $\vec{V}_s$ . The friction effect,  $F$ , is then resolved in the  $x_1 - y_1$  system as follows:

$$F = \frac{-C_D}{h} |\vec{V}_s|^2 \vec{V}_s \quad (a)$$

$$|\vec{V}_s| = |\vec{V}_m| = \sqrt{U_1^2 + V_1^2} \quad (b)$$

(3.1.16)

$$F_x = \frac{-C_D}{h} |\vec{V}_s|^2 \cos s \quad (c)$$

$$F_y = \frac{-C_D}{h} |\vec{V}_s|^2 \sin s \quad (d)$$

where

$$s = \alpha + \beta$$

Noting

$$\sin s = \sin (\alpha + \beta) = \sin \alpha \cos \beta + \sin \beta \cos \alpha$$

$$\cos s = \cos (\alpha + \beta) = \cos \alpha \cos \beta - \sin \alpha \sin \beta$$

we obtain:

$$\cos \alpha = \frac{U_1}{\sqrt{U_1^2 + V_1^2}} \quad (a)$$

$$\sin \alpha = \frac{V_1}{\sqrt{U_1^2 + V_1^2}} \quad (b)$$

$$\cos \beta = \frac{-(\ln \hat{z}_o + A_m)}{\sqrt{B_m^2 + (\ln \hat{z}_o + A_m)^2}} \quad (c)$$

$$\sin \beta = \frac{B_m}{\sqrt{B_m^2 + (\ln \hat{z}_o + A_m)^2}} \quad (d)$$

Using the above formulae, we finally obtain:

$$\cos s = \frac{-(\ln \hat{z}_o + A_m) U_1 - V_1 B_m}{\sqrt{U_1^2 + V_1^2} \sqrt{B_m^2 + (\ln \hat{z}_o + A_m)^2}} \quad (a)$$

$$\sin s = \frac{U_1 B_m - (\ln \hat{z}_o + A_m) V_1}{\sqrt{(U_1^2 + V_1^2) (B_m^2 + (\ln \hat{z}_o + A_m)^2)}} \quad (b)$$

42. In implementing the turning angle-drag coefficient procedures, a tabular approach is followed. For  $|\vec{V}_m| \in (.8, 80 \text{ kts})$ ,  $C_D$  and  $\beta$  are calculated for a water surface. Thus for an arbitrary field point,  $|\vec{V}_m|$  is known (at the previous time step) and  $C_D$  and  $\beta$  may be determined from the tabular values.

### The Posing of the Initial Value Problem

43. Since the pressure gradient is time invariant in the moving Cartesian coordinate system fixed to the storm center, the local acceleration in this system is zero and the solution to the motion equation is a steady state solution. The steady state solution is obtained by formulating an initial value problem and marching the computations in time until the computed windfield becomes steady. In this section, we consider the specification of the initial windfield and the exterior boundary conditions.

### Initial Windfield Specification

44. Let us consider the equations of steady horizontal motion in polar coordinates as written below:

$$v_r \frac{\partial v_r}{\partial r} + v_\theta \frac{\partial v_r}{r \partial \theta} - \frac{v_\theta^2}{r} = f v_\theta - \frac{1}{\rho} \frac{\partial p}{\partial r} \quad (a)$$

(3.3.1)

$$v_r \frac{\partial v_\theta}{\partial r} + v_\theta \frac{\partial v_\theta}{r \partial \theta} - \frac{v_\theta v_r}{r} = -f v_r - \frac{1}{\rho} \frac{\partial p}{r \partial \theta} \quad (b)$$

where  $v_r$ ,  $v_\theta$  represent the radial and tangential velocity components.

45. Consider a circular pressure field as in a hurricane (concentric isobars with their centers at  $r = 0$ ). Then  $\partial P / \partial \theta = 0$ . If we assume that the velocity distribution has circular symmetry, then  $\partial v_r / \partial \theta = \partial v_\theta / \partial \theta = 0$ . If we take  $v_r = 0$ , the second equation is satisfied. Replacing  $v_\theta$  with  $c$  the first equation becomes:

$$\underbrace{\frac{c^2}{r}}_{C_e} + \underbrace{f c}_{C_o} - \underbrace{\frac{1}{\rho} \frac{\partial P}{\partial r}}_P = 0 \quad (3.3.2)$$

This equation represents a balance between centrifugal, Coriolis, and pressure gradient forces. Consider the case of cyclonic flow around a low. The force balance is represented as sketched below in Figure II-8.

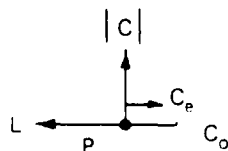


Figure II-8 Cyclonic Flow Force Balance

The solutions to the above equation are as follows and represent the so-called gradient wind:

$$c = \frac{fr}{2} \pm \sqrt{\frac{f^2 r^2}{4} + \frac{r}{S} \frac{\partial P}{\partial r}} \quad (3.3.3)$$

For  $c = v_\theta > 0$ , a counterclockwise motion (cyclonic in the Northern Hemisphere), is obtained. Thus the plus root in the above equation is considered to represent this flow condition. For a low  $\partial P / \partial r > 0$  and the square root can never become imaginary so that all values of pressure gradient are possible.

46. The gradient wind condition is specified as the initial windfield condition over the computational domain. In order to determine the gradient wind at an arbitrary field point, the radial pressure derivative must be determined. This is determined by assuming a circularly symmetric pressure field defined as follows:

$$P(r) = P_o + (P_n - P_o) e^{-R/r}$$

Therefore,

$$\frac{\partial P}{\partial r} = \frac{(P_n - P_o) R}{r^2} e^{-R/r}$$

Thus the gradient wind becomes:

$$c = \frac{fr}{2} + \sqrt{\frac{f^2 r^2}{4} + \frac{R(P_n - P_o)}{r^2} e^{-R/r}} \quad (3.3.4)$$

For large  $r$ , this formula represents  $c$  as the difference of two nearly equal terms, as a result the following equivalent form is used by Cardone [14]:

$$c = \frac{\frac{R(P_n - P_o)}{r\rho} e^{-R/r}}{\frac{1}{2}fr + \sqrt{\frac{1}{2}fr^2 + \frac{R(P_n - P_o)}{r\rho} e^{-R/r}}} \quad (3.3.5)$$

#### Outermost Boundary Conditions

47. At the outermost boundary, the acceleration and horizontal diffusion are assumed negligible. A balance between Coriolis force, pressure gradient force and surface friction is assumed as shown below.

$$f\hat{k} \times (\vec{v} - \vec{v}_g) = -\frac{1}{\rho} \nabla P_c - \frac{C_D}{h} \left| \vec{v} + \vec{v}_c \right| (\vec{v} + \vec{v}_c) \quad (3.4.1)$$

Considering unit vectors  $\hat{i}$ ,  $\hat{j}$ , and  $\hat{k}$  in the x, y, and z directions, the above equation is written in component form as follows: (3.4.2)

$$\begin{vmatrix} \hat{i} & \hat{j} & \hat{k} \\ 0 & 0 & f \\ u - u_g^f + \hat{u}_c & v - v_g^f + \hat{v}_c & 0 \end{vmatrix} = -\frac{1}{\rho} \left( \frac{\partial P_c}{\partial x} \hat{i} + \frac{\partial P_c}{\partial y} \hat{j} \right)$$

$$- \frac{C_D}{h} \left| \vec{v} + \vec{v}_c \right| \left[ (u + \hat{u}_c) \hat{i} + (v + \hat{v}_c) \hat{j} \right]$$

x components: (3.4.3)

$$-f(v - v_g^f + \hat{v}_c) = -\frac{1}{\rho} \frac{\partial P_c}{\partial x} - \frac{C_D}{h} \sqrt{(u + \hat{u}_c)^2 + (v + \hat{v}_c)^2} (u + \hat{u}_c)$$

y components: (3.4.4)

$$f(u - u_g^f + \hat{u}_c) = -\frac{1}{\rho} \frac{\partial P_c}{\partial y} - \frac{C_D}{h} \sqrt{(u + \hat{u}_c)^2 + (v + \hat{v}_c)^2} (v + \hat{v}_c)$$

48. In order to develop the computational method, it is necessary to use the following relationships:



$$-f [(v + \hat{v}_c) - v_g^f] = -\frac{1}{\sigma} \frac{\partial P_c}{\partial x} - \frac{C_D}{h} \sqrt{(u + \hat{u}_c)^2 + (v + \hat{v}_c)^2} (u + \hat{u}_c) \quad (a)$$

(3.4.5)

$$f [(u + \hat{u}_c) - u_g^f] = -\frac{1}{\sigma} \frac{\partial P_c}{\partial y} - \frac{C_D}{h} \sqrt{(u + \hat{u}_c)^2 + (v + \hat{v}_c)^2} (v + \hat{v}_c) \quad (b)$$

$$-f (v + v_g^f) = -\frac{1}{\sigma} \frac{\partial P_c}{\partial x} - \frac{C_D}{h} \sqrt{u^2 + v^2} u \quad (a)$$

(3.4.6)

$$f (u + u_g^f) = -\frac{1}{\sigma} \frac{\partial P_c}{\partial y} - \frac{C_D}{h} \sqrt{u^2 + v^2} v \quad (b)$$

$$-fv = -\overbrace{\frac{1}{\sigma} \frac{\partial P_c}{\partial x} - fv_g^f}^{-P_x} - \frac{C_D}{h} \sqrt{u^2 + v^2} u \quad (a)$$

(3.4.7)

$$fu = -\overbrace{\frac{1}{\sigma} \frac{\partial P_c}{\partial y} + fu_g^f}^{-P_y} - \frac{C_D}{h} \sqrt{u^2 + v^2} v \quad (b)$$

$$-fv = -P_x - \frac{C_D}{h} \sqrt{u^2 + v^2} u \quad (a)$$

(3.4.8)

$$fu = -P_y - \frac{C_D}{h} \sqrt{u^2 + v^2} v \quad (b)$$

From Equation (3.4.8) obtain the following supplemental relations:

$$\frac{C_D}{h} (u^2 + v^2) = -\frac{P_x \sqrt{u^2 + v^2} + fv \sqrt{u^2 + v^2}}{u} \quad (a)$$

(3.4.9)

$$\frac{C_D}{h} (u^2 + v^2) = -\frac{P_y \sqrt{u^2 + v^2} + fu \sqrt{u^2 + v^2}}{v} \quad (b)$$

From Equation (3.4.8) (a) and (b) we also obtain:

$$P_x = fv - \frac{C_D}{h} \sqrt{u^2 + v^2} u \quad (a)$$

(3.4.10)

$$P_y = -fu - \frac{C_D}{h} \sqrt{u^2 + v^2} v \quad (b)$$

Thus, we may obtain after some algebra:

$$P_x^2 + P_y^2 = (u^2 + v^2) \left[ f^2 + \left( \frac{C_D}{h} \right)^2 (u^2 + v^2) \right] \quad (3.4.11)$$

Note:

$$\begin{aligned} f^2 + \left( \frac{C_D}{h} \right)^2 (u^2 + v^2) &= \frac{f^2}{2} + \sqrt{\left[ \frac{f^2}{2} + \left( \frac{C_D}{h} \right)^2 (u^2 + v^2) \right]^2} \\ &= \frac{f^2}{2} + \sqrt{\frac{f^4}{4} + \left( \frac{C_D}{h} \right)^2 f^2 (u^2 + v^2) + \left( \frac{C_D}{h} \right)^4 (u^2 + v^2)^2} \\ &= \frac{f^2}{2} + \sqrt{\frac{f^4}{4} + \frac{C_D^2}{h^2} \left[ f^2 (u^2 + v^2) + \left( \frac{C_D}{h} \right)^2 (u^2 + v^2)^2 \right]} \end{aligned}$$

and from Equation (3.4.11)

$$= \frac{f^2}{2} + \sqrt{\frac{f^4}{4} + \left( \frac{C_D}{h} \right)^2 (P_x^2 + P_y^2)}$$

Thus obtain:

$$P_x^2 + P_y^2 = (u^2 + v^2) \left[ \frac{f^2}{2} + \sqrt{\frac{f^4}{4} + \left( \frac{C_D}{h} \right)^2 (P_x^2 + P_y^2)} \right] \quad (3.4.12)$$

or

$$u^2 + v^2 = (P_x^2 + P_y^2) / \left[ \frac{f^2}{2} + \sqrt{\frac{f^4}{4} + \frac{C_D^2}{h} (P_x^2 + P_y^2)} \right] \quad (3.4.13)$$

Equation (3.4.13) relates  $u$  and  $v$  to  $P_x$ ,  $P_y$ ,  $C_D$ ,  $h$ , and  $f$ .

Let us consider Equation (3.4.8) (a). Multiply by  $f$  and subtract

$-\frac{C_D}{h} P_y \sqrt{u^2 + v^2}$  from both sides to obtain:

$$vf^2 - \frac{C_D}{h} P_y \sqrt{u^2 + v^2} - \frac{C_D}{h} fu \sqrt{u^2 + v^2} = fP_x - \frac{C_D}{h} \sqrt{u^2 + v^2} P_y \quad (a)$$

(3.4.14)

$$v \left[ f^2 + \frac{C_D}{h} \left( \frac{P_y \sqrt{u^2 + v^2}}{v} - fu \sqrt{u^2 + v^2} \right) \right] = fP_x - \frac{C_D}{h} \sqrt{u^2 + v^2} P_y \quad (b)$$

Using Equation (3.4.13) (b) we may obtain:

$$v \left[ f^2 + \left( \frac{C_D}{h} \right)^2 (u^2 + v^2) \right] = fP_x - \frac{C_D}{h} \sqrt{u^2 + v^2} P_y \quad (3.4.15)$$

Using Equation (3.4.13) next obtain:

$$v = \frac{fP_x - \frac{C_D}{h} \sqrt{u^2 + v^2} P_y}{f^2 + \left( \frac{C_D}{h} \right)^2 \left\{ (P_x^2 + P_y^2) / \left[ \frac{f^2}{2} + \sqrt{\frac{f^4}{4} + \left( \frac{C_D}{h} \right)^2 (P_x^2 + P_y^2)} \right] \right\}} \quad (3.4.16)$$

Then to solve for  $u$  employ Equation (3.4.18) (b); e.g.

$$u = \frac{-P_y - \frac{C_D}{h} v \sqrt{(P_x^2 + P_y^2) / \left[ \frac{f^2}{2} + \sqrt{\frac{f^4}{4} + \left( \frac{C_D}{h} \right)^2 (P_x^2 + P_y^2)} \right]}}{f} \quad (3.4.17)$$

The numerical algorithm is constructed in the following manner:

$$1. \quad AA = \left( \frac{C_D}{h} \right)^2 \left( p_x^2 + p_y^2 \right)$$

$$2. \quad SK = \frac{AA}{\left( \frac{f^2}{2} + \sqrt{AA + \frac{f^4}{4}} \right)}$$

$$3. \quad BK = SK$$

$$V = \frac{f p_x - BK p_y}{f^2 + SK}$$

$$u = - \frac{(p_y + V BK)}{f}$$

#### Planetary Boundary Layer Approach Numerical Solution

49. A numerical solution is sought to Equation (3.1.7). In order to resolve the highly curved flows a nested grid system is employed. Finite difference approximations are employed on this nested grid system to effect the solution. In this section we develop the nested grid system conventions, the general finite difference approximations, and the treatment of the inner-mesh boundary conditions.

#### Nested Grid System Conventions

50. A nested grid system of order five is employed such that ( $\Delta_{i+1} = 2\Delta_i$ ,  $i = 1, \dots, 4$ ) the grid spacing doubles as one proceeds outward from the inner mesh. The setup for the first two grids is as sketched in Figure II-9. A similar relationship for the computational time step is employed; e.g., ( $\Delta t_{i+1} = 2\Delta t_i$ ,  $i = 1, \dots, 4$ ). The length of each side of grid 1 is equal to  $20\Delta_1$ . If as in the usual application,  $\Delta_1 = 5$  km, then  $\Delta_5 = \Delta_1 \cdot 2^4 = [( \Delta_1 \cdot 2 ) \cdot 2 ] \cdot 2 = 80$  km and the entire grid encompasses  $(1600 \text{ km})^2$ . Within the present computer code,  $\Delta t_1 = 10\Delta_1$ ; e.g., for  $\Delta_1 = 5$  km then  $\Delta t_1 = 50$  seconds.

<u>N</u>		<u>N + 1</u>
(1, 1)	≡	(6, 6)
(1, 21)	≡	(16, 6)
(21, 1)	≡	(6, 16)
(21, 21)	≡	(16, 16)

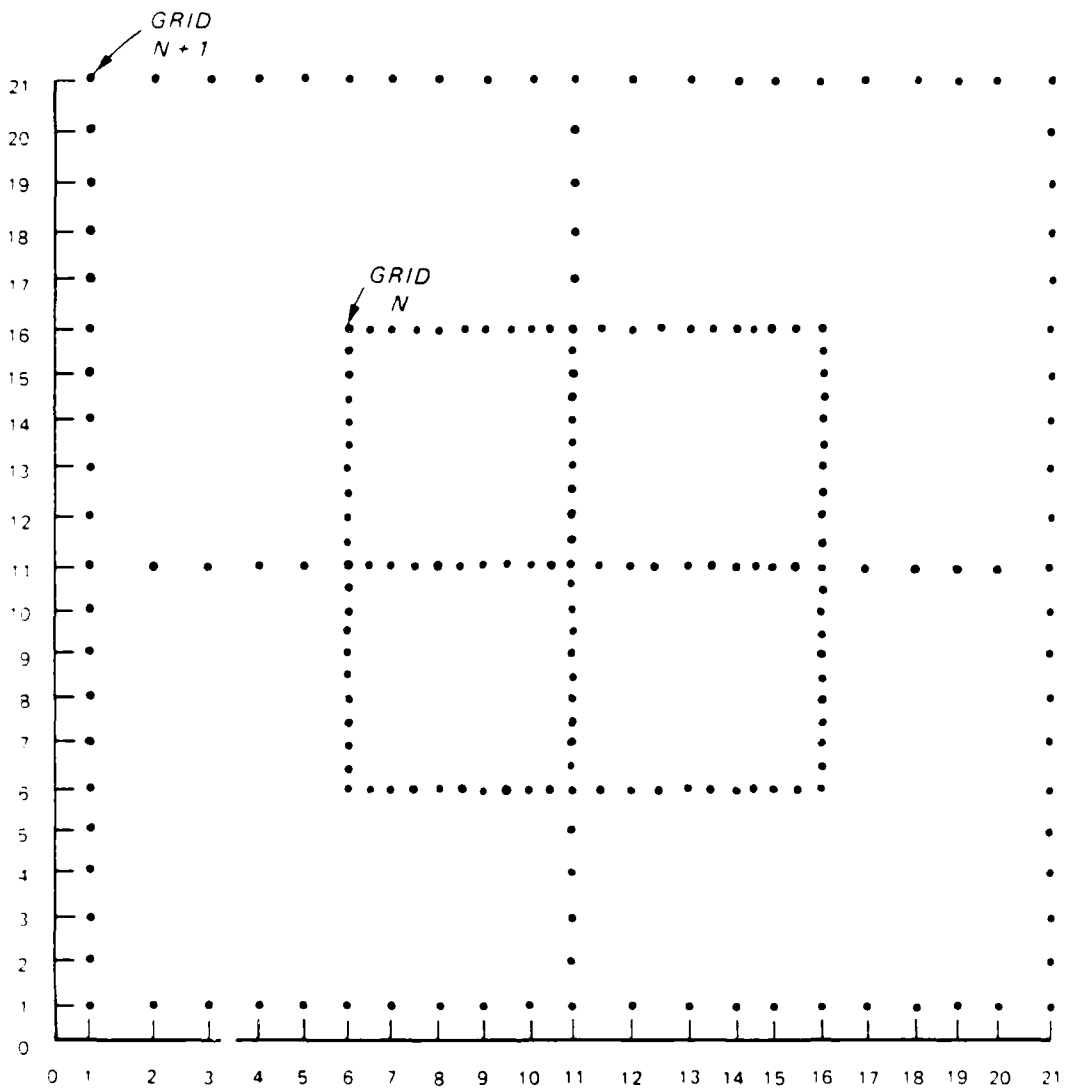


Figure II-9. Nested Grid System Convention

General Finite  
Difference Approximations

51. The finite difference formulation is the same for every grid. Therefore the formulation for the nth grid is presented with the subscript n omitted for ease of notation. The approximations for Equation (3.1.7) (b) and (c) are written in the following general form. (Note a general variable  $\phi(x, y, t)$  corresponds to a finite difference analog  $\phi(i\Delta, j\Delta, \tau)$ , where  $\tau = k\Delta t$ ).

$$\frac{u^{\tau+1} - u^{\tau}}{\Delta t} = -U^{\tau} + f v^{\tau+1} - P_u + H_u^{\tau} - F_u^{\tau} \quad (a)$$

(4.2.1)

$$\frac{v^{\tau+1} - v^{\tau}}{\Delta t} = -V^{\tau} - f u^{\tau+1} - P_v + H_v^{\tau} - F_v^{\tau} \quad (b)$$

where

$P_u, P_v \equiv$  Components of the known pressure gradient force (time invariant)

$U^{\tau}, V^{\tau} \equiv$  Finite difference approximations of the advective terms

$H_u^{\tau}, H_v^{\tau} \equiv$  Finite difference approximations of the horizontal diffusion  
of momentum

$F_u^{\tau}, F_v^{\tau} \equiv$  Surface friction terms

The treatment of the Coriolis force is implicit. Equation set (4.2.1) above is solved for  $u^{\tau+1}$  and  $v^{\tau+1}$  in the following manner.

Letting

$$B1 \equiv u^{\tau} + \Delta t \left( -U^{\tau} - P_u + H_u^{\tau} - F_u^{\tau} \right)$$

$$B2 \equiv v^{\tau} + \Delta t \left( -V^{\tau} - P_v + H_v^{\tau} - F_v^{\tau} \right)$$

then Equation (4.1) becomes:

$$u^{\tau+1} = B1 + f \Delta t v^{\tau+1} = B1 + FTL * v^{\tau+1}$$

$$v^{\tau+1} = B2 - f \Delta t u^{\tau+1} = B2 - FTL * u^{\tau+1} \quad (4.2.2)$$

where  $FTL = f \Delta t$

Solving the first equation for  $v^{\tau+1}$  and substituting the relation for  $v^{\tau+1}$  in the second equation one obtains:

$$\frac{u^{\tau+1} - B1}{FTL} = B2 - FTL * u^{\tau+1} \quad (4.2.3)$$

Solving for  $u^{\tau+1}$  one obtains:

$$u^{\tau+1} = \frac{FTL * B2 + B1}{(1 + FTL^2)} \quad (4.2.4)_a$$

Finally substituting in the first relation for  $v^{\tau+1}$  one obtains

$$v^{\tau+1} = \frac{B2 - FTL * B1}{(1 + FTL^2)} \quad (4.2.4)_b$$

Equation (4.2.4) represents the forms employed for computing  $u^{\tau+1}$  and  $v^{\tau+1}$ . In order to compute B1 and B2,  $(u^{\tau}, v^{\tau})$ ,  $(P_v, P_v)$ ,  $(H_u^{\tau}, H_v^{\tau})$ , and  $(F_u^{\tau}, F_v^{\tau})$  must be determined. We discuss the determination of these terms in turn below.

#### Finite Difference Approximations to the Advective Terms $(U^{\tau}, V^{\tau})$

52. Let us initially define the following difference operators:

$$\delta_x(\phi_{i,j}^{\tau}) = \frac{1}{\Delta} \left( \phi_{i+1/2,j}^{\tau} - \phi_{i-1/2,j}^{\tau} \right) \quad (a)$$

$$\delta_y(\phi_{i,j}^{\tau}) = \frac{1}{\Delta} \left( \phi_{i,j+1/2}^{\tau} - \phi_{i,j-1/2}^{\tau} \right) \quad (b)$$

(4.2.5)

$$\delta_x^D(\phi_{i,j}^{\tau}) = \frac{1}{\sqrt{2}\Delta} \left( \phi_{i+1/2,j+1/2}^{\tau} - \phi_{i-1/2,j-1/2}^{\tau} \right) \quad (c)$$

$$\delta_y^D(\phi_{i,j}^{\tau}) = \frac{1}{\sqrt{2}\Delta} \left( \phi_{i-1/2,j+1/2}^{\tau} - \phi_{i+1/2,j-1/2}^{\tau} \right) \quad (d)$$

Then employing these operators, we have:

$$u^{\tau} = \alpha \left[ u_{i,j}^{\tau} \delta_x (u_{i-\epsilon,j}^{\tau}) + v_{i,j}^{\tau} \delta_y (u_{i,j-r}^{\tau}) \right] \quad (a)$$

$$+ \beta \left[ u_{i,j}' \delta_x^D (u_{i-\epsilon',j-\epsilon'}^{\tau}) + v_{i,j}' \delta_y^D (u_{i+r',j-r'}^{\tau}) \right] \quad (4.2.6)$$

$$v^{\tau} = \alpha \left[ u_{i,j}^{\tau} \delta_x (v_{i-\epsilon,j}^{\tau}) + v_{i,j}^{\tau} \delta_y (v_{i,j-r}^{\tau}) \right] \quad (b)$$

$$+ \beta \left[ u_{i,j}' \delta_x^D (v_{i-\epsilon',j-\epsilon'}^{\tau}) + v_{i,j}' \delta_y^D (v_{i+r',j-r'}^{\tau}) \right]$$

where

$$u_{i,j}' = (u_{i,j}^{\tau} + v_{i,j}^{\tau}) / 2$$

$$v_{i,j}' = (-u_{i,j}^{\tau} + v_{i,j}^{\tau}) / 2$$

$$\epsilon = \frac{1}{2} u_{i,j}^{\tau} / |u_{i,j}^{\tau}|$$

$$r = \frac{1}{2} v_{i,j}^{\tau} / |v_{i,j}^{\tau}|$$

$$\epsilon' = \frac{1}{2} u_{i,j}' / |u_{i,j}'|$$

$$r' = \frac{1}{2} v_{i,j}' / |v_{i,j}'|$$

In the usual application  $\alpha = \beta = .5$ . The terms times  $\alpha$  represent upstream differencing while the terms times  $\beta$  correspond to diagonal upstream differencing.

Finite Difference Approximation to  
the Momentum Diffusion Terms ( $H_u$ ,  $H_v$ )

53. Let us introduce two additional finite difference operators as follows:



$$\left(\overline{\phi_{i,j}^\tau}\right)^x = \frac{1}{2} \left(\phi_{i+1/2,j}^\tau + \phi_{i-1/2,j}^\tau\right) \quad (a)$$

(4.4.1)

$$\left(\overline{\phi_{i,j}^\tau}\right)^y = \frac{1}{2} \left(\phi_{i,j+1/2}^\tau + \phi_{i,j-1/2}^\tau\right) \quad (b)$$

The approximations are then given as follows:

$$H_u = \delta_x \left[ \overline{K_H^y} \delta_x(u_{i,j}^\tau) \right] + \delta_y \left[ \overline{K_H^x} \delta_y(u_{i,j}^\tau) \right] \quad (a)$$

(4.4.2)

$$H_v = \delta_x \left[ \overline{K_H^y} \delta_x(v_{i,j}^\tau) \right] + \delta_y \left[ \overline{K_H^x} \delta_y(v_{i,j}^\tau) \right] \quad (b)$$

In the calculation of  $K_H$  :

$$D_T = \delta_x(\overline{u^y}) - \delta_y(\overline{v^x}) \quad (a)$$

(4.4.3)

$$D_S = \delta_x(\overline{v^y}) - \delta_y(\overline{u^x}) \quad (b)$$

Let us expand the first term in the approximation for  $H_u$  ( $H_v$  is analogous to  $H_u$  with  $u$  replaced by  $v$ ) .

$$\begin{aligned} \delta_x \left[ \overline{K_H^y} \delta_x(u_{i,j}^\tau) \right] &= \delta_x \left[ \frac{(K_{H,i,j+1/2} + K_{H,i,j-1/2})}{2} \frac{u_{i+1/2,j}^\tau - u_{i-1/2,j}^\tau}{\Delta} \right] = \\ &= \frac{(K_{H,i+1/2,j+1/2} + K_{H,i+1/2,j-1/2})}{2} \frac{(u_{i+1,j}^\tau - u_{i,j}^\tau)}{\Delta^2} - \\ &= \frac{(K_{H,i-1/2,j+1/2} + K_{H,i-1/2,j-1/2})}{2} \frac{(u_{i,j}^\tau - u_{i-1,j}^\tau)}{\Delta^2} = F_1 (u_{i+1,j}^\tau - u_{i,j}^\tau) \\ &\quad - F_2 (u_{i,j}^\tau - u_{i-1,j}^\tau) \end{aligned} \quad (4.4.4)$$

Noting  $K_{H,i,j} = f(D_{T,i,j}, D_{S,i,j})$  where

$$D_{T_{i,j}} = \delta_x \frac{(u_{i,j+1/2}^\tau + u_{i,j-1/2}^\tau)}{2} - \delta_y \frac{(v_{i+1/2,j}^\tau + v_{i-1/2,j}^\tau)}{2}$$

$$D_{S_{i,j}} = \delta_x \frac{(v_{i,j+1/2}^\tau + v_{i,j-1/2}^\tau)}{2} - \delta_y \frac{(u_{i+1/2,j}^\tau + u_{i-1/2,j}^\tau)}{2}$$

Expanding further we obtain the following relations for  $D_{T_{i,j}}$  and  $D_{S_{i,j}}$  :

$$\begin{aligned} D_{T_{i,j}} &= \frac{(u_{i+1/2,j+1/2}^\tau + u_{i+1/2,j-1/2}^\tau)}{2\Delta} - \frac{(u_{i-1/2,j+1/2}^\tau + u_{i-1/2,j-1/2}^\tau)}{2\Delta} \\ &\quad - \frac{(v_{i+1/2,j+1/2}^\tau + v_{i-1/2,j+1/2}^\tau)}{2\Delta} - \frac{(v_{i+1/2,j-1/2}^\tau + v_{i-1/2,j-1/2}^\tau)}{2\Delta} \end{aligned} \quad (4.4.5)$$

A similar relationship is obtained for  $D_{S_{i,j}}$  with  $u$  and  $v$  exchanged.

$$\begin{aligned} \text{Note: } F_1 &= f_1 \left( K_{H_{i+1/2,j+1/2}}, K_{H_{i+1/2,j-1/2}} \right) \\ F_2 &= f_2 \left( K_{H_{i-1/2,j+1/2}}, K_{H_{i-1/2,j-1/2}} \right) \end{aligned}$$

Then from the relations above:

$$\begin{aligned} F_1 &= f_1 \left( u_{i+1,j+1}^\tau, u_{i+1,j}^\tau, u_{i,j+1}^\tau, u_{i,j}^\tau, v_{i+1,j+1}^\tau, v_{i,j+1}^\tau, v_{i+1,j}^\tau, v_{i,j}^\tau, \right. \\ &\quad \left. u_{i+1,j}^\tau, u_{i+1,j-1}^\tau, u_{i,j}^\tau, u_{i,j-1}^\tau, v_{i+1,j}^\tau, v_{i,j}^\tau, v_{i+1,j-1}^\tau, v_{i,j-1}^\tau \right) \\ &\quad \vdots u, v \\ F_2 &= f_2 \left( u_{i,j+1}^\tau, u_{i,j}^\tau, u_{i-1,j+1}^\tau, u_{i-1,j}^\tau, v_{i,j+1}^\tau, v_{i-1,j+1}^\tau, v_{i,j}^\tau, v_{i-1,j}^\tau, \right. \\ &\quad \left. u_{i,j}^\tau, u_{i,j-1}^\tau, u_{i-1,j}^\tau, u_{i-1,j-1}^\tau, v_{i,j}^\tau, v_{i-1,j}^\tau, v_{i,j-1}^\tau, v_{i-1,j-1}^\tau \right) \\ &\quad \vdots u, v \end{aligned}$$

Thus we note that the first term of  $H_u$  involves  $u_{i,j}$  and  $v_{i,j}$  at the following nine locations:  $[(i,j) | i,j \in (-1, 0, +1)]$ . All other terms in the expressions for  $H_u$  and  $H_v$  involve  $u_{i,j}$  and  $v_{i,j}$  at these same nine field points.

Pressure Gradient  
Force Terms ( $P_u$ ,  $P_v$ )

54. The pressure gradient terms consist of two components, the geostrophic wind and the hurricane pressure field. The model user specifies through input the x and y components of the geostrophic wind. The radial pressure field in the hurricane is determined as previously developed in the section on the initial value problem; namely,

$$\frac{\partial P_c}{\partial r} = \frac{(P_n - P_o) R}{r^2} e^{-R/r}.$$

55. It is necessary to compute  $\partial P_c / \partial x$  and  $\partial P_c / \partial y$ . This is accomplished by using the relationships between Cartesian and polar coordinate systems as shown below.

$$\begin{aligned} x &= r \cos \theta & r &= \sqrt{x^2 + y^2} \\ y &= r \sin \theta \end{aligned} \tag{a}$$

$$\frac{\partial P_c}{\partial x} = \frac{\partial P_c}{\partial r} \frac{\partial r}{\partial x} = \frac{\partial p}{\partial r} \left( \frac{x}{r} \right) = \frac{\partial p}{\partial r} \cos \theta \tag{b}$$

(4.5.1)

$$\frac{\partial P_c}{\partial y} = \frac{\partial P_c}{\partial r} \frac{\partial r}{\partial y} = \frac{\partial p}{\partial r} \left( \frac{y}{r} \right) = \frac{\partial p}{\partial r} \sin \theta \tag{c}$$

Determination of the  
Friction Terms ( $F_u$ ,  $F_v$ )

56. The computation of  $F_u$  and  $F_v$  has been previously presented in earlier work on the turning angle concept. In the computer code, the following approach is used.

1. Compute  $SPH = \frac{C_D}{h} |\vec{v}_s|$

2. Then

$$F_x = \frac{SPH * [U_l (\ln \hat{z}_o + A_m) + V_l B_m]}{\sqrt{B_m^2 + (\ln \hat{z}_o + A_m)^2}}$$

$$F_y = \frac{SPH * [V_l (\ln \hat{z}_o + A_m) - U_l B_m]}{\sqrt{B_m^2 + (\ln \hat{z}_o + A_m)^2}}$$

In the code the tangential and normal drag coefficients are expressed as follows:

$$C_T = \frac{(\ln \hat{z}_o + A_m) C_D}{\sqrt{B_m^2 + (\ln \hat{z}_o + A_m)^2}} \quad (4.6.1)$$

$$C_N = \frac{B_m C_D}{\sqrt{B_m^2 + (\ln \hat{z}_o + A_m)^2}}$$

Thus, we finally obtain:

$$F_x = \frac{|\vec{v}_s|}{h} (U_l C_T + V_l C_N) \quad (a)$$

(4.6.2)

$$F_y = \frac{|\vec{v}_s|}{h} (V_l C_T + U_l C_N) \quad (b)$$

#### Inner Mesh Boundary Conditions

57. The computational sequence is constructed such that one proceeds from the outer grid to the inner grids. To advance the solution  $\Delta t_5$ , the computations are performed in the following manner:

<u>Sequence No.</u>	<u>Grid Nest Number</u>	<u>Sequence No.</u>	<u>Grid Nest Number</u>
1	5	18	3
2	4	19	2
3	3	20	1
4	2	21	1
5	1	22	2
6	1	23	1
7	2	24	1
8	1	25	3
9	1	26	2
10	3	27	1
11	2	28	1
12	1	29	2
13	1	30	1
14	2	31	1
15	1		
16	1		
17	4		

The computational sequence may be written in a shorter form using factorial notation as follows:  $5!1!2!1!3!1!2!1!4!1!2!1!3!1!2!1!$ . These numbers appear in array LEVEL and are passed to Subroutine COMQUT to control the computations. We note to advance the solution  $\Delta t_5 : 16\Delta t_1, 8\Delta t_2, 4\Delta t_3, 2\Delta t_2$  computations are performed. The computations are performed such that one advances in time from the innermost to the outermost grids. In this manner, the exterior (outside) boundary condition for grid nest  $i$  may be determined from the values on grid nest  $i+1$ . The interior (inside) boundary condition for grid nest  $i$  may always be determined or in fact is always known, since it involves performing the finite difference computations extrapolating the grid corresponding to grid nest  $i$  within grid nest  $i-1$ . In advancing computations on grid  $i$ , the new values (UN, VN arrays) on grid  $i-1$  must be at the previous time level on grid  $i$  for the above extrapolation process to remain valid. The computational sequence insures that this is indeed the case.

58. For grid nest 5 the exterior boundary conditions correspond to the far field conditions previously presented.

59. The exterior boundary conditions for grid nest  $i$  are, as previously outlined, determined from conditions on grid nest  $i+1$ . A spatial interpolation is needed since the points on grid nest  $i$  are twice as dense as on grid  $i+1$ . A temporal interpolation may or may not be required. If the grid time level (to be advanced) on  $i$  is equal to the advanced time level on grid  $i+1$  no temporal interpolation is required; otherwise, the boundary values on grid nest  $i$  are determined from the average of the values at the old and advanced time levels of points on grid nest  $i+1$ . The first grid nest number in each of the 16 factorial sequence presented above requires no temporal interpolation. All other grid nest levels in each of the 16 factorial sequences require temporal interpolation.

60. Under the above approach it is necessary to update the old time level arrays (U, V) on a given grid nest only when the time level on that grid nest is to be advanced.

61. It is also instructive to examine the range of indices involved in the exterior boundary transfer, interior boundary transfer, and interior region computations. The indice ranges are presented in Table II-2 below.

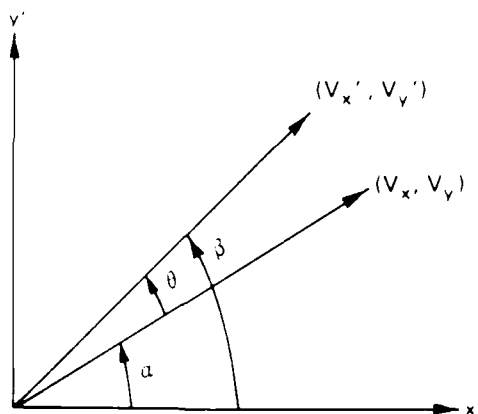
Table II-2  
Range of Indices for Boundary and Interior Regions

	<u>I (X Direction) Range</u>	<u>J (Y Direction) Range</u>
Interior Region		
Nest 1	2-20*J	2-20*I
Nests 2-5	2-6, 16-20*J	2-6, 16-20*I
External Boundary	1, 21*J	1, 21*I
Interior Boundary		
Nest 1	N/A	N/A
(Nests 2-5)	7, 15 Jε(7, 15)	7, 15 Iε(7, 15)

### Finite Difference Solution Adjustment

62. If one considers the case in which  $\hat{w}_c$ ,  $\hat{w}_g$ ,  $K_o$ , and  $C_D$  are all zero, the analytic solution corresponds to the gradient wind field determined from the  $P_c$  pressure field. Since there is no friction ( $C_D = 0$ ), the radial component of the wind is exactly zero.

63. In the numerical solution, a negative radial component of wind is present, e.g., the numerical solution produces winds with excessive inflow. Cardone et al. [14] have rotated the numerical solution winds outward by  $8^\circ$  in order to remove this computational bias. This is accomplished computationally with reference to Figure II-10 in the following manner.



$$V_x^2 + V_y^2 = V_{x'}^2 + V_{y'}^2 \quad (a)$$

$$\text{TAN } \beta = \frac{V_{y'}}{V_{x'}} \quad \text{TAN } \alpha = \frac{V_y}{V_x} \quad (b)$$

$$\beta - \theta = \alpha \quad (c)$$

Figure II-10. Vector Rotation Notation

Consider

$$\sin \alpha = \sin (\beta - \theta) = \sin \beta \cos \theta - \sin \theta \cos \beta$$

Then

$$\frac{V_y}{\sqrt{V_x^2 + V_y^2}} = \frac{V'_y}{\sqrt{V'^2_x + V'^2_y}} \cos\theta - \sin\theta \frac{V'_x}{\sqrt{V'^2_x + V'^2_y}}$$

From (a) in Figure II-10 above:

$$V_y = V'_y \cos\theta - V'_x \sin\theta \quad (4.8.1)$$

Next consider,

$$\cos\alpha = \cos(\beta - \theta) = \cos\beta \cos\theta + \sin\beta \sin\theta$$

Then

$$\frac{V_x}{\sqrt{V_x^2 + V_y^2}} = \frac{V'_x}{\sqrt{V'^2_x + V'^2_y}} \cos\theta + \frac{V'_y}{\sqrt{V'^2_x + V'^2_y}} \sin\theta$$

From (a) in Figure II-10 above:

$$V_x = V'_x \cos\theta + V'_y \sin\theta \quad (4.8.2)$$

Equations (4.8.1) and (4.8.2) determine the coordinates of the rotated vector  $(V_x, V_y)$  in terms of the numerical solution vector  $(V'_x, V'_y)$ . Note  $\theta = 8^\circ$ ,  $\sin\theta = .1391731$ ,  $\cos\theta = .99026897$ . These terms are found in Sub-routine OUTFLO.

#### Determination of Surface Stress and Wind Speed at Anemometer Level

64. The magnitude of surface stress is equal to  $\rho U_*^2$ , where  $\rho$  is the density of air (dependent on temperature and pressure) and  $U_*$  is the friction velocity appropriate for the given surface. The turning angle associated with the mean wind speed and surface represents the angle through which the mean wind speed is turned inward for the given surface.

65. The following logarithmic velocity law is assumed to hold for the given surface condition.

$$U_z = \frac{U_*}{K} \ln \left( \frac{z}{z_0} \right) \quad (4.9.1)$$

where  $z = 10$  meters for  $u_{10}$ , the wind speed at anemometer level.



### Numerical Structure of the Generalized Hurricane Submodel

66. A generalized hurricane model has been constructed by incorporating the parametric approaches within the five level nested grid structure of the planetary boundary layer numerics. This approach was followed in order to provide a direct comparison of winds calculated at common grid points. In addition, the overall structure of the hurricane windfields generated by the two approaches may also be directly compared. A transfer tape has been constructed employing the following format:

IJPM, NAME, IDAYH, IHRH, NZZ, NPOS, IDXN  
XLAT(I), XLONG(I), TPOS(I), I = 1, NPOS)

If IJPM > 0: PINF, CP, RAD, VF, THETA, FLINE

For each snapshot: TNZ (NSNAP + LL), DELP, RADIUS(1), UN, VN

where

IJPM  $\equiv$  joint probability method storm (For IJPM = 0, a standard user specified storm track is assumed)  
NAME  $\equiv$  storm name (usually storm year and month)  
IDAYH  $\equiv$  storm day  
IHRH  $\equiv$  storm hour initial time in GMT  
NZZ  $\equiv$  number of snapshots  
NPOS  $\equiv$  number of storm positions  
IDXN  $\equiv$  minimum spacing of the innermost grid in km  
XLAT(I)  $\equiv$  latitude of storm position I in degrees N  
XLONG(I)  $\equiv$  longitude of storm position I in degrees W  
TPOS(I)  $\equiv$  time in hour relative to initial storm hour (IHRH) of position I  
PINF  $\equiv$  far field storm pressure (mb)  
CP  $\equiv$  central pressure (mb)  
RAD  $\equiv$  radius (nm)  
VF  $\equiv$  forward speed (kts)  
THETA  $\equiv$  line angle (degrees clockwise from North)  
FLINE  $\equiv$  storm path number  
TNZ (NSNAP + LL)  $\equiv$  snapshot time in hours relative to IHRH

DELP  $\equiv$  Central Pressure Depression (in Hg)

UN  $\equiv$  x-velocity field components over the complete five level nested grid

VN  $\equiv$  y-velocity field components over the complete five level nested grid

67. The transfer tape is accessed by the Program HGRAPH, the hurricane model graphics package as well as Program LAKE, the hydrodynamic model. The generalized hurricane model employs a snapshot philosophy. In hindcasting or forecasting mode, the model user specifies storm positions over time and at appropriate points in time the following hurricane characteristics:

	Forward Speed (kts)
	Direction (Clockwise from North in degrees)
	Radius (nm)
	Far field pressure (mb)
	Central pressure (mb)
For PBL	{ Steering flow (m/sec)
Formulation	{ Steering flow direction (Counter-clockwise from East in
only	{ degrees)

68. The model then computes UN and VN over the nested grid for each snapshot. In this approach, if storm characteristics are invariant with respect to time only a single snapshot need be computed. The model user may select through variable IWIND either a planetary boundary layer windfield determination or a parametric approach. Within the parametric approach either the SPH or TTM windfield formulation may be selected by specifying the appropriate value of IFORM. Sample input data sets are presented in Tables II-3 and II-4, respectively for each approach. If the model user specifies  $IJPM > 0$ , a straight line storm track is determined by the model as discussed subsequently in the joint probability method storm geometry section. A test data set for joint probability method storm geometry is given in Table II-5. Within the joint probability mode either windfield approach may be selected.

Table II-3

SPH Parametric SPH Formulation Input Data Set


---

```

$NAME1
IB=0,IWIND=1,IJPM=0,
$END
1749 008
    26.      11.
3
    25.1      77.57      0.
    25.2      77.8      1.
    26.8      80.1      13.
    27.05      80.617      16.
    27.17      80.817      17.
    27.375      81.0583      18.
    28.3      82.2      25.
    29.3      82.55      31.
5
    0.      13.      17.      25.      31.
    0.      0.      22.5      14.1      1015.      975.      295.
    0.      0.      22.5      14.      1015.      954.      308.
    0.      0.      22.5      13.1      1015.      961.      308.
    0.      0.      22.5      11.9      1015.      971.      309.
    0.      0.      22.5      10.4      1015.      984.      343.
8
$NAME4
AZRX=35.,ALP=10.,
$END
$NAME4
AZRX=48.,ALP=10.,
$END
$NAME4
AZRX=48.,ALP=10.,
$END
$NAME4
AZRX=49.,ALP=10.,
$END
$NAME4
AZRX=83.,ALP=10.,
$END

```

---

Table II-4

Planetary Boundary Layer PBL Formulation Input Data Set


---

```

$NAME1
IB=1,IWIND=0,IJPM=0,
$END
1749 003
    26.      11.
3
    25.1      77.57      0.
    25.2      77.8      1.
    26.8      80.1      13.
    27.05      80.617      16.
    27.17      80.817      17.
    27.375      81.0583      18.
    28.3      82.2      25.
    29.3      82.55      31.
5
    0.      13.      17.      25.      31.
    0.      155.      22.5      14.1      1015.      975.      295.
    0.      142.      22.5      14.      1015.      954.      308.
    0.      142.      22.5      13.1      1015.      961.      308.
    0.      141.      22.5      11.9      1015.      971.      309.
    0.      107.      22.5      10.4      1015.      984.      343.
$NAME4
GARP=.035,
$END

```

---

Table II-5

Joint Probability Method Storm Geometry Test Data Set


---

```

$NAME1
  IB=1, IWIND=1, IJPM=1,
$END
  26.92      80.83
  5
    28.      82.5      26.5      81.88      25.2      81.      25.5      80.1
    28.2      80.625
    29.91      28.73      12.      15.      45.      0.      90.      1.
  1      0      0
$NAME4
  42MX=55., ALP=10.,
$END

```

---

69. Due to the possibility of temporal variations of the land/water boundary of Lake Okeechobee over the course of a hurricane event, it is necessary to employ a dynamic reduction factor methodology. The changing land surface will introduce a time varying reduction to overwater winds in the vicinity of the boundary. To incorporate this effect dynamically, the wind reduction scheme employed by Reid [3] had been incorporated directly in the hydrodynamic model. This approach is in contrast to the previous approach employed by Reid [3] in determining the reduction factors within the hurricane model.

## Generalized Hurricane Submodel Interpolation (Grid) Concepts

70. Within either the parametric or planetary boundary layer approach of the generalized hurricane model, computations are performed on a nested five level grid in order to provide for direct windfield comparisons. Several levels of interpolation are performed in the hydrodynamic model as indicated in Table II-6. Each interpolation is presented in turn below.

Table II-6

Interpolation Structure Employed in the Hydrodynamic Model

---

- I. Temporal Snapshot Interpolation
- II. Uniform Hurricane Grid Spatial Interpolation
- III. Stretched Hydrodynamic Grid Spatial Interpolation

---

Temporal Snapshot Interpolation

71. The storm position in latitude and longitude coordinates over time with respect to the start of the storm is written on the transfer tape. Within the hydrodynamic model all times are also with respect to the start of the storm. A temporal interpolation is performed every KSI time steps within the hydrodynamic model to determine the snapshot windfield over the five level nested grid system employed in the hurricane model.

# Uniform Hurricane Grid Spatial Interpolation

72. In order to interpolate the windfield on the five level nested grid to a uniform hurricane grid, it is first necessary to determine the new position in latitude and longitude coordinates of the storm center. Latitude and longitude coordinates at the center of each hurricane cell are interpolated at every time step from the transferred position coordinate history.

73. Consider the following relations available from spherical trigonometry for the spherical triangle shown in Figure II-11 below:

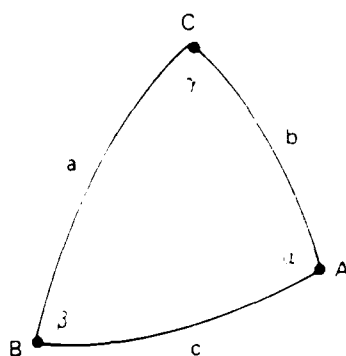


Figure II-11. Spherical Triangle

$$\tan \frac{\alpha}{2} = \sqrt{\frac{\sin \frac{(a+c-b)}{2} \sin \frac{(a+b-c)}{2}}{\sin \frac{(a+b+c)}{2} \sin \frac{(b+c-a)}{2}}} \quad (6.2.1)$$

$$\text{hav } c = \text{hav } (a - b) + \sin a \sin b \text{ hav } c \quad (6.2.2)$$

74. We are concerned with two points, PO, the eye of the hurricane, and, PI, an arbitrary field point corresponding to the center of each uniform grid cell at which wind speed and direction are desired. Both points are specified in latitude, longitude conventions as follows:

$$PO = [\lambda_1, L_1], \quad PI = [\lambda_2, L_2]$$

75. As such C corresponds to the North Pole for PO and PI in the northern hemisphere (our region of concern), B corresponds to PI, and A to PO. Furthermore, we observe:

$$b = \text{co}_L(\lambda_1) = 90^\circ - \lambda_1 \quad (a)$$

$$a = \text{co}_L(\lambda_2) = 90^\circ - \lambda_2 \quad (b) \quad (6.2.3)$$

$$\gamma = \text{DL}_0(L_1, L_2) = L_2 - L_1 \quad (c)$$

Thus for the case of concern, Equations (6.2.1) and 6.2.2) above become:

$$\tan^2 \frac{\alpha}{2} = \frac{\sin(90^\circ - \lambda_2 + C - 90^\circ + \lambda_1)/2 \sin(180^\circ - \lambda_1 - \lambda_2 - C)/2}{\sin(180^\circ - \lambda_1 - \lambda_2 + C)/2 \sin(90^\circ - \lambda_1 + C - 90^\circ + \lambda_2)/2} \quad (6.2.1)$$

$$\tan^2 \frac{\alpha}{2} = \frac{\sin(\lambda_1 - \lambda_2 + C)/2 \overbrace{\sin(90^\circ - \lambda_1 + \lambda_2 + C)/2}^{\cos(\lambda_1 + \lambda_2 + C)/2}}{\underbrace{\sin(90^\circ - (\lambda_1 + \lambda_2 - C)/2)}_{\cos(\lambda_1 + \lambda_2 - C)/2} \sin(\lambda_2 - \lambda_1 + C)/2}$$

(Note:  $0^\circ < \alpha < 180^\circ$  and thus  $0^\circ < \frac{\alpha}{2} < 90^\circ$ )

$$\text{hav } c = \text{hav}(\lambda_1 + \lambda_2) + \cos \lambda_1 \cos \lambda_2 \text{hav } (L_2 - L_1) \quad (6.2.2)$$

(Note:  $\text{hav}(x - y) = \text{hav}(y - x)$ ; since  $\text{hav } x = \sin^2 \frac{x}{2} = (1 - \cos x)/2$  and if  $y = \text{hav}(x)$ ,  $x \in (0, 180^\circ)$ )

66. In computation, one uses Equation (6.2.2) to determine  $c$ . Equation (6.2.1) is then used to determine  $\alpha$ .

67. If  $c$  as computed from Equation (6.2.2) is very small, then  $\lambda_1 = \lambda_2$  and Equation (6.2.1) is not used. Instead, one considers plane trigonometric relationships.

68. Consider the following diagram shown in Figure II-12 in which the bearing from PO to PI is measured clockwise from North; the locations of PI in each of four quadrants is shown as well as the signs of the coordinate distances. The horizontal distance (signed),  $H$ , and vertical distance (signed),  $V$ , are given by the following relations:

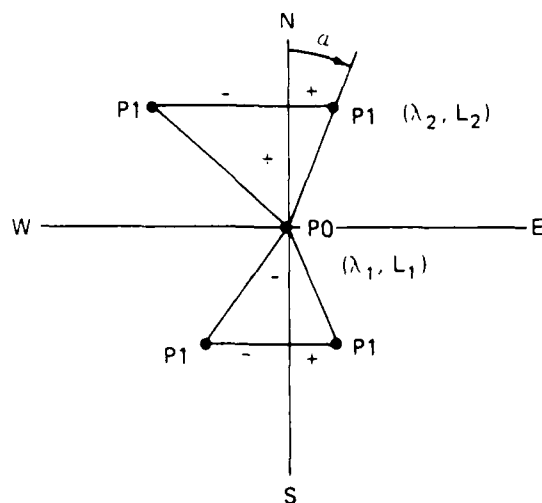


Figure II-12. Plane Triangle

$$H = (L_1 - L_2) \cos(\lambda_1 + \lambda_2)/2 = (L_1 - L_2) \cos \lambda_1 = (L_1 - L_2) \cos \lambda_2 \quad (a)$$

(6.2.4)

$$V = (\lambda_2 - \lambda_1) \quad (b)$$

Then

$$\alpha = \text{ATAN2} (H, V) .$$

79. Once the distance and bearing are known for uniform grid cell center, an additional procedure is employed to locate the four surrounding points on the grid nest. A bilinear interpolation as given by the following relationship is used to interpolate winds to the uniform grid.

$$\begin{aligned} YW_{i,j} = & f_{11} \text{UNI}_{II+1,JJ+1,IZ} + f_{12} \text{UNI}_{II+1,JJ+2,IZ} \\ & + f_{21} \text{UNI}_{II+2,JJ+1,IZ} + f_{22} \text{UNI}_{II+2,JJ+2,IZ} \end{aligned} \quad (a)$$

(6.2.5)

$$\begin{aligned} XW_{i,j} = & -f_{11} \text{VNI}_{II+1,JJ+1,IZ} - f_{12} \text{VNI}_{II+1,JJ+2,IZ} \\ & - f_{21} \text{VNI}_{II+2,JJ+1,IZ} - f_{22} \text{VNI}_{II+2,JJ+2,IZ} \end{aligned} \quad (b)$$

where

$YW_{i,j} \equiv$  y component of wind on the uniform grid at cell center  $i,j$

$XW_{i,j} \equiv$  x component of wind on the uniform grid at cell center  $i,j$



$f_{11}, f_{12}, f_{21}, f_{22} \equiv$  interpolation parameters which sum to one and are dependent on the relation of the cell center  $(i,j)$  to each of the four surrounding cells on the nested grid; e.g.,  $(II+1, JJ+1, IZ)$ ,  $(II+1, JJ+2, IZ)$ ,  $(II+2, JJ+1, IZ)$ , and  $(II+2, JJ+2, IZ)$ , where  $II, JJ$  correspond to  $x$  and  $y$  cell indices and  $IZ$  is the nest number

$UNI_{II,JJ,IZ} \equiv$  x-wind component at  $x$  index  $II$ ,  $y$  index  $JJ$ , and nest index  $IZ$

$VNI_{II,JJ,IZ} \equiv$  y-wind component at  $x$  index  $II$ ,  $y$  index  $JJ$ , and nest index  $IZ$

The uniform grid is in the WIFM convention ( $y$  to the right,  $x$  pointed down) and as a result, the  $y$  WIFM axis corresponds to the  $x$  Cartesian coordinate, while the  $x$  WIFM axis corresponds to minus the  $y$  Cartesian coordinate. This coordinate transformation is embodied in the above two interpolation equations.

80. The pressure anomaly in feet of water is computed using Equation (2.1.2) at the center of each cell of the uniform grid. This uniform grid is employed as an intermediate grid in order to determine a wind reduction factor for each octant of wind direction for each grid cell. In addition, a fetch associated with the appropriate octant of wind direction is also determined for the wave calculations. The details of these procedures follow the approach by Reid [3] based upon results in Reference 4. Wind reduction factors and fetches are computed every KSI time steps.

#### Sketched Hydrodynamic Grid Spatial Interpolation

81. The bilinear interpolation procedure previously employed is used to interpolate the wind and pressure field to the nonuniform stretched grid. Pressure and wind velocity components are determined at cell centers of the stretched grid. The wind velocity components are transformed to the corresponding stress components via the drag coefficient formulation presented in Part IV.

#### Joint Probability Method Storm Track Geometry

82. Within the joint probability method, straight line storm tracks are assumed. Although there is some evidence, that parabolic tracks might be employed in order to fit recurving storms, this approach was not followed in the present study. Rather the geometry as shown in Figure II-13 was assumed.

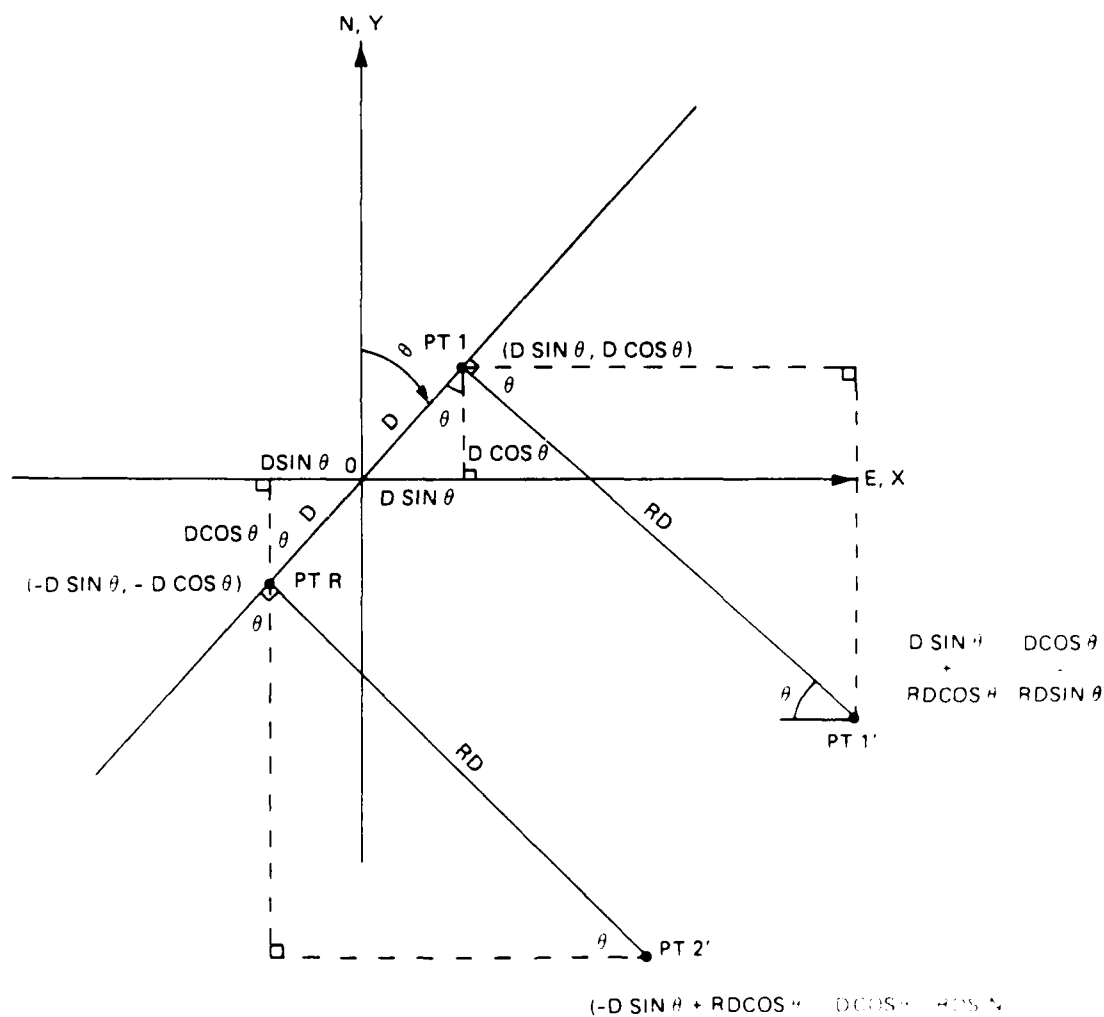


Figure II-13. Joint Probability Method Storm Track Geometry

83. Note the storm direction,  $\theta$ , as measured clockwise from North is equal to  $270^\circ + \theta$ . The storm direction,  $\theta_x$ , as measured counter-clockwise from East (the x-axis) is equal to  $180^\circ - \theta$ .

84. Figure II-13 considers the case for a storm band at  $\theta$  oriented in the first of four quadrants as shown for the general case shown in Figure II-14.

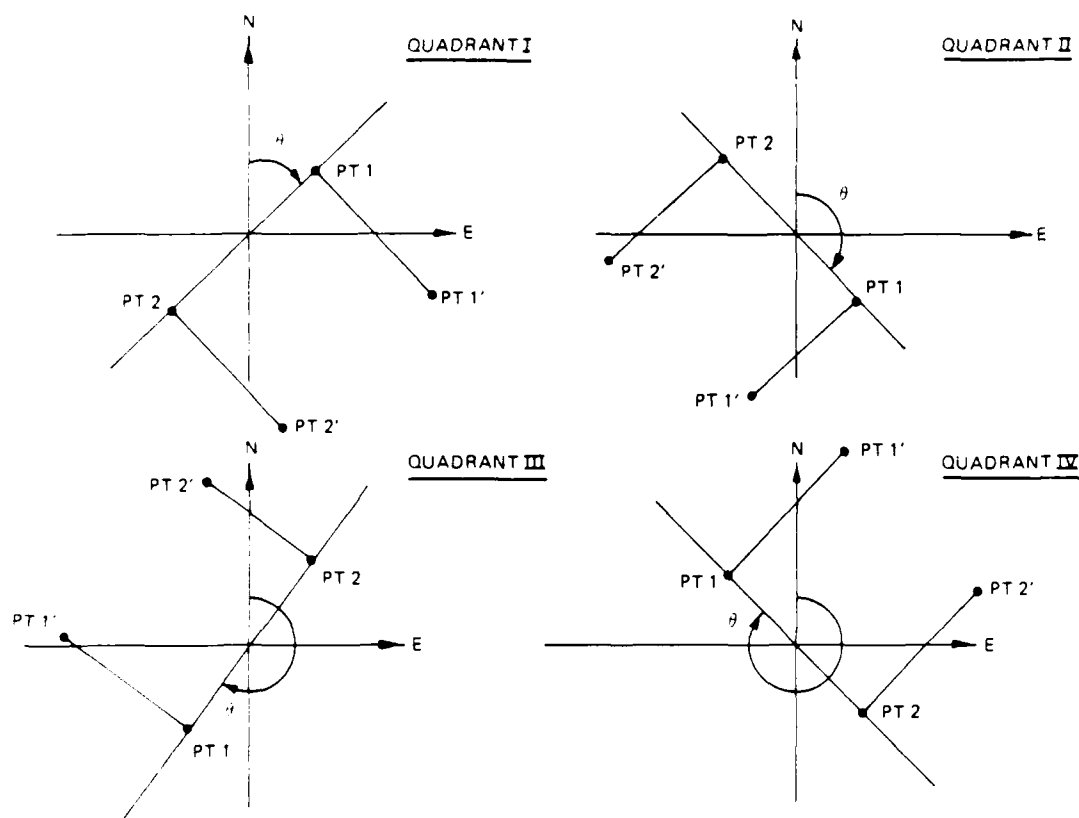


Figure II-14. General Joint Probability Method Storm Track Cases

85. Observe that the pair  $P + 1, P + 1'$  corresponds to  $D$ , while the pair  $P + 2, P + 2'$  corresponds to  $-D$ .

86. In general, the formulas for  $P + 1, P + 1', P + 2$ , and  $P + 2'$  shown in Figure II-13 hold for all  $\theta$ .

87. In actual application to Lake Okeechobee, the origin  $O$  corresponds to the latitude and longitude of the center of the lake.  $D = nR$ , where  $n = (-2, 2)$  and  $R$  is the storm radius.  $RD$  corresponds to 3 times the storm radius, e.g.,  $RD = 3R$ . The number of hours considered in the hurricane simulation,  $n_T$ , is given by the following relationship:

$$n_T = 5R/V_F \quad (7.1)$$

where

$n_T$   $\equiv$  simulation length (hrs)

$R$   $\equiv$  storm radius (nm)

$V_F$   $\equiv$  storm speed (kts)

The storm position is then determined by using the following relation:

$$Y_i = Y_0 + (nR \cos\theta - 3R \sin\theta)/60 + iV_F \sin(180 - \theta)/60 \quad (a)$$

(7.2)

$$X_i = X_0 + (nR \sin\theta + 3R \cos\theta)/(60 \cos Y_i) - iV_F \cos(180 - \theta)/(60 \cos Y_i) \quad (b)$$

$$i = 1, \dots, n_T, \quad n \in (-2, -1, 0, 1, 2)$$

where

$X_i$   $\equiv$  longitude of the storm position at storm hour  $i$

$X_0$   $\equiv$  longitude of the lake center

$Y_i$   $\equiv$  latitude of the storm position at storm hour  $i$

$Y_0$   $\equiv$  latitude of the lake center

$R$   $\equiv$  radius of the storm (nm)

$\theta$   $\equiv$  bearing of the storm line (clockwise from North in degrees)

$V_F$   $\equiv$  storm speed (in kts)

$i$   $\equiv$  integer signifying storm hour

$n$   $\equiv$  path number of the given storm

These relationships were subsequently slightly modified as discussed in Part IX.

88. In order to consider the influence of overland storm filling the coastline configuration is first specified using the following ordered pairs:

$$[\theta_1, r_1], \dots, [\theta_j, r_j], \dots, [\theta_n, r_n] \quad j = 1, n \quad (7.3)$$

where

$\theta_j \equiv$  bearing clockwise from North ( $^\circ$ ) for point  $j$

$r_j \equiv$  distance from the shoreline to the center of the lake (nm) for point  $j$

In application to Lake Okeechobee, the points shown in Table II-7 are used.

89. A dummy point ( $0^\circ$ , 9999 nm) or ( $360^\circ$ , 9999 nm) is added to the array of coastal points in order to allow for determining time over land for some storm tracks. The actual coastline is specified between the angles 8.08 and 306.47 degrees clockwise from North.

90. For each storm hour,  $i$ , the distance  $D_i$  and bearing clockwise from North,  $\beta_i$ , of the storm position with respect to the lake center is determined. For  $\theta_j < \beta_i < \theta_{j+1}$ , a test is made on  $r = r_j + (r_{j+1} - r_j) (\beta_i - \theta_j) / (\theta_{j+1} - \theta_j)$ , the interpolated distance to the shoreline for  $\beta_i$ . If  $D_i \leq r$ , then the storm is considered to be overland for the given hour. For each storm path, the number of hours the storm is overland is determined. The total number of hours the storm is overland is then used to reduce the storm central pressure. An additional snapshot corresponding to the reduced central pressure is then computed employing the following relation.

$$\Delta P' = \Delta P(1 - .013h)^2$$

where

$\Delta P' \equiv$  reduced central pressure (in Hg)

$\Delta P \equiv$  original overwater central pressure (in Hg)

$h \equiv$  number of hours storm is over land

Table II-7  
Florida Coastline Specification With Respect To Lake Okeechobee

<u>Segment No. 1</u>			
Angle (CLW N)	360.00	Distance (NM)	9999.00
<u>Segment No. 2</u>			
Angle (CLW N)	306.47	Distance (NM)	110.02
<u>Segment No. 3</u>			
Angle (CLW N)	246.11	Distance (NM)	61.66
<u>Segment No. 4</u>			
Angle (CLW N)	185.11	Distance (NM)	103.61
<u>Segment No. 5</u>			
Angle (CLW N)	122.62	Distance (NM)	46.54
<u>Segment No. 6</u>			
Angle (CLW N)	8.03	Distance (NM)	77.57
<u>Segment No. 7</u>			
Angle (CLW N)	0.00	Distance (NM)	9999.00

### PART III: HYDRODYNAMIC MODEL: THEORETICAL DEVELOPMENT

91. The hydrodynamic equations are developed in turn for both the long and short wave model components. The long wave equations are presented in two dimensional vertically integrated form. The time averaging concepts necessary in describing the turbulence are not considered in the derivations.

#### Long wave equations

92. The general equations of the classical hydrodynamics for incompressible flow are given following Lai's development as follows [17].

$$\frac{\partial u}{\partial x} + \frac{\partial v}{\partial y} + \frac{\partial w}{\partial z} = 0 \quad (1.1)$$

$$\rho \frac{Du}{Dt} = \rho F_x - \frac{\partial p}{\partial x} + \mu \Delta^2 u \quad (1.2)$$

$$\rho \frac{Dv}{Dt} = \rho F_y - \frac{\partial p}{\partial y} + \mu \Delta^2 v \quad (1.3)$$

$$\rho \frac{Dw}{Dt} = \rho F_z - \frac{\partial p}{\partial z} + \mu \Delta^2 w \quad (1.3)$$

with

$$\frac{D}{Dt} = \frac{\partial}{\partial t} + u \frac{\partial}{\partial x} + v \frac{\partial}{\partial y} + w \frac{\partial}{\partial z}$$

$$\Delta^2 = \frac{\partial^2}{\partial x^2} + \frac{\partial^2}{\partial y^2} + \frac{\partial^2}{\partial z^2}$$

where

$x, y, z \equiv$  Cartesian coordinates

$u, v, w \equiv$  Velocity components in the  $x, y$ , and  $z$  directions, respectively

$F_x, F_y, F_z \equiv$  Body forces in the  $x, y$ , and  $z$  directions, respectively

$\rho \equiv$  Fluid density

$\mu \equiv$  Fluid viscosity

$p \equiv$  Pressure

$t \equiv$  Time

The following assumptions are made:

- a. The water is not deep compared with the length of the wave and the shallow water theory applies.
- b. The vertical velocity of flow is small.
- c. The vertical acceleration of the fluid particle is very small compared with the acceleration of gravity,  $g$ , and hence, can be neglected.
- d. The pressure is hydrostatic (from the above assumption).
- e. The frictional resistance coefficient for unsteady flow is the same as that for steady flow, thus can be approximated from the Chezy or Manning equation.
- f. Only shear stresses due to horizontal velocity components are significant.
- g. The bottom of the embayment is rigid or relatively stable and fixed with respect to time.
- h. The water is nonhomogenous but incompressible. The density induced flow appears only in the pressure gradient terms.

#### Continuity equation

93. If we consider (1.1) and integrate over the vertical from the bottom  $z_b(x,y)$  to the surface  $\eta(x,y,t)$  we obtain

$$\int_{z_b}^{\eta} \frac{\partial u}{\partial x} dz + \int_{z_b}^{\eta} \frac{\partial u}{\partial y} dz + w(\eta) - w(z_b) = 0 \quad (1.1.1)$$

From Leibniz rule we may write

$$\frac{\partial}{\partial x} \int_{z_b}^{\eta} u dz = u(\eta) \frac{\partial \eta}{\partial x} - u(z_b) \frac{\partial z_b}{\partial x} + \int_{z_b}^{\eta} \frac{\partial u}{\partial x} dz \quad (1.1.2)$$

$$\frac{\partial}{\partial y} \int_{z_b}^{\eta} v dz = v(\eta) \frac{\partial \eta}{\partial y} - v(z_b) \frac{\partial z_b}{\partial y} + \int_{z_b}^{\eta} \frac{\partial v}{\partial y} dz \quad (1.1.3)$$

Employ the kinematic boundary condition; namely, for  $F(x,y,z,t) = 0$  as a boundary surface assume any particle on the surface remains on it implies



$$\frac{DF}{Dt} = \frac{\partial F}{\partial t} + u \frac{\partial F}{\partial x} + v \frac{\partial F}{\partial y} + w \frac{\partial F}{\partial z} = 0$$

94. Consider  $z = \eta(x, y, t)$  at the free surface, then  
 $F = z - \eta(x, y, t) = 0$ . Hence

$$\frac{DF}{Dt} = 0 \Rightarrow \frac{\partial \eta}{\partial t} + u \frac{\partial \eta}{\partial x} + v \frac{\partial \eta}{\partial y} = w \quad (1.1.4)$$

At the bottom  $z = Z_b(x, y)$ .  
Hence

$$\frac{DF}{Dt} = 0 \Rightarrow u \frac{\partial Z_b}{\partial x} + v \frac{\partial Z_b}{\partial y} = w \quad (1.1.5)$$

Returning to (1.1.1)

$$\begin{aligned} \frac{\partial}{\partial x} \int_{Z_b}^{\eta} u \, dz + \underline{\underline{u(Z_b) \frac{\partial Z_b}{\partial x}}} - \underline{\underline{u(\eta) \frac{\partial \eta}{\partial x}}} + \frac{\partial}{\partial y} \int_{Z_b}^{\eta} v \, dz + \underline{\underline{v(Z_b) \frac{\partial Z_b}{\partial y}}} \\ - v(\eta) \frac{\partial \eta}{\partial y} + \underline{\underline{w(\eta)}} - \underline{\underline{w(Z_b)}} = 0 \end{aligned} \quad (1.1.6)$$

The sum of the        terms is zero from the bottom boundary condition. The sum of the        terms is equal to  $\partial \eta / \partial t$  from the free surface boundary conditions. Thus we obtain:

$$\frac{\partial \eta}{\partial t} + \frac{\partial}{\partial x} \int_{Z_b}^{\eta} u \, dz + \frac{\partial}{\partial y} \int_{Z_b}^{\eta} v \, dz = 0 \quad (1.1.7)$$

Denoting

$$\bar{u} = \frac{1}{\eta - Z_b} \int_{Z_b}^{\eta} u \, dz \text{ and } \bar{v} = \frac{1}{\eta - Z_b} \int_{Z_b}^{\eta} v \, dz$$

one obtains

$$\frac{\partial \bar{r}}{\partial t} + \frac{\partial}{\partial x} [(\bar{r} - z_b) \bar{u}] + \frac{\partial}{\partial y} [(\bar{r} - z_b) \bar{v}] = 0 \quad (1.1.8)$$

Letting  $h = \bar{r} - z_b$  and dropping the bar notation with the understanding henceforth we are considering vertically averaged quantities one obtains

$$\frac{\partial r}{\partial t} + \frac{\partial}{\partial x} (hu) + \frac{\partial}{\partial y} (hv) = 0 \quad (1.1.9)$$

#### Equations of motion

95. Consider the  $z$  motion equation in which  $Dw/Dt = 0$ ,  $u \frac{\partial}{\partial x} w = 0$  from assumptions 2, 3 and 6, respectively. Thus we obtain

$$\rho F_z - \frac{\partial p}{\partial z} = 0 \quad (1.2.1)$$

$F_z$  is replaced by  $-g$  due to the following assumptions

- a. The vertical component of the Coriolis force is negligible with respect to  $g$ .
- b. The vertical tide generating force component is negligible with respect to  $g$ .

If we integrate the above relation from an arbitrary level  $z$  to the water surface obtain

$$p(z) = p(\eta) + \int_z^\eta \rho g \, dr \quad (1.2.2)$$

To depth we consider the following relations to hold, in which the bar quantities are depth averages and the prime quantities the local fluctuation from these averages.

$$\rho(z) = \bar{\rho} + \rho'(z) \quad (1.2.3)$$

$$p(z) = \bar{p} + p'(z) \quad (1.2.4)$$

$$\int_{z_b}^{\eta} \rho' \, dz = \int_{z_b}^{\eta} p' \, dz = 0 \quad (1.2.5)$$

Taking the partial derivative of (1.2.2) with respect to  $x$  obtain:

$$\frac{\partial p}{\partial x} = \frac{\partial p(\eta)}{\partial x} + \frac{\partial}{\partial x} \left[ \int_z^\eta \rho g \, dr \right] \quad (1.2.6)$$

Integrating (1.2.6) over the vertical we write:

$$\underbrace{\int_{z_b}^\eta \frac{\partial(\bar{p} + p')}{\partial x} \, dz}_{\textcircled{1}} = \underbrace{\int_{z_b}^\eta \frac{\partial p(\eta)}{\partial x} \, dz}_{\textcircled{2}} + \underbrace{\int_{z_b}^\eta \frac{\partial}{\partial x} \int_z^\eta \rho g \, dr \, dz}_{\textcircled{3}} \quad (1.2.7)$$

Let us consider terms  $\textcircled{1} - \textcircled{3}$ , separately, in turn. Evaluating  $\textcircled{1}$  invoke Leibniz rule

$$\begin{aligned} \int_{z_b}^\eta \frac{\partial}{\partial x} (\bar{p} + p') \, dz &= \frac{\partial}{\partial x} \int_{z_b}^\eta (\bar{p} + p') \, dz \\ &+ (\bar{p} + p') \Big|_{z_b} \frac{\partial z_b}{\partial x} - (\bar{p} + p') \Big|_\eta \frac{\partial \eta}{\partial x} \end{aligned} \quad (1.2.8)$$

Note further from (1.2.5),

$$\begin{aligned} \frac{\partial}{\partial x} \int_{z_b}^\eta (\bar{p} + p') \, dz &= \frac{\partial}{\partial x} [\bar{p}(\eta - z_b)] \\ &= (\eta - z_b) \frac{\partial \bar{p}}{\partial x} + \bar{p} \left( \frac{\partial \eta}{\partial x} - \frac{\partial z_b}{\partial x} \right) \end{aligned} \quad (1.2.9)$$

Thus we finally obtain for ① the following expression:

$$\int_{z_b}^{\eta} \frac{\partial}{\partial x} (\bar{p} + p') dz = (\eta - z_b) \frac{\partial \bar{p}}{\partial x} + p' \Big|_{z_b} \frac{\partial z_b}{\partial x} - p' \Big|_{\eta} \frac{\partial \eta}{\partial x} \quad (1.2.10)$$

If we let  $h = \eta - z_b$  and assume  $p' \Big|_{z_b} \frac{\partial z_b}{\partial x}$ ,  $p' \Big|_{\eta} \frac{\partial \eta}{\partial x} = 0$ , then we obtain

$$\int_{z_b}^{\eta} \frac{\partial}{\partial x} (\bar{p} + p') dz = h \frac{\partial \bar{p}}{\partial x} \quad (1.2.11)$$

Evaluating ② note  $\partial p(\eta)/\partial x$  is not a function of depth; thus we obtain

$$\int_z^{\eta} \frac{\partial p(\eta)}{\partial x} dz = \frac{\partial p(\eta)}{\partial x} (\eta - z_b) = h \frac{\partial p_a}{\partial x} \quad (1.2.12)$$

where

$$p_a = p(\eta)$$

Next consider the iterated integral expression for ③ as follows:

$$\begin{aligned} \frac{\partial}{\partial x} \int_z^{\eta} \rho g dr &= g \frac{\partial}{\partial x} [\bar{\rho}(\eta - z)] \\ &= g \left[ \frac{\partial \bar{\rho}}{\partial x} (\eta - z) + \bar{\rho} \frac{\partial (\eta - z)}{\partial x} \right] \end{aligned} \quad (1.2.13)$$

Note

$$\int_{z_b}^{\eta} g \frac{\partial \bar{\rho}}{\partial x} (\eta - z) dz = g \frac{\partial \bar{\rho}}{\partial x} \int_{\eta - z_b}^0 -s ds = g \frac{\partial \bar{\rho}}{\partial x} \frac{h^2}{2} \quad (1.2.14)$$

if

$$s = r - z$$

$$ds = -dz$$

Observe from Leibniz rule

$$g\bar{\rho} \int_{z_b}^{\eta} \frac{\partial(r-z)}{\partial x} dz = g\bar{\rho} \left[ \frac{\partial}{\partial x} \int_{z_b}^{\eta} (r-z) dz + (\eta - z_b) \frac{\partial z_b}{\partial x} - \cancel{(\eta - \eta) \frac{\partial \eta}{\partial x}} \right] \quad (1.2.15)$$

Letting  $h = \eta - z_b$  obtain:

$$g\bar{\rho} \int_{z_b}^{\eta} \frac{\partial(r-z)}{\partial x} dz = g\bar{\rho} \left( \frac{\partial}{\partial x} \left( \frac{h^2}{2} \right) + h \frac{\partial z_b}{\partial x} \right) = g\bar{\rho} h \left( \frac{\partial h}{\partial x} + \frac{\partial z_b}{\partial x} \right) = g\bar{\rho} h \frac{\partial \eta}{\partial x} \quad (1.2.16)$$

and the evaluation ③ is complete. Assembling all our results we obtain finally

$$h \frac{\partial \bar{p}}{\partial x} = \frac{\partial p_a}{\partial x} + \bar{\rho} g h \frac{\partial \eta}{\partial x} + g \frac{h^2}{2} \frac{\partial \bar{\rho}}{\partial y} \quad (1.2.17)$$

Analogously, the expression for the  $y$  gradient is given by

$$h \frac{\partial \bar{p}}{\partial y} = h \frac{\partial p_a}{\partial y} + \bar{\rho} g h \frac{\partial \eta}{\partial y} + g \frac{h^2}{2} \frac{\partial \bar{\rho}}{\partial y} \quad (1.2.18)$$

Thus we have employed the  $z$  motion equation to evaluate the horizontal pressure gradients in the  $x$  and  $y$  motion equations. The expressions obtained above for these gradients include the atmospheric pressure anomaly, the water surface elevation gradient, and the density gradient. In the present study, density gradients will not be considered.

96. Let us next consider the material derivative (left hand side) of (1.2) the  $x$  motion equation. Expanding the material derivative and adding (1.1) we obtain

$$\begin{aligned} & \rho \left[ \frac{\partial u}{\partial t} + u \frac{\partial u}{\partial x} + v \frac{\partial u}{\partial y} + w \frac{\partial u}{\partial z} + u \left( \frac{\partial u}{\partial x} + \frac{\partial v}{\partial y} + \frac{\partial w}{\partial z} \right) \right] \\ &= \rho \left[ \frac{\partial u}{\partial t} + \frac{\partial(u^2)}{\partial x} + \frac{\partial(uv)}{\partial y} + \frac{\partial(uw)}{\partial z} \right] \\ &= \frac{\partial(\rho u)}{\partial t} + \frac{\partial(\rho u^2)}{\partial x} + \frac{\partial(\rho uv)}{\partial y} + \frac{\partial(\rho uw)}{\partial z} \end{aligned} \quad (1.2.19)$$

Integrating the last result over the vertical (which also holds for compressible flow)

$$\begin{aligned} & \int_{z_b}^{\eta} \frac{\partial(\rho u)}{\partial t} dz + \int_{z_b}^{\eta} \frac{\partial(\rho u^2)}{\partial x} dz \\ &+ \int_{z_b}^{\eta} \frac{\partial(\rho uv)}{\partial y} dz + \int_{z_b}^{\eta} \frac{\partial(\rho uw)}{\partial z} dz \end{aligned} \quad (1.2.20)$$

Again employing Leibniz rule

$$\begin{aligned} & \frac{\partial}{\partial t} \int_{z_b}^{\eta} (\rho u) dz = \int_{z_b}^{\eta} \frac{\partial}{\partial t} (\rho u) dz \\ &+ \rho u \bigg|_{\eta} \frac{\partial \eta}{\partial t} - (\rho u) \bigg|_{z_b} \frac{\partial z_b}{\partial t} \end{aligned} \quad (1.2.21)$$

$$\frac{\partial}{\partial x} \int_{z_b}^{\eta} (\rho u u) dz = \int_{z_b}^{\eta} \frac{\partial(\rho u u)}{\partial x} dz + \rho u u \Big|_{\eta} \frac{\partial \eta}{\partial x} - \rho u u \Big|_{z_b} \frac{\partial z_b}{\partial x} \quad (1.2.22)$$

$$\frac{\partial}{\partial y} \int_{z_b}^{\eta} (\rho u v) dz = \int_{z_b}^{\eta} \frac{\partial(\rho u v)}{\partial y} dz + \rho u v \Big|_{\eta} \frac{\partial \eta}{\partial y} - \rho u v \Big|_{z_b} \frac{\partial z_b}{\partial y} \quad (1.2.23)$$

$$\int_{z_b}^{\eta} \frac{\partial}{\partial z} (\rho u w) dz = \rho u w \Big|_{\eta} - \rho u w \Big|_{z_b} \quad (1.2.24)$$

97. Notice in the above  $\partial z_b / \partial t = 0$ , since the bottom is assumed rigid. Denoting terms in (1.1.4) by ①, and those in (1.1.5) by ②, we obtain the following

$$\begin{aligned} \frac{\partial}{\partial t} \int_{z_b}^{\eta} (\rho u) dz &= \text{①} \left. \rho u \right|_{\eta} \frac{\partial \eta}{\partial t} + \text{①} \int_{z_b}^{\eta} \frac{\partial(\rho u u)}{\partial x} dz \\ &+ \text{②} \left. \rho u u \right|_{z_b} \frac{\partial z_b}{\partial x} - \text{①} \left. \rho u u \right|_{\eta} \frac{\partial \eta}{\partial x} + \text{①} \int_{z_b}^{\eta} \frac{\partial(\rho u v)}{\partial y} dz \\ &+ \text{②} \left. \rho u v \right|_{z_b} \frac{\partial z_b}{\partial y} - \text{①} \left. \rho u v \right|_{\eta} \frac{\partial \eta}{\partial y} + \text{①} \left. \rho u w \right|_{\eta} - \text{②} \left. \rho u w \right|_{z_b} \end{aligned} \quad (1.2.25)$$

The above expression reduces to the following:

$$\frac{\partial}{\partial t} \int_{z_b}^n (\rho u) dz + \frac{\partial}{\partial x} \int_{z_b}^n (\rho u u) dz + \frac{\partial}{\partial y} \int_{z_b}^n (\rho u v) dz \quad (1.2.26)$$

The following terms are next defined

$$h\bar{u} = (n - z_b) \bar{u} = \int_{z_b}^n u(z) dz, h\bar{v} = (n - z_b) \bar{v} = \int_{z_b}^n v(z) dz \quad (1.2.27)$$

where

$$u(z) = \bar{u} [1 + u'(z)]$$

$$v(z) = \bar{v} [1 + v'(z)]$$

Thus

$$h\bar{u} = \int_{z_b}^n \bar{u} dz + \int_{z_b}^n \bar{u} u' dz = h\bar{u} + \bar{u} \int_{z_b}^n u' dz \quad (1.2.28)$$

$$h\bar{v} = \int_{z_b}^n \bar{v} dz + \int_{z_b}^n \bar{v} v' dz = h\bar{v} + \bar{v} \int_{z_b}^n v' dz \quad (1.2.29)$$

Therefore we must have

$$\int_{z_b}^n u' dz = \int_{z_b}^n v' dz = 0 \quad (1.2.30)$$

98. Rewriting (1.2.26) and employing assumption 8 we obtain



$$\begin{aligned} & \rho \frac{\partial}{\partial t} (\bar{u}h) + \rho \frac{\partial}{\partial x} \int_{z_b}^{\eta} \bar{u} \bar{u} [1 + 2u'(z) + u'(z)^2] dz \\ & + \rho \frac{\partial}{\partial y} \int_{z_b}^{\eta} \bar{u} \bar{v} [1 + u'(z) + v'(z) + u'(z)v'(z)] dz \end{aligned} \quad (1.2.31)$$

Let

$$\beta = \frac{1}{h} \int_{z_b}^{\eta} \{1 + [u'(z)]^2\} dz = \frac{1}{h} \int_{z_b}^{\eta} [1 + u'(z)v'(z)] dz$$

Noting the depth integral of the product of a bar and primed quantity is zero, we finally obtain

$$\rho \left[ \frac{\partial}{\partial t} (\bar{u}h) + \frac{\partial}{\partial x} (\beta \bar{u}h) + \frac{\partial}{\partial y} (\beta \bar{u}v h) \right] \quad (1.2.32)$$

Analogously, one obtains the following expression for the left hand side of the y-motion equation (1.3) after integration over depth

$$\rho \left[ \frac{\partial}{\partial t} (\bar{v}h) + \frac{\partial}{\partial x} (\beta \bar{u}v h) + \frac{\partial}{\partial y} (\beta \bar{v}h) \right] \quad (1.2.33)$$

where

$$\beta = \frac{1}{h} \int_{z_b}^{\eta} \{1 + [v'(z)]^2\} dz = \frac{1}{h} \int_{z_b}^{\eta} [1 + u'(z)v'(z)] dz$$

Thus  $\beta$  in (1.2.32) and in (1.2.33) is the same quantity and is usually assumed equal to unity.

99. Let us now consider the right hand side of the x and y motion equations. Considering the  $F_x$  and  $F_y$  terms, we obtain

$$F_x = \rho v + g_x + G_x \quad F_y = -\rho u + g_y + G_y \quad (1.2.34)$$

where  $G$  is the tide-generating force,  $\Omega$  is the Coriolis factor,  
 $\Omega = 2\omega \sin \phi$  ( $\omega \equiv$  angular velocity of the earth rotation,  $\phi$  is latitude),  
and  $g_x$ ,  $g_y$  are the components of gravity in the horizontal. Assume the following:

1.  $g_x$ ,  $G_x \ll \Omega v$ ,
2.  $g_y$ ,  $G_y \ll \Omega u$ ,

then,

$$F_x = \Omega v, \quad F_y = -\Omega u$$

Integrating over the vertical

$$\int_{z_b}^{\eta} \Omega v \, dz = \Omega \bar{v} h \qquad \int_{z_b}^{\eta} -\Omega u \, dz = -\Omega \bar{u} h \qquad (1.2.35)$$

where  $\bar{u}$ ,  $\bar{v}$  are vertically averaged velocity components, and  $h = \eta - z_b$ .

100. For a turbulent flow an eddy viscosity  $\epsilon$  is employed in the place of the dynamic viscosity  $\mu$ . The terms become using  $\epsilon_h$  and  $\epsilon_v$  for horizontal and vertical eddy viscosity, respectively:

$$\begin{aligned} \epsilon_h \left( \frac{\partial^2 u}{\partial x^2} + \frac{\partial^2 u}{\partial y^2} \right) + \epsilon_v \frac{\partial^2 u}{\partial z^2} \\ \epsilon_h \left( \frac{\partial^2 v}{\partial x^2} + \frac{\partial^2 v}{\partial y^2} \right) + \epsilon_v \frac{\partial^2 v}{\partial z^2} \end{aligned} \qquad (1.2.36)$$

101. The horizontal eddy viscosity terms are much smaller than the vertical eddy viscosity terms and have been neglected by some modellers. We consider the terms here in the following manner. If we consider the  $u$  equation and note  $u = \bar{u} + u'$ , integrate over the vertical, and employ Leibniz rule, the following relation is obtained for the  $\epsilon$  terms.

$$\int_{z_b}^{\eta} \frac{\partial^2 (\bar{u} + u')}{\partial x^2} dz = \frac{\partial}{\partial x} \int_{z_b}^{\eta} (\bar{u} + u') dz + \frac{\partial u}{\partial x} \bigg|_{z_b} \frac{\partial z_b}{\partial x} - \frac{\partial u}{\partial x} \bigg|_{\eta} \frac{\partial \eta}{\partial x} \quad (1.2.37)$$

$$\int_{z_b}^{\eta} \frac{\partial^2 (\bar{u} + u')}{\partial x^2} dz = \frac{\partial}{\partial x} \left[ \int_{z_b}^{\eta} (\bar{u} + u') dz + u \bigg|_{z_b} \frac{\partial z_b}{\partial x} - u \bigg|_{\eta} \frac{\partial \eta}{\partial x} \right] + \frac{\partial u}{\partial x} \bigg|_{z_b} \frac{\partial z_b}{\partial x} - \frac{\partial u}{\partial x} \bigg|_{\eta} \frac{\partial \eta}{\partial x} \quad (1.2.38)$$

It is assumed that all derivative terms may be neglected, thus

$$\int_{z_b}^{\eta} \frac{\partial^2 (\bar{u} + u')}{\partial x^2} dz = \frac{\partial^2}{\partial x^2} (h\bar{u}) = h \frac{\partial^2 \bar{u}}{\partial x^2} + 2 \frac{\partial h}{\partial x} \frac{\partial \bar{u}}{\partial x} + \bar{u} \frac{\partial^2 h}{\partial x^2} \quad (1.2.39)$$

It is further assumed the second and third terms are negligible. If similar assumptions are made for the other terms in (1.2.36) we obtain

$$\begin{aligned} \epsilon_h \left( \frac{\partial^2 u}{\partial x^2} + \frac{\partial^2 u}{\partial y^2} \right) dz &= \epsilon_h \left[ \frac{\partial^2 (h\bar{u})}{\partial x^2} + \frac{\partial^2 (h\bar{u})}{\partial y^2} \right] \\ &= \epsilon_h h \left( \frac{\partial^2 \bar{u}}{\partial x^2} + \frac{\partial^2 \bar{u}}{\partial y^2} \right) \end{aligned} \quad (1.2.40)$$

$$\int_{z_b}^{\eta} \epsilon_h \left( \frac{\partial^2 v}{\partial x^2} + \frac{\partial^2 v}{\partial y^2} \right) dz = \epsilon_h \left[ \frac{\partial^2 (h\bar{v})}{\partial x^2} + \frac{\partial^2 (h\bar{v})}{\partial y^2} \right]$$

$$= \epsilon_h h \left( \frac{\partial^2 \bar{v}}{\partial x^2} + \frac{\partial^2 \bar{v}}{\partial y^2} \right) \quad (1.2.41)$$

These terms are retained in the motion equations and serve to stabilize the numerical approximations. The vertical eddy viscosity terms are integrated over the vertical as follows:

$$\int_{z_b}^{\eta} \epsilon_v \frac{\partial^2 u}{\partial z^2} dz = \epsilon_v \left( \frac{\partial u}{\partial z} \Big|_{\eta} - \frac{\partial u}{\partial z} \Big|_{z_b} \right) = \tau_{sx} - \tau_{bx} \quad (1.2.42)$$

$$\int_{z_b}^{\eta} \epsilon_v \frac{\partial^2 v}{\partial z^2} dz = \epsilon_v \left( \frac{\partial v}{\partial z} \Big|_{\eta} - \frac{\partial v}{\partial z} \Big|_{z_b} \right) = \tau_{sy} - \tau_{by} \quad (1.2.43)$$

where

$\tau_{sx}$  ,  $\tau_{sy}$  = surface stresses

$\tau_{by}$  ,  $\tau_{bx}$  = bottom stresses

102. Consider the bottom stress,  $\tau_b$  , as follows:

$$\tau_b = C_f \rho \frac{V_f^2}{2}$$

where

$C_f$  = a drag coefficient

$V_f$  = the fluid velocity

Letting Chezy  $c = \sqrt{2g/C_f}$

obtain:

$$\tau_b = \frac{\rho g}{c} v_f^2 \quad (1.2.44)$$

Resolve  $\tau_b$  along the x and y directions noting  $v_f = \sqrt{\bar{u}^2 + \bar{v}^2}$  to obtain:

$$\tau_{bx} = \frac{\rho g}{c} v_f \bar{u} \quad \tau_{by} = \frac{\rho g}{c} v_f \bar{v} \quad (1.2.45)$$

103. The surface stress  $\tau_s$  may have a similar form; namely,

$$\tau_s = c'_f \frac{\rho_a v_w^2}{2}$$

where

$c'_f \equiv$  drag coefficient

$\rho_a \equiv$  air density

$v_w \equiv$  wind speed

Assuming the shear stress varies linearly with depth we obtain

$$\frac{\partial \tau}{\partial z} = \frac{\tau_s + \tau_b}{h} = \frac{\tau_s}{h} \left( 1 + \frac{\tau_b}{\tau_s} \right) = \frac{\lambda \tau_s}{h} = \frac{\partial p_{wd}}{\partial s} \quad (1.2.46)$$

where

$\lambda \equiv (\tau_b / \tau_s + 1)$

$p_{wd} \equiv$  pressure intensity produced by the wind

$s \equiv$  distance in the downwind direction

Integrating (1.2.46) over the vertical

$$\int_{z_b}^n \frac{\partial \tau}{\partial z} dz = \int_{z_b}^n \frac{c'_f \lambda \rho_a v_w^2}{2h} dz = K V^2 \quad (1.2.47)$$

where

$$K = (c'_f \lambda \rho_a) / 2$$

If  $\theta$  is the angle between the wind direction and the  $+x$  axis,

$$\tau_{sx} = KV_w^2 \cos \theta \quad (1.2.48)$$

$$\tau_{sy} = KV_w^2 \sin \theta \quad (1.2.49)$$

104. Assembling our results, we obtain the final expression for the depth integrated motion equations

$$\begin{aligned} \rho \frac{\partial}{\partial t} (\bar{u}h) + \rho \frac{\partial}{\partial x} (\beta \bar{u}^2 h) + \rho \frac{\partial}{\partial y} (\beta \bar{u} \bar{v} h) = \rho \bar{\omega} \bar{v} h + h \epsilon_h \left( \frac{\partial^2 \bar{u}}{\partial x^2} + \frac{\partial^2 \bar{u}}{\partial y^2} \right) \\ - h \left( \frac{\partial \rho}{\partial x} \bar{a} + \bar{\rho} g \frac{\partial \eta}{\partial x} + \frac{gh}{2} \frac{\partial \bar{\rho}}{\partial x} \right) - \frac{\rho g (\bar{u} + \bar{v})^{1/2} \bar{u}}{c^2} + KV_w^2 \cos \theta \end{aligned} \quad (1.2.50)$$

$$\begin{aligned} \rho \frac{\partial}{\partial t} (\bar{v}h) + \rho \frac{\partial}{\partial x} (\beta \bar{u} \bar{v} h) + \rho \frac{\partial}{\partial y} (\beta \bar{v}^2 h) = -\rho \bar{\omega} \bar{u} h + h \epsilon_h \left( \frac{\partial^2 \bar{v}}{\partial x^2} + \frac{\partial^2 \bar{v}}{\partial y^2} \right) \\ - h \left( \frac{\partial \rho}{\partial y} \bar{a} + \bar{\rho} g \frac{\partial \eta}{\partial y} + \frac{gh}{2} \frac{\partial \bar{\rho}}{\partial y} \right) - \frac{\rho g (\bar{u} + \bar{v})^{1/2} \bar{v}}{c^2} + KV_w^2 \sin \theta \end{aligned} \quad (1.2.51)$$

Setting  $\beta = 1$  and expanding the left-hand side of the above two equations one obtains

$$\begin{aligned} \rho \left[ h \frac{\partial \bar{u}}{\partial t} + \bar{u} \left( \frac{\partial \eta}{\partial t} - \frac{\partial z}{\partial t} \right) + 2\bar{u}h \frac{\partial \bar{u}}{\partial x} + \left( \frac{\partial \eta}{\partial x} - \frac{\partial z}{\partial x} \right) \bar{u}^2 + \bar{u} \bar{v} \left( \frac{\partial \eta}{\partial y} - \frac{\partial z}{\partial y} \right) \right. \\ \left. + h \bar{u} \frac{\partial \bar{v}}{\partial y} + \bar{v} \frac{\partial \bar{u}}{\partial y} \right] = \rho \left[ h \frac{\partial \bar{u}}{\partial t} + \bar{u} \left( \frac{\partial \eta}{\partial t} + h \frac{\partial \bar{u}}{\partial x} + \bar{u} \frac{\partial h}{\partial x} + \bar{v} \frac{\partial h}{\partial y} + h \frac{\partial \bar{v}}{\partial y} \right) \right. \\ \left. + h \bar{u} \frac{\partial \bar{u}}{\partial x} + h \bar{v} \frac{\partial \bar{u}}{\partial y} \right] = \rho h \left\{ \frac{\partial \bar{u}}{\partial t} + \bar{u} \frac{\partial \bar{u}}{\partial x} + \bar{v} \frac{\partial \bar{u}}{\partial y} + \frac{\bar{u}}{h} \left[ \frac{\partial \eta}{\partial t} + \frac{\partial}{\partial x} (h \bar{u}) \right. \right. \\ \left. \left. + \frac{\partial}{\partial y} (h \bar{v}) \right] \right\} = \rho h \frac{D \bar{u}}{D t} \end{aligned} \quad (1.2.52)$$

$$\begin{aligned}
&= \left[ h \frac{\partial \bar{v}}{\partial t} + \bar{v} \left( \frac{\partial \eta}{\partial t} - \frac{\partial^2 z}{\partial t^2} \right)^0 + 2\bar{v}h \frac{\partial \bar{v}}{\partial y} + \bar{v}^2 \frac{\partial h}{\partial y} + \bar{u}\bar{v} \frac{\partial h}{\partial x} + h \left( \bar{u} \frac{\partial v}{\partial x} + \bar{v} \frac{\partial u}{\partial x} \right) \right] \\
&= \left[ h \frac{\partial \bar{v}}{\partial t} + \bar{v} \left( \frac{\partial \eta}{\partial t} + h \frac{\partial \bar{v}}{\partial y} + \bar{v} \frac{\partial h}{\partial y} + \bar{u} \frac{\partial h}{\partial x} + h \frac{\partial u}{\partial x} \right) + h\bar{v} \frac{\partial v}{\partial y} + h\bar{u} \frac{\partial v}{\partial x} \right] \\
&+ sh \left\{ \frac{\partial \bar{v}}{\partial t} + \bar{u} \frac{\partial \bar{v}}{\partial x} + \bar{v} \frac{\partial \bar{v}}{\partial y} + \frac{\bar{v}}{h} \left[ \frac{\partial \eta}{\partial t} + \frac{\partial}{\partial x} (\bar{u}h) + \frac{\partial}{\partial y} (\bar{v}h) \right] \right\} \\
&= \rho h \frac{\partial \bar{v}}{\partial t} \quad (1.2.53)
\end{aligned}$$

Letting  $\epsilon_h = \rho \epsilon$  ( $\epsilon$  is a kinematic eddy viscosity) and dropping the bar notation we obtain the final form of the equations:

$$\begin{aligned}
\frac{\partial u}{\partial t} + u \frac{\partial u}{\partial x} + v \frac{\partial u}{\partial y} = \Omega v + \epsilon \left( \frac{\partial^2 u}{\partial x^2} + \frac{\partial^2 u}{\partial y^2} \right) - g \frac{u(u+v)^{1/2}}{c^2 h} + \frac{K}{\rho h} v_w^2 \cos \theta \\
- \frac{1}{\rho} \left( \frac{\partial p_a}{\partial x} + \bar{\rho} g \frac{\partial \eta}{\partial x} + \frac{gh}{2} \frac{\partial \bar{\rho}}{\partial x} \right) \quad (1.2.54)
\end{aligned}$$

$$\begin{aligned}
\frac{\partial v}{\partial t} + u \frac{\partial v}{\partial x} + v \frac{\partial v}{\partial y} = -\Omega u + \epsilon \left( \frac{\partial^2 v}{\partial x^2} + \frac{\partial^2 v}{\partial y^2} \right) - g \frac{v(u+v)^{1/2}}{c^2 h} + \frac{K}{\rho h} v_w^2 \sin \theta \\
- \frac{1}{\rho} \left( \frac{\partial p_a}{\partial y} + \bar{\rho} g \frac{\partial \eta}{\partial y} + \frac{gh}{2} \frac{\partial \bar{\rho}}{\partial y} \right) \quad (1.2.55)
\end{aligned}$$

### Forcing functions

105. In the simulation of hurricane induced water level fluctuations, it is necessary to consider the atmospheric pressure anomaly and wind stress terms in the motion equations. The formulations employed are presented in detail in turn below.

## Atmospheric Pressure Anomaly

106. The pressure field computed in the hurricane model is developed in units of inches of mercury (Hg). Employing the manometer equation, we obtain:

$$\rho_m g h_m = 12 \rho_w g h_w \quad (1.3.1)$$

where

$\rho_m$   $\equiv$  Density of mercury (26.3877 slugs/ft<sup>3</sup> 1 ATM at 68°F)

$\rho_w$   $\equiv$  Density of water (1.9403 slugs/ft<sup>3</sup> 1 ATM at 68°F)

$g$   $\equiv$  gravity

$h_m$   $\equiv$  inches of mercury

$h_w$   $\equiv$  ft of water

Therefore  $h_w = 1.14 h_m$ . Examining Equations (1.2.54) and (1.2.55), we obtain the following relationships for the pressure gradient terms. Assume

$$\bar{\phi} = \phi, \quad \frac{\partial \bar{\phi}}{\partial x} = \frac{\partial \phi}{\partial x} = 0.$$

$$P_x = -\frac{1}{\bar{\phi}} \left( \frac{\partial p_a}{\partial x} + \rho g \frac{\partial r}{\partial x} \right) \quad P_y = -\frac{1}{\bar{\phi}} \left( \frac{\partial p_a}{\partial y} + \rho g \frac{\partial r}{\partial y} \right) \quad (1.3.2)$$

107. In the above equations,  $p_a = \rho_w g h_w$ . Employing this relation, the equations may be written in the following form:

$$P_x = -g \frac{\partial(h_w + r)}{\partial x} \quad P_y = -g \frac{\partial(h_w + r)}{\partial y} \quad (1.3.3)$$

Alternatively, one may employ a hurricane pressure deficit concept defined as follows:

$$\Delta P = P_w - P_2 \quad (1.3.4)$$

where

$\Delta P$  = hurricane pressure deficit (in Hg)

$P_w$  = asymptotic (far field) pressure (in Hg)

$P_2$  = local atmospheric pressure at (x,y) (in Hg)



If we define,  $\eta_a = 1.14 \Delta P$  and assume  $P_w$  is a constant, then we obtain:

$$\frac{\partial P_a}{\partial x} = - \rho g \frac{\partial \eta_a}{\partial y} \quad \frac{\partial P_a}{\partial y} = - \rho g \frac{\partial \eta_a}{\partial x} \quad (1.3.5)$$

If we employ (1.3.5) in (1.3.2) the following alternative form, which is employed in the current model is obtained:

$$P_x = - g \frac{\partial (\eta - \eta_a)}{\partial x} \quad P_y = - g \frac{\partial (\eta - \eta_a)}{\partial y} \quad (1.3.6)$$

### Surface Wind Stress

108. The hurricane wind loading is implemented as a surface stress in each horizontal motion equation (Refer to Equations 1.2.54 and 1.2.55). In the previous development  $K = (c_f' \lambda_{0a})/2$  and is dimensionless. If  $\lambda \approx 2$ , then  $K \approx P_a c_f'$ . Several investigators had developed relationships based upon observed wind data for  $c_f'$ . These relationships are presented in turn below, in which  $C_D = c_f'$ .

### Van Dorn Formulation

109. Professor W. G. Van Dorn measured the wind induced slope of the surface in an 800 foot model-yacht pond [18] and presented the following result.

$$C_D \times 10^3 = \begin{cases} .895 & U_{10} < 7.2 \text{ m/sec} \\ .895 + 2.034(1 - 7.2/U_{10})^{**2} & U_{10} \geq 7.2 \text{ m/sec} \end{cases}$$

where

$C_D$  = overwater neutral 10 meter drag coefficient

$U_{10}$  = sustained (10 min) average windspeed at 10 m

110. This formula has been traditionally used in hurricane wind-stress applications in numerical storm surge modelling. The formula was developed using windspeeds less than 15 m/sec.

### Charnock Formulation

111. Charnock [19] proposed the following relation:

$$z_0 = \frac{u_*^2}{g} \quad (11.1)$$

where

$z_0$  = aerodynamic roughness length (m)

$u_*$  = friction velocity (m/sec)

$g$  = gravitational constant (9.81 m/sec<sup>2</sup>)

$\rho = 1.225$

112. G. R. Garratt [20] has noted that observations of wind stress and wind profiles over the ocean reported in the literature over the past 20 years are consistent with the above relation. For practical purposes, Charnock's relation may be approximated in the range  $u_* = 0.5$  to 20 m/sec by either of the following forms as developed by Garratt [10]:

$$z_0 = 0.185 u_*^{1.5} \quad \text{Charnock Power Law} \quad (11.2)$$

$$z_0 = 0.0115 u_*^2 + 0.002 \quad \text{Charnock Linear Law} \quad (11.3)$$

where  $u_*$  and  $z_0$  are as previously defined.

### Wu Formulations

113. Wu [21] suggested the following power law as the simplest form to approximate the aerodynamic roughness coefficient in open sea:

$$z_0 = 0.000185 u_*^3 = 0.5 \frac{u_*^3}{g} \quad \text{Wu Power Law} \quad (11.4.5)$$

where  $u_*$  and  $z_0$  are as previously defined. This form is very similar to the Charnock Power Law presented above.

114. Wu has developed the following law similar to the Charnock Linear Law which may be used in hurricane conditions [21, 22]:

$$C_D \times 10^3 = .8 + 0.65 U_{10} \quad \text{Wu Linear Law} \quad (1.4.6)$$

where  $C_D$  and  $U_{10}$  are as previously defined.

#### Powell Formulation

115. Four diagnostic marine boundary-layer models were evaluated for applicability to the hurricane regime. Model results also included the 10 meter level neutral drag coefficients [23]. Powell suggests the following relation as an alternative to the Deacon relationship employed by Rosenthal [24] in the National Hurricane and Experimental Meteorological Laboratory computer model.

$$C_D \times 10^3 = 1.0236 + 5.366 \times 10^{-2} U_{10} \quad \text{Powell Law} \quad (1.4.7)$$

$$C_D \times 10^3 = 1.1 + 4.0 \times 10^{-2} U_{10} \quad \text{Deacon Law} \quad (1.4.8)$$

where  $C_D$  and  $U_{10}$  are as previously defined. The Powell Law has been developed based upon data from seven hurricanes and is the form which will be used during the study.

#### Implicit Formulations

116. The following set of relationships is used to determine the neutral ten meter drag coefficient.

$$\begin{aligned} u_* &= \kappa u_{10} / \ln(10/z_o) & (a) \\ z_o &= a/g u_*^2 & (b) \\ C_D &= (u_*/U_{10})^2 & (c) \end{aligned} \quad (1.4.9)$$

where

$U_*$   $\equiv$  friction velocity

$\kappa$   $\equiv$  von Karman's constant

$z_0$  Aerodynamic roughness  
 $g$  Gravity  
 $a$  Charnock's constant  
 and  $C_D$ ,  $U_{10}$  are as previously defined.

Alternative values have been used for  $\alpha$  and  $a$  as shown in Table III-1 below.

Table III-1  
Coefficient Values for Implicit Drag Formulations

<u>Investigator</u>	<u>a</u>	<u><math>\alpha</math></u>
Cardone [14]	.0350	.35
Wu [21]	.0185	.40
Garratt [20]	.0144	.41

#### Surface Wind Stress Evaluation

117. In order to compare results obtained from the above drag laws over a range of ten-meter windspeeds Program DRAG as listed in Appendix A was developed after Prater [25]. Results are shown in Table III-2 for  $10 \leq U_{10} \leq 120$  kts at 10 knot increments. The first line associated with a given wind speed contains the drag coefficients predicted by each formulation. The second line associated with the given windspeed contains the ratio of the various drag coefficients to the van Dorn coefficient, which has long been used as the standard. As observed the ratios are all greater than one and in general increase with windspeed. At all windspeeds, there are variations of over 30%. Variations on the order of 50-100% may occur at hurricane windspeeds.

Table 111-2  
Overwater Neutral 10 Meter Drag Coefficients

OVERWATER NEUTRAL 10 METER DRAG COEFFICIENTS

KNOTS	VAN DORN	DEALON	POWELL	CHARN PWK	WU PWK	CHARN LIN	WU LIN	CARDONE	WU	GAKKATI
10	.895E-03	.131E-02	.130E-02	.108E-02	.112E-02	.109E-02	.113E-02	.898E-03	.109E-02	.110E-02
...	1.0000	1.4588	1.4524	1.2103	1.2669	1.2230	1.2673	1.0034	1.2160	1.2384
20	.108E-02	.151E-02	.158E-02	.149E-02	.160E-02	.144E-02	.147E-02	.123E-02	.147E-02	.147E-02
...	1.0000	1.4019	1.4618	1.3822	1.4875	1.3350	1.3622	1.1414	1.3621	1.3654
30	.147E-02	.172E-02	.185E-02	.180E-02	.196E-02	.178E-02	.180E-02	.153E-02	.180E-02	.180E-02
...	1.0000	1.1653	1.2567	1.2185	1.3328	1.2105	1.2235	1.0381	1.2230	1.2182
40	.175E-02	.192E-02	.213E-02	.205E-02	.227E-02	.213E-02	.214E-02	.182E-02	.212E-02	.210E-02
...	1.0000	1.0960	1.2129	1.1683	1.2927	1.2132	1.2182	1.0390	1.2095	1.1978
50	.195E-02	.213E-02	.240E-02	.227E-02	.254E-02	.247E-02	.247E-02	.212E-02	.244E-02	.240E-02
...	1.0000	1.0919	1.2331	1.1650	1.3006	1.2686	1.2678	1.0878	1.2517	1.2328
60	.209E-02	.233E-02	.268E-02	.247E-02	.278E-02	.282E-02	.281E-02	.243E-02	.276E-02	.271E-02
...	1.0000	1.1166	1.2819	1.1814	1.3286	1.3478	1.3422	1.1627	1.3222	1.2951
70	.220E-02	.254E-02	.296E-02	.265E-02	.300E-02	.316E-02	.314E-02	.276E-02	.310E-02	.302E-02
...	1.0000	1.1563	1.3455	1.2069	1.3656	1.4395	1.4294	1.2555	1.4106	1.3742
80	.228E-02	.275E-02	.323E-02	.282E-02	.321E-02	.351E-02	.347E-02	.311E-02	.345E-02	.334E-02
...	1.0000	1.2046	1.4179	1.2369	1.4070	1.5385	1.5243	1.3636	1.5129	1.4654
90	.235E-02	.295E-02	.351E-02	.298E-02	.340E-02	.385E-02	.381E-02	.349E-02	.382E-02	.368E-02
...	1.0000	1.2584	1.4956	1.2690	1.4503	1.6421	1.6239	1.4866	1.6274	1.5671
100	.240E-02	.316E-02	.378E-02	.312E-02	.359E-02	.420E-02	.414E-02	.390E-02	.421E-02	.403E-02
...	1.0000	1.3159	1.5770	1.3020	1.4944	1.7488	1.7268	1.6253	1.7539	1.6785
110	.244E-02	.336E-02	.406E-02	.326E-02	.376E-02	.454E-02	.448E-02	.436E-02	.463E-02	.440E-02
...	1.0000	1.3759	1.6610	1.3354	1.5386	1.8577	1.8319	1.7818	1.8929	1.7998
120	.248E-02	.357E-02	.434E-02	.340E-02	.393E-02	.489E-02	.481E-02	.486E-02	.508E-02	.479E-02
...	1.0000	1.4378	1.7468	1.3688	1.5825	1.9682	1.9386	1.9589	2.0455	1.9313

### Bottom Friction

118. In the treatment of hurricane induced water levels in Lake Okeechobee, it is necessary to consider the role of bottom friction in Equations (1.2.54) and (1.2.55). A Chezy C formulation is employed, which is based on the following relationship in terms of Manning's  $n$  roughness.

$$C = \frac{1.49}{n^*} R^{1/6} \quad (1.4.1)$$

where

$C$  = Chezy C

$n^*$  = Manning's  $n$  roughness (effective)

$R$  = hydraulic radius (depth)

The user specifies Manning's  $n$  versus stilled water depth correspondence. This correspondence is further modified by employing the following relationship to account for the canopy effects of vegetation near the shoreline.

$$n^* = \begin{cases} n (1 + k_1 e^{-d/k_2}) & d \leq d^* \\ n & d > d^* \end{cases} \quad (1.4.2)$$

where

$n^*$  = Effective Manning's  $n$  roughness

$k_1$  = Canopy coefficient number one

$k_2$  = Canopy coefficient number two

$d$  = Water depth

$d^*$  = Canopy water depth

Equations (1.4.1) and (1.4.2) are used to determine the Chezy C for each cell at each time step in the numerical solution. Observe in this approach as the water depth decreases,  $n^*$  increases and C decreases. Since C appears in the denominator in both motion equations (1.2.54) and (1.2.55), the magnitude of these friction terms increases.

# Development of the transformed long wave hydrodynamic equations

(19) The following coordinate transformation is considered:

$$x = x_1 + b_1 \frac{\partial \eta}{\partial x_1} \quad \Rightarrow \quad x_1 = \left( \frac{x - a_1}{b_1} \right) \quad (11.5.1)$$

$$y = y_1 + b_2 \frac{\partial \eta}{\partial x_1} \quad \Rightarrow \quad y_1 = \left( \frac{y - a_2}{b_2} \right) \quad (11.5.2)$$

Then  $\eta$  is an arbitrary hydrodynamic variable  $\eta = \eta(x, y)$

$$\frac{\partial \eta}{\partial x} = \frac{\partial \eta}{\partial x_1} \frac{\partial x_1}{\partial x} \quad \frac{\partial \eta}{\partial y} = \frac{\partial \eta}{\partial x_1} \frac{\partial x_1}{\partial y}$$

$$\frac{\partial^2 \eta}{\partial x^2} = \frac{\partial}{\partial x_1} \left( \frac{\partial \eta}{\partial x} \right) \frac{\partial x_1}{\partial x} = \frac{\partial}{\partial x_1} \left( \frac{\partial \eta}{\partial x_1} \frac{\partial x_1}{\partial x} \right) \frac{\partial x_1}{\partial x} = \frac{\partial x_1}{\partial x} \left[ \frac{\partial^2 \eta}{\partial x_1^2} \frac{\partial x_1}{\partial x} + \frac{\partial}{\partial x_1} \left( \frac{\partial x_1}{\partial x} \right) \left( \frac{\partial \eta}{\partial x_1} \right) \right]$$

$$\frac{\partial^2 \eta}{\partial y^2} = \frac{\partial}{\partial x_1} \left( \frac{\partial \eta}{\partial y} \right) \frac{\partial x_1}{\partial y} = \frac{\partial}{\partial x_1} \left( \frac{\partial \eta}{\partial x_1} \frac{\partial x_1}{\partial y} \right) \frac{\partial x_1}{\partial y} = \frac{\partial x_1}{\partial y} \left[ \frac{\partial^2 \eta}{\partial x_1^2} \frac{\partial x_1}{\partial y} + \frac{\partial}{\partial x_1} \left( \frac{\partial x_1}{\partial y} \right) \left( \frac{\partial \eta}{\partial x_1} \right) \right]$$

Now introduce  $\xi_1 = ix dx_1$  and  $\xi_2 = iy dx_1$  then

$$\frac{\partial \eta}{\partial x} = \frac{1}{\mu_1} \frac{\partial \eta}{\partial \xi_1} \quad \frac{\partial \eta}{\partial y} = \frac{1}{\mu_2} \frac{\partial \eta}{\partial \xi_1}$$

$$\frac{\partial^2 \eta}{\partial x^2} = \frac{1}{\mu_1^2} \left[ \frac{1}{\mu_1} \frac{\partial^2 \eta}{\partial \xi_1^2} + \frac{\partial}{\partial \xi_1} \left( \frac{1}{\mu_1} \right) \left( \frac{\partial \eta}{\partial \xi_1} \right) \right] \quad (11.5.3)$$

$$\frac{\partial^2 \eta}{\partial y^2} = \frac{1}{\mu_2^2} \left[ \frac{1}{\mu_2} \frac{\partial^2 \eta}{\partial \xi_1^2} + \frac{\partial}{\partial \xi_1} \left( \frac{1}{\mu_2} \right) \left( \frac{\partial \eta}{\partial \xi_1} \right) \right] \quad (11.5.4)$$

(20). Consider the continuity balance, Equation (1.1.9), the two components of momentum, Equations (1.2.54) and (1.2.55), and the appropriate pressure gradient terms in Equations (1.3.5) and (1.3.6), for the respective momentum equations. If we substitute  $d$  for  $h$  we obtain the following set of four dynamic equations written in subscript notation:

$$\rho_a \left( \frac{du}{dt} + u \frac{du}{dx} + v \frac{du}{dy} \right) - \rho_a \left( \frac{\partial u}{\partial x} + \frac{\partial v}{\partial y} \right) = F_x \quad (a)$$

$$\rho_a \left( \frac{dv}{dt} + u \frac{dv}{dx} + v \frac{dv}{dy} \right) - \rho_a \left( \frac{\partial v}{\partial x} + \frac{\partial u}{\partial y} \right) = F_y \quad (b)$$

$$\rho_a \left( \frac{dw}{dt} + u \frac{dw}{dx} + v \frac{dw}{dy} \right) = R \quad (c)$$

where

- $\frac{d}{dt}$  = time derivative
- $F_x$  = wind stressed etc.
- $R$  = rainfall rate
- $\rho_a$  = air density
- $\mu$  = viscosity coefficient
- $\eta$  = hydrostatic elevation due to atmospheric pressure anomaly
- $\zeta$  = water surface elevation with respect to the lake datum
- $\xi$  = bottom elevation with respect to the lake datum

where in Equation (1.1.9), the right hand side has been set to the rainfall rate in the above equation set. Note also that in Equation (1.5.8) (a) and (b)

$$F_x = \frac{\rho_a}{\rho_d} V_w^2 \cos \theta$$

$$F_y = \frac{\rho_a}{\rho_d} V_w^2 \sin \theta$$

where  $\rho_a$  is the density of air.

Noting that  $\rho$  corresponds to either  $u$  or  $v$  or  $w$  we rewrite Equation (1.5.8) in transformed form as follows:



$$\underline{u_t + \frac{u}{u_1} (u)_{x_1} + \frac{v}{u_2} (u)_{x_2} - fv + g \frac{(n - n_a) \alpha_1}{u_1} + \frac{gu}{C^2 d} (u^2 + v^2)^{1/2}} \quad (a)$$

$$- \left[ \frac{1}{u_1} (u)_{x_1 x_1} + \frac{1}{u_1} \frac{1}{u_1} u_{x_1} + \frac{1}{u_2} u_{x_2 x_2} + \frac{1}{u_2} \left( \frac{1}{u_2} \right)_{\alpha_2} u_{\alpha_2} \right] = F_{x_1}$$

$$\underline{v_t + \frac{u}{v_1} (v)_{x_1} + \frac{v}{v_2} (v)_{x_2} + fu + g \frac{(n - n_a) \alpha_2}{v_2} + \frac{gv}{C^2 d} (u^2 + v^2)^{1/2}} \quad (1.5.9)$$

$$- \left[ \frac{1}{v_1} (v)_{x_1 x_1} + \frac{1}{v_1} \frac{1}{v_1} v_{x_1} + \frac{1}{v_2} v_{x_2 x_2} + \frac{1}{v_2} \left( \frac{1}{v_2} \right)_{\alpha_2} v_{\alpha_2} \right] = F_{x_2}$$

$$\underline{u_t + \frac{1}{u_1} (du)_{x_1} + \frac{1}{v_2} (dv)_{x_2}} = R \quad (c)$$

Equation set (1.5.9) is the object of numerical approximation. In the initial development, a linear form of the equations is considered by setting all underlined terms to zero. In addition,  $u_1$ ,  $u_2$ , and  $d$  are all considered constant.

### Short Wave Equations

(21. In order to aid in the development, let us define the following wave parameters.

- H Wave height measured from trough to crest
- $H_s$  Significant wave height, defined as the average height of the highest one-third of the waves recorded in a specific time period
- L Wave length from crest to following crest
- T Wave period (time) from crest to crest
- d Average depth of water in the wave-generating area
- F Fetch or wave-generating distance
- U Windspeed over the fetch

- t Duration of the wind over the fetch
- MWL Mean water level
- WTL Wind induced level
- $T_s$  Significant period, defined as the dominant period in the groups of highest waves recorded in a specific time period
- g Gravity

#### Semi-empirical equation development

122. Traditional approaches have involved the development of semi-empirical equations for  $H_s$  and  $T_s$  in terms  $U$ ,  $F$ ,  $t$ , and  $d$ . In deep water, the so-called SMB Method after Swerdrup, Munk, and Bretschneider [26] is embodied in the following three equations presented in the Shore Protection Manual (SPM) [27].

$$\frac{gH_s}{U^2} = 0.283 \tanh \left[ 0.0125 \left( \frac{gF}{U^2} \right)^{0.42} \right], \quad (2.1.1)$$

$$\frac{gT_s}{2U} = 1.20 \tanh \left[ 0.077 \left( \frac{gF}{U^2} \right)^{0.25} \right], \quad (2.1.2)$$

and,

$$\frac{gt}{U} = K \exp \left( \left\{ A \left[ \ln \left( \frac{gF}{U^2} \right) \right]^2 - B \ln \left( \frac{gF}{U^2} \right) + C \right\}^{1/2} + D \ln \left( \frac{gF}{U^2} \right) \right) \quad (2.1.3)$$

where

$$\exp (x) = e^{(x)}$$

$$\ln = \log_e$$

$$K = 6.5882$$

$$A = 0.0161$$

$$B = 0.3692$$

$$C = 2.2024$$

and

$$D = 0.8798$$

Given  $U$  and  $t$ , solve Equation (2.1.3) for  $F$  and set  $F = F_m$ . Then compute  $F_{eff} = \min(F, F_m)$ , where  $F$  is given. If  $F_{eff} = F$ , the wave growth is duration limited. If  $F_{eff} = F_m$ , then wave growth is fetch limited. Finally, employ (2.1.1) and (2.1.2) with  $U$  and  $F_{eff}$  to compute  $H_s$  and  $T_s$ .

123. In the above method, a constant windspeed is assumed to act for a duration  $t$  over a fetch  $F$  to generate the deepwater waves. The wave growth can be limited by fetch length or by wind duration.

124. More recently, work has focused on the development of directional wave spectral models, in which an energy distribution is determined versus frequency for each direction. Significant wave height and period are directly determined for each direction based upon characteristics of the energy versus frequency distribution.

125. The directional wave spectrum approach is adjudged to be outside the limits of project resources. The SMB method has also been extended to shallow water as described in the following two equations presented in the SPM [2], in which a friction factor  $f_f = .01$  and percolation effects have been considered.

$$\frac{gH_s}{U^2} = 0.283 \tanh \left[ 0.530 \left( \frac{gd}{U^2} \right)^{0.75} \right] \tanh \left\{ \frac{0.0125 \frac{gF}{U^2}^{0.42}}{\tanh \left[ 0.833 \left( \frac{gd}{U^2} \right)^{0.375} \right]} \right\} \quad (2.1.4)$$

and

$$\frac{gT_s}{U} = 1.20 \tanh \left[ 0.833 \left( \frac{gd}{U^2} \right)^{0.375} \right] \tanh \left\{ \frac{0.077 \frac{gF}{U^2}^{0.25}}{\tanh \left[ 0.833 \left( \frac{gd}{U^2} \right)^{0.375} \right]} \right\} \quad (2.1.5)$$

Note  $H_s$  and  $T_s$  are determined in terms of  $F$ ,  $U$ ,  $d$ , and  $f_f = .01$ .

126. Recently Equation (2.1.1) through (2.1.5) have been updated based upon wave spectral model studies (CETN-I-7 Equations 1-3 [29] and CETN-I-6 Equations 4-5 [28]). Since conditions in Lake Okeechobee relate to shallow water wave generation, the updated shallow water relations are presented only as follows.

$$\frac{g^H}{U_A} = 0.283 \tanh \left[ 0.530 \left( \frac{g^d}{U_A^2} \right)^{3/4} \right] \tanh \left\{ \frac{0.00565 \frac{g^F}{U_A^2}^{1/2}}{\tanh \left[ 0.530 \left( \frac{g^d}{U_A^2} \right)^{3/4} \right]} \right\} \quad (2.1.6)$$

$$\frac{g^T}{U_A} = 7.54 \tanh \left[ 0.833 \left( \frac{g^d}{U_A^2} \right)^{3/8} \right] \tanh \left\{ \frac{0.0379 \frac{g^F}{U_A^2}^{1/3}}{\tanh \left[ 0.833 \left( \frac{g^d}{U_A^2} \right)^{3/8} \right]} \right\} \quad (2.1.7)$$

$$\frac{g^T}{U_A} = 5.37 \times 10^2 \left( \frac{g^T}{U_A} \right)^{7/3} \quad (2.1.8)$$

127. Note in the above equations the windspeed  $U$  has been replaced by an adjusted windspeed,  $U_A$ . The following assumptions are made in determining  $U_A$  as outlined in CETN-I-5 [30]:

- a. The windfields are well organized and can be adequately described by the use of an average windspeed and direction over the entire fetch.
- b. The windspeed should be corrected to the 10 meter level.
- c. The windspeed should be representative of the average windspeed measured over the fetch. That is, for long fetches with more than one wind station the windspeed is averaged for the stations. The windspeed is further adjusted for the minimum duration; the average windspeed for the duration is determined from the wave forecasting curves. This process may need to be repeated to obtain the final adjusted value of,  $U_A$ .
- d. The windspeed must be adjusted to account for the non-constant coefficient of drag.
- e. When the fetch length is 10 miles (16 km) or less, the wind has not fully adjusted to the frictional characteristics of the waves. In such cases, the overwater windspeed will be estimated to be 110 percent of the overland windspeed,  $U_L$ . Thermal effect on stability of the air in this case is not applicable.
- f. When the fetch length is greater than 10 miles (16 km), thermal stability effects must be included in the windspeed transformation.

128. The adjusted windspeed,  $U_A$ , will be provided directly by the numerical hurricane models and Equation (2.1.6) and (2.1.7) will be used to compute  $H_s$  and  $T_s$  based upon  $F$ ,  $d$ , and  $U_A$ . Wave computations are to be made at hourly intervals. Equation (2.1.5) will be employed to compute wind duration,  $t$ . For compatibility with Equation (2.1.6) and (2.1.7),  $t$  (.33, 1.5) hours as indicated in Figure 2 in [31]. Since water depths are usually less than 30 feet in Lake Okeechobee even under storm conditions, wave growth may be limited by depth.

#### CW-167 Curves

129. A second approach utilizes curves developed during the Comprehensive Project CW-167 [31] on Lake Okeechobee. Figures 20 and 21 in [31] are represented by the following relation:

$$H_s = U_A^2 g \min \left[ .003563252 \left( \frac{gF}{U_A^2} \right)^{.44815352}, .184389447 \left( \frac{gd}{U_A^2} \right)^{.690091176} \right] \quad (2.2.1)$$

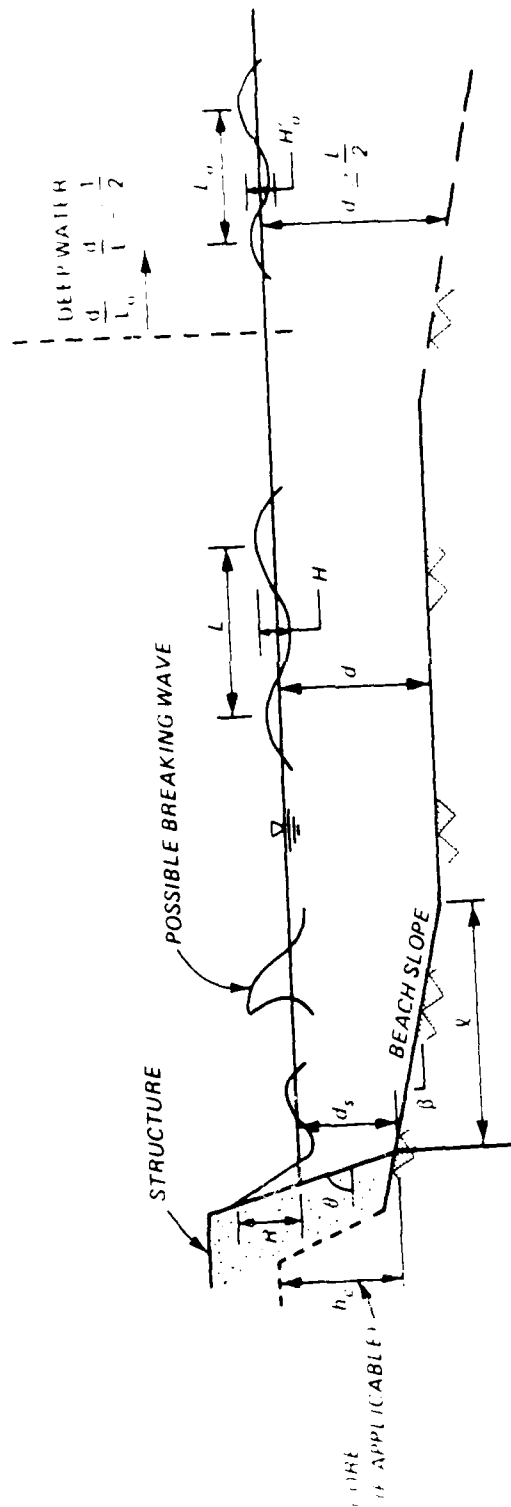
where  $H_s$ ,  $U_A$ ,  $F$ ,  $d$ , and  $g$  are as defined previously. Figure 26 in [31] is represented as follows:

$$T = 6.262018214 \frac{U_A}{g} \left( \frac{gd}{U_A^2} \right)^{.405683871} \quad (2.2.2)$$

where  $T$ ,  $U_A$ ,  $d$ , and  $g$  are as previously defined.

#### Wave runup

130. Wave runup has been measured in the laboratory using physical models with respect to mean water level and as a result, wave set-up is implicitly included. No separate analysis is developed here to distinctly separate out wave set-up from the total runup. Consider Figure III-1 taken from Stoa [32] to define the variables applicable to runup. The beach slope,  $\beta$ , is used in conjunction with Figure 7-4 in the SPM [27], to determine the maximum wave height which may be expected to break on the beach prior to reaching the structure. If  $H_s$  as previously computed is greater than the maximum breaker height,  $H_{mb}$ ,  $H_s$  is set equal to  $H_{mb}$ . The modified



WAVE CHARACTERISTICS

AD-A178 103

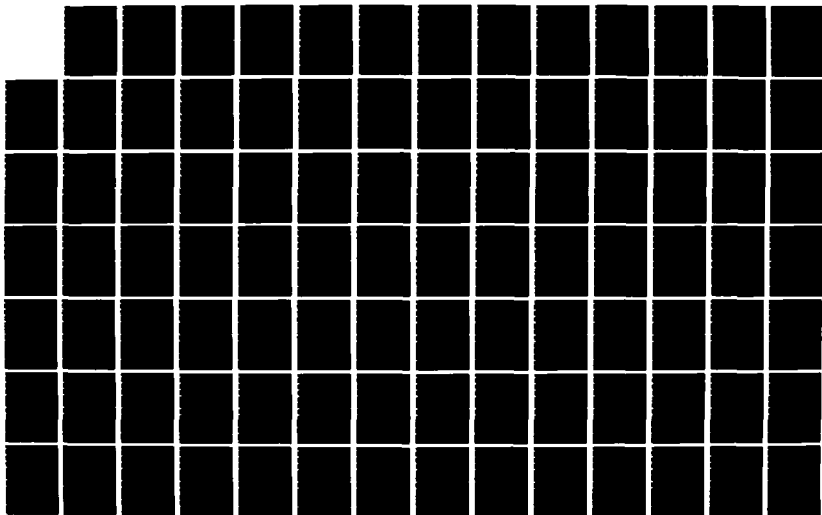
A NUMERICAL INVESTIGATION OF HURRICANE INDUCED WATER  
LEVEL FLUCTUATIONS I. (U) COASTAL ENGINEERING RESEARCH  
CENTER VICKSBURG MS R A SCHMAIZ JUN 86 CERC-MP-86-12

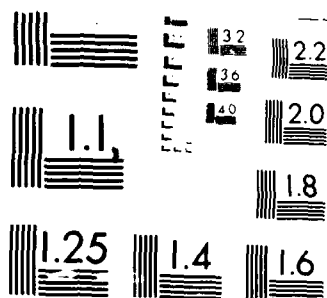
2/3

UNCLASSIFIED

F/G 8/8

NL





MICROCOPY RESOLUTION TEST CHART  
NATIONAL BUREAU OF STANDARDS-1963-A



deepwater waveheight,  $H'_0$ , associated with  $H_{mb}$  is computed using Figure 7-5 in the SPM [27].

131. Procedures developed by Stoa [32] for a horizontal nearshore bottom are employed as shown in Figure III-2. Equation 8 in Stoa [32] as referenced in this figure is as follows:

$$\frac{R}{H'_0} = (\cot \theta)^{-1.04} (4.23) 10^{2(q-1)} \left( \frac{H'_0}{gT^2} \right)^{q-1} \quad \text{for } \cot \theta \geq 2 \quad (2.3.1)$$

where variables are as indicated in Figure III-1. In order to determine  $q$ , Figure 4 in Stoa [32] is utilized for  $\cot \theta = 6$  or  $8$ , which represent the range of levee slope conditions at Lake Okeechobee. All computed values of runup are multiplied by values in Figure 50 in Stoa [32] to account for physical model scale effects.

#### Wave overtopping

132. Weggel [33] based upon an analysis of physical model results has presented the following equation to predict wave overtopping:

$$Q = \left( g Q_o^* H_o'^3 \right)^{1/2} \exp \left[ - \frac{.217}{2\alpha} \ln \left( \frac{R + h - d_s}{R - h + d} \right) \right] \quad (2.4.1)$$

where

- $Q \equiv$  overtopping rate ( $L^2/T$ ) per unit length of levee
- $g \equiv$  gravity
- $Q_o^* \equiv$  overtopping rate ( $L^2/T$ ) per unit length for a levee with crest elevation at the stiller water level (empirical)
- $H'_0 \equiv$  deep water significant wave height
- $R \equiv$  runup height measured vertically from the stiller water level, e.g., the height to which the water would runup if the levee were high enough to preclude overtopping
- $h \equiv$  height of the levee above the bottom
- $d_s \equiv$  water depth at the levee toe
- $\alpha \equiv$  empirical coefficient

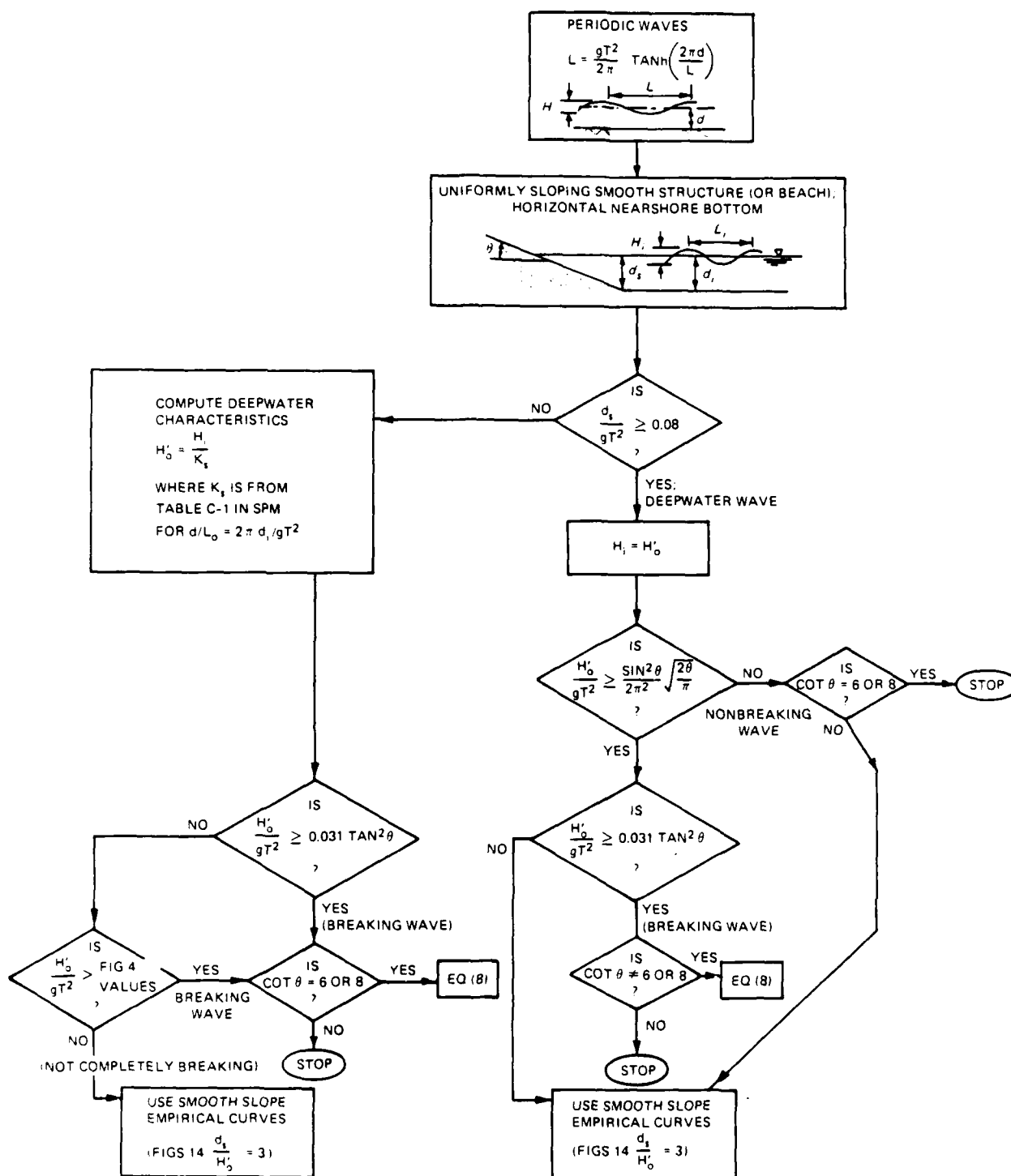


Figure III-2. Lake Okeechobee Runup Mechanics (after Stoa [32] Figure 6)

133. Note  $\alpha$  and  $Q_0^*$  are empirically determined coefficients which depend on incident wave characteristics and levee geometry. Approximate values of  $\alpha$  and  $Q_0^*$  for various slopes and structure types are given in Figures 7-24 through 7-32 in the SPM [27] as function of wave steepness,

$H'_o/gT^2$ , and relative height,  $d_s/H'_o$ . Weggel [33] has suggested that the following two relations be employed in cases where more exact values are not available. His procedure uses theoretical results for wave overtopping on smooth slopes, assumes a 1:10 beach slope as do Figures 7-24 through 7-32, and yields conservative overtopping rates.

$$\alpha = .06 - .0143 \ln (\sin \theta) \quad (a)$$

(2.4.2)

$$Q_o^* = \frac{\left(\frac{\epsilon}{2\pi}\right)^2 \left(\frac{H_s}{H'_o}\right)^2 \tanh^2\left(\frac{2\pi d_s}{L}\right)}{H'_o / gT^2} \quad (b)$$

where

$\theta \equiv$  levee slope

$L \equiv$  wave length

$H_s \equiv$  significant wave height

$\epsilon \equiv$  parameter based upon wave slope

$T \equiv$  wave period

$a$ ,  $Q_o^*$ ,  $H'_o$ ,  $d_s$ , and  $q$  are as previously defined.

134. For a sinusoidal wave,  $\epsilon = 1/2\pi$ , and assumes a maximum value relative to a coidal wave shape. The above relations with  $\epsilon = 1/2\pi$  are used in the numerical model. Equation (2.4.1) does not need to be corrected for scale effects if the scale-corrected runup,  $R$ , is used in the equation. Onshore wind effects increase the overtopping rate at a given levee section. As a guide, the following multiplication factor is presented in the SPM [27]:

$$k' = 1.0 + w_f \left( \frac{h - d_s}{R} + .1 \right) \sin \theta \quad (2.4.3)$$

where

$k' \equiv$  multiplication factor due to onshore winds

$w_f \equiv$  onshore windspeed coefficient

$h$ ,  $d_s$ ,  $R$  and  $\theta$  are as previously defined.

The following relations are suggested for  $w_f$  :

$$\begin{aligned} w_f &= .5 V_{ws} / 30 & 0 \leq V_{ws} \leq 30 \text{ mph} \\ w_f &= .5 + 1.5 (V_{ws} - 30) / 30 & 30 < V_{ws} \leq 60 \text{ mph} \\ w_f &= 2 & V_{ws} > 60 \text{ mph} \end{aligned} \quad (2.4.4)$$

where  $V_{ws}$  is the onshore wind in miles per hour. This multiplication factor is used in the numerical model in order to make the most conservative overtopping rate estimate.

135. Equation (2.4.1) assumes that the levee crown elevation is greater than the stilled water elevation; i.e.,  $0 < (h - d_s)/R < 1$ . Let us consider, the two cases not included. If  $(h - d_s)/R \geq 1$ , then  $Q = 0$ ; i.e., no overtopping occurs. If  $(h - d_s)/R \leq 0$ , the situation is as indicated in Figure III-3.

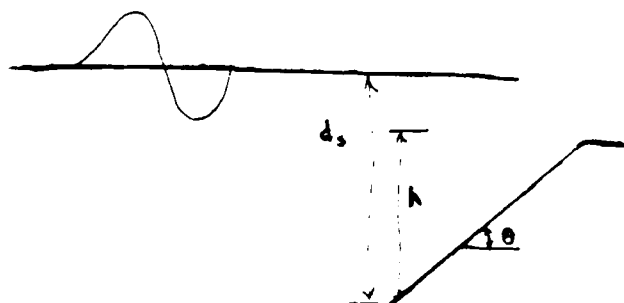


Figure III-3. Overtopping Case for  $(h - d_s)/R \leq 0$

136. Consider a surface wave represented by  $W(x) = H_s/2 \sin 2\pi x/L$ , where  $x$  is a distance along the wave. The elevation of the water surface is then  $w_e(x) = w(x) + d_s$ . If we assume,  $d_s - h \leq H_s/2$ , then we seek to find  $x_o$ , such that  $w_e(x_o) = d_s - h$ . The following relation may be used.

$$x_o = \frac{L}{2\pi} \sin^{-1} \left( - \frac{2(d_s - h)}{H_s} \right) \quad x_o \in \left( 0, -\frac{L}{4} \right) \quad (2.4.5)$$

where all quantities are as previously defined. To obtain the volume of water passing over the levee, the following approach is utilized:

$$V = \int_{x_0}^{L/2-x_0} w e(x) dx = \int_{x_0}^{L/2-x_0} \left[ (d_s - h) + \frac{H_s}{L} \sin \frac{2\pi x}{L} \right] dx \quad (2.4.6)$$

$$V = \frac{(d_s - h)L}{2} - 2 (d_s - h) x_0 - \frac{H_s L}{4\pi} \left\{ \cos \left[ \frac{2\pi}{L} \left( \frac{L}{2} - x_0 \right) \right] - \cos \left( \frac{2\pi x_0}{L} \right) \right\}$$

137. The overtopping rate per unit length of levee,  $Q$ , is then equal to  $V$  divided by the wave period  $T$ . This approach assumes a sinusoidal wave shape but does not include the effects of onshore winds.

#### PART IV: HYDRODYNAMIC MODEL: NUMERICAL IMPLEMENTATION

##### Long Wave Equations

138. The hydrodynamic model consists of a long and short wave component. The long-wave equations as previously developed are solved on a space-staggered grid employing an alternating direction implicit (ADI) scheme. The details of this numerical implementation are presented initially. In the second section, the numerical approach used to implement the previously developed short wave equations is presented. The essential ingredient in the numerical implementation is the methodology for determining fetch in curved hurricane windfields. The numerical implementations are presented in turn below.

##### Development of the stabilizing correction scheme for the long-wave equations

139. In order to develop the finite difference approximations, first consider the following reduced form of equation set (1.5.9) in which all underlined terms are set to zero.

$$u_t + \frac{g}{\mu_1} \eta_{\alpha_1} = 0 \quad (a)$$

$$u_t + \frac{g}{\mu_2} \eta_{\alpha_2} = 0 \quad (b) \quad (1.1.1)$$

$$\eta_t + \frac{d}{\mu_1} u_{\alpha_1} + \frac{d}{\mu_2} v_{\alpha_2} = 0 \quad (c)$$

The above equations essentially ignore surface and bottom stress, Coriolis force, convective acceleration, lateral diffusion, rainfall, and atmospheric pressure anomaly. Observe further that the depth is also considered constant. Stretching functions  $\mu_1$  and  $\mu_2$  are also constant.

140. Equation set (1.1.1) is written in vector form as follows:

$$u_t + Au_{\alpha_1} + Bu_{\alpha_2} = 0 \quad (1.1.2)$$

$$\begin{bmatrix} \eta_t \\ u_t \\ v_t \end{bmatrix} + \begin{bmatrix} 0 & \frac{d}{u_1} & 0 \\ \frac{g}{u_1} & 0 & 0 \\ 0 & 0 & 0 \end{bmatrix} \begin{bmatrix} \eta_{\alpha_1} \\ u_{\alpha_1} \\ v_{\alpha_1} \end{bmatrix} + \begin{bmatrix} 0 & 0 & \frac{d}{u_2} \\ 0 & 0 & 0 \\ \frac{g}{u_2} & 0 & 0 \end{bmatrix} \begin{bmatrix} \eta_{\alpha_2} \\ u_{\alpha_2} \\ v_{\alpha_1} \end{bmatrix} = \begin{bmatrix} 0 \\ 0 \\ 0 \end{bmatrix}$$

In what follows the transformed position and time coordinate  $(\alpha_1, \alpha_2, t)$  is represented on the space staggered grid shown in Figure IV-1 by  $(n\Delta\alpha_2, m\Delta\alpha_1, k\Delta t)$ . Note all grid dimensions are uniform in the transformed plane grid. The water surface elevation,  $\eta$ , field is computed over the cell centered field. The  $y - \alpha_2$  direction velocity component field is computed over a field defined by staggering the cell centered field to right half a grid cell. Similarly, the  $x - \alpha_1$  direction velocity component field is computed over a field defined by staggering the cell centered field to the bottom half a grid cell.

141. As a prelude to the actual formulation of the difference equations, let us consider the following definitions:

$$\eta_{n,m}^{k+I} \equiv \text{water surface elevation at } (n, m) \text{ at time level } k + I$$

$$u_{n,m+1/2}^{k+I} \equiv \alpha_1 - \text{velocity component at } (n, m+1/2) \text{ at time level } k + I$$

$$v_{n,m+1/2}^{k+I} \equiv \alpha_2 - \text{velocity component at } (n+1/2, m) \text{ at time level } k + I$$

$$I \in (-1, 0, 1)$$

Observe in Figure IV-1, the still water depth field  $h$ , is specified on the cell-centered grid. The depth convention employed is shown in Figure IV-2 for conditions at time level  $k$ . It is assumed  $h_{n,m} \gg \eta_{n,m}^k$  and  $d_{n,m}^k \approx -h_{n,m}$  a constant for all time levels  $k$ .

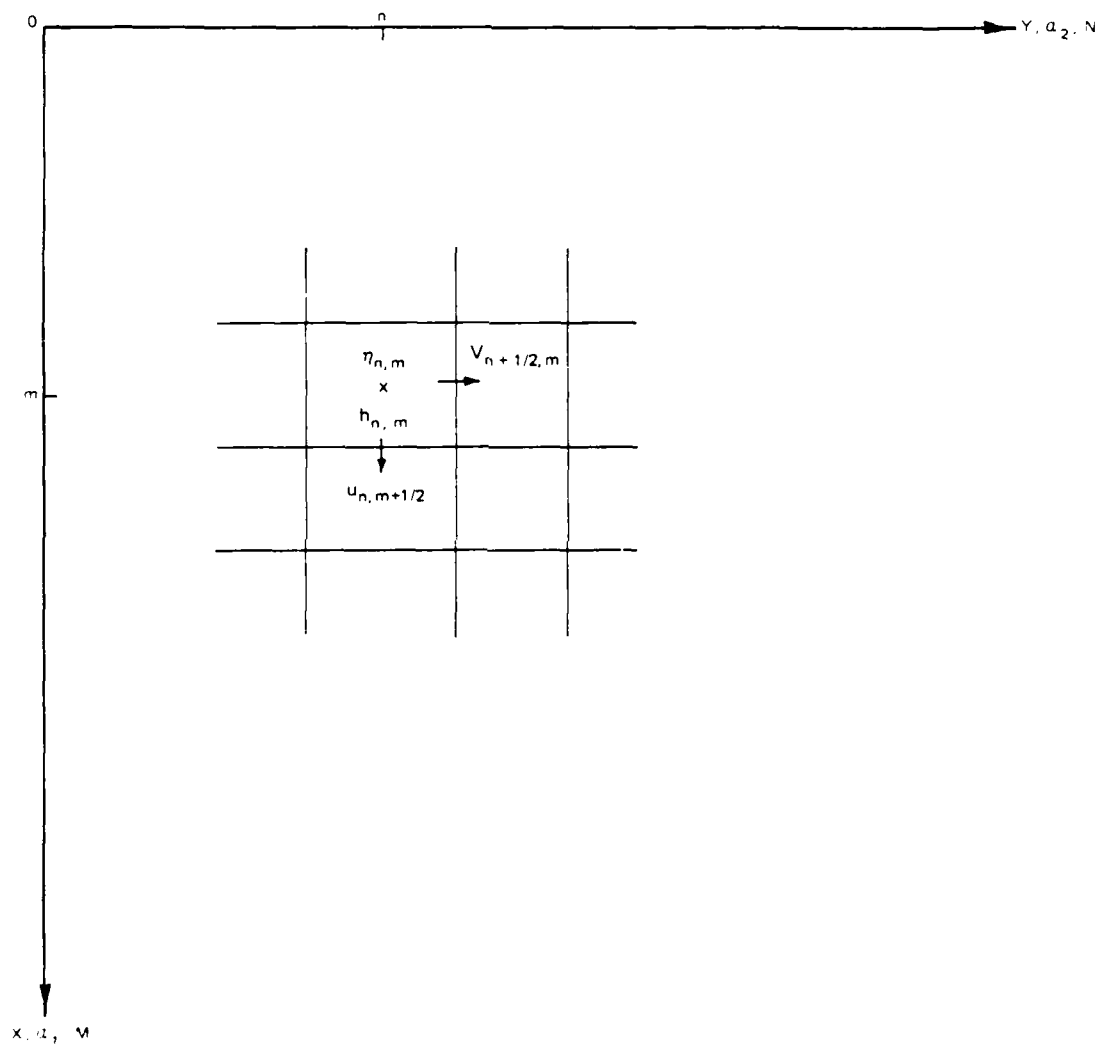


Figure IV-1. Staggered grid variable orientation



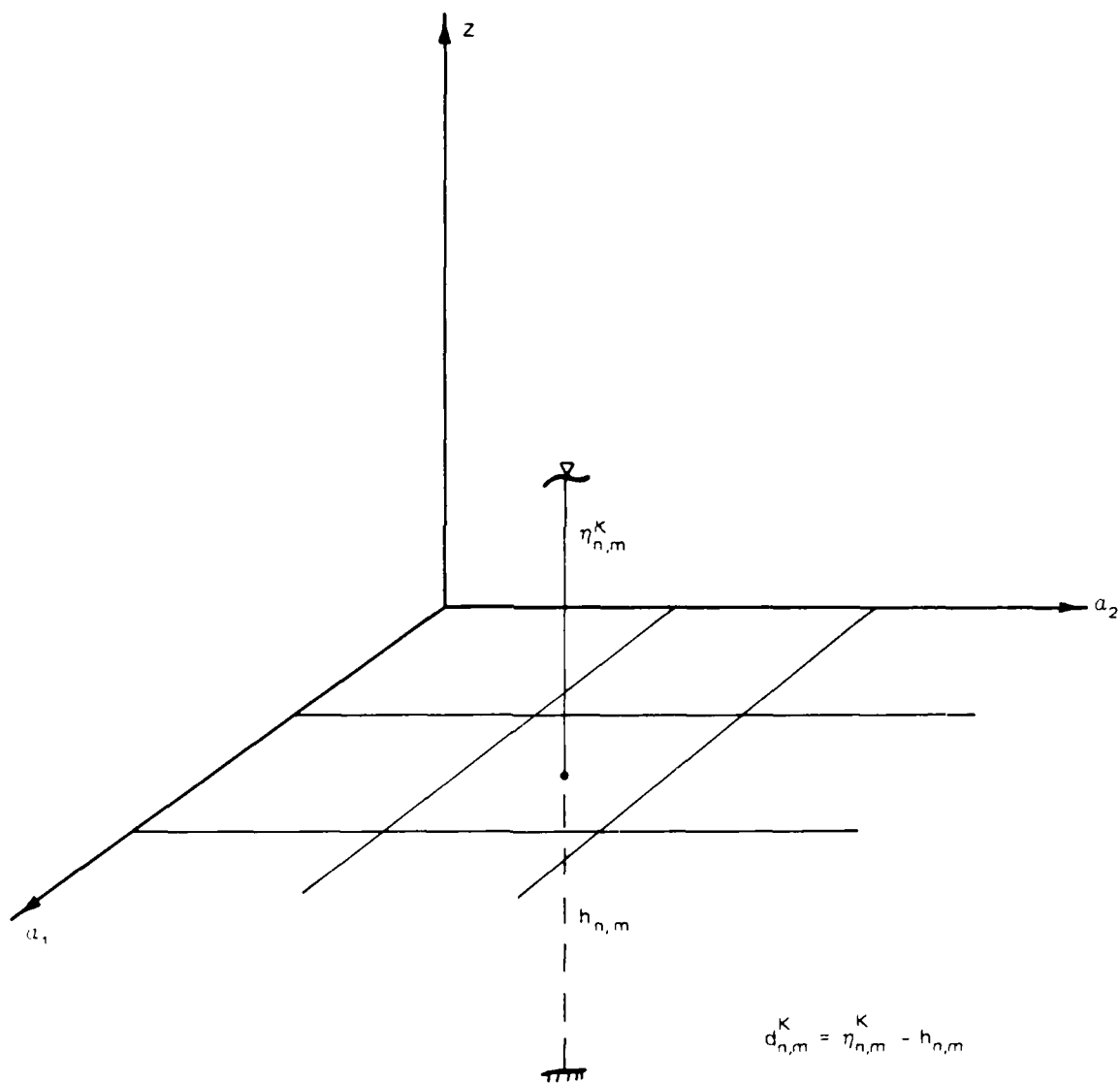


Figure IV-2. Datum convention employed within the space staggered grid system

142. In developing the general approach, consider the following three time level finite difference scheme:

$$\frac{u^{k+1} - u^{k-1}}{2\Delta t} + \frac{\delta x}{2} \left[ A(u^{k+1} + u^{k-1}) \right] + \frac{\delta y}{2} \left[ B(u^{k+1} + u^{k-1}) \right] = 0 \quad (1.1.3)$$

where

$$u^k = \begin{bmatrix} \eta_{n,m}^k \\ u_{n,m+1/2}^k \\ v_{n+1/2,m}^k \end{bmatrix}$$

$$\delta x u^k = \begin{bmatrix} \frac{\eta_{n,m+1}^k - \eta_{n,m}^k}{\mu_1 \Delta \alpha_1} \\ \frac{u_{n,m-1/2}^k - u_{n,m+1/2}^k}{\mu_1 \Delta \alpha_1} \\ 0 \end{bmatrix}$$

$$\delta y u^k = \begin{bmatrix} \frac{\eta_{n+1,m}^k - \eta_{n,m}^k}{\mu_2 \Delta \alpha_2} \\ 0 \\ \frac{v_{n+1/2,m}^k - v_{n-1/2,m}^k}{\mu_2 \Delta \alpha_2} \end{bmatrix}$$

Observe from Equation (1.1.2) that in matrix A associated with  $u_{\alpha_1}$  the third column contains all zeros. Therefore, no entry is required in the third row for  $\delta x$ . Similarly, in matrix B associated with  $u_{\alpha_2}$ , the second column contains all zeros. Thus, no entry is required in  $\delta y$  for the second row.

143. If we define the operators  $\lambda_x = \Delta t \delta x A$  and  $\lambda_y = \Delta t \delta y B$  to operate  $u^{k\pm 1}$  from left to right, we may rewrite (1.1.3) in the following form:

$$(I + \lambda_x + \lambda_y) u^{k+1} = (I - \lambda_x - \lambda_y) u^{k-1} \quad (1.1.4)$$

144. Adding  $\lambda_x \lambda_y (u^{k+1} - u^{k-1})$  to the left hand side of the above equation we obtain a factorization. The addition of the term  $\lambda_x \lambda_y (u^{k+1} - u^{k-1})$  does not make the difference approximation inconsistent and the truncation error remains  $O[\Delta t^2, \Delta x^2, \Delta y^2]$  for  $\mu_1 = \mu_2 = 1$ .

145. We have thus achieved an approximation of the following form:

$$(I + \lambda_x)(I + \lambda_y)u^{k+1} = (I - \lambda_x)(I - \lambda_y)u^{k-1} \quad (1.1.5)$$

If an intermediate solution level  $u^*$  is introduced, there are many possible schemes, which may be used to split the above equation. The present formulation employs a stabilizing correction scheme as given below.

$$(I + \lambda_x)u^* = (I - \lambda_x - 2\lambda_y)u^{k-1} \quad (a)$$

(1.1.6)

$$(I + \lambda_y)u^{k+1} = u^* + \lambda_y u^{k-1} \quad (b)$$

Equation (1.1.6)(a) is treated in the  $\alpha_1 - x$  sweep, while equation (1.1.6)(b) is handled in the  $\alpha_2 - y$  sweep. Hence, the name multi-operational (two sweeps) alternating direction (first  $\alpha_1 - x$  then  $\alpha_2 - y$ ) implicit finite difference method of stabilizing corrections.

146. In order to form the foundation for the approximation of the complete nonlinear hydrodynamic equations, let us first expand equation set (1.1.6)

$\alpha_1 - x$  sweep (Equation 1.1.6 (a))

$$\left\{ \begin{bmatrix} 1 & 0 & 0 \\ 0 & 1 & 0 \\ 0 & 0 & 1 \end{bmatrix} + \Delta t \delta x \begin{bmatrix} 0 & \frac{d}{u_1} & 0 \\ \frac{g}{u_1} & 0 & 0 \\ 0 & 0 & 0 \end{bmatrix} \right\} \begin{bmatrix} r_{n,m}^* \\ u_{n,m+1/2}^* \\ v_{n+1/2,m}^* \end{bmatrix} = \left\{ \begin{bmatrix} 1 & 0 & 0 \\ 0 & 1 & 0 \\ 0 & 0 & 1 \end{bmatrix} - \Delta t \delta x \begin{bmatrix} 0 & \frac{d}{u_1} & 0 \\ \frac{g}{u_1} & 0 & 0 \\ 0 & 0 & 0 \end{bmatrix} - 2\Delta t \delta y \begin{bmatrix} 0 & 0 & \frac{d}{u_2} \\ 0 & 0 & 0 \\ \frac{g}{u_2} & 0 & 0 \end{bmatrix} \right\} \begin{bmatrix} r_{n,m}^{k-1} \\ u_{n,m+1/2}^{k-1} \\ v_{n+1/2,m}^{k-1} \end{bmatrix} \quad (1.1.7)$$

147. In further expanding the above equation, the difference operators  $\delta x$  and  $\delta y$  are applied to the matrix vector products. The  $\delta_x$  and  $\delta_y$  are performed on  $u$  from right to left. Therefore, we obtain for the x-sweep:

$$\begin{aligned} \eta_{n,m}^* + \frac{\Delta t d}{u_1 \Delta \alpha_1} (u_{n,m+1/2}^* - u_{n,m-1/2}^*) &= \eta_{n,m}^{k-1} \\ - \frac{\Delta t d}{u_1 \Delta \alpha_1} (u_{n,m+1/2}^{k-1} - u_{n,m-1/2}^{k-1}) &- \frac{2\Delta t d}{u_2 \Delta \alpha_2} (v_{n+1/2,m}^{k-1} - v_{n-1/2,m}^{k-1}) \end{aligned} \quad (a)$$

$$u_{n,m+1/2}^* + \frac{\Delta t g}{u_1 \Delta \alpha_1} (\eta_{n,m+1}^* - \eta_{n,m}^*) = u_{n,m+1/2}^{k-1} \quad (1.1.8)$$

$$- \frac{\Delta t g}{u_1 \Delta \alpha_1} (u_{n,m+1}^{k-1} - u_{n,m}^{k-1}) \quad (b)$$

$$v_{n+1/2,m}^* = v_{n+1/2,m}^{k-1} - \frac{2\Delta t g}{u_2 \Delta \alpha_2} (\eta_{n+1,m}^{k-1} - \eta_{n,m}^{k-1}) \quad (c)$$

$\delta_y$  - y sweep (Equation 1.1.6(b))

$$\left\{ \begin{bmatrix} 1 & 0 & 0 \\ 0 & 1 & 0 \\ 0 & 0 & 1 \end{bmatrix} + \Delta t \delta y \begin{bmatrix} 0 & 0 & \frac{d}{u_2} \\ 0 & 0 & 0 \\ \frac{g}{u_2} & 0 & 0 \end{bmatrix} \right\} \begin{bmatrix} \eta_{n,m}^{k+1} \\ u_{n,m+1/2}^{k+1} \\ v_{n+1/2,m}^{k+1} \end{bmatrix} \quad (1.1.9)$$

$$= \begin{bmatrix} \eta_{n,m}^* \\ u_{n,m+1/2}^* \\ v_{n+1/2,m}^* \end{bmatrix} + \Delta t \delta y \begin{bmatrix} 0 & 0 & \frac{d}{u_2} \\ 0 & 0 & 0 \\ \frac{g}{u_2} & 0 & 0 \end{bmatrix} \begin{bmatrix} \eta_{n,m}^{k-1} \\ u_{n,m+1/2}^{k-1} \\ v_{n+1/2,m}^{k-1} \end{bmatrix}$$

Expanding the above equation for each component, we obtain:

$$\begin{aligned}
\eta_{n,m}^{k+1} + \frac{\Delta t d}{\mu_2 \Delta \alpha_2} \left( v_{n+1/2,m}^{k+1} - v_{n-1/2,m}^{k+1} \right) \\
= \eta_{n,m}^* + \frac{\Delta t d}{\mu_2 \Delta \alpha_2} \left( v_{n+1/2,m}^{k-1} - v_{n-1/2,m}^{k-1} \right) \quad (a)
\end{aligned}$$

$$u_{n,m+1/2}^{k+1} = u_{n,m+1/2}^* \quad (b) \quad (1.1.10)$$

$$\begin{aligned}
v_{n+1/2,m}^{k+1} + \frac{\Delta t g}{\mu_2 \Delta \alpha_2} \left( \eta_{n+1,m}^{k+1} - \eta_{n,m}^{k+1} \right) \\
= v_{n+1/2,m}^* + \frac{\Delta t g}{\mu_2 \Delta \alpha_2} \left( \eta_{n+1,m}^{k-1} - \eta_{n,m}^{k-1} \right) \quad (c)
\end{aligned}$$

If we now substitute (1.1.8)(c) into (1.1.10)(c) and substitute (1.1.10)(b) into (1.1.8)(a) and (b) we obtain the following forms for the two sweeps.

x-sweep

$$\begin{aligned}
\eta_{n,m}^* + \frac{\Delta t d}{\mu_1 \Delta \alpha_1} \left( u_{n,m+1/2}^{k+1} - u_{n,m-1/2}^{k+1} \right) &= \eta_{n,m}^{k-1} \\
- \frac{\Delta t d}{\mu_1 \Delta \alpha_1} \left( u_{n,m+1/2}^{k-1} - u_{n,m-1/2}^{k-1} \right) - \frac{2 \Delta t d}{\mu_2 \Delta \alpha_2} \left( v_{n+1/2,m}^{k-1} - v_{n-1/2,m}^{k-1} \right) &\quad (a) \\
&\quad (1.1.11)
\end{aligned}$$

$$\begin{aligned}
u_{n,m+1/2}^{k+1} + \frac{\Delta t g}{\mu_1 \Delta \alpha_1} \left( \eta_{n,m+1}^* - \eta_{n,m}^* \right) &= u_{n,m+1/2}^{k-1} \\
- \frac{\Delta t g}{\mu_1 \Delta \alpha_1} \left( \eta_{n,m+1}^{k-1} - \eta_{n,m}^{k-1} \right) &\quad (b)
\end{aligned}$$

$$\begin{aligned} \text{v-sweep} \\ \eta_{n,m}^{k+1} + \frac{\Delta t d}{u_2 \Delta x_2} \left( v_{n+1/2,m}^{k+1} - v_{n-1/2,m}^{k+1} \right) = \eta_{n,m}^* \\ + \frac{\Delta t d}{u_2 \Delta x_2} \left( v_{n+1/2,m}^{k-1} - v_{n-1/2,m}^{k-1} \right) \quad (a) \end{aligned} \quad (1.1.12)$$

$$\begin{aligned} v_{n+1/2,m}^{k+1} + \frac{\Delta t g}{u_2 \Delta x_2} \left( \eta_{n+1,m}^{k+1} - \eta_{n,m}^{k+1} \right) = v_{n+1/2,m}^{k-1} \\ - \frac{\Delta t g}{u_2 \Delta x_2} \left( \eta_{n+1,m}^{k-1} - \eta_{n,m}^{k-1} \right) \quad (b) \end{aligned}$$

148. If in Equation sets (1.1.11) and (1.1.12), all terms on the right-hand sides are brought over to the left-hand sides and the resulting equations are divided by  $2\Delta t$ , the finite difference approximations are obtained in a more standard form. Equation (1.1.11)(a) represents the approximation to the continuity equation (Equation (1.1.1)(c)), Equation (1.1.11)(b) represents the approximation to the  $a_1 - x$  motion equation. (Equation (1.1.1)(a)), and Equation (1.1.12)(b) represents the approximation to the  $a_2 - v$  motion equation (Equation (1.1.1)(b)). Equation (1.1.12)(a) is a stabilizing correction to obtain  $\eta_{n,m}^{k+1}$  from  $\eta_{n,m}^*$  and involves only  $a_2$ -component velocity terms.

149. We are now in position to obtain approximations for the nonlinear hydrodynamic set (Equation set (1.5.9)). We do so in a two step process. In step one, we relax the assumption  $\mu_1 = \mu_2 = 1$  and that  $f_{n,m} = -h_{n,m}$ . Equations (1.1.11) and (1.1.12) now become:

x-sweep

$$\begin{aligned} \eta_{n,m}^* &+ \frac{\Delta t}{(u_1)_m \Delta \alpha_1} \left( \frac{\alpha_1}{d} u^{k+1} \Big|_{n,m+1/2} - \frac{\alpha_1}{d} u^{k+1} \Big|_{n,m-1/2} \right) \\ &= \eta_{n,m}^{k-1} - \frac{\Delta t}{(u_1)_m \Delta \alpha_1} \left( \frac{\alpha_1}{d} u^{k-1} \Big|_{n,m+1/2} - \frac{\alpha_1}{d} u^{k-1} \Big|_{n,m-1/2} \right) \end{aligned} \quad (a)$$

$$- \frac{2\Delta t}{(u_2)_n \Delta \alpha_2} \left( \frac{\alpha_2}{d} v^{k-1} \Big|_{n+1/2,m} - \frac{\alpha_2}{d} v^{k-1} \Big|_{n-1/2,m} \right)$$

(1.1.11)

$$\begin{aligned} u_{n,m+1/2}^{k+1} &+ \frac{\Delta t g}{(u_1)_{m+1/2} \Delta \alpha_1} \left( \eta_{n,m+1}^* - \eta_{n,m}^* \right) \\ &= u_{n,m+1/2}^{k-1} - \frac{\Delta t g}{(u_1)_{m+1/2} \Delta \alpha_1} \left( \eta_{n,m+1}^{k-1} - \eta_{n,m}^{k-1} \right) \end{aligned} \quad (b)$$

y-sweep

$$\begin{aligned} \eta_{n,m}^{k+1} &+ \frac{\Delta t}{(u_2)_n \Delta \alpha_2} \left( \frac{\alpha_2}{d} v^{k+1} \Big|_{n+1/2,m} - \frac{\alpha_2}{d} v^{k+1} \Big|_{n-1/2,m} \right) \\ &= \eta_{n,m}^* - \frac{\Delta t}{(u_2)_n \Delta \alpha_2} \left( \frac{\alpha_2}{d} v^{k-1} \Big|_{n+1/2,m} - \frac{\alpha_2}{d} v^{k-1} \Big|_{n-1/2,m} \right) \end{aligned} \quad (a)$$

(1.1.12)

$$\begin{aligned} v_{n+1/2,m}^{k+1} &+ \frac{\Delta t g}{(u_2)_{n+1/2} \Delta \alpha_2} \left( \eta_{n+1,m}^{k+1} - \eta_{n,m}^{k+1} \right) \\ &= v_{n+1/2,m}^{k-1} - \frac{\Delta t g}{(u_2)_{n+1/2} \Delta \alpha_2} \left( \eta_{n+1,m}^{k-1} - \eta_{n,m}^{k-1} \right) \end{aligned} \quad (b)$$

150. Observe in Equations (1.1.11) and (1.1.12), all stretching functions  $u_1$  and  $u_2$  are evaluated at the center of the appropriate differences shown in their respective parentheses. The depth is evaluated at time level  $k$  at the location of the corresponding velocity as follows:

$$\frac{\alpha_2}{d_{n\pm 1/2,m}} = \left[ \left( \eta_{n\pm 1,m}^k - h_{n\pm 1,m} \right) + \left( \eta_{n,m}^k - h_{n,m} \right) \right] / 2 \quad (a) \quad (1.1.13)$$

$$\frac{\alpha_1}{d_{n,m\pm 1/2}} = \left[ \left( \eta_{n,m\pm 1}^k - h_{n,m\pm 1} \right) + \left( \eta_{n,m}^k - h_{n,m} \right) \right] / 2 \quad (b)$$

151. In step two, the previously deleted (underlined) terms in Equation set (1.5.9) are considered. In the continuity equation, the rainfall term is introduced in Equation (1.1.11)(a) by adding,  $2\Delta t R_{m,n}^k$ , to the right hand side, where  $R_{m,n}^k$  is the rainfall rate at  $(n,m)$  at time level  $k$ . Note Equation (1.1.12)(a) is not changed. For the  $\alpha_1 - x$  motion equation, the convective acceleration ①, Coriolis ②, atmospheric pressure anomaly ③, bottom friction ④, lateral momentum diffusion ⑤, and wind stress ⑥ terms are approximated in the following manner to obtain:



$\alpha_1$  - x sweep Motion Equation

$$\frac{1}{2\Delta t} \left( u^{k+1} - u^{k-1} \right)_{n,m+1/2} + \frac{1}{2(\mu_1)_{m+1/2} \Delta \alpha_1} u^k_{n,m+1/2} \left( u^k_{n,m+3/2} \right. \quad (1)$$

$$\left. - u^k_{n,m-1/2} \right) + \frac{1}{2(\mu_2)_n \Delta \alpha_2} v^k_{n,m+1/2} \left( u^k_{n+1,m+1/2} - u^k_{n-1,m+1/2} \right) \quad (2)$$

$$- f v^k_{n,m+1/2} + \frac{g}{2(\mu_1)_{m+1/2} \Delta \alpha_1} \left\{ (\eta^* + \eta^{k-1})_{n,m+1} - (\eta^* + \eta^{k-1})_{n,m} \right. \quad (3)$$

$$\left. - 2 \left[ (\eta_a^k)_{n,m+1} - (\eta_a^k)_{n,m} \right] \right\} + g \left( \frac{u^{k+1}}{c^2 d \alpha_1} \right)_{n,m+1/2} \cdot \left[ \left( u^{k-1}_{n,m+1/2} \right)^2 \right. \quad (4)$$

$$\left. + \left( v^{k-1}_{n,m+1/2} \right)^2 \right]^{1/2} - \varepsilon_1 \left\{ \left[ \frac{1}{(\mu_1)_{m+1/2} \Delta \alpha_1} \right]^2 \left( u^k_{n,m+3/2} + u^k_{n,m-1/2} \right. \right. \quad (5)$$

$$\left. - 2u^k_{n,m+1/2} \right) + \frac{1}{2(\mu_1)_{m+1/2} \Delta \alpha_1^2} \left[ \left( \frac{1}{\mu_1} \right)_{m+1} - \left( \frac{1}{\mu_1} \right)_m \right] \left( u^k_{n,m+3/2} \right. \quad (6)$$

$$\left. - u^k_{n,m-1/2} \right) \left\} - \varepsilon_2 \left\{ \left[ \frac{1}{(\mu_2)_n \Delta \alpha_2} \right]^2 \left( u^k_{n+1,m+1/2} + u^k_{n-1,m+1/2} - 2u^k_{n,m+1/2} \right) \right. \quad (7)$$

$$\left. + \frac{1}{2(\mu_2)_n \Delta \alpha_2^2} \left[ \left( \frac{1}{\mu_2} \right)_{n+1/2} - \left( \frac{1}{\mu_2} \right)_{n-1/2} \right] \left( u^k_{n+1,m+1/2} - u^k_{n-1,m+1/2} \right) \right\} \quad (8)$$

$$- F^k_{\alpha_1} = 0 \quad (9)$$

The approximation of each term is discussed briefly below:

① Convective acceleration term

All differences are centered in space and in time (at time level  $k$ ) in order to maintain stability. Since the  $\alpha_1 - x$  motion equation is evaluated at  $(n, m+1/2)$  and  $\alpha_2 - x$  velocity components are available only at  $(n+1/2, m)$ , it is necessary to define

$$\bar{v}_{n, m+1/2}^k = \left( v_{n+1/2, m}^k + v_{n-1/2, m}^k + v_{n+1/2, m+1}^k + v_{n-1/2, m+1}^k \right) / 4$$

② Coriolis term

The approximation is centered at time level  $k$  with  $\bar{v}_{n, m+1/2}^k$  as previously defined. Note  $f$  is equivalent to  $\Omega$  as defined under Equation (1.2.34) in PART III.

③ Atmospheric pressure anomaly term

The approximation is centered in time and in space with  $\eta_a$  defined above Equation (1.3.5) in PART III.

④ Bottom friction term

Note a Chezy C approach is used as given by Equation (1.4.1) in PART III and is a time dependent quantity based upon water depth. Since water depth is available at  $(n, m)$  and the  $\alpha_1 - x$  velocity component is calculated at  $(n, m+1/2)$ ,  $\bar{c}_{n, m+1/2}^k = \left( c_{n, m+1}^k + c_{n, m}^k \right) / 2$ . It is also necessary to employ  $\bar{v}_{n, m+1/2}^{k-1}$  as defined previously with  $k-1$  substituted for  $k$ . The  $\alpha_1 - x$  velocity component is taken at time level  $k+1$ , while the magnitude of water velocity is computed using quantities of time level  $k-1$ . This form of the friction term has been used by several investigators and is generally believed to be the most stable form of approximation for this term.

⑤ Lateral diffusion term

Observe all differences are centered in time at level  $k$  and in space. All stretching functions are evaluated at  $m+1/2$ . All differences in stretching functions are centered at  $m+1/2$ .

⑥ Wind stress term

This term is evaluated at time level  $k$  and is defined as follows

$$F_{\alpha_1}^k = \frac{\rho_a}{\rho_w} \left[ \left( c_{o\omega x}^k \right) \Big|_{n,m} v_{n,m}^k + \left( c_{o\omega x}^k \right) \Big|_{n,m+1} v_{n,m+1}^k \right] / \frac{\alpha_1}{d} \Big|_{n,m+1/2} \quad (1.1.15)$$

where

$\rho_a$   $\equiv$  density of air

$\rho_w$   $\equiv$  density of water

$c_{o\omega x}^k$   $\equiv$  drag coefficient at (n,m) at time level k

$\omega x_{n,m}^k$   $\equiv$   $\alpha_1$  - x wind velocity component at (n,m) at time level k

$v_{n,m}^k$   $\equiv$  wind magnitude at (n,m) at time level k

152. Let us now consider, the  $\alpha_2$  - y motion equation; e.g., Equation (1.5.9)(c). In analogy to the  $\alpha_1$  - x motion equation, the convective acceleration ①, Coriolis ②, atmospheric pressure anomaly ③, bottom friction ④, lateral momentum diffusion ⑤, and wind stress ⑥ terms are approximated to obtain:

$$\frac{1}{2\Delta t} (v^{k+1} - v^{k-1})_{n+1/2,m} + \frac{1}{2u_1\Delta\alpha_1} u_{n+1/2,m}^k v_{n+1/2,m+1}^k$$

①

$$- v_{n+1/2,m-1}^k + \frac{1}{2u_2\Delta\alpha_2} v_{n+1/2,m}^k v_{n+3/2,m}^k - v_{n-1/2,m}^k + f_{n+1/2,m}^k u_{n+1/2,m}^k$$

①

②

$$+ \frac{g}{2u_2\Delta\alpha_2} \left\{ (\eta^{k+1} + \eta^{k-1})_{n+1,m} - (\eta^{k+1} + \eta^{k-1})_{n,m} \right.$$

$$\left. - 2 \left[ (\eta_a^k)_{n+1,m} - (\eta_a^k)_{n,m} \right] \right\} + g \left( \frac{v^{k+1}}{c^2 d \alpha_2} \right)_{n+1/2,m} \cdot \left[ \left( \frac{u^{k-1}}{u_{n+1/2,m}} \right)^2 \right.$$

③

④

(1.1.16)

$$+ \left( v_{n+1/2,m}^{k-1} \right)^2 \Big]^{1/2} - \epsilon_1 \left\{ \left( \frac{1}{u_1 \Delta \alpha_1} \right)^2 \left( v_{n+1/2,m+1}^k + v_{n+1/2,m-1}^k \right. \right.$$

④

⑤

$$\left. - 2v_{n+1/2,m}^k \right) + \frac{1}{2u_1\Delta\alpha_1^2} \left[ \left( \frac{1}{u_1} \right)_{m+1/2} - \left( \frac{1}{u_1} \right)_{m-1/2} \right] \left( v_{n+1/2,m+1}^k \right.$$

⑤

$$\left. - v_{n+1/2,m-1}^k \right\} - \epsilon_2 \left\{ \left( \frac{1}{u_2 \Delta \alpha_2} \right)^2 \left( v_{n+3/2,m}^k + v_{n-1/2,m}^k - 2v_{n+1/2,m}^k \right) \right.$$

⑤

$$+ \frac{1}{2u_2\Delta\alpha_2^2} \left[ \left( \frac{1}{u_2} \right)_{n+1} - \left( \frac{1}{u_2} \right)_n \right] \left( v_{n+3/2,m}^k - v_{n-1/2,m}^k \right) \Big\} - F_{\alpha_2}^k = 0$$

⑤

⑥

Analogous comments regarding these approximations hold with  $u, u_1$  being replaced by  $v, u_2$  etc. In Equation (1.1.15),  $wx^k$  is replaced by  $wy^k$  and  $\frac{x_1}{d}_{n,m+1/2}$  by  $\frac{x_2}{d}_{n+1/2,m}$ .

153. Assembling all results, the final sweep equations may be written in the following manner.

$\alpha_1$  - x sweep

$$-a_{m-1/2} u_{n,m-1/2}^{k+1} + \eta_{n,m}^* + a_{m+1/2} u_{n,m+1/2}^{k+1} = A_m \quad \text{Continuity (a)}$$

(1.1.17)

$$-a_m \eta_{n,m}^* + \bar{a}_{m+1/2} u_{u,m+1/2}^{k+1} + a_{m+1} \eta_{n,m+1}^* = B_{m+1/2} \quad \text{Momentum (b)}$$

where

$$a_{m-1/2} = \frac{\Delta t}{(\nu_1)_m \Delta \alpha_1} \frac{\alpha_1}{d} \Big|_{n,m-1/2}$$

$$a_{m+1/2} = \frac{\Delta t}{(\nu_1)_m \Delta \alpha_1} \frac{\alpha_1}{d} \Big|_{n,m+1/2}$$

$$A_m = \eta_{n,m}^{k-1} + 2R_n^k \Delta t + \frac{\Delta t}{(\nu_1)_m \Delta \alpha_1} \left( u_{d-1}^{k-1} \Big|_{n,m-1/2} - u_{d-1}^{k-1} \Big|_{n,m+1/2} \right) + \frac{2\Delta t}{(\nu_2)_n \Delta \alpha_2} \left( v_{d-1}^{k-1} \Big|_{n-1/2,m} - v_{d-1}^{k-1} \Big|_{n+1/2,m} \right)$$

$$a_m = \frac{g \Delta t}{(\nu_1)_{m+1/2} \Delta \alpha_1}$$

$$a_{m+1} = a_m$$

$$\bar{a}_{m+1/2} = \left\{ 1 + \left( \frac{2g \Delta t}{\bar{\alpha}_d^{k-1}} \right)_{n,m+1/2} \left[ \left( u_{n,m+1/2}^{k-1} \right)^2 + \left( v_{n,m+1/2}^{k-1} \right)^2 \right]^{1/2} \right\}$$

$$\begin{aligned}
B_{m+1/2} = & u_{n,m+1/2}^{k-1} + \Delta t \left( \frac{v_{n,m+1/2}^k}{v_{n,m+1/2}^k} \left[ 2f - \frac{u_{n+1,m+1/2}^k - u_{n-1,m+1/2}^k}{(\mu_2)_n \Delta \alpha_2} \right] \right. \\
& - \frac{u_{n,m+1/2}^k}{(\mu_1)_{m+1/2} \Delta \alpha_1} \left( u_{n,m+3/2}^k - u_{n,m-1/2}^k \right) - \frac{g}{(\mu_1)_{m+1/2} \Delta \alpha_1} \left\{ \eta_{n,m+1}^{k-1} - \eta_{n,m}^{k-1} \right. \\
& \left. \left. - 2 \left[ (\eta_a)_{n,m+1}^k - (\eta_a)_{n,m}^k \right] \right\} + 2\epsilon_1 \left\{ \left[ \frac{1}{(\mu_1)_{m+1/2} \Delta \alpha_1} \right]^2 \left( u_{n,m+3/2}^k \right. \right. \right. \\
& \left. \left. + u_{n,m-1/2}^k - 2u_{n,m+1/2}^k \right) + \frac{1}{2(\mu_1)_{m+1/2} \Delta \alpha_1^2} \left[ \left( \frac{1}{\mu_1} \right)_{m+1} - \left( \frac{1}{\mu_1} \right)_m \right] \left( u_{n,m+3/2}^k \right. \right. \right. \\
& \left. \left. - u_{n,m-1/2}^k \right) \right\} + 2\epsilon_2 \left\{ \left[ \frac{1}{(\mu_2)_n \Delta \alpha_2} \right]^2 \left( u_{n+1,m+3/2}^k + u_{n-1,m+1/2}^k - 2u_{n,m+1/2}^k \right) \right. \\
& \left. + \frac{1}{2(\mu_2)_n \Delta \alpha_2} \left[ \left( \frac{1}{\mu_2} \right)_{n+1/2} - \left( \frac{1}{\mu_2} \right)_{n-1/2} \right] \left( u_{n+1,m+1/2}^k - u_{n-1,m+1/2}^k \right) \right\} + 2F_{x_1}^k \Big)
\end{aligned}$$

$x_2$  - y sweep

$$-a_{n-1/2} v_{n-1/2,m}^{k+1} + \eta_{n,m}^{k+1} + a_{n+1/2} v_{n+1/2,m}^{k+1} = A_n \quad \text{Continuity (a)} \quad (1.1.18)$$

$$-a_n \eta_{n,m}^{k+1} + \bar{a}_{n+1/2} v_{n+1/2,m}^{k+1} + a_{n+1} \eta_{n+1,m}^{k+1} = B_{n+1/2} \quad \text{Momentum (b)}$$

where

$$a_{n-1/2} = \frac{\Delta t}{(\mu_2)_n \Delta \alpha_2} \frac{\alpha_2}{d} \eta_{n-1/2,m}$$

$$a_{n+1/2} = \frac{\Delta t}{(\mu_2)_n \Delta \alpha_2} \frac{\alpha_2}{d} n+1/2, m$$

$$A_n = \pi_{n,m}^* + \frac{\Delta t}{(\mu_2)_n \Delta \alpha_2} \left[ \left( v_{n+1/2,m}^{k-1} \right) - \left( v_{n-1/2,m}^{k-1} \right) \right]$$

$$a_n = \frac{g \Delta t}{(\mu_2)_{n+1/2} \Delta \alpha_2}$$

$$a_{n+1} = a_n$$

$$\bar{a}_{n+1/2} = \left\{ 1 + \frac{2g\Delta t}{\left( \frac{2}{c} \right)_{n+1/2}^{\alpha_2}} \left[ \left( u_{n+1/2,m}^{k-1} \right)^2 + \left( v_{n+1/2,m}^{k-1} \right)^2 \right]^{1/2} \right\}$$

$$\begin{aligned} B_{n+1/2} = & v_{n+1/2,m}^{k-1} + \Delta t \left\{ \bar{u}_{n+1/2,m}^k \left[ 2f + \frac{v_{n+1/2,m+1}^k - v_{n+1/2,m-1}^k}{(\mu_1)_m \Delta \alpha_1} \right] \right\} \\ & + \frac{v_{n+1/2,m}^k}{(\mu_2)_{n+1/2} \Delta \alpha_2} \left( v_{n+3/2,m}^k - v_{n-1/2,m}^k \right) + \frac{g}{(\mu_2)_{n+1/2} \Delta \alpha_2} \left\{ \eta_{n+1,m}^{k-1} - \eta_{n,m}^{k-1} \right. \\ & \left. - 2 \left[ (\eta_a)_{n+1,m}^k - (\eta_a)_{n,m}^k \right] \right\} - 2\epsilon_1 \left\{ \left[ \frac{1}{(\mu_1)_m \Delta \alpha_1} \right]^2 \left( v_{n+1/2,m+1}^k \right. \right. \\ & \left. \left. + v_{n+1/2,m-1}^k - 2v_{n+1/2,m}^k \right) + \frac{1}{2(\mu_1)_m \Delta \alpha_1^2} \left[ \left( \frac{1}{\mu_1} \right)_{m+1/2} - \left( \frac{1}{\mu_1} \right)_{m-1/2} \right] \right. \\ & \left. \left( v_{n+1/2,m+1}^k - v_{n+1/2,m-1}^k \right) \right\} - 2\epsilon_2 \left\{ \left[ \frac{1}{(\mu_2)_{n+1/2} \Delta \alpha_2} \right]^2 \left( v_{n+3/2,m}^k \right. \right. \\ & \left. \left. + v_{n-1/2,m}^k - 2v_{n+1/2,m}^k \right) + \frac{1}{2(\mu_2)_{n+1/2} \Delta \alpha_2^2} \left[ \left( \frac{1}{\mu_2} \right)_{n+1} - \left( \frac{1}{\mu_2} \right)_n \right] \left( v_{n+3/2,m}^k \right. \right. \\ & \left. \left. - v_{n-1/2,m}^k \right) \right\} - 2F_{\alpha_2}^k \end{aligned}$$

154. Alternatively, the sweep equations may be expressed in operator form as shown in Table IV-1.

#### Tridiagonal matrix solution

155. It is instructive to study the computational structure embodied in Equation set (1.1.17). Consider the computational stencils for the continuity and  $\alpha_1$  momentum equations as shown in Figures IV-3 and IV-4, respectively. The locations of the pertinent hydrodynamic variables are as shown in Figure IV-1. The computational stencils show the dependence of the computations on the surrounding hydrodynamic variables at different levels in time. Observe in both Figures IV-3 and 4, that for a given  $m$ , the variables at the most advanced time level all lie on a straight line of constant  $n$ . Since at the most advanced time level, the variable of interest (either  $\eta_{n,m}^*$  or  $u_{n,m+1/2}^{k+1}$ ) is a function of its nearest neighbors along constant  $n$  (either  $u_{n,m-1/2}^{k+1}$  or  $\eta_{n,m}^*$  and  $\eta_{n,m+1}^*$ ), the difference schemes are implicit.

156. The solution procedure for the  $x - \alpha_1$  sweep is for each  $n$ , determine the number of computational segments and their beginning and end locations in the grid. The number of computational segments and their locations beginning and end are a function of the grid system and the boundary conditions. In order to illustrate the procedures, consider  $n = N$  and one computational segment defined by specifying  $u_{N,MS-1/2}^{k+1}$  and  $\eta_{N,ME+1}^*$ . The matrix equation assumes the following format.

$$\eta_{N,MS}^* + a_{MS+1/2} u_{N,MS+1/2}^{k+1} = A_{MS} + a_{MS-1/2} u_{N,MS-1/2}^{k+1} \quad (1.2.1)$$

$$-a_{MS} \eta_{N,MS}^* + \bar{a}_{MS+1/2} u_{N,MS+1/2}^{k+1} + a_{MS+1} \eta_{N,MS+1}^* = B_{MS+1/2} \quad (1.2.2)$$

.

.

.

$$-a_{J-1/2} u_{N,J-1/2}^{k+1} + \eta_{N,J}^* + a_{J+1/2} u_{N,J+1/2}^{k+1} = A_J \quad (1.2.3)$$



Table IV-1  
Finite Difference Approximation in Operator Form  
of the Complete Hydrodynamic Equations Set

$$\delta \alpha_1(F_{n,m}) = F_{n,m+(1/2)} - F_{n,m-(1/2)}$$

$$\delta \alpha_2(F_{n,m}) = F_{n+(1/2),m} - F_{n-(1/2),m}$$

$$\delta \alpha_1 \delta \alpha_1(F_{n,m}) = F_{n,m+1} - F_{n,m-1} = \delta \alpha_1 \delta \alpha_1(F_{n,m})$$

$$\delta \alpha_2 \delta \alpha_2(F_{n,m}) = F_{n+1,m} - F_{n-1,m} = \delta \alpha_2 \delta \alpha_2(F_{n,m})$$

$$\delta \alpha_1 \delta \alpha_1 F_{n,m} = F_{n,m+1} + F_{n,m-1} - 2F_{n,m} = \delta \alpha_1 \delta \alpha_1 F_{n,m}$$

$$\delta \alpha_2 \delta \alpha_2 F_{n,m} = F_{n+1,m} + F_{n-1,m} - 2F_{n,m} = \delta \alpha_2 \delta \alpha_2 F_{n,m}$$

$$\frac{\alpha_1}{F_{n,m}} = \frac{F_{n,m+1} + F_{n,m}}{2} \frac{\alpha_2}{F_{n,m}} = \frac{F_{n+1,m} + F_{n,m}}{2}$$

$$F_{n,m} = \frac{F_{n+(1/2),m-(1/2)} + F_{n+(1/2),m+(1/2)} + F_{n-(1/2),m-(1/2)} + F_{n-(1/2),m+(1/2)}}{4}$$

x-sweep

$$\frac{1}{2\Delta t} \left( u^{k-1} - u^{k+1} \right) + \frac{1}{2u_1 \Delta \alpha_1} \left[ \delta \alpha_1 \left( u^{k+1} \frac{\alpha_1}{d} k + u^{k-1} \frac{\alpha_1}{d} k \right) \right]$$

$$+ \frac{1}{u_2 \Delta \alpha_2} \left[ \delta \alpha_2 \left( v^{k-1} \frac{\alpha_1}{d} k \right) \right] = 0 \quad \text{at } (n,m)$$

(Continued)

Table IV-1 (Concluded)

$$\begin{aligned}
& \frac{1}{2\Delta t} (u^{k+1} - u^{k-1}) + \frac{1}{2u_1\Delta x_1} u^k \delta_{2x_1}(u^k) + \frac{1}{2u_2\Delta x_2} \bar{v}^k \delta_{2x_2}(u^k) - f_v^k \\
& + \frac{g}{2u_1\Delta x_1} \left[ \delta_{x_1} \left( \eta^* + \eta^{k-1} - 2\eta_a^k \right) \right] + \frac{g}{\left( \frac{x_1}{c} - 2 \frac{x_1}{d} \right)^k} u^{k+1} \left[ (u^{k-1})^2 + (\bar{v}^{k-1})^2 \right]^{1/2} \\
& - \varepsilon \left[ \frac{1}{(u_1\Delta x_1)^2} \delta_{x_1 x_1}(u^k) + \frac{1}{(u_2\Delta x_2)^2} \delta_{x_2 x_2}(u^k) + \frac{1}{2u_1\Delta x_1^2} \delta_{x_1} \left( \frac{1}{u_1} \right) \delta_{2x_1}(u^k) \right. \\
& \quad \left. + \frac{1}{2u_2\Delta x_2^2} \delta_{x_2} \left( \frac{1}{u_2} \right) \delta_{2x_2}(u^k) = F_{x_1}^k \right] \quad \text{at } (n, m+1/2)
\end{aligned}$$

y-sweep

$$\begin{aligned}
& \frac{1}{2\Delta t} (v^{k+1} - v^k) + \frac{1}{2u_2\Delta x_2} \left[ \delta_{x_2} \left( v^{k+1} \frac{x_2}{d} - v^{k-1} \frac{x_2}{d} \right) \right] = 0 \quad \text{at } (n, m) \\
& \frac{1}{2\Delta t} (v^{k+1} - v^{k-1}) + \frac{1}{2u_1\Delta x_1} \bar{u}^k \delta_{2x_1}(v^k) + \frac{1}{2u_2\Delta x_2} v^k \delta_{2x_2}(v^k) + f_u^k \\
& + \frac{g}{2u_2\Delta x_2} \left[ \delta_{x_2} \left( \eta^{k+1} + \eta^{k-1} - 2\eta_a^k \right) \right] + \frac{g}{\left( \frac{x_1}{c} - 2 \frac{x_1}{d} \right)^k} v^{k+1} \left[ (u^{k-1})^2 + (v^{k-1})^2 \right]^{1/2} \\
& - \varepsilon \left[ \frac{1}{(u_1\Delta x_1)^2} \delta_{x_1 x_1}(v^k) + \frac{1}{(u_2\Delta x_2)^2} \delta_{x_2 x_2}(v^k) + \frac{1}{2u_1\Delta x_1^2} \delta_{x_1} \left( \frac{1}{u_1} \right) \delta_{2x_1}(v^k) \right. \\
& \quad \left. + \frac{1}{2u_2\Delta x_2^2} \delta_{x_2} \left( \frac{1}{u_2} \right) \delta_{2x_2}(v^k) \right] = F_{x_2}^k \quad \text{at } (n+1/2, m)
\end{aligned}$$

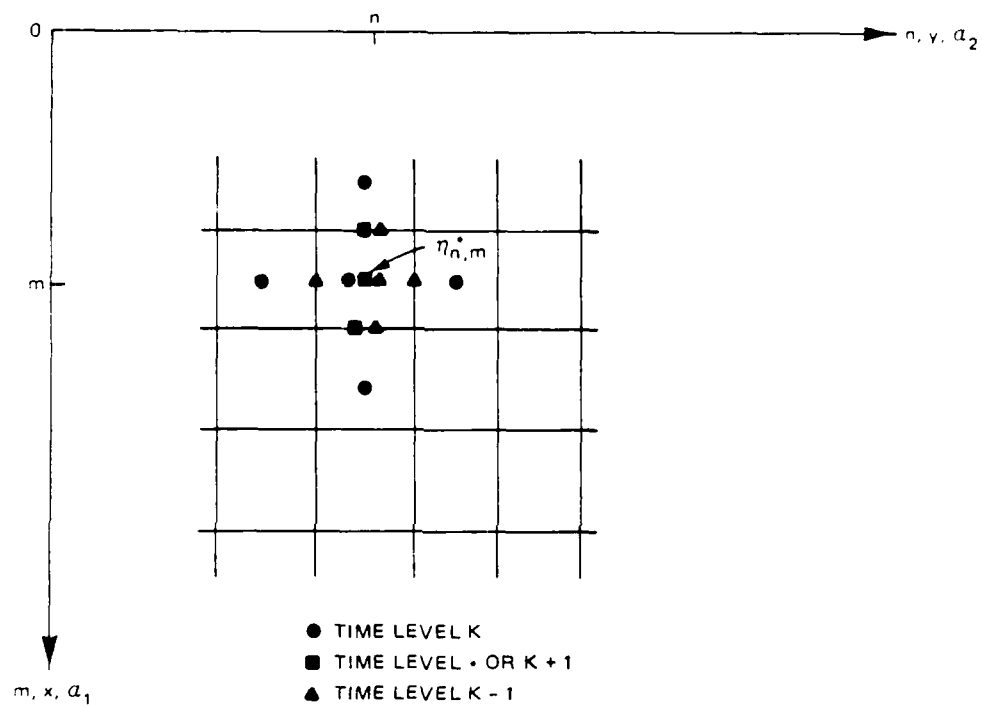


Figure IV-3. Computation stencil for the  $x - \alpha_1$  sweep continuity equation

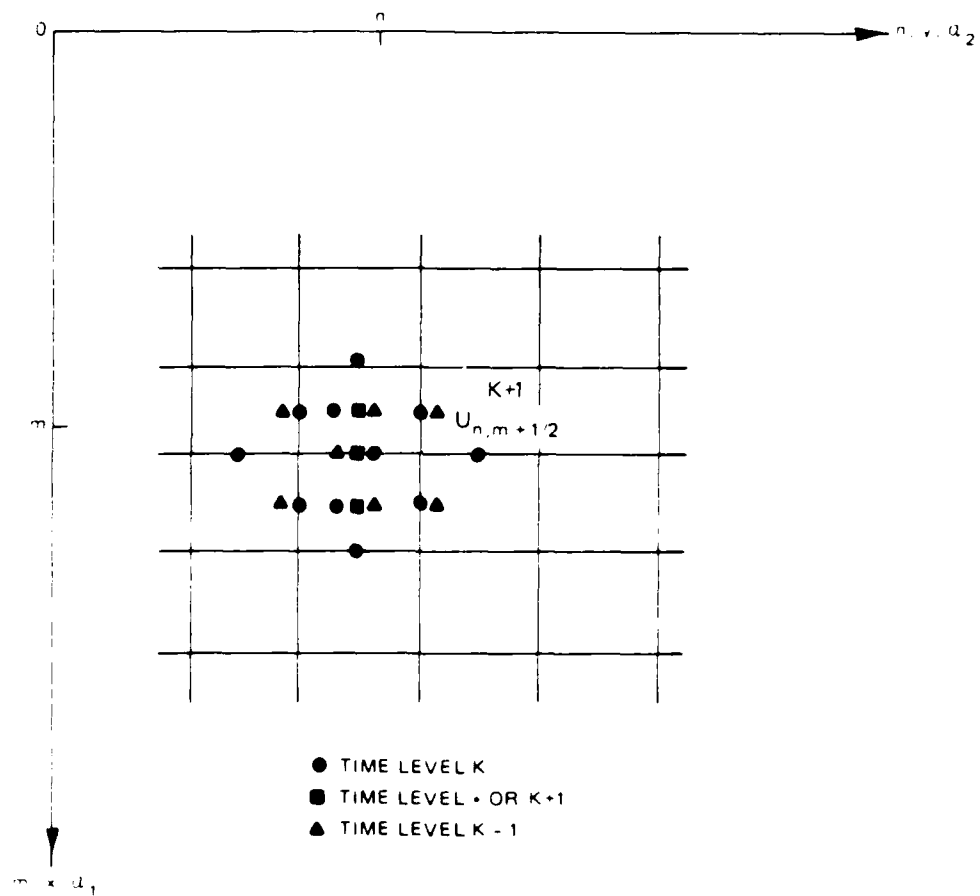


Figure IV-4. Computational stencil for the  $x - x_1$  sweep momentum equation

$$-a_{J,N,J} \eta_{N,J}^* + \bar{a}_{J+1/2} u_{n,J+1/2}^{k+1} + a_{J+1} \eta_{N,J+1}^* = B_{J+1/2} \quad (1.2.4)$$

.

.

.

$$-a_{ME-1/2} u_{N,ME-1/2}^{k+1} + \eta_{N,ME}^* + a_{ME+1/2} u_{N,ME+1/2}^{k+1} = A_{ME} \quad (1.2.5)$$

$$-a_{ME} \eta_{N,ME}^* + \bar{a}_{ME+1/2} u_{N,ME+1/2}^{k+1} = B_{ME-1/2} - a_{ME+1} \eta_{N,ME+1}^* \quad (1.2.6)$$

Observe the tridiagonal structure of the above matrix for  $n = N$ . Let us seek the following general structure

$$\eta_{n,m}^* = -P_m u_{n,m+1/2}^{k+1} + Q_m \quad (a)$$

$$\begin{aligned} m &= MS, \dots, ME \\ n &= N \end{aligned} \quad (1.2.7)$$

$$u_{n,m+1/2}^{k+1} = -R_m \eta_{n,m+1}^* + S_m \quad (b)$$

157. In order to determine  $P_m$ ,  $Q_m$ ,  $R_m$ , and  $S_m$ , first rewrite Equation (1.2.1):

$$\eta_{N,MS}^* = -a_{MS+1/2} u_{N,MS+1/2}^{k+1} + \left( A_{MS} + a_{MS-1/2} u_{N,MS-1/2}^{k+1} \right) \quad (1.2.8)$$

and

$$P_{MS} = a_{MS+1/2}, \quad Q_{MS} = A_{MS} + a_{MS-1/2} u_{N,MS-1/2}^{k+1}$$

158. Let us next substitute (1.2.8) into (1.2.2) to obtain:

$$\begin{aligned} -a_{MS} \left( -P_{MS} u_{N,MS+1/2}^{k+1} + Q_{MS} \right) + \bar{a}_{MS+1/2} u_{N,MS+1/2}^{k+1} \\ + a_{MS+1} \eta_{N,MS+1}^* = B_{MS+1/2} \end{aligned} \quad (1.2.9)$$

159. Rearranging the above equation, we obtain:

$$u_{N,MS+1/2}^{k+1} = \frac{-a_{MS+1} n_{N,MS+1}^* + (B_{MS+1/2} + a_{MS} Q_{MS})}{\bar{a}_{MS+1/2} + a_{MS} P_{MS}}$$

$$R_{MS} = \frac{a_{MS+1}}{\bar{a}_{MS+1/2} + a_{MS} P_{MS}} \quad (1.2.10)$$

$$S_{MS} = \frac{B_{MS+1/2} + a_{MS} Q_{MS}}{\bar{a}_{MS+1/2} + a_{MS} P_{MS}}$$

160. In order to obtain, the general form for  $P_m$ ,  $Q_m$  consider the next equation; e.g.,

$$-a_{MS+1/2} (-R_{MS} n_{N,MS+1}^* + S_{MS}) + n_{N,MS+1}^* + a_{MS+3/2} u_{N,MS+3/2}^{k+1} = A_{MS+1}$$

Rearranging this equation, we obtain:

$$n_{N,MS+1}^* = \frac{-a_{MS+3/2} u_{N,MS+3/2}^{k+1} + (A_{MS+1} + a_{MS+1/2} S_{MS})}{1 + a_{MS+1/2} R_{MS}}$$

$$P_{MS+1} = \frac{a_{MS+3/2}}{1 + a_{MS+1/2} R_{MS}} \quad (1.2.11)$$

$$Q_{MS+1} = \frac{A_{MS+1} + a_{MS+1/2} S_{MS}}{1 + a_{MS+1/2} R_{MS}}$$

We therefore hypothesize the following general formulas:

$$\begin{aligned} P_m &= \frac{a_{m+1/2}}{1 + a_{m-1/2} R_{m-1}} & Q_m &= \frac{A_m + a_{m-1/2} S_{m-1}}{1 + a_{m-1/2} R_{m-1}} \\ R_m &= \frac{a_{m+1}}{\bar{a}_{m+1/2} + a_m P_m} & S_m &= \frac{B_{m+1/2} + a_m Q_m}{\bar{a}_{m+1/2} + a_m P_m} \end{aligned} \quad (1.2.12)$$

161. Observe the above formulas may need to be modified for  $P_m$  and  $Q_m$  for  $m = MS$ , and for  $R_m$  and  $S_m$ ,  $m = ME$ . Returning to the  $P_m$  and  $Q_m$  for  $m = MS$ , note  $u_{N,MS-1/2}^{k+1}$  is specified. Let us rewrite this in the following form

$$u_{N,MS-1/2}^{k+1} = R_{MS-1} \eta_{N,MS}^* + S_{MS-1} \rightarrow R_{MS-1} = 0, \quad S_{MS-1} = u_{N,MS-1/2}^{k+1} \quad (1.2.13)$$

If we define  $R_{MS-1}$  and  $S_{MS-1}$  as above then the general equation holds for  $m = MS$  as well. Let us now consider, the last equation (Equation 1.2.6) and assume the general solution form for  $\eta_{N,ME}^*$ :

$$\begin{aligned} -a_{ME} \left( -P_{ME} u_{N,ME+1/2}^{k+1} + Q_{ME} \right) + \bar{a}_{ME+1/2} u_{N,ME+1/2}^{k+1} \\ = B_{ME+1/2} - a_{ME+1} \eta_{N,ME+1}^* \end{aligned} \quad (1.2.14)$$

$$u_{N,ME+1/2}^k = \frac{-a_{ME+1} \eta_{N,ME+1}^* + B_{ME+1/2} + a_{ME} Q_{ME}}{(\bar{a}_{ME+1/2} + a_{ME} P_{ME})}$$

Therefore

$$R_{ME} = \frac{a_{ME+1}}{\bar{a}_{ME+1/2} + a_{ME} P_{ME}} \quad \text{and} \quad S_{ME} = \frac{B_{ME+1/2} + a_{ME} Q_{ME}}{\bar{a}_{ME+1/2} + a_{ME} P_{ME}}$$

We note that the standard formulas hold for  $R_{ME}$  and  $S_{ME}$ . We therefore have developed the procedure outlined in Table IV-1 for column  $n$  in the grid. Step 2 is the forward elimination step and Step 3 is the backward substitution step of the Thomas algorithm.

162. The treatment of other starting and ending conditions is shown for  $(u_{N,MS-1/2}^{k+1}, u_{N,ME+1/2}^{k+1})$ ,  $(\eta_{N,MS}^*, \eta_{N,ME+1}^*)$ , and  $(\eta_{N,MS}^*, u_{N,ME+1/2}^{k+1})$  in Tables IV-2, IV-3, and IV-4, respectively.

#### Boundary conditions

163. For a solid boundary at the lower end of a computational segment  $u_{N,MS-1/2}^{k+1} = 0$ . For a river or other flow input,  $u_{N,MS-1/2}^{k+1} = Q(t)$ , a

Table IV-1

Tridiagonal Matrix Solution Procedure ( $x - \alpha_1$  sweep):

$$\underline{u_{N,MS+1/2}^{k+1} , \quad r_{N,ME+1}^*}$$

$$1. \quad R_{MS-1} = 0$$

$$S_{MS-1} = u_{N,MS-1/2}^{k+1}$$

$$2. \quad T1 = 1 + a_{m-1/2} R_{m-1}$$

$$P_m = -a_{m+1/2}/T1$$

$$Q_m = (A_m + a_{m-1/2} S_{m-1})/T1$$

$$T2 = \bar{a}_{m+1/2} + a_m P_m$$

$$R_m = a_{m+1}/T2$$

$$S_m = (B_{m+1/2} + a_m Q_m)/T2$$

$$m = MS, ME, 1$$

$$3. \quad u_{n,m+1/2}^{k+1} = -R_m r_{n,m+1}^* + S_m$$

$$m = ME, MS, -1$$

$$r_{n,m}^* = -P_m u_{n,m+1/2}^{k+1} + Q_m$$

$$n = N$$



Table IV-2

Tridiagonal Matrix Solution Procedure ( $x = x_1$  sweep):

$$u_{N,MS-1/2}^{k+1}, u_{N,ME+1/2}^{k+1}$$

1. Same as Step 1 Table IV-1

2. Same as Step 2 Table IV-1 for  $m = MS, ME-1, 1$

$$T1 = 1 + a_{m-1/2} R_{ME-1}$$

$$P_{ME} = a_{ME+1/2} / T1$$

$$Q_{ME} = (A_{ME} + a_{ME-1/2} S_{ME-1}) / T1$$

$$3. \quad u_{N,ME}^* = -P_{ME} u_{N,ME+1/2}^{k+1} + Q_{ME}$$

$$\left. \begin{aligned} u_{n,m+1/2}^k &= -R_m u_{n,m+1}^* + S_m \\ u_{n,m}^* &= -P_m u_{n,m+1/2}^k + Q_m \end{aligned} \right\}$$

$$m = ME-1, MS, -1$$

$$n = N$$

Table IV-3

Tridiagonal Matrix Solution Procedure ( $x = x_1$  sweep):

$$\bar{u}_{N,MS}^* , \bar{u}_{N,ME+1}^*$$

$$1. \quad R_{MS} = a_{MS+1} / \bar{a}_{MS+1/2} \qquad S_{MS} = (a_{MS} \bar{u}_{N,MS}^* + B_{MS+1/2}) / \bar{a}_{MS+1/2}$$

2. Same as Step 2 Table IV-1 for  $m = MS+1, ME$

$$3. \quad \left. \begin{aligned} u_{n,m+1/2}^{k+1} &= -R_m \bar{u}_{n,m+1}^* + S_m \\ \bar{u}_{n,m}^* &= -P_m u_{n,m+1/2}^{k+1} + Q_m \end{aligned} \right\} \quad \begin{aligned} m &= ME, MS+1, -1 \\ n &= N \end{aligned}$$

$$u_{N,MS+1/2}^{k+1} = -R_{MS} \bar{u}_{N,MS+1}^* + S_{MS}$$

Table IV-4  
Tridiagonal Matrix Solution Procedure ( $x = x_1$  sweep):

---


$$\bar{r}_{N,MS}^* , \quad u_{N,ME-1/2}^{k+1}$$


---

1. Same as Step 1 in Table IV-3 for  $R_{MS}$  and  $S_{MS}$

2. Same as Step 2 in Table IV-1 for  $m = MS+1, ME-1, 1$

$P_{ME}$  and  $Q_{ME}$  as computed in Step 2 Table IV-2

3.  $\bar{r}_{N,ME}^* = -P_{ME} u_{N,ME+1/2}^{k+1} + Q_{ME}$

$$u_{n,m+1/2}^{k+1} = -R_m \bar{r}_{n,m+1}^* + S_m \quad \left. \begin{array}{l} \\ \\ \end{array} \right\} \quad \begin{array}{l} m = ME-1, MS+1, -1 \\ n = N \end{array}$$

$$\bar{r}_{n,m}^* = -P_m u_{n,m+1/2}^{k+1} + Q_m$$

$$u_{N,MS+1/2}^{k+1} = -R_{MS} \bar{r}_{N,MS+1}^* + S_{MS}$$


---

specified flow velocity. Alternatively, the user may specify the flow rate and the velocity is computed by dividing this by the effective flow area.

164. For a tidal boundary at the lower end of a computational segment,  $\eta_{n,MS}^* = \sum_i A_i \cos(w_i t + \phi_i)$ , where  $A_i$ ,  $w_i$ , and  $\phi_i$  are specified. Alternatively the user may specify a table of values over time. In addition, it is possible to save elevations at appropriate locations on a global grid and later use these elevations to drive a refined grid.

165. The treatment of the upper computational segment boundary is similar to that just presented.

166. After completing the above procedures for  $n = 2, NMAX - 1$ , the grid is swept in the other direction (row wise) for each  $m$ . In the  $y - \alpha_2$  sweep Equation set (1.1.18) is considered. The computational stencils for the continuity and  $\alpha_2$  momentum equations are as shown in Figures IV-5, and IV-6, respectively. Observe in both Figures IV-5 and IV-6, that for a given  $n$ , the variables at the most advanced time level all lie on a straight line of constant  $m$ . Since at the most advanced time level, the variable of interest (either  $\eta_{n,m}^{k+1}$  or  $v_{n+1/2,m}^{k+1}$ ) is a function of its nearest neighbors along constant  $m$  either  $(v_{n+1/2,m}^{k+1}$  or  $\eta_{n,m}^{k+1}, \eta_{n+1,m}^{k+1})$ , the difference schemes are implicit.

167. The solution procedure for the  $y - \alpha_2$  sweep is for each  $m$ , determine the number of computational segments and their beginning and end locations in the grid. The number of computational segments and their locations are a function of the grid and boundary conditions. The computational procedures for the  $y - \alpha_2$  sweep are completely analogous to these presented in Tables IV-1 through IV-4 for the  $x - \alpha_1$  sweep. Boundary condition considerations also remain analogous.

#### Programming considerations

168. The above algorithms have been programmed in the FORTRAN language. Since FORTRAN array element variables cannot be referenced using fractional indices, the index system shown in Figure IV-7 below has been developed. Thus variables defined at cell faces will take the same index as the center cell

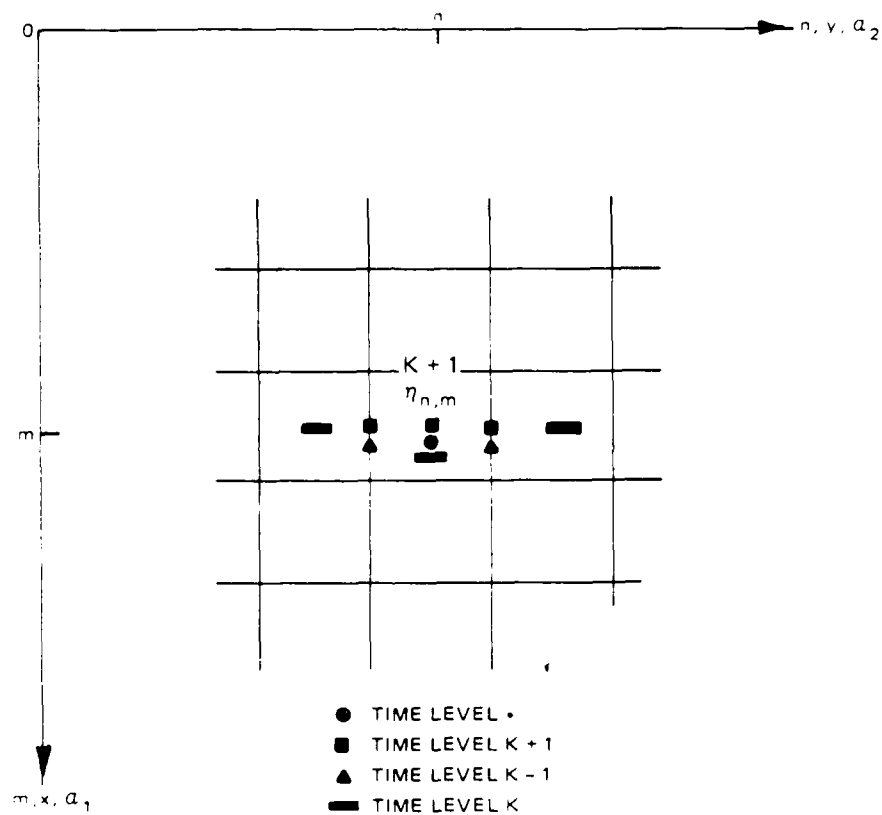


Figure IV-5. Computational stencil for the  $y - a_2$  sweep continuity equation

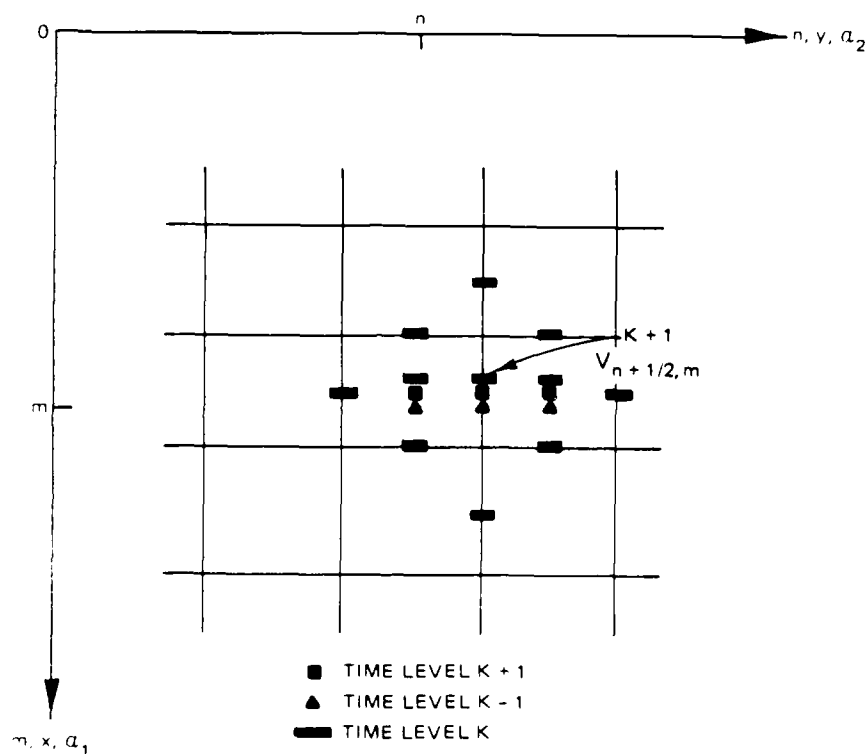
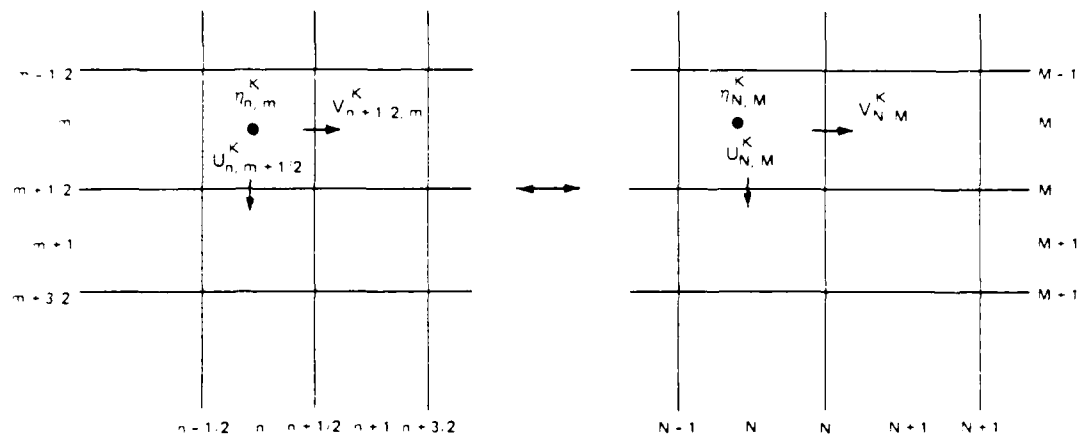


Figure IV-6. Computational stencil for the  $y - x_2$  sweep continuity equation



$$\begin{aligned}
 \text{SEM}(N, M) &= \eta_{n,m}^{K-1} \\
 \text{SE}(N, M) &= \eta_{n,m}^K \\
 \text{SEP}(N, M) &= \eta_{n,m}^{K+1} \\
 \text{UM}(N, M) &= U_{n,m+1/2}^{K-1} \\
 \text{U}(N, M) &= U_{n,m+1/2}^K \\
 \text{UP}(N, M) &= U_{n,m+1/2}^{K+1} \\
 \text{VM}(N, M) &= V_{n+1/2,m}^{K-1} \\
 \text{V}(N, M) &= V_{n+1/2,m}^K \\
 \text{VP}(N, M) &= V_{n+1/2,m}^{K+1} \\
 \text{H}(N, M) &= h_{n,m} \\
 \text{C}(N, M) &= c_{n,m} \\
 \text{PHED}(N, M) &= \eta_{\theta,n,m}^K
 \end{aligned}$$

Figure IV-7. WIFM Hydrodynamic Variable Indexing System

variable to the left or below, whichever is appropriate. A separate index system is developed for the stretching functions  $u_1$  and  $u_2$  as follows:

$$XMU(2M-1) \equiv (u_1)_m \quad m \text{ and } M \in (1, NMAX)$$

$$XMU(2M) \equiv (u_1)_{m+1/2}$$

$$YNU(2N-1) \equiv (u_1)_n \quad n \text{ and } N \in (1, NMAX)$$

$$YNU(2N) \equiv (u_1)_{n+1/2}$$

169. Thus the stretching function at the center of the cells has an odd array reference, while on the cell faces, its reference is even. The following variable associations are employed for the  $x_1 - x$  and  $x_2 - y$  sweeps:

$x_1 - x$  sweep

$$(N,M) \leftrightarrow II$$

$$XU \leftrightarrow XMU(2*M)$$

$$(N,M+1) \leftrightarrow JJ$$

$$XU1 \leftrightarrow XMU(2*M-1)$$

$$(N+1,M) \leftrightarrow I12$$

$$YU \leftrightarrow YNU(2*N-1)$$

$$(N-1,M) \leftrightarrow I11$$

$$A(M) \equiv A_m$$

$$TMP3(M) \equiv \bar{a}_{m+1/2}$$

$$TMP1(M) \equiv a_{m-1/2}$$

$$TMP4(M) \equiv a_{m+1}, a_m$$

$$TMP2(M) \equiv a_{m+1/2}$$

$$B(M) \equiv B_{m+1/2}$$

$$P(M), Q(M), R(M), S(M) \equiv P_m, Q_m, R_m, S_m$$



### $\alpha_2 - y$ sweep

$(N,M) \leftrightarrow JJ$	$XU \leftrightarrow XMU(2*M-1)$
$(N+1,M) \leftrightarrow JJ2$	$YU1 \leftrightarrow YNU(2*N-1)$
$(N-1,M) \leftrightarrow JJ1$	$YU \leftrightarrow YNU(2*N)$
$(N,M+1) \leftrightarrow LL1$	
$(N,M-1) \leftrightarrow LL2$	

$A(N) \equiv A_n$	$TMP3(N) \equiv \bar{a}_{n+1/2}$
$TMP1(N) \equiv a_{n-1/2}$	$TMP4(N) \equiv a_{n+1}, -a_n$
$TMP2(N) \equiv a_{n+1/2}$	$B(N) \equiv B_{n+1/2}$

$P(N), Q(N), R(N), S(N) \equiv P_n, Q_n, R_n, S_n$

### Cell face flag conventions

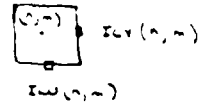
170. In order to control the beginning and end of the  $x - \alpha_1$  and  $y - \alpha_2$  sweeps each cell face is given a two-digit code. The code is used also to determine boundary types and convective acceleration (advection) approximations in the vicinity of flow boundaries. The code conventions are as indicated in Table IV-5 below. The u-face cell code is associated with the v-velocity and is stored in array ICU; e.g.  $ICU_{n,m} \equiv u_{n,m}$ . Similarly, the v-face cell code is associated with the v-velocity and is stored in array ICV; e.g.,  $ICV_{n,m} \equiv v_{n,m}$ .

### Numerical approximation of the convective acceleration terms

171. If one considers Equation (1.1.14) for  $\alpha_1 - x$  sweep and Equation (1.1.16) for the  $\alpha_2 - y$  sweep, the terms underlined designated by ①, constitute the convective acceleration terms. These terms are approximated using

Table IV-5

## Face Cell Flag Convention



$n_1$	$n_2$	$n$	$n_2$
<u>1</u> Exposed Barrier	$n_2$ barrier no. If $n_2 > 9$ $n_2 = 0$	<u>7</u> Transmission Boundary	0 lower boundary 1 upper boundary 6 Channel Match to 2-0 7 Ponding Condition 8 K/V
<u>2</u> Overtopping Barrier	$n_2$ barrier no. If $n_2 > 9$ $n_2 = 0$	<u>8</u> Elevation Input	9 Extrapolated wave $n_2$ input no. $n_2 = 0$ $n_2 = 0$ $n_a$ on bdy
<u>3</u> Global Grid Cond. on LUN 24	$n_2$ not used (Advection code)	<u>9</u> Flow Input	$n_2$ input no. $n_2 = 0$ $n_2 = 0$ $\frac{\partial u}{\partial n} = 0$ on bdy
<u>4</u> Submerged Barrier	$n_2$ barrier no. If $n_2 > 9$ $n_2 = 0$		
<u>5</u> Land/ (Water or land Boundary)	0		
<u>6</u> Water  ADV = 1  ADV = 2	0 No advection 1 nx-direction 2 ny-direction 3 nx, y 4 nv ax 5 nx ay 6 ax 7 ay 8 ax ay  a = approx. n = normal		

centered differencing. However, in the vicinity of external boundaries (land/water interface) or near internal barriers, either the variables are not defined at appropriate locations on the computational stencils Fig. IV-3-IV-6 or it may be inappropriate to form the differences across the flow obstructions. In the hydrodynamic program, these terms are not approximated in such cases; that is, the motion equations are linearized. In addition, the lateral diffusion terms (the underlined terms designated by ⑤) are also ignored, when the convective acceleration terms are not approximated. This is accomplished by specifying ADV = 1 on input. Subroutine ADVBAR is used to set the  $n_2$  digit for wet cells surrounding barriers.

172. One-sided difference approximations are made for both convective acceleration and lateral diffusion terms if the user specifies ADV = 2. These options are still in the test and research phase and are not intended at this time for general use.

#### Computational line development

173. Let us first consider the form of the recursion equations used in the program for the  $\alpha_1 - x$  sweep. Using the program variable notation:

$$SEP(N,M) = -P(M) * UP(N,M) + Q(M)$$

$$M = ME, MS, -1 \quad (1.7.1)$$

$$UP(N,M-1) = -R(M-1) * SEP(N,M) + S(M-1)$$

174. Consider the general form of a computational segment as shown in Figure IV-8. Let us now consider the case of a solid boundary at the lower end of the computational segment. Since the ICU(N,M) flag is searched until ICU(N,M)/10 equals 6, MS = M, such that ICU(N,M)/10 is 6. In this case, UP(N,MSS) = 0. In order to achieve this, R(MSS) = S(MSS) = 0. This corresponds to the case in which  $u_{n,ms-1/2}^{k+1} = 0$ . Consider the case, when the user specifies a velocity,  $u^*$ , at u-cell face (N,M). In this instance, MS = MS+1, and R(MSS) = 0, S(MSS) =  $u^*$  where MSS = MS-1. This corresponds to the case for which  $u_{n,ms+1/2}^{k+1}$  is specified. Alternatively, consider the case when the user specifies an elevation,  $\eta^*$ , at the center of cell (N,MS) in this case MS = MS+1 and R(MS-1) and S(MS-1) are computed directly in terms of  $\eta^*$ . This corresponds to the case in which  $\eta_{n,m}^*$  is specified.



MS = START OF THE COMPUTATIONAL SEGMENT  
ME = END OF THE COMPUTATIONAL SEGMENT

Figure IV-8. General form of a computational segment  
for the  $x - \alpha_1$  sweep

175. Consider now the upper end of the computational boundary. In the case of a solid boundary,  $ME = M$ , such that  $ICU(N,M)/10$  equals 5. In this case,  $UP(N,ME) = 0$ . Notice, however, in the above equation pair,  $UP(N,M-1)$  and  $SEP(N,M)$ , correspond to the center and left side of cell  $(N,M)$ . Therefore, we may compute  $SEP(N,ME)$  directly in terms of the zero boundary velocity. The specification of a flow velocity is treated in exactly the same manner, since it is specified at the same location as a solid boundary. Both these cases correspond to specifying  $u_{n,me+1/2}^{k+1}$ . Consider the specification of an elevation,  $\eta^*$ , at cell  $(N,ME)$ . In this again,  $ME = ME-1$ , and it is necessary to first calculate,  $UP(N,ME)$  in terms of  $\eta^*$ . This corresponds to specifying  $\eta_{n,me}^*$ . Observe analogous considerations hold for the  $\alpha_2 - y$  sweep.

#### Sub-grid barriers

176. Butler [34] has represented flow restrictions on cell faces through a thin wall barrier concept. The width of the barrier essentially is assumed zero and does not enter the computations. Barriers in the Lake Okeechobee Study are of the following two types:

- a. Exposed barrier.
- b. Dynamic barrier.

Exposed barriers are considered to fall within two categories. Category one barriers may be specified to breach in a manner presented subsequently. Category two barriers may be overtopped without breaching. Flow information for both categories is written to tape for subsequent input to a link-node drainage model. Dynamic barriers may alternate between submerged and exposed conditions through the simulation. Within the Lake Okeechobee Study, these barriers are used to represent the tree islands and are assumed initially to be exposed.

177. The model user specifies barrier face condition through input as follows:

ITYP  $\equiv$  Type of barrier face (1 exposed, 2 dynamic)  
 IDIR  $\equiv$  Direction of restriction (1 flow restricted on u-face, 2 flow restricted on v-face)  
 INDX  $\equiv$  Index number used to specify the admittance coefficient for submerged conditions  
 I1  $\equiv$  Grid index of barrier line  
 I2 }  $\equiv$  Barrier extends from cell I2 to I3  
 I3 }  
 I4  $\equiv$  Barrier configuration index  
     0 link-node overtopping barrier  
 I5  $\equiv$   
     NCR breechable link-node barrier with NCR cross-sections  
 I6  $\equiv$  Barrier face condition and transmission code  
 DUM1  $\equiv$  Barrier toe elevation (msl)  
 DUM2  $\equiv$  Barrier lakeside side slope  
 DUM3  $\equiv$  Nearshore beach slope  
 DUM4  $\equiv$  Barrier crest elevation (msl)

The above information is saved in the following arrays for each barrier face, where KBT is a barrier face counter:

IBARR(KBT,1)  $\leftarrow$  IDIR  
 IBARR(KBT,2)  $\leftarrow$  ITYP  
 IBARR(KBT,3)  $\leftarrow$  INDX  
 IBARR(KBT,4)  $\leftarrow$  N  
 IBARR(KBT,5)  $\leftarrow$  M  
 IBARR(KBT,6)  $\leftarrow$  I6 (If I6 = 0, IBARR(KBT,6) = 17)  
 IBARR(KBT,7)  $\leftarrow$  I5  
 KBARO(KBT)  $\leftarrow$  I4

BARR(KBT,1) ← DUM1

BARR(KBT,2) ← DUM2

BARR(KBT,3) ← CVMGZ (DUM2, DUM3, DUM3)

All type 1 barriers are either overtopped or breechable barriers

KBAROO(KGG) ← KBT      Link-node model overtopping barrier index

KBAR(KFTB) ← KBT      Link-node model breechable barrier index

For each cross-section  $J=1, 15$ , the user specifies:

(ELEVCR(J,KFTB),  $J=1, 15$ ) the final cross-section elevation after breaching

178. A cell face flag is computed as follows:

IDIR = 1, u face barrier

IDIR = 2, v face barrier

$ICU_{N,M} = 10 * ITYP + INDX$

$ICV_{N,M} = 10 * ITYP + INDX$

179. For the case in which advection (the convective terms in the motion equation) is considered, one may employ subroutine ADVBAR to linearize the motion equation approximation in the vicinity of the barriers. We present in turn the computational procedures for each barrier face.

#### Exposed Barrier Face

180. This barrier face may never experience any type of flow. The face flag ( $ICU_{n,m}$  or  $ICV_{n,m}$ ) equals  $1n$ , where  $n < (0,9)$ . This face flag is divided by 10 to yield a face type of 1. The face type is examined in the x and y sweeps of the grid within the ADI procedure in order to establish computational segments. For a face type of 1 the computational segment is either initiated or terminated with  $u_{n,m}^{k+1} = 0$  or  $v_{n,m}^{k+1} = 0$ . The velocity at barrier face is thus set to zero. This condition is maintained throughout the simulation. The barrier thus allows no flow (velocity zero) through itself.

181. The barriers may also be breached. The model user specifies an initial breach time in hours relative to the start of the simulation and a duration of breaching also in hours. For each cross-section in each breechable barrier one computes a breach rate per time step. This rate is assumed to be uniform over the duration of breaching activity.

182. In this manner it is possible to simulate breach characteristics occurring over many grid cell faces or only over a part of a single grid cell

face. The types of failure cross-sections that can be simulated are shown in Figure IV-9. The following notation is used in the figure,  $h_{ij}^k$ , corresponds to the levee height at time  $k$  for levee  $i$  for cross-section  $j$ .

183. Each levee section associated with a grid cell face will be associated with a node in the link-node model. The flow rate ( $L^3/T$ ) and water surface elevation associated with either overtopping or breaching will be written to disc for each levee section along a grid cell face at each time step in the hydrodynamic simulation of the lake. The flow rate computations are as follows:

Multi-cell face breach:

$$q_i^k = C_o \sqrt{g} \sum_{j=1}^{nc_i} \left( \eta_i^k - h_{ij}^k \right)^{3/2} (L^2/T) \quad (a)$$

(1.8.1)

$$v_i^k = q_i^k \Delta S_i (L^3/T) \quad (b)$$

with  $h_{ij}^0 = ZB_{ij}$

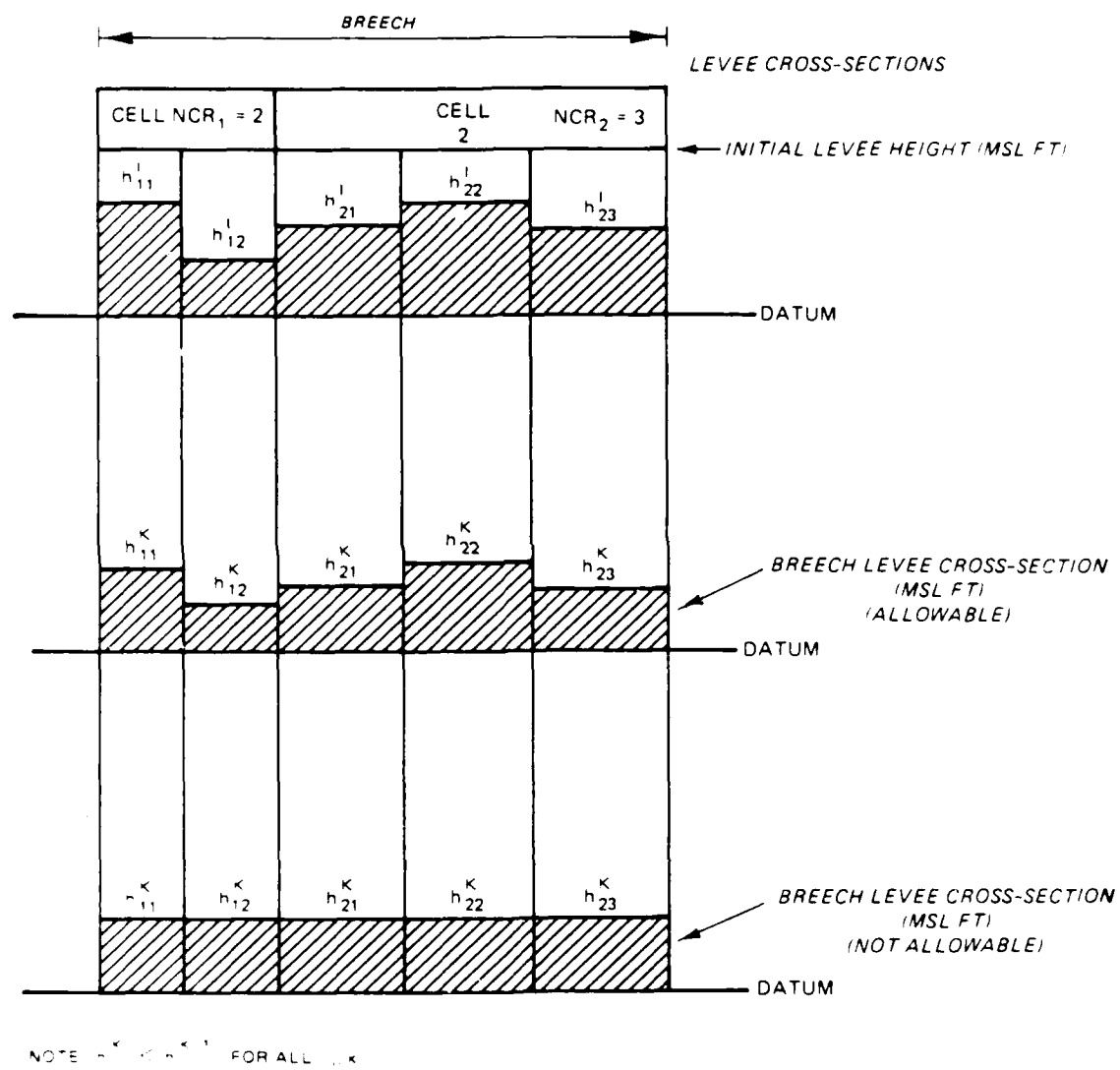


Figure IV-9. Cell breach mechanics



Single cell face breach:

$$q_i^k = C_o \sqrt{g} \left( r_i^k - h_i^k \right)^{3/2} (L^2/T) \quad (a)$$

(1.8.2)

$$v_i^k = q_i^k \Delta S_i (L^3/T) \quad (b)$$

with  $h_i^0 = ZB_i$

where

$q_i^k$  = flow rate per unit width of breach at time step  $k$  for cell  $i$

$r_i^k$  = water surface elevation at time step  $k$  for cell  $i$

$ZB_i$  = levee elevation for cell  $i$  (msl)

$ZB_{ij}$  = levee elevation for cell  $i$  cross section increment  $j$  (msl)

$nc_i$  = number of increments in cross section for cell  $i$

$h_i^k$  = breach height for cell  $i$  at time step  $k$

$h_{ij}^k$  = breach height for cell  $i$  at time step  $k$  cross section increment  $j$

$\Delta S_i$  = cell face width along the breach at cell  $i$

$v_i^k$  = flow rate caused by breaching during time step  $k$  at cell  $i$

The link node model will access the above disc file. The inflow at an arbitrary node  $I$  from Lake Okeechobee will be developed as the sum of all flows at WIFM cell faces assigned to node  $I$ . Thus assuming equal time steps (300 sec) in the WIFM and link-node models.

$$Q_I^* = \sum_{i=1}^{n_I} v_i^k r_i^k \quad (a)$$

(1.8.3)

$$r_i^k = \begin{cases} 1 & \text{if } u_I^k < h_i^k \\ 0 & \text{if } u_I^k \geq h_i^k \end{cases} \quad (b)$$

where

$Q_I^k$   $\equiv$  flow rate from Lake Okeechobee into node I at time step k

$r_i^k$   $\equiv$  factor to either allow or disallow flow from cell face i at time step k into node I

$v_i^k$   $\equiv$  flow rate at cell face i at time step k

$h_i^k$   $\equiv$  elevation at cell face i at time step k

$H_I^k$   $\equiv$  Node I elevation at time step k

As may be observed from the above equation, flow from the lake at cell face i at time step k is not allowed if the node elevation is greater than the cell elevation in WIFM. The coupling mechanism is essentially one-way with water passing from the lake to the link-node drainage model. Water is not allowed to pass from the drainage model into the lake. This coupling provides a conservative estimate of flood levels outside the lake appropriate for evacuation and water conservation area planning.

#### Dynamic Barrier Face

184. This type of barrier face changes dynamically as water levels rise and fall throughout the course of the simulation. A counting mechanism is employed such that a given face type must hold for a user specified number of time steps. This procedure is similar to those used in the flood/dry scheme and eliminates instabilities in the solution introduced by discrete changes in barrier face type.

185. The computational procedures are performed in Subroutine FLOODY prior to considering the flood/dry cells. The order in which the barriers are processed is reversed each time step to remove computational bias. All barriers are indexed within the DO 650 loop. For ITYP = 1 (exposed barriers in a breechable state) control is transferred to the end of the loop and the next barrier is considered. These barriers are handled prior to entering the DO 650 loop as discussed previously. Dynamic barriers are in one of two possible states (ITYP = 2 exposed condition or ITYP = 4 submerged).

186. The following elevations are defined in order to develop the methodology for handling these barriers:

$$T1 = \eta_{n,m}^{k+1} + \Delta a_{n,m} + dt \quad (a)$$

$$T2 = \eta_{n,m+1}^{k+1} + \Delta a_{n,m+1} \quad (b)$$

(1.8.4)

$$T3 = \eta_{n+1,m}^{k+1} + \Delta a_{n+1,m} \quad (c)$$

$$T4 = h_B + \epsilon_b \quad (d)$$

where

$\eta_{n,m}^{k+1} \equiv$  water surface elevation at location (n,m) at time k+1 with respect to model datum (12.5 msl)

$\Delta a_{n,m} \equiv$  cumulative water surface adjustments at location (n,m) at time k+1

$dt \equiv$  model datum adjustment to barrier datum (12.5)

$h_B \equiv$  barrier elevation (msl)

$\epsilon_b \equiv$  minimum amount of water for water surface adjustments

Next define the following variables:

Case I: IDIR = 1 (Barrier to the  $x - \alpha_1$  velocity component)

$$T5 = T2 + dt$$

$$T6 = ICU_{II}$$

$$IG = (n,m+1)$$

(1.8.5)

$$DS1 = \Delta \alpha_1 (\nu_1)_m$$

$$DS2 = \Delta \alpha_1 (\nu_1)_{m+1}$$

$$DL = \Delta \alpha_2 (\nu_2)_n$$

Case II: IDIR = 2 (Barrier to the  $y - x_2$  velocity component)

$$T5 \leftarrow T3 + dt$$

$$T6 \leftarrow ICV_{II}$$

$$IG \leftarrow (n+1, n)$$

(1.8.6)

$$DS1 \leftarrow \Delta \alpha_2 (u_2)_n$$

$$DS2 \leftarrow \Delta \alpha_2 (u_2)_{n+1}$$

$$DL \leftarrow \Delta \alpha_1 (u_1)_m$$

Let us now consider the submerged condition (ITYP = 4). IBART<sub>I</sub> is incremented and compared to KS3, which is specified through user input. If IBART<sub>I</sub> = KS3, then a check on T1 and T5 is performed else no further processing is performed on this barrier. If both T1, T5 > T4, the barrier is still submerged and the next barrier is considered.

187. If the above condition does not hold, the barrier type is set to 2 corresponding to an overtopped condition. The face change counter IBART<sub>I</sub> is set to one. The cell face flag is also appropriately modified; e.g., 20 is subtracted from ICU<sub>n,m</sub> or ICV<sub>n,m</sub>. The next barrier is then considered.

188. Consider next the overtopped condition (ITYP = 2). IBART<sub>I</sub> is incremented and compared to KS4, which is specified through user input. If IBART<sub>I</sub> = KS4, then a check on T1 and T5 is performed else no further processing is performed on this barrier. If both T1 and T5 are greater than T4, the barrier condition is changed to submerged and the IBART<sub>I</sub> counter reset to 1. For T1 or T5 < T4, the following quantities are computed:

$$h_{\max} = \max (T1, T5)$$

If  $h_{\max} < h_b$ , consider the next barrier

$$h_{\min} = \min (T1, T5)$$

If  $h_b < h_{\min}$  then set  $h_{\max} = 0.5 * (T1 + T2)$

(1.8.7)

$$dbc = h_{\max} - h_b$$

$g = CO_{INDX} dbc^{3/2}$ , which corresponds to the flow per unit barrier length

$$\Delta r_1 = g\tau/DS1, \text{ where } \tau \text{ is the time step length}$$

$$\Delta r_2 = -g\tau/DS2$$

The elevation increments are adjusted in a cumulative fashion as follows:

$$\Delta a_{n,m} = \Delta a_{n,m} + \Delta r_1 \quad (a)$$

(1.8.8)

$$\Delta a_{IG} = \Delta a_{IG} + \Delta r_2 \quad (b)$$

The most advanced time level velocities  $UP_{II}$  or  $VP_{II}$  are set to zero. The depth adjustments  $\Delta r_1$  and  $\Delta r_2$  are limited such that the elevation adjustment to the cell with the largest water surface elevation, will not cause that elevation to be less than  $h_b + \epsilon_b$ .

#### Flooding and drying methodology

189. Leendertse [35] was perhaps the first investigator to develop a flooding/drying capability in the simulation of a tidal flat problem. The initial approach was to make discrete changes (on the faces of grid cells) between land and water directly on the finite difference grid. In so doing, one must be aware that the discrete changes in the computational boundaries may introduce noise into the finite difference computation. In general, when new cells enter the computation, their initial water depth is relatively small resulting in a large value of bottom friction, which in turn will dampen out

oscillations (noise) introduced by the new boundary change. This frictional dampening mechanism is in agreement with the physical process and does naturally stabilize the computations. However, in order to allow this mechanism time to work, it is usually necessary not to change the boundary too often; i.e., not every time step. This approach is also in keeping with the general philosophy of applying finite difference techniques to relatively slowly changing processes.

190. In developing a technique for treating a moving boundary problem, the above concepts are assumed to form the computational foundation. In addition, the consideration of economy must also be introduced, since the flooding/drying techniques must be incorporated in addition to the finite difference computations over the interior. In order to formulate the most appropriate approach for Lake Okeechobee, a review of techniques is first presented. The details of the Lake Okeechobee problem are next presented followed by the development of the most appropriate moving boundary techniques.

#### Original Leendertse Technique [35]

191. The search for the next boundary is made at intervals larger than the time step. This enables the computational noise generated by the boundary change to die off before it is time to reexamine the boundary location. Thus the selection of the next boundary is not influenced by the perturbations caused by the last boundary change.

192. If in a particular field (cell) a cross section decreases to less than a preset value (greater than zero), then that field (cell) is removed from the computation. During rising water levels, grid points are added to the computation if the average of the adjacent fields which are underwater results for all four sides of the field (cell) in cross sections which are larger than the above-mentioned preset value. If this is the case, the water level in the new field (cell) is set to the average value of the adjacent fields (cells) in the computation.

193. The principle of these type of boundary changes while very simple to write is very complex to implement computationally.

Revised Leendertse Technique [36]

194. In order to aid the description of the revised land-water boundaries, a representation portion of the space staggered grid employed is shown in Figure IV-10.

195. The volume element associated with each grid cell  $j,k$  at time level  $n$  is defined as follows:

$$VOL_{j,k}^n = \left[ \eta_{j,k}^n + \frac{1}{4} (h_{j-1/2,k-1/2} + h_{j-1/2,k+1/2} + h_{j+1/2,k-1/2} + h_{j+1/2,k+1/2}) \right] \Delta x^2 \quad (1.9.1)$$

The cross section depth between grid cell  $j,k$  and  $j+1,k$  at time level  $n$  is given by the following relation:

$$TP_{j,k}^n = \frac{1}{2} \left( \eta_{j+1,k}^n + \eta_{j,k}^n + h_{j+1/2,k+1/2} + h_{j+1/2,k-1/2} \right) \quad (1.9.2)$$

The three cross section depths between grid cell  $j,k$  and the other three surrounding grid cells are defined similarly. The Chezy coefficient,  $C$ , which is computed at each water-level location, is used to designate whether a grid cell is wet or dry. A value of  $C = 0$  designates land, while a positive value signifies water.

196. There are two checks made to determine whether a grid cell that is currently wet should become dry. If after each calculation of the new water level a negative volume is obtained for the grid cell, then that cell is removed from the computation (made dry). This is performed by setting the Chezy coefficient to zero as well as the velocity components on each of the four cell faces. In order to include the influence of the new land point on the adjacent water levels and velocities, the previous row or column (note an ADI scheme is being employed) of recursion formulas, velocities, and water levels is recalculated with the point taken as dry. In addition, the calculation of all velocities and water levels along present row or column (row or column in which the grid cell became dry) are repeated before the computation proceeds to the next row or column. When a grid cell becomes dry, it is assumed that a

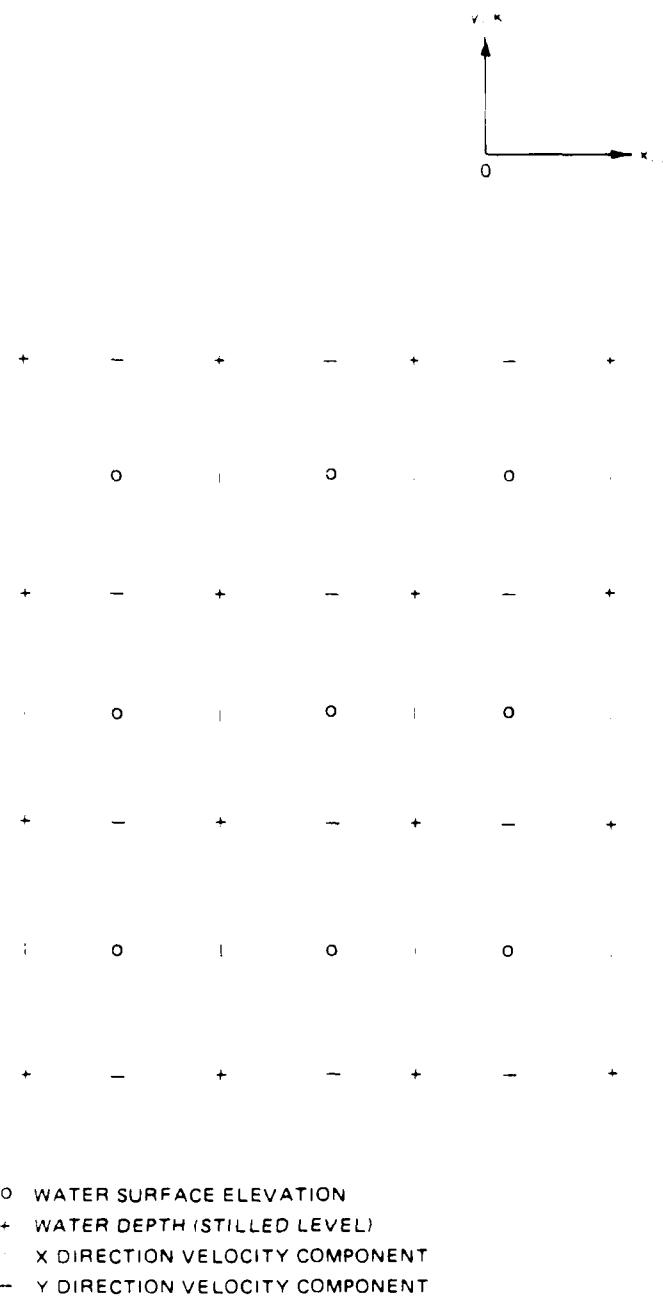


Figure IV-10. Representative Space Staggered Grid System



thin layer of water will remain on it. The depth of this water is set to the level calculated in the previous time step, since this calculation did not yield a negative volume element. The second check employs the cross section depth concept. If any one of the four cross section depths associated with a grid cell become negative, the grid cell is taken out of the computations; i.e., the  $U$  value at this grid cell is set to zero along with all cell face velocities.

197. Since a negative volume or negative cross section might be calculated at any point in time in the computation, the above two checks are made at each time step. Therefore discrete changes in the system boundaries can occur at each time step. In order to prevent the occurrence of a large number of changes in consecutive time steps, the following boundary change patterned after the original procedure is used.

198. If any of the four cross section depths associated with a grid cell become less than a positive preset value, then that grid point is taken out of the computation. Since a positive preset value is used, this condition is more restrictive than the above two checks. The water level is set at its current value and is maintained at this level until the point floods. By performing this more restrictive procedure at intervals larger than the time step, it is found that a large proportion of the boundary changes are made, while only a few changes occur because of negative volumes or cross section depths. Thus the effect of local discontinuities generated by discrete boundary changes is reduced.

199. The flooding procedure also was revised from the original method. For a dry grid cell each of the four surrounding grid cells are checked to see if they are wet. If one or more of the neighboring cells are wet, then the water levels of these grid cells are averaged. If this average water level is larger than the level retained on the dry grid cell, then this grid cell may be allowed to flood. A check is made on the cross section depth between the dry grid cell and each of the surrounding wet grid cells. If any of these cross sections are negative, the point remains dry. If all are positive, the grid cell is added back to the computational field. The water level is set at the value which was allowed to remain when the cell became dry. Note it appears that a cell must dry before it can flood; i.e., the tidal flat simulation is initiated at high tide. The check for flooding is also made at

intervals larger than the time step in order to reduce the discrete boundary change effects introduced by new flood cells.

#### Original Butler Technique [34]

200. In the development of the Waterways Implicit Flooding Model (WIFM), an alternating direction implicit solution technique has been employed. A cell face flag system has been developed in order to determine in each sweep where the computational line should begin and end. This cell face flag system is modified in the flood/dry procedure to designate the moving boundary. Once a cell face has been opened it may not be closed for a user specified number of time steps (greater than one). Similarly, if a face has been closed it may not be opened for a user specified number of time steps (greater than one). These procedures are similar to those developed by Leendertse [35,36] and tend to reduce the noise generated by discrete changes in the boundary affected by opening and closing cell faces.

201. Butler [34] has associated four cell face states. A face may be partially open, open, partially closed or closed. In the partially open state, a weir formula is used to effect a volume transfer between the adjoining cells. No cell face velocity is computed. In the open state, the appropriate momentum equation is used to determine the cell face velocity. In the partially closed state, a volume transfer concept based on a fraction of cell water depth is used to drain water between adjoining cells. No cell face velocity is computed. In the closed state, the cell face velocity is zero. Under this approach a cell face velocity is associated only when a cell face is open or closed.

202. As noted above, a cell face concept is used in implementing the computations. For a given cell  $(i,j)$ , a  $u$  face  $(i,j+1/2)$  and a  $v$  face  $(i+1/2,j)$  are designated in the code with the same  $(I,J)$  index. Thus one may associate each cell  $(I,J)$  with two faces. Butler [34] sets up a list of cells which may either flood or dry. In effect, these cells are used to identify the faces which may change state during the simulation.

203. The model user specifies the following variables to control the flood/dry operation:

EPSD  $\equiv$  minimum amount of water allowed on a cell in order for the cell to still be considered wet

(Note this corresponds to Leendertse's [35] small positive preset value)

XLAND  $\equiv$  an elevation such that if the bottom elevation of the cell is greater than XLAND, the cell will never flood

XSCOUR  $\equiv$  an elevation such that if the bottom elevation of the cell is smaller than XSCOUR, the cell will never dry

CD<sub>i</sub>, i=1,20  $\equiv$  weir coefficients for initial transfer of water onto a dry cell which is to become wet

CAYD<sub>i</sub>, i=1,20  $\equiv$  recession coefficients for draining flooded cells which will become dry

KS1  $\equiv$  minimum number of time steps to hold a cell face open which had previously been closed

KS2  $\equiv$  minimum number of time steps to hold a cell face closed which had previously been open

204. The implementation of the flood/dry procedures is effected in Subroutine FLOODY, which is called for each time step in the simulation. The general structure of this subroutine is shown in Table IV-6. Computations are first performed for the u cell faces and then for the v cell faces. The weir computations are order independent, since the elevations used do not account for cumulative modifications. The drain computations, however, are order dependent.

205. In analogy to the Leendertse [35,36] procedures, the cell Chezy C is set to zero for a flood cell, which has become dry. Alternatively, if a cell face is opened and constitutes one of the four sides of a given cell, then that cell is considered wet and assigned a positive Chezy C.

206. In general, the history of a cell face and the hydrodynamic computations are impossible to specify a priori. They are an extremely complex function of topography and storm characteristics. Instances may occur in which it becomes difficult to distinguish between the partially open and partially closed cell face states. In each case  $u_{n,m} = 0$ ,  $ICU_{n,m} = 50$ ; however, one must determine whether to use the drainage concept or the weir formulation. Within the drainage concept, water is transferred downhill as determined by topography and not water surface elevation. The user specifies recession coefficients as previously mentioned, which determine the fraction

Table IV-6  
Subroutine FLOODY General Structure

- 
- I. Flood/Dry Cell Face Logic
    - A. Examine u Cell Face State (try to open)
      - (i) Partially open--weir equation
      - (ii) Partially closed--drain
      - (iii) Completely open--momentum equation
    - B. Examine v Cell Face State (try to open)
      - (i) Partially open--weir equation
      - (ii) Partially closed--drain
      - (iii) Completely open--momentum equation
    - C. Examine u Cell face State (try to close)
      - (i) Partially closed--drain
      - (ii) Close--set face velocity to zero
    - D. Examine v Cell Face State (try to close)
      - (i) Partially closed--drain
      - (ii) Closed--set face velocity to zero
  - II. Perform Flood/Dry Cell Chezy C Check
  - III. Update Surface Elevations
-

of the "uphill" water depth to transfer. In general, the characterization of flooding and drying may be controlled by the user through the specification of KSI , KSJ , EPSD , and the CAYD array. The user also has some control over the drainage through the specification of the bottom elevation of each cell in the flood plain.

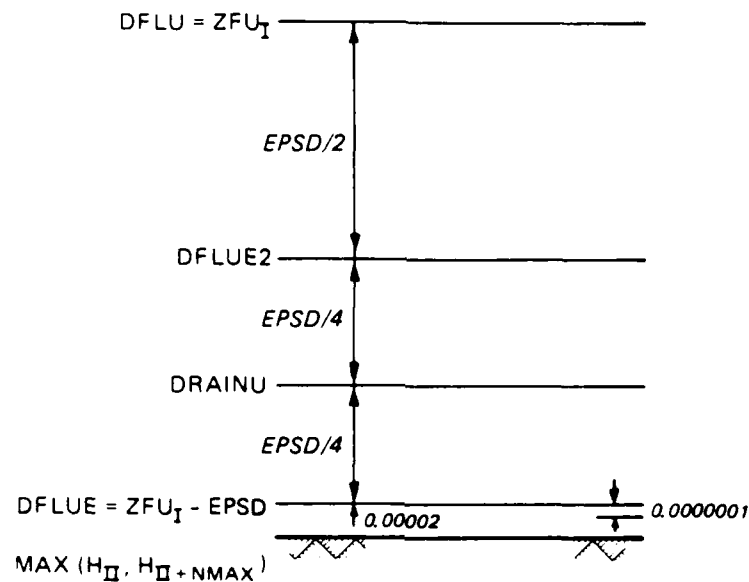
Revised Technique by Butler and Prater [37]

207. In conjunction with a surge study for the southern shore of Long Island, the flooding and drying methods have been substantially revised. The major modifications are listed in Table IV-7 below. Elevation variables instrumented in the computations have been revised as shown in Figure IV-11.

Table IV-7  
WIFM Flood/Dry Modifications

- 
- I. The face states are redefined as follows:
    - IPS, JPS = 0  $\equiv$  Cell vulnerable to a change in state
    - IPS, JPS = 1  $\equiv$  Partially open (weir equation)
    - IPS, JPS = 2  $\equiv$  Partially closed (drainage relations)
  - II. The weir relations are now used to assign a cell face velocity. This velocity is limited by assuming ( $\partial u / \partial t = -g \partial h / \partial x$  or  $\partial v / \partial t = -g \partial h / \partial y$ ); weir relations are now cumulative.
  - III. The drainage relations are modified to drain based upon water surface as opposed to bottom cell elevations. A drainage equalization check is also made.
  - IV. All water surface elevation adjustments are accumulated (cumulative) as they are performed. Therefore the cell face computations are no longer order independent. Thus in alternate time steps u faces are considered before v faces. In addition the order of the potential flood/dry cells is reversed sequentially.
-

PART a: FACE OPENING LOGIC



PART b: FACE DRAINING LOGIC

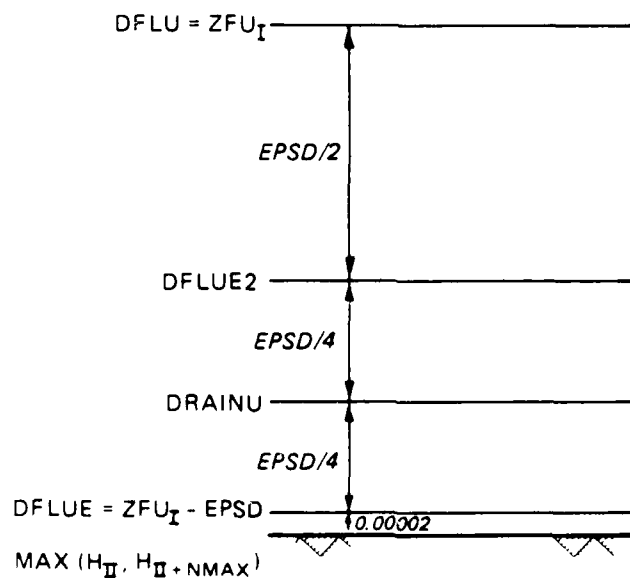


Figure IV-11. Revised elevation concepts (Continued)

PART c: FACE CLOSING LOGIC

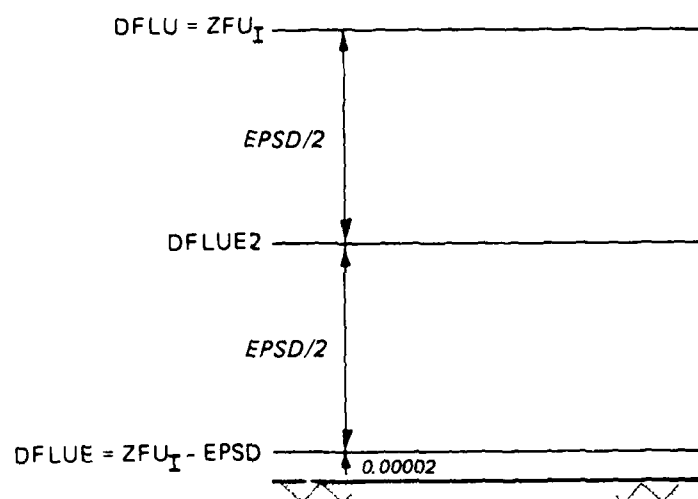


Figure IV-11 (Concluded)

208. The general nature of the computations is similar to the original procedures. These procedures are subject to user control through the specification of KS1 , KS2 , CD , CAYD , and EPSD .

209. Butler [34,37] is the first investigator to our knowledge to have employed a drainage concept. The CAYD array controls the fraction of the water depth to be transferred in one time step and is somewhat empirical in nature. Several investigators [28,39] have used the weir equation to initially transfer water onto a dry cell. This mechanism is used to establish sufficient water on a dry cell in a mass conservative manner, such that the momentum equation may be solved.

210. Both the original and revised flood/dry procedures are extremely complex. It is indeed difficult to account for all flooding and drying possibilities.

#### Lake Okeechobee Study Procedures

211. Since the computations are identical for the u and v cell faces, the detailed description will be presented only for the u cell face. Within the DO 45 Loop in Subroutine DIGEST, the water surface elevations for all three time levels are initialized to the cell bottom elevation. Within the DO 450 Loop in Subroutine DIGEST a flood elevation range is established for each cell face of each potential flood/dry cell as follows:

$$DFLU = ZFU_I = \max(H_{II}, H_{II+NMAX}) + EPSD + 0.2$$

$$DFLV = ZFV_I = \max(H_{II}, H_{II+1}) + EPSD + 0.2$$

$$DFLUF = DFLU - EPSD = \max(H_{II}, H_{II+JMAX}) + 0.2$$

$$DFLVE = DFLV - EPSD = \max(H_{II}, H_{II+1}) + 0.2$$

where

DFLU = Upper u face elevation level for flooding/drying

DFLV = Upper v face elevation level for flooding/drying



DFLUE  $\equiv$  Lower u face elevation level for flooding/drying

DFLVE  $\equiv$  Lower v face elevation level for flooding/drying

Note an offset of 0.2 feet has been used with respect to the cell bottom elevation.

212. The cell face states are saved in variable IPS for the u face and JPS for the v face. These variables are initialized to zero and are updated at the end of each pass through Subroutine FLOODY. In addition, a cell face counter (IQU for the u face and IQV for the v face) is initialized to zero and updated at the end of each pass through the routine as well. These two variables are packed as shown in Table IV-8 in integer variables IFLOD<sub>I</sub> and IPAS<sub>I</sub>, where I=1, KFT, the number of flood/dry cells.

Table IV-8  
Flood/Dry Logic Control Variables

$$\text{IFLOD}_I = \text{IFL} + (10^9) \text{IQU} + (10^6) \text{IQV}$$

$\uparrow$  u cell face counter  
 $\uparrow$  v cell face counter

$$\text{IFL} = 1000 * N + M$$

$\nwarrow$   $\nearrow$   
 Grid cell indices

$$\text{IPAS}_I = (10^1) \text{IPS} + \text{JPS}$$

$\uparrow$  u face status indicator       $\uparrow$  v face status indicator

213. Three distinct cell face states are distinguished:

IPS = 0      Cell face fully open or initially closed

IPS = 1      Cell face partially open one side

IPS = 2      Cell face partially open both sides

ISP = 3      Cell face closed after being fully open

214. The u-face opening logic proceeds as follows:

1. Do not attempt to open a cell-face previously closed, unless it has been closed for KSI time steps. Define  $T1 = r_{n,m}^{k+1}$  and  $T2 = r_{n,m+1}^{k+1}$ .
2. For  $T1$  and  $T2 > DFLUE$ ,  $IPS = 2$ , perform the procedures shown in Table IV-9.
3. For either  $T1$  or  $T2 > DFLUE$ ,  $IPS = 1$ , perform the following procedure; illustrated for the case  $T1 > DFLUE$ .

$$Q = \min \left[ C_d (T1 - DFLUE)^{1/2}, (\mu_1)_m (\Delta \alpha_1)^2 (\mu_1)_{m+1} |T1 - T2| / \tau \Delta \alpha ((\mu_1)_m + (\mu_1)_{m+1}) \right]$$

$$\Delta n_1 = -Q \tau / (\mu_1)_m \Delta \alpha_1$$

$$\Delta n_2 = Q \tau / (\mu_1)_{m+1} \Delta \alpha_1$$

$$r_{n,m}^{k+1} = r_{n,m}^{k+1} + \Delta n_1$$

$$r_{n,m+1}^{k+1} = r_{n,m+1}^{k+1} + \Delta n_2$$

Analogous procedures hold for the case  $T2 > DFLUE$ .

4. If  $T1$  and  $T2 < DFLUE$ , consider the next flood cell face.

215. Cell face conditions are then examined for closing. The u-face closing logic proceeds as follows:

1. With  $T1$  and  $T2$  defined as previously, if  $T1$  and  $T2 > DFLU - EPSD/2$ , consider the next flood cell face.
2. If  $T1$  or  $T2$  or both are less than  $DFLU - EPSD/2$ , consider the cell face.

$$ICU_{II} = 50$$

↑  
n,m

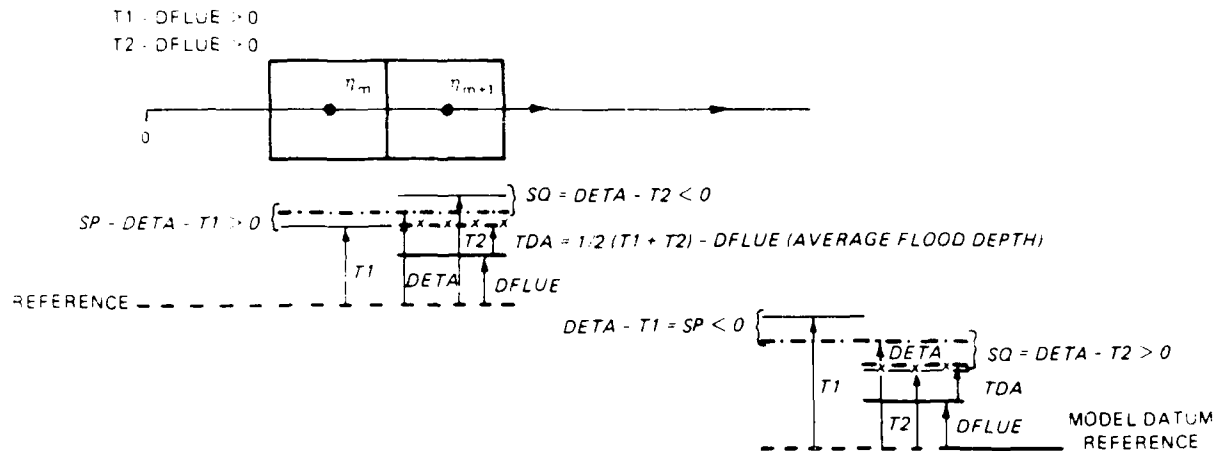
$$UP_{II} = 0$$

↑  
n,m

$$IQU = 1$$

$$IPS = 3$$

Table IV-9  
U-Face Opening Two-Sided Procedure



$$d_1 = \Delta \alpha_1 (u_1)_m, \quad d_2 = \Delta \alpha_1 (u_1)_{m+1}$$

$$DETA = d_n = \frac{d_1 T1 + d_2 T2}{d_1 + d_2}$$

$$SP = d_1 - T1 < 0, \quad SQ = d_n - T2 > 0$$

$$TDA = \frac{(T1 + T2)}{2} - DFLUE$$

$$Q = \min \left\{ d (TDA)^{3/2}, (u_1)_m (\Delta \alpha_1)^2 (u_1)_{m+1} |T1 - T2| / \tau \Delta \alpha_1 [(u_1)_m + (u_1)_{m+1}] \right\}$$

$$T12 = T1 - T2 \quad \text{If } T12 = 0 \text{ consider the next flood cell face.}$$

(Continued)

(Sheet 1 of 3)

Table IV-9 (Continued)

$T12 < 0$	$T12 > 0$
$d_{r2} = -Q\tau/d_2 < 0$	$d_{r1} = -Q\tau/d_1 < 0$
If $d_{r2} < SQ$ , then use SP and SQ as computed above for corrections. If $d_{r2} > SQ$ , compute	If $d_{r1} < SP$ , then use SP and SQ as computed above for corrections. If $d_{r1} > SP$ , compute
$d_{r1} = -d_{r2} * d_2/d_1$	$d_{r2} = -d_{r1} * d_1/d_2$
Set $SP + d_{r1}$	
$SQ + d_{r2}$	

IF  $(SP + T1) \leq H_{II}$  consider next flood cell face; i.e., do not allow negative water depth for cell II.

IF  $(SQ + T2) \leq H_{MM1}$  consider next flood cell face; i.e., do not allow negative water depth for cell MM1.

Else,  $SEM_{II} = SP + SEM_{II}$   
 $SEM_{MM1} = SQ + SEM_{II}$  } Note corrections are cumulative

IPS = 1 (Cell starting to open)

Next compute cell face velocity:

$$Q' = \frac{-0.5g\tau}{(u_1)_{m+1/2}} \left( \tau_{n,m+1}^{k+1} + \tau_{n,m+1}^k - \tau_{n,m}^{k+1} - \tau_{n,m}^k \right)$$

$$DPTH = \max \left[ 0.5 \left( \tau_{n,m+1}^k - h_{n,m+1} + \tau_{n,m}^k - h_{n,m} \right), EPSD2 \right]$$

(Continued)

(Sheet 2 of 3)

Table IV-9 (Concluded)

$$Q' = DPTH * (U_{II} + Q')$$

If  $|Q'| > Q$ , then  $Q = \text{sign}(a, Q')$

$$UP_{II} = Q/DPTH$$

<p>If <math>(SP + T1) &lt; H_{II} + EPSD</math>  <math>(SQ + T2) &lt; H_{MM1} + EPSD</math></p>	}	Consider next flood cell face
---	---	-------------------------------

Else, set cell to fully open (normal) status

$$ICU_{II} = 60$$

$$IQU = 1, \quad IPS = 0$$

216. As in the revised technique of Butler and Prater [37], all water surface elevation adjustments are accumulated. Therefore, the cell face computations are order dependent. Thus in alternate time steps  $u$  faces are considered before  $v$  faces and vice versa. In addition, the order of the potential flood/dry cell list is reversed each time step. The drainage concept has been eliminated in the interest of computational economy. In addition, only cell face closing are considered for both  $u$  and  $v$  faces each time step as indicated as follows:

Odd Time Step Number:

$u$  face opening

$u$  face closing

$v$  face closing

Even Time Step Number:

$v$  face opening

$v$  face closing

$u$  face closing

217. If during the computations in Subroutine MOIN a negative water depth is encountered in a flood/dry cell, this cell is immediately removed from the computation by setting its Chezy  $C$  and all three time levels of its water cell face velocities to zero. In addition, all three time levels of water surface elevation are set equal to the cell bottom elevation. The amount of water at time level  $k-1$  is accumulated and distributed equally over all wet cells not on the boundary as an adjustment on most recently computed water surface elevation. A critical Courant number is computed and output to indicate potential difficulty. Within Subroutine UPDATE, it is possible to add  $WPSD2$  feet of water to non-flood cells which develop negative water depth. If this occurs for several cells, then  $DSCOUR$  needs to be further decreased in order to include these cells as flood cells.

Development of the numerical implementation of the short wave equation

218. The short wave equations (2.1.6-2.1.7 of Part III and 2.2.1 and 2.2.2 of Part III) require the specification of a fetch length and average water depth. In hurricane events which pass over Lake Okeechobee, the lake windfields are highly curved. The following approach was developed to develop

an effective fetch in such cases. In addition, the dynamic land/water boundary must be taken into account in order to develop fetch lengths. It is assumed that the tree islands or other subgrid barriers do not influence the windfield sufficiently to be taken into account in the fetch determination procedure as outlined below.

- a. Compute ZTRY(J,I) array for J = 1 , NLAX , and I = 1 , MLAX over the uniform hurricane auxiliary grid. If ZTRY(J,I) is greater than or equal to 0.5 cell (J,I) is considered dry.

- b. Define the following eight ordered direction pairs:

Octant No:	1	2	3	4	5	6	7	8
IXKS	1	1	0	-1	-1	-1	0	1
IYKS	0	1	1	1	0	-1	-1	-1

- c. Wave calculations are performed along all hydrodynamic grid faces along the levee. The effective depth used in the wave equations is taken as the water depth at that time in the cell of the WIFM grid. Since grid cells are on the order of 0.35 square miles in size, and the wave height may be depth limited, this procedure is considered acceptable. It may be desirable to consider the effect of alternative depth considerations.

- d. In order to integrate the fetch calculation procedures with the ZTRY array logic, it is necessary to transform the locations of levee subgrid barriers on the WIFM hydrodynamic grid to the uniform hurricane auxiliary grid. Consider a levee section transformed to cell (J\*, I\*) on this uniform grid. The fetch, F , is computed as follows:

(1) Set F = 0 .

(2) Determine the direction octant number from which the wind is blowing.

(3) Determine the appropriate direction order pair IXKS\* , IYKS\* .

(4) Compute a fetch length scale,  $\Delta S_F$  , where

$$\Delta S_F = \sqrt{(IXKS^*)^2 + (IYKS^*)^2} \Delta S$$

and  $\Delta S$  is the uniform grid spacing.

(5) F = I $\Delta S_F$  , where I is such that

$$ZTRY(J^* + iIYKS^* , I^* + iIXKS^*) < 0.5$$

for  $1 \leq i \leq I$  and

$$ZTRY(J^* + (I + 1)IYKS^* , I^* + (I + 1)IXKS^*) \geq 0.5$$

219. The fetch is considered zero if the wind magnitude is zero. The implementation of the runup and overtopping computational procedures were essentially performed by Mr. David L. Leenknecht, while he was at the New Orleans District. Several curves were computerized as shown in the Table IV-10. The wave computations are performed every KSl time steps. In present applications, KSl = 12 corresponding to a 1 hr interval for a hydrodynamic time step of 300 seconds. Wave overtopping volumes are not written on the disc transfer file for input to the Link-Node drainage model in the present model version. However, these volumes are computed and are written on the output file.

Table IV-10  
Wave Computation Routines

<u>Subroutine or Function Name</u>	<u>Purpose</u>	<u>Technical Source*</u>
Function Eq. 8	Eq. 8 Fig. 20	TP-78-2 Stoa [32]
Function Fig. 75	Figure 7-5	SPM [27]
Function Eq. 7	Overtopping equation	J. R. Weggel [33]
Function Fig. 50	Figure 50	TP-78-2 Stoa [32]
Function Eq. 79	Overtopping equation	J. R. Weggel [33]
Subroutine RUNUP	Figure 6, Pg. 25	TP-78-2 Stoa [32]
Function Fig. 74	Figure 7-4	SPM [27]
Function Fig. 75	Figure 5	TP-78-2 Stoa [32]

220. The major computational routines comprising the model and their purpose are as follows:

- a. Subroutine WAVES---Shallow water model driving routine
- b. Subroutine SWAVEL---Shallow water wave height and period
  - (i) CETN - I - 6 [28]
  - (ii) CW-167 Curves [31]
- c. Subroutine WAVEL---Newton-Raphson determination of the shallow water wave length



d. Subrouting DEEP---Determination of the shoaling factor and deepwater wave height and length

211. The incorporation of short wave computations directly within the long-wave model represents an extension over previously employed methods. Within the federally supported flood insurance studies, short wave maximum heights were computed ipso facto after the long wave peak surge values were known. The fetch determination procedures as well as the wind magnitude were not as accurate as the methods developed here for Lake Okeechobee.

## PART V: SEICHE CALIBRATION AND VERIFICATION OF THE LONG WAVE MODEL

### Global grid development

222. In order to study long-wave phenomena on Lake Okeechobee, it is necessary to construct a grid on which the hydrodynamic computations are carried out. The resolution of the grid determines the time step and the number of cells over which computations are performed. In order to forecast hurricane phenomena for various possible storm intensities and tracks, it is necessary to construct a grid such that simulations on the order of 24-36 hours not be cost prohibitive. For this purpose, a  $64 \times 48$  (3072 cell) grid was constructed as shown in Figure V-1. The grid spacing is uniform in the horizontal and variable in the vertical with larger spacings in the center of the lake, where less resolution is required. Each direction is mapped independently using a time sharing code (Program MAPIT); the results are shown in Table A-1 (Appendix A).

223. The maximum spatial resolution is 3333.3 ft. For a gravity wave speed of approximately 20 fps, an explicit time step of 180 seconds is more than adequate. In the alternating direction implicit scheme employed, a time step of 360 seconds is used corresponding to a Courant number of two.

224. The geometrical and topographic characteristics of the Lake Okeechobee system are resolved on the global grid developed above. Jacksonville District (SAJ) personnel digitized the topography as shown in Table A-2 employing nautical chart 11428, 18th Edition, Aug. 23/80. All land elevations are with respect to mean sea level and are shown as positive numbers. At the outermost boundary of the grid an arbitrary elevation of 59 feet was specified. This elevation is such that no water elevation will exceed it even in worst case hurricane simulations; thus, all water will be contained on the computational grid. Water depths are specified with respect to a datum plane located 12.5 ft above mean sea level and are preceded by a minus sign. The model datum plane is taken as the depth datum plane. The levee system and tree islands are specified as barriers occupying a complete side of a grid cell. Their geometrical and physical characteristics were provided by SAJ and are presented in Tables A-3 and A-4, respectively. The general configuration of the levees and Tree Islands are shown in Figure V-2. Gage locations where water surface elevation data are available are also as indicated in Figure V-2 and Table A-5.

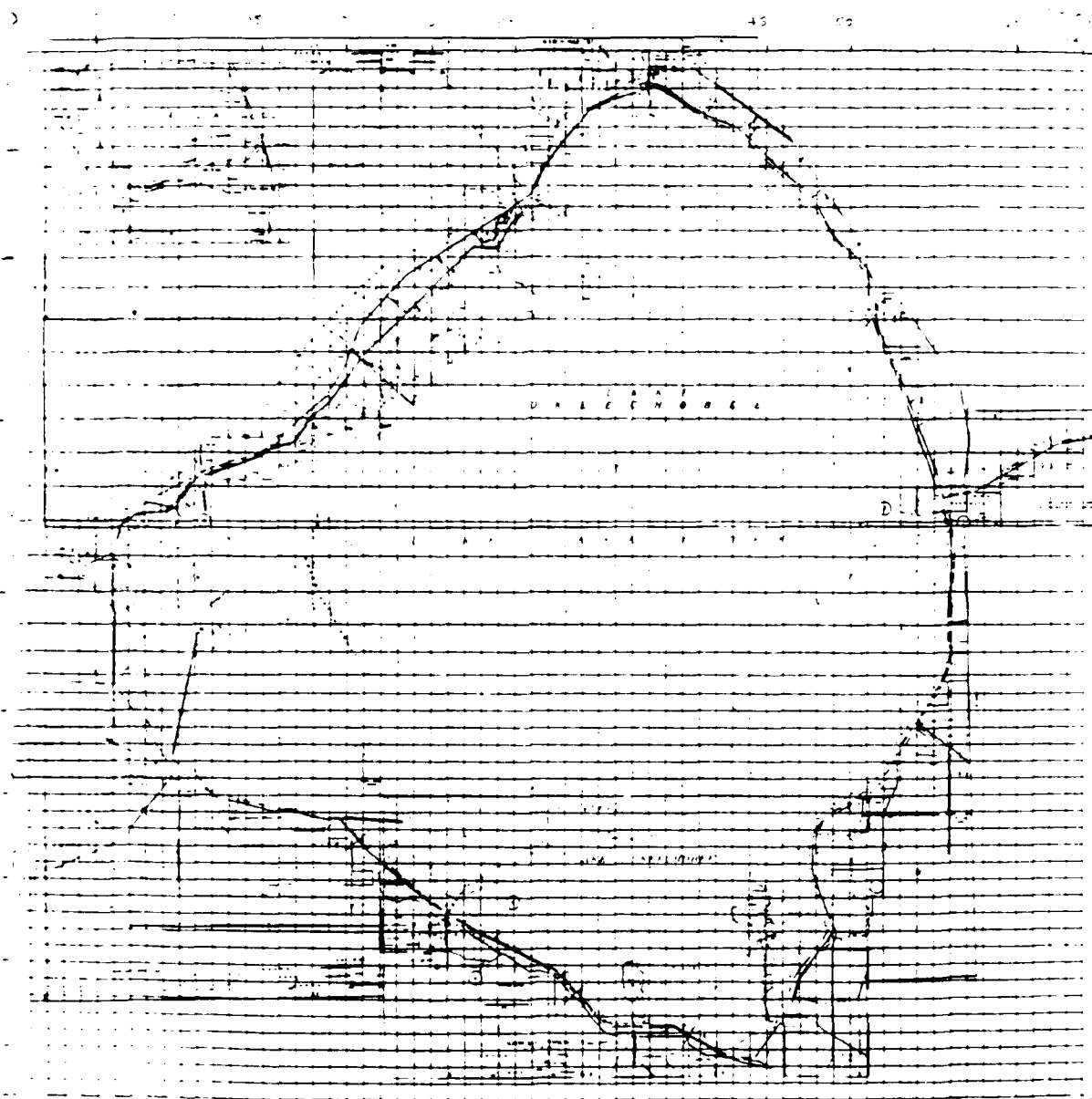
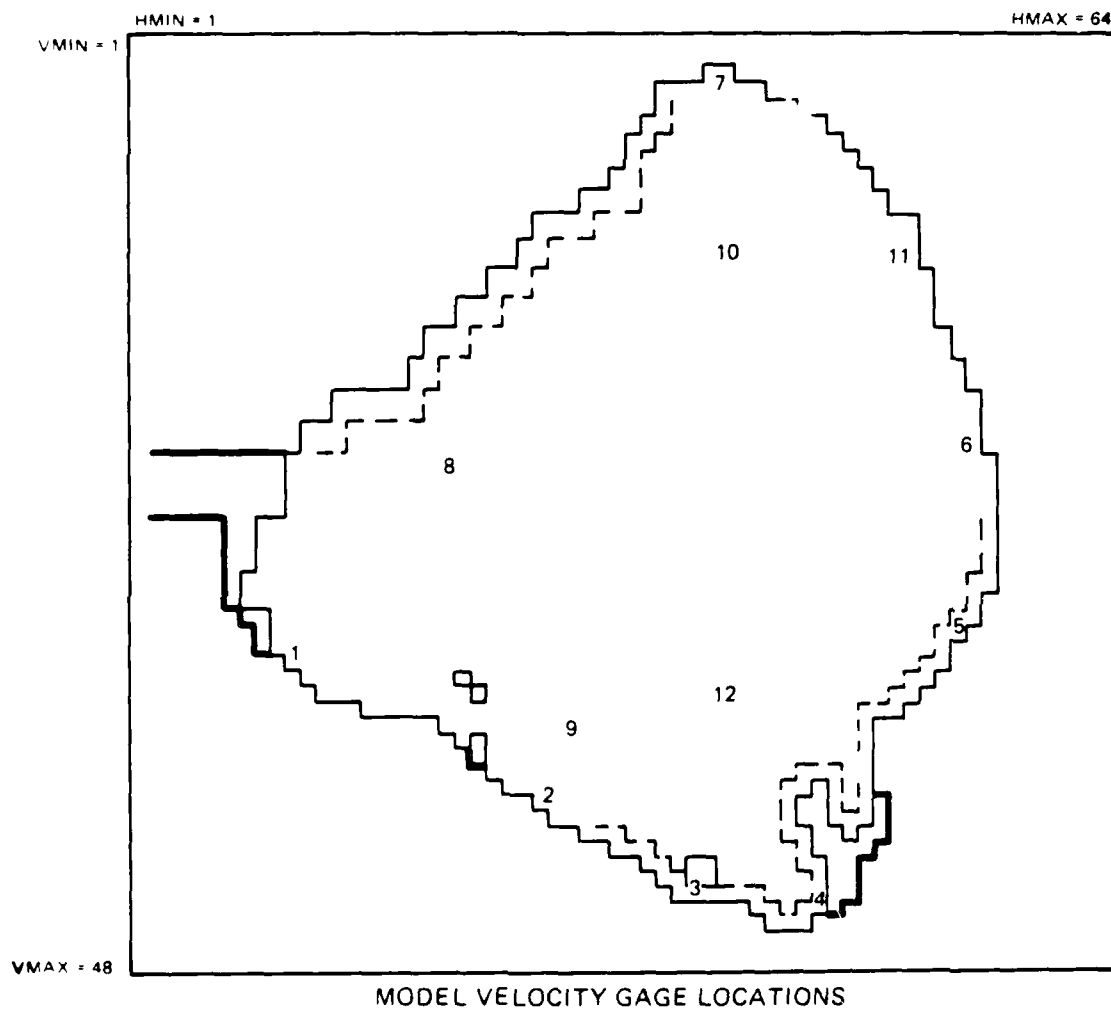


Figure V-1. Global Hydrodynamic Grid



LEGEND

- TREE ISLAND
- LEVEE NOT CORRESPONDING TO THE SHORELINE
- SHORELINE
- GAGE # LOCATION (SEE TABLE IV)

Figure V-2. General Levee and Tree Island Configuration

### Seiche Phenomena

225. Consider a spatially uniform wind acting over the lake for a given period of time. The wind exerts a surface stress on the water in the direction of the wind. During the seiche generation phase, the water sets up on the downwind side of the lake and sets down in the upwind side of the lake. If the wind remains constant for a sufficiently long period of time, a so-called static wind tide is established. The term "static" is used to denote a condition in which all transient water level fluctuations due to the time variation and start-up of the wind have been damped out by the lake frictional mechanisms.

226. During the seiche decay phase, the wind approaches zero and the static water level surface oscillates until the lake frictional mechanism removes all the potential energy associated with the initial water surface displacement.

227. This hypothetical seiche phenomena is sketched in Figure V-3. In actuality, the wind in the seiche generation phase may not be spatially uniform and the wind magnitude may not remain constant for a sufficiently long period of time to develop a static wind tide. During the seiche decay phase, the wind magnitude will usually be low but not completely zero.

228. Consider the physical mechanisms occurring in each phase of the seiche. In the generation phase, the wind exerts a surface stress on the water. The bottom stress is also in the wind direction; i.e., in the same direction as the surface stress due to the return flow (flow reversal) at the bottom. In a two-dimensional vertically integrated model, the return flow phenomena cannot be simulated. The velocity is integrated over the vertical to produce an average velocity. The bottom stress occurs in the direction opposite to the averaged velocity vector. During the static tide phase, the surface wind force is balanced by the pressure gradient forces and the velocity in the water body approaches zero; therefore, there are no bottom stresses. During the decay phase, the wind surface stress approaches zero; the pressure gradient force supplies the energy to move the water; and, this energy is dissipated by the bottom stress.

229. In order to calibrate the bottom stress, it is necessary to simulate the seiche decay phase, since it represents the only surface stress acting on the water body. In order to calibrate the wind surface stress, it

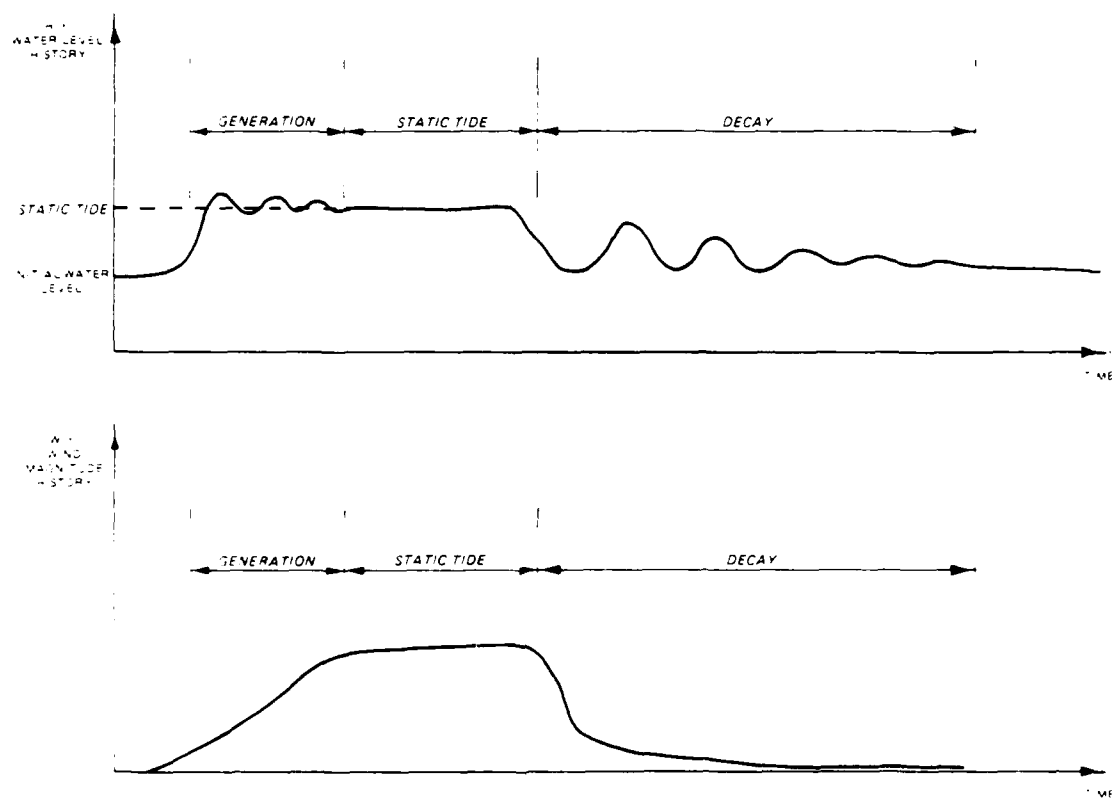


Figure V-3. Hypothetical Seiche Phenomena

is necessary to simulate the static tide case, since then the only surface stress applied to the water body is due to the wind. Once both the bottom friction and surface wind stresses have been calibrated, it should be possible theoretically to simulate the complete seiche (generation static tide, and decay phase). However, in practice, the difference between the static tide level and the initial water surface at a given gaging station is approximately .5 feet. In addition, the initial water surface elevations at any given time are not equal at all gaging stations. The vertical control was accomplished through first order leveling and is probably accurate to .1 feet. The specification of the initial water surface is further complicated by the availability of data at only 6-7 stations. The above constraints make it extremely difficult to simulate the complete seiche. As a result, the work presented here focuses on the seiche decay phase and the calibration and verification of the bottom friction mechanics. The August 12-13, 1968 seiche was used to calibrate the bottom friction mechanics, while the August 20-21, 1964 seiche was used to verify the calibrated friction. These two periods were considered by Whitaker and Reid [40] in their numerical study of Lake Okeechobee and were selected so that the results of the present study could be compared with this previous work.

#### August 12-13, 1968 seiche calibration

230. Wind and stage data were obtained from the Jacksonville District at the locations shown in Table A-6. Measured water surface elevations at MGS-2 and HGS-6 are shown in Figure V-4. The period from 2000 HRS on August 12 through 1200 HRS on August 13 was simulated. This period corresponded to the seiche decay phase. The wind data are presented in Table A-7. As noted from Table A-7, all wind magnitudes are less than 5 mph except for a few readings at Port Mayaca. Water surface elevation characteristics are given in Table A-8. Average station water surface elevations are within a .1 feet except at LS-12, which appears to be .1-.2 feet high. Recorded lake station elevations correspond extremely well with the outside gage readings at all stations over the measured period. Gage timing information is shown in Table A-9. All recorded timings are within 1-2 hours over a period of approximately one month.

231. In order to account for vegetation effects, the following effective bottom friction mechanism is calibrated:

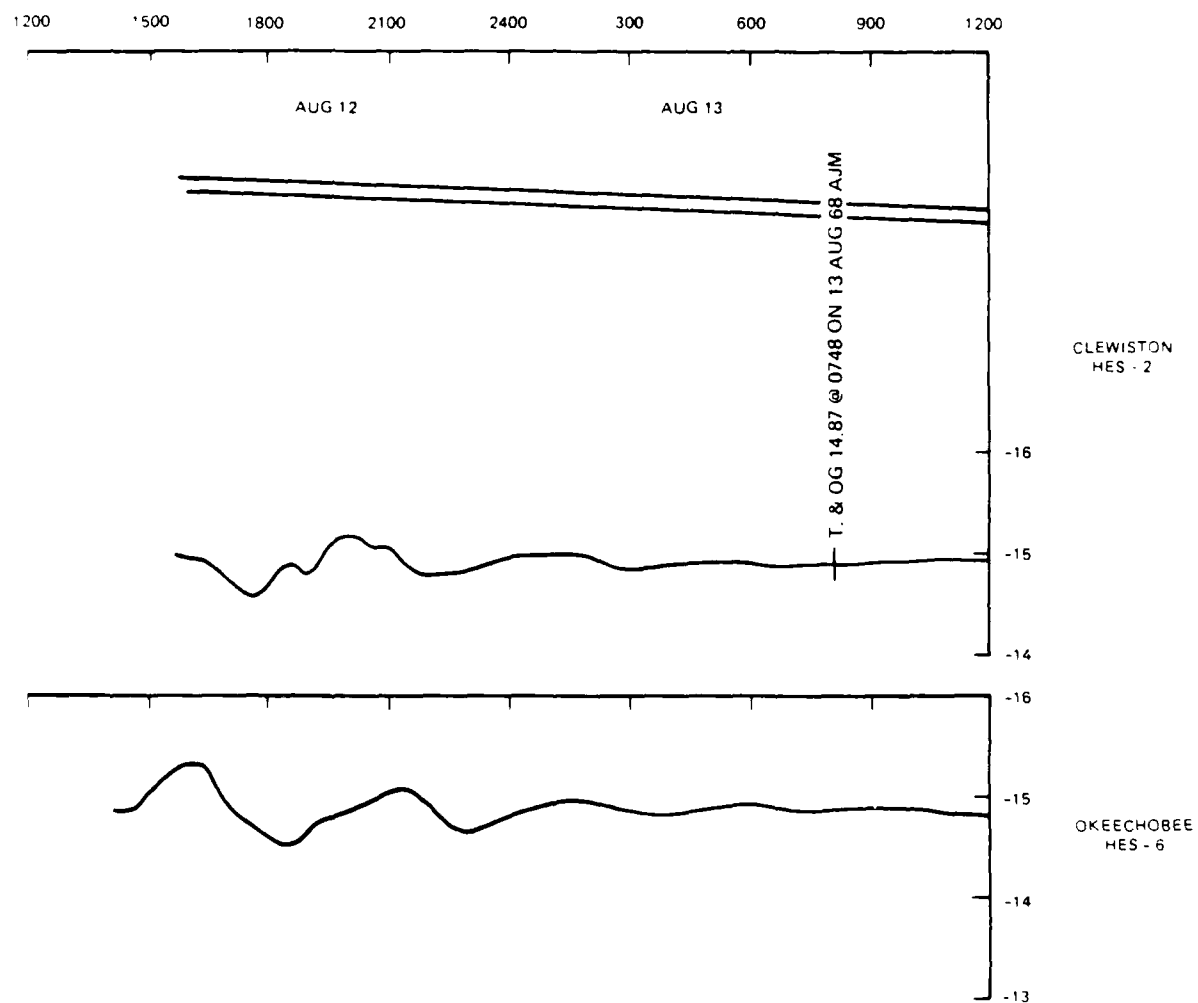


Figure V-4. Aug 12-13, 1968 Seiche Hydrographs



$$n^* = \begin{cases} n_d \left( 1 + cd_1 e^{-d/cd_2} \right) & d < d_{can} \\ n & d \geq d_{can} \end{cases}$$

where

$n^*$  = effective Manning's  $n$  roughness

$n_d$  = Manning's  $n$  dependent upon water depth with respect to model datum,  $d$

$cd_1$  = Canopy coefficient 1 with respect to water depth  $d$

$cd_2$  = Canopy coefficient 2 with respect to water depth  $d$

$d_{can}$  = Canopy friction depth

The relations given in Table A-10 were calibrated. The factor  $(1 + cd_1 e^{-d/cd_2})$  is evaluated in Table A-11 for various values of depth less than or equal to the canopy friction depth.

232. In order to illustrate the friction specification, consider water cell (33, 33). From Table A-2, the water depth with respect to model datum is eight feet. Consulting the friction versus depth relationship table, we note eight feet is in depth range 4, and  $n_d = .018$ . From the next table, the canopy multiplication factor for 8 feet equals 1.5413. Therefore, the effective roughness  $n^*$  for cell (33, 33), equals  $(1.5413) \times .018 = .0277$ . This value is used throughout the course of the simulation, due to the fact the water depth remains essentially constant in seiche computations.

233. In order to specify initial conditions, the following approach was used. All velocities were assumed equal to zero. The initial water surface as shown in Table A-12 was developed by employing Subrouting TILT as documented in Appendix D. For the August 12-13, 1968 Seiche, a plane was used to specify the initial water surface. The plane passed through the Clewiston HGS-2 recorded level (15.20 ft) and through the Okeschobee HGS-6 recorded level (14.52 ft) at 2000 HRS on 12 August. No lateral tilt was used. The measured data at half hour intervals are shown in Table A-13 from 2000 HRS 12 measured levels in Plates B-1 through B-7 (Appendix B).

In interpreting, the ordinate 0.00 NGVD corresponds to 15.0 ft MSL. In the top half of the Plates, the simulated levels not including the tree islands are shown. Simulation results including the tree islands are

shown in the lower half of the plates for the sake of comparison. At most stations, the tree islands appear to exert a very small influence on the water levels during the seiche. Simulated water levels correspond well with measured levels at all stations except LS-12. As noted from Table A-8, the mean at LS-12 is .1-.2 ft higher than at all other stations. This suggests that there may be a geodetic leveling problem at LS-12 of .1-.2 feet; i.e., it may be appropriate to subtract .1-.2 feet from the recorded level at LS-12. If this is done, the simulated levels would match the adjusted levels very closely at LS-12.

#### August 20-21, 1964 seiche verification

235. Wind and stage data were obtained from the Jacksonville District at the locations shown in Table A-13. Measured water surface levels at HGS-2 and HGS-6 are shown in Figure V-5 in order to illustrate the seiche phenomena. The period from 1730 HRS on August 20 through 0900 HRS on August 21 was simulated. As may be determined from the wind data presented in Table A-14, this corresponded to the seiche decay phase. All wind magnitudes are less than 5 mph throughout most of the period at all gages except for a few hours at Port Mayaca. Water surface elevation characteristics are given in Table A-15. Average station water surface elevations are within .1 foot except at HGS-2 and LS-16. LS-16 appears to be .05-.1 feet high. Recorded lake station elevations correspond extremely well with the outside gage readings at all stations over the measured period. Gage timing information is shown in Table A-16. HGS-2 and HGS-6 were reset prior to the simulated seiche and should be extremely accurate timewise. LS-14 and 16 exhibited fairly substantial (4.5-5.5 hrs) timing errors in contrast to the Port Mayaca .5 hr error over a one month period.

236. The effective bottom friction mechanism in Equation (2.1.1) and the depth versus friction range relation in Table A-10, and the canopy coefficients in Table A-11, were used in the simulation. The initial water surface was specified as a skewed parabola as outlined in Appendix B with no lateral tilt passing through the points shown in Table A-17. The measured data at half hour intervals are shown in Table A-18 from 1730 HRS 20 August to 0900 HRS 21 August. Simulated water levels are compared versus measured levels in Figures A-1 through A-16. In interpreting the estimates, 1.0 HGVD corresponds to 1.0 ft above the datum. In Figure A-16, the simulated levels not

1200 1500 1600 2100 2400 0300 0600 0900 1200

OKEECHOBEE  
HGS-6

14  
13  
12

1

Figure 11. Aug. 1-5, 1964, etche hydrographs

including the tree islands are shown. Simulation results including the tree islands are shown in the lower half of the plates for the sake of comparison. At the majority of the stations, the tree island appear to exert a very small influence on the shape of hydrographs. Simulated water levels correspond well with measured levels at all stations except at LS-16. As noted from Table A-15, a geodetic leveling problem at LS-16 on the order of .1 feet may be indicated. If .1 feet is subtracted from the recorded levels at LS-16, the simulated levels would more nearly correspond to these adjusted levels.

## PART VI: AUGUST 1949 HURRICANE

### General Storm Characteristics

237. The August 26-27, 1949, hurricane was used to verify the previously calibrated bottom friction relationships developed in the seiche work presented in Part V. Two separate hurricane models were used to develop 10-meter 10-minute average sustained overwater windspeeds for use in the hydrodynamic sub-model. The Powell wind stress formula [23] was used to compute surface wind stress in the hydrodynamic sub-model from the 10-meter 10-minute average windfields. The overwater windfields were reduced over Lake Okeechobee dynamically based upon land/water boundaries developed in the hydrodynamic simulation.

238. Initially results are presented for the two hurricane sub-models in terms of 10-meter 10-minute average overwater winds. The August 26-27, 1949 hurricane with a maximum central pressure intensity of 1.8 in Hg represents the most severe storm to have influenced Lake Okeechobee for which measured water level, wind and pressure data are available. Therefore, in a study of wind generated water levels on the lake, this storm must be considered. The track of the storm is shown in Figure VI-1. As may be observed the storm passed directly over the northern section of the lake. Due to the counterclockwise circulation around the low pressure center and the track, wind directions shift dramatically from out of the North to out of the South during the course of the storm.

### Hurricane sub-model simulation results (SPH and PBL)

239. In both hurricane simulations, the position of the storm is as given in Table A-1 in hours after the initial position corresponding to 0000 Greenwich mean time on August 26, 1949. Thirty-one hours of windfield information is computed employing five snapshots. Snapshot data employed in the SPH hurricane simulation are presented in Table A-20. Snapshot windfield results are presented in Plates B-13 through B-17 in graphical form. The entire spatial windfield is presented and centered with respect to the eye in these figures. Observe the inflow angle is constant at each radial distance.

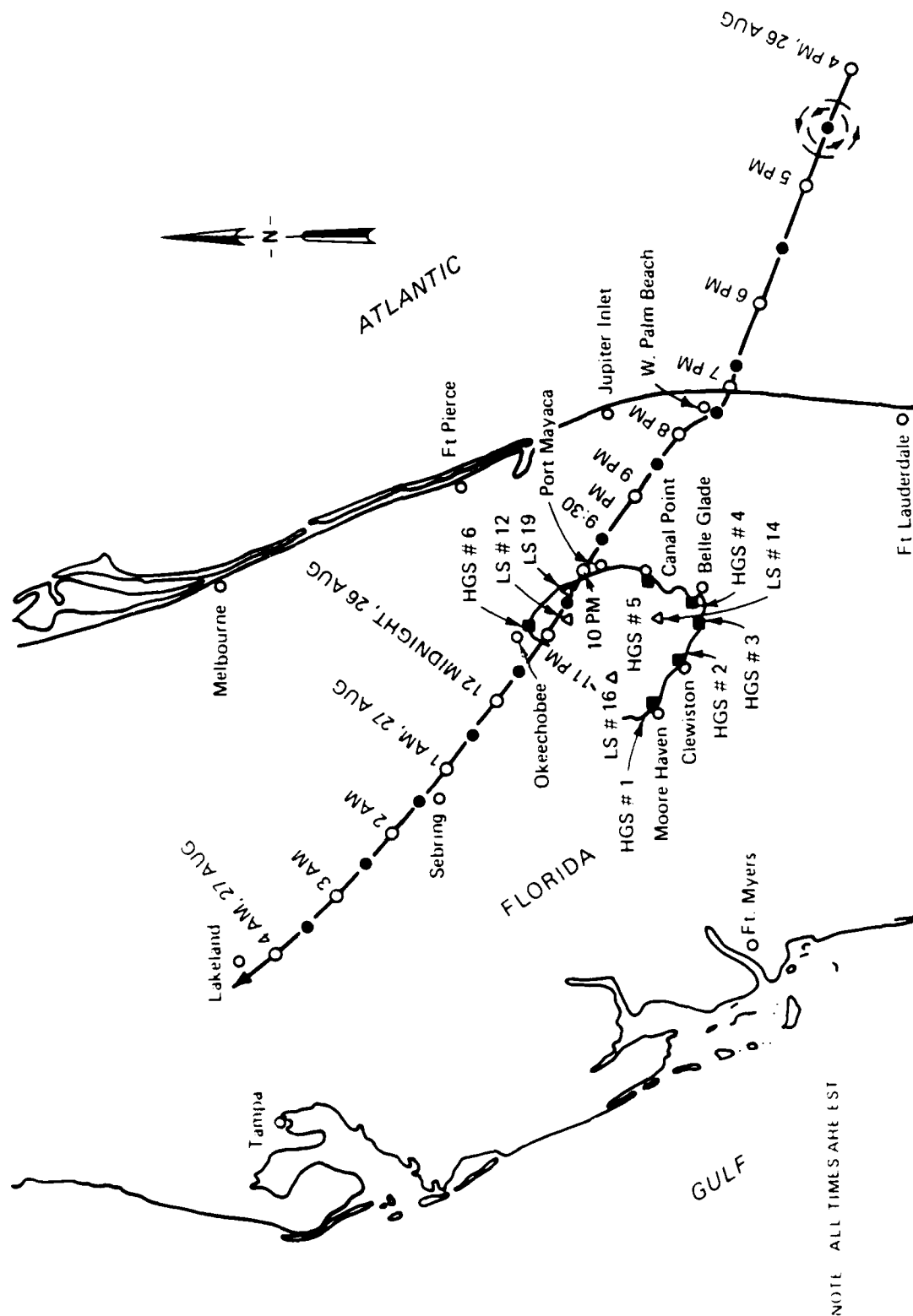


Figure VI-1. August 1949 Hurricane Track

240. The isovel patterns are shown in Plates B-18 through B-22 for each corresponding snapshot. The wind structure only on the first two inner most grids of the five level nest is shown in these figures. Single digit numbers represent isovel contours at a factor of ten in knots. Snapshot data employed in the PBL hurricane simulation are shown in Table A-21. Note the data correspond to those employed in the SPH simulation with the exception of the steering flow. Steering flow is not used directly in the SPH simulation. In the PBL simulation, a shearing flow of 9 meters/sec is specified in the direction of storm motion. This represents a typical value for storms in this region. Snapshot windfield results are presented in Plates B-23 through B-27 in graphical form in the same format as for the corresponding SPH results. Observe the inflow angle is computed dynamically in the PBL simulation and is no longer constant at each radial distance. Isovel patterns are given in SPH corresponding format in Plates B-28 through B-32 for the PBL simulation. The resulting structure is quite different than the SPH result. Maximum gradient winds (kts) and maximum and PBL simulations in Table A-22 for each snapshot. PBL simulations results are generally 3-8 knots less than SPH maximum wind results.

241. Since the land/water boundary influences the reduction factor array to adjust the 10-m 10-minute average windfield, which in turn drives the hydrodynamics determining the land/water boundary, in effect a dynamic feedback loop is being simulated. It is necessary then to consider the hydrodynamic/windfield computations as a coupled system.

242. Results for the windfield solution and pressure field at gage locations shown in Figure VI-2 are presented in Plates B-33 through B-46 for the PBL simulation and in Plates B-47 through B-60 for the SPH simulation. The double hat windspeed distributions computed at HGS-6, Port Mayaca, LS-12, and LS-19 are in agreement with observed profiles shown in CW-167 [31]. The central pressure distributions are the same in both SPH and PBL simulations and correspond to the Schloemer profile. The spatial structure of the windfield in the vicinity of Lake Okeechobee is shown in Plates B-61 through B-68 for the PBL and in Plates B-69 through B-76 for the SPH simulation. Observe how the windfield increases overwater. At simulation time 17 hours corresponding to 2300 HRS EST on 26 August, the placement of the eye in the northeastermost corner of the lake is excellent agreement with placement

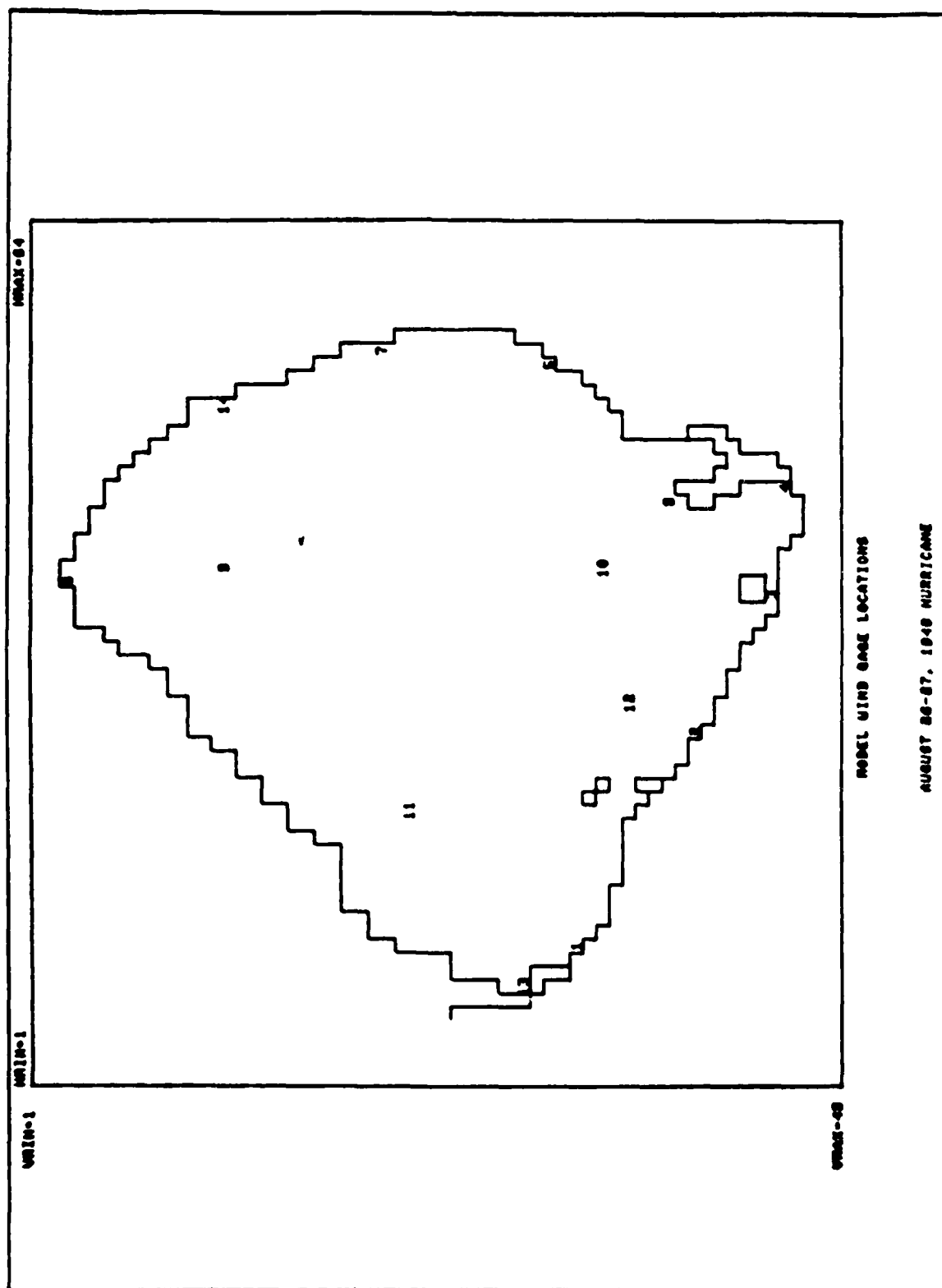


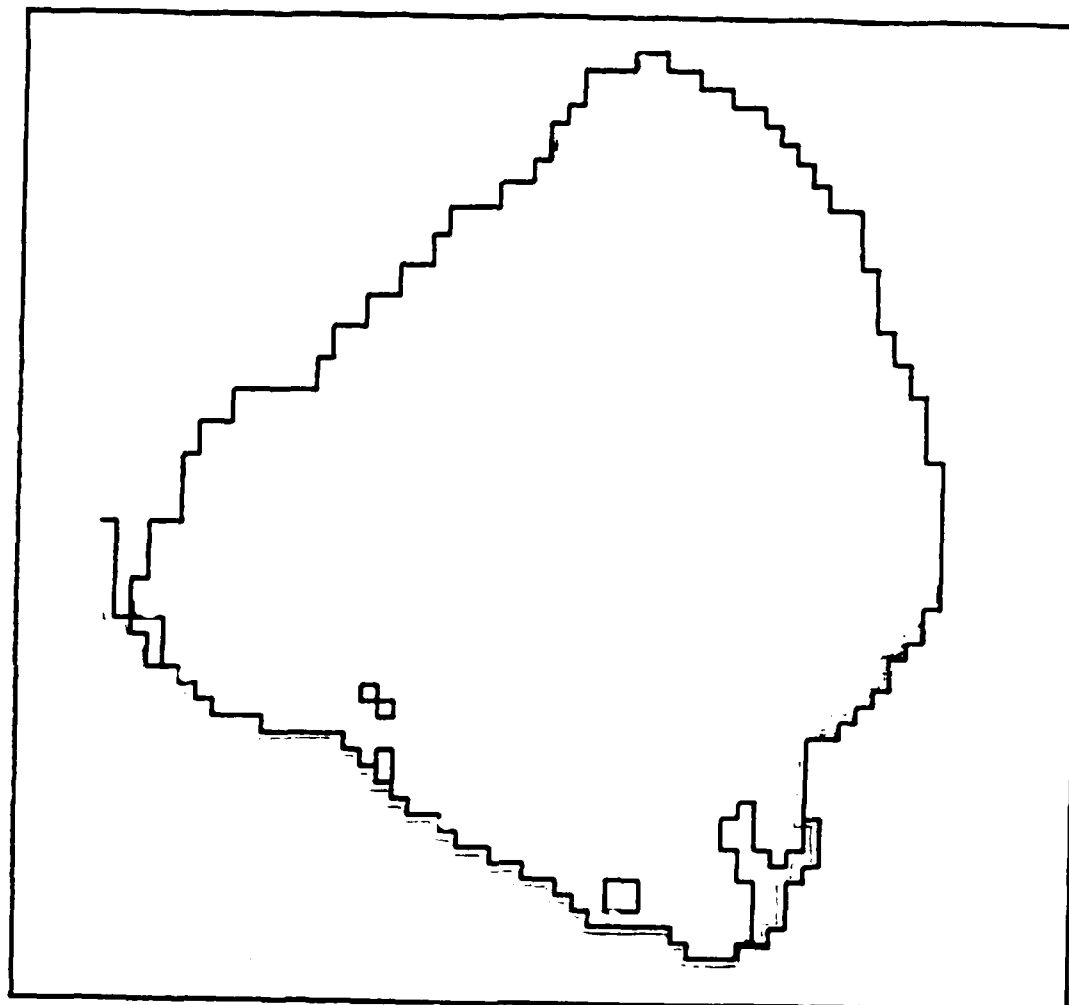
Figure VI-2.



data shown in CW-167 [31]. Note the general wind direction and structure are similar except near the eye of the storm. Hourly predicted windspeed and direction data for both PBL and SPH simulations are compared versus measured data in Table A-23. For the first 8-9 hours PBL and SPH winds are in close agreement. However from hour 14 through 22 SPH winds are as much as 20-25 kts stronger at some gage locations. Near the end of the storm, results are in closer agreement. This suggests that in the near eye region the general structure of the windfields are considerably different but are essentially the same in the storm regions greater than two to three radii to maximum winds. Actual hydrodynamic results are presented in turn for each hurricane simulation.

PBL hydrodynamic  
sub-model simulation results

243. A period of 28 hours starting at 0600 HRS EST on 26 August 1949 was simulated using a time step of 150 seconds. Convective acceleration terms were considered in the middle of the lake. The previously presented PBL windfield and Schloemer pressure field were used to derive the hydrodynamics. No inflows or rainfall were considered. The levee configuration for the August 1949 hurricane is presented in Figure VI-3. Simulated water level histories are compared with observed water level histories in Plates B-77 through B-85. All elevations in Plates B-77 through B-85 are with respect to an initial lake level of 14.0 ft msl (plot zero). Simulated levels are in reasonably good agreement with observed levels except at HGS-5, HGS-6, and LS-16. The simulated level at HGS-6 (Okeechobee) is approximately 4 feet below the observed level. The timing of the simulated peaks and troughs in water level records is generally in close agreement with the observed data. This fact substantiates the general storm track and windfield structure produced by the PBL simulation. Simulated current histories (vertically integrated) are shown in Plates B-86 through B-92. General current structure over the entire lake is represented in Plates B-93 through B-100. Maximum current magnitude is on the order of 3.0-4.0 ft/s. Simulated significant wave heights and periods are compared with data in Table A-24. Maximum simulated significant wave heights are on the order of 2.0 feet with corresponding periods of approximately 4.5 seconds. Maximum still water levels are presented in Table A-25. Boxed cells represent flooded areas. Areal extent of simulated flooded areas is in agreement with data presented in CW-167 [31]. Minimum stilled water depths



AUGUST 26-27, 1949 HURRICANE

Figure VI-3.

are shown in Table A-26. Boxed cells represent areas initially wet, which dried sometime during the simulation. A minimum depth of 1 foot or less was used as the demarcation. The areal extent of exposed areas shown is in general agreement with data presented in CW-167 [31].

SPH hydrodynamic  
sub-model simulation results

2.4. The same 28 hour period was simulated employing a time step of 150 seconds. The previously presented SPH windfield and Schloemer pressure field were used to drive the hydrodynamics. No inflows or rainfall were considered. Simulated water level histories with respect to an initial lake level of 14.0 ft msl (plot zero) are compared with observed level histories in Plates B-101 through B-109. Simulated waterlevels exceed measured water levels in the south-western section of the lake and are in good agreement with observed levels in the other lake sections. At HGS-6 (Okeechobee) the simulated peak is approximately 1.5 feet less than the observed maximum. Rainfall is estimated to account for approximately .5 foot of this difference. The timing of the simulated peaks and troughs in water level histories is in agreement with observed data. The general storm track and windfield structure produced by the SPH simulation is thereby substantiated. Simulated vertically integrated currents are shown in Plates B-110 through B-116. Global current structure is presented in Plates B-117 through B-124. Maximum current magnitude is on the order of 4.5 fps. Simulated significant wave heights and periods are compared with measured data in Table A-27. Maximum simulated significant wave heights are approximately 6 feet with periods of approximately 10 seconds. Maximum surge levels are presented in Table A-28. Boxed cells represent flooded areas. Areal extent of simulated flood areas corresponds to data in CW-167 [31]. Minimum stilled water depths are shown in Table A-29. Boxed cells represent areas initially wet, which dried sometime during the simulation. A minimum depth of 1 foot was used to define these areas. The areal extent of exposed areas is in general agreement with CW-167 [31] data.

Comparison of PBL and SPH  
hydrodynamic simulation results

2.5. SPH simulated water levels exceed PBL levels at all gage stations. SPH results correspond closer to measured results in the south and north-

eastern sections of the lake. PBL results correspond closer to measured results in the southwestern section of the lake. Wave heights and periods are larger for the SPH simulation than these produced in the PBL simulation. As may be noted by comparing Table A-25 and A-26 with Tables A-28 and A-29, areas of inundation and exposure are larger in areal extent in the SPH simulation. All of these results are a direct consequence of the near eye structure of the two windfields. As previously noted, the near eye structure is quite different and SPH wind velocities exceed PBL velocities by as much as 20 knots in magnitude. Directional characteristics are generally the same, however may differ by up to 25-30°.

246. It is a difficult task in general to simulate the overwater windfield over Lake Okeechobee for the August 1949 hurricane due to eye pressure adjustments to land and subsequent readjustments to water and then readjustments to land. It appears based upon these two simulations that the major unknown and source of discrepancy between measured and simulated water level fluctuations is the windfield itself.

247. In order to observe the magnitude of this discrepancy in general, two additional storms are considered in turn in subsequent parts.

## PART VII: OCTOBER 1950 HURRICANE

### General storm characteristics

248. The October 17-18, 1950 (King) Hurricane was considered to further verify the forecasting/hindcasting capability of the complete modeling system. The SPH hurricane model formulation was used to produce 10-meter 10-minute average sustained overwater windspeeds to drive the hydrodynamic model. The overwater windfields were reduced over Lake Okeechobee dynamically based upon land/water boundaries developed in the hydrodynamic simulation.

249. The October 17-18, 1950 (King) Hurricane possessed a maximum central pressure depression of 1.74 in Hg while off the Florida coast. The radius of the storm was only 6 nm and the forward speed ranged from 8.9 to 12.7 kts. The storm track is presented in Figure VII-1. As may be observed, the storm passed directly over Lake Okeechobee entering east of Clewiston and exiting west of Okeechobee. The position of the storm is given in Table VII-1 in hours after the initial position corresponding to 2300 HRS Greenwich Mean Time on October 17, 1950.

### SPH hurricane sub-model simulation results

250. Twenty-four hours of windfield information is computed employing three snapshots. Snapshot data employed in the SPH hurricane simulation are presented in Table VII-2. Snapshot windfield results are presented in Plates B-125 through B-127 in graphical form. The entire spatial windfield is presented and centered with respect to the eye in these figures. Observe the inflow angle is constant at each radial distance. The isovel patterns are shown in Plates B-128 through B-130 for each corresponding snapshot. The wind structure is shown only on the first two innermost grids of the five level nest. Single digit numbers represent isovel contours at a factor of ten in knots.

251. Recalling the land/water boundary and the windfield over the lake interior is a dynamic feedback system, consider results for the windfield solution and pressure field at gage locations shown in Figure VI-2 as presented in Plates B-131 through B-144. The spatial structure of the winds over Lake Okeechobee is presented in Plates B-145 through B-150. Note the winds increase overwater as they feel the influence of the lake. Computed and observed winds are compared in Table A-30 for snapshot times in Table VII-2.

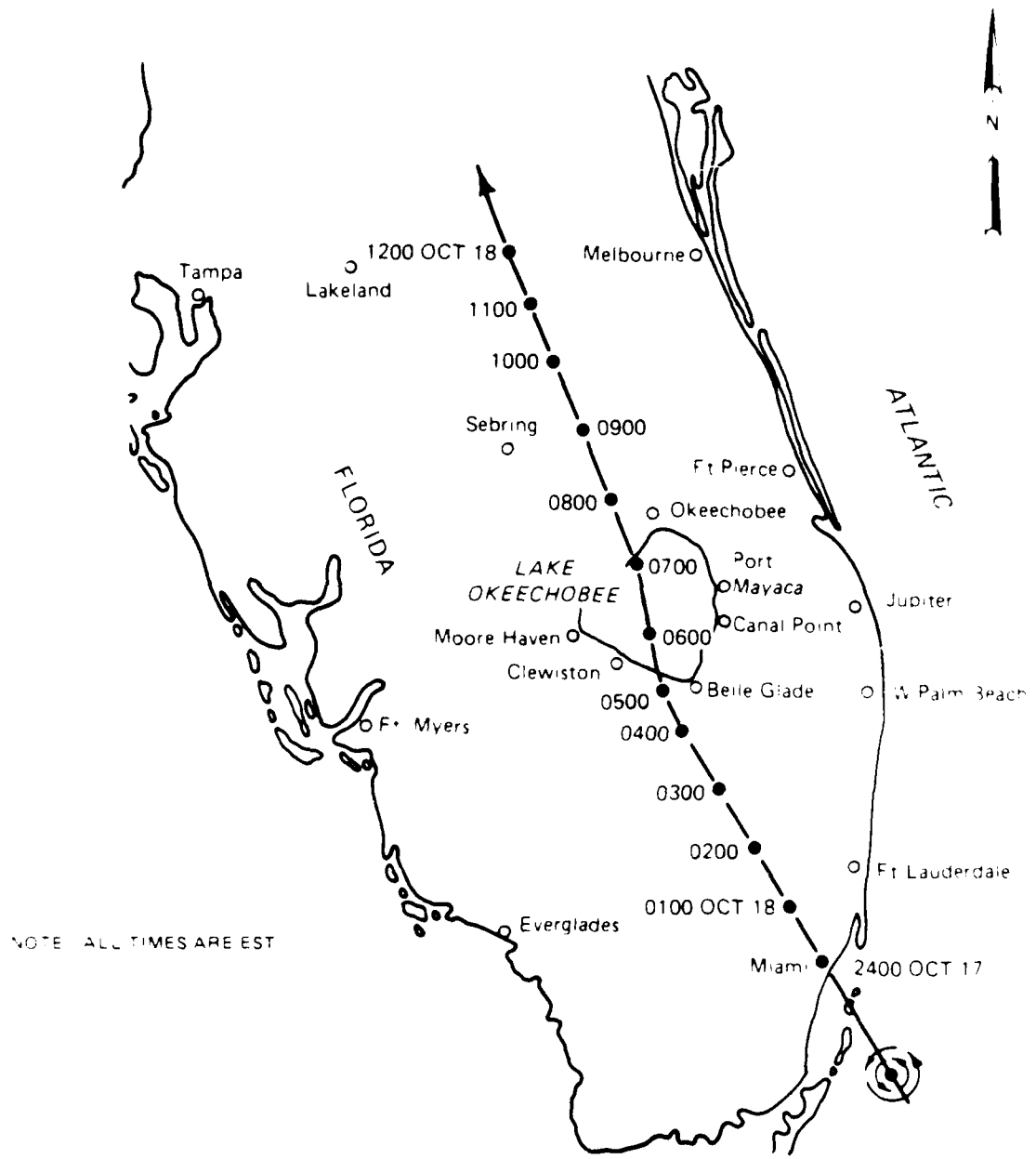


Figure VII-1. October 17-18, 1950 (King) Hurricane Track

Table VII-1  
October 1950 (Day 17 Hour 23 GMT) Position Data

<u>Time</u>	<u>Latitude (oN)</u>	<u>Longitude (oW)</u>
0.	24.56	84.10
1.	24.7	84.1
6.	25.8	84.11
11.	26.67	84.14
12.	26.83	84.14
13.	27.07	84.14
24.	29.75	84.17

Table VII-2  
October 1950 (Day 17 Hour 23 GMT) Snapshot Data

<u>Time</u>	<u>Inflow Angle (o)</u>	<u>Bearing of Maximum Winds (o)</u>	<u>Radius nm</u>	<u>Forward speed Kts</u>	<u>Far Field Pressure mb</u>	<u>Central Pressure mb</u>	<u>Storm Surge ft</u>
0.	10.	82.	5.	11.7	1011.	1005.	1.0
11.	10.	75.	5.	11.7	1011.	1005.	1.0
24.	10.	75.	5.	11.7	1011.	1005.	1.0

Computed wind characteristics are in general agreement with measured values at most locations.

SPH hydrodynamic sub-model simulation results

252. A period of 23.5 hours starting at 1800 HRS EST on 17 October 1950 was simulated using a time step of 150 seconds. Convective acceleration terms were considered in the middle of the lake. The previously presented SPH wind-field and the Schloemer pressure field were used to provide meteorological

the water level configuration was simulated for the area. Simulated water level contours (1 ft intervals) (plot area) are shown in Plates B-151 through B-163. The simulated water level is in agreement with observed levels at the station at Newiston. Simulated water level contours are shown in Plates B-164 through B-170. The simulated water level is approximately 4.0 fps. The general water level configuration is presented in Plates B-171 through B-180. The water level is in the corresponding overlake area. The water level is shown in Plates B-150, respectively. The water level is in the current structure. Simulated water level contours are compared with measured data in Plate B-181. The water level represents the single shoreline wave. The water level heights are less than 2.0 ft with periods of 10 to 20 seconds. Significant flooding occurred during the October 1963 storm and Terry Islands remained dry.



AD-A178 103

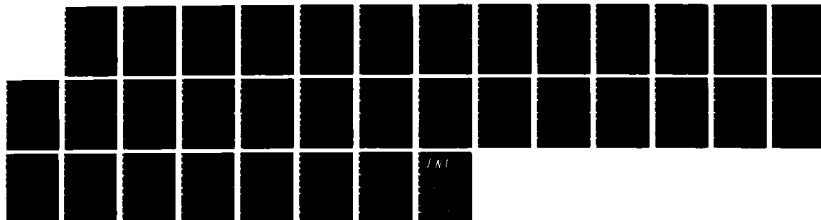
A NUMERICAL INVESTIGATION OF HURRICANE INDUCED WATER  
LEVEL FLUCTUATIONS I. (U) COASTAL ENGINEERING RESEARCH  
CENTER VICKSBURG MS R A SCHMAIZ JUN 86 CERC-MP-86-12

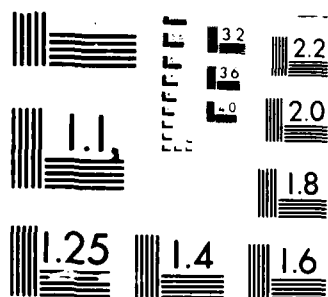
3/3

UNCLASSIFIED

F/G 8/8

NL





MICROCOPY RESOLUTION TEST CHART  
NATIONAL BUREAU OF STANDARDS-1963-A

## PART VIII: SEPTEMBER 1979 HURRICANE

### General storm characteristics

253. The September 3-4, 1979 (Hurricane David) was considered in order to further test the hindcasting capability of the total modeling system under the present levee configuration. The SPH hurricane model formulation was used again to produce 10-meter 10-minute average sustained overwater windspeeds.

254. The September 3-4, 1979 (Hurricane David) possessed a maximum central depression of 1.18 in Hg while paralleling the east coast of Florida. The storm radius was 12 nm with a forward speed of 10 knots. The storm track is presented in Figure VIII-1. The storm paralleled the east coast of Florida eventually making landfall near Savannah, Georgia. The position of the storm is given in Table VIII-1 in hours after the initial position corresponding to 0400 HRS Greenwich Mean Time on September 3, 1979.

### SPH hurricane sub-model simulation results

Thirty-six hours of windfield information is computed using one snapshot, whose characteristics are presented in Table VIII-2. Snapshot windfield results are shown in Plate B-77 in graphical form, with constant inflow angle centered about the eye. The corresponding isovel pattern is shown in Plate B-78 in previous format. Single digit numbers represent isovel contours at a factor of ten in knots.

255. Noting the land/water boundary and the windfield interact as a dynamic feedback system, consider results of the windfield solution and pressure field at gage locations shown in Figure VI-2 as presented in Plates B-79 through B-92. The spatial structure of the overlake winds is presented in Plates B-93 through B-99. Note the winds increase overwater. Computed and observed winds are compared at Okeechobee in Table A-32 for windfield structure times. Computed winds are somewhat less than observed winds. In reference to Table VIII-2, for a central pressure deficit of 40 mb the SPH winds are a maximum of 67 knots, which is less than the 85 knot maximum winds shown in Figure VIII-1 in the vicinity of the lake.

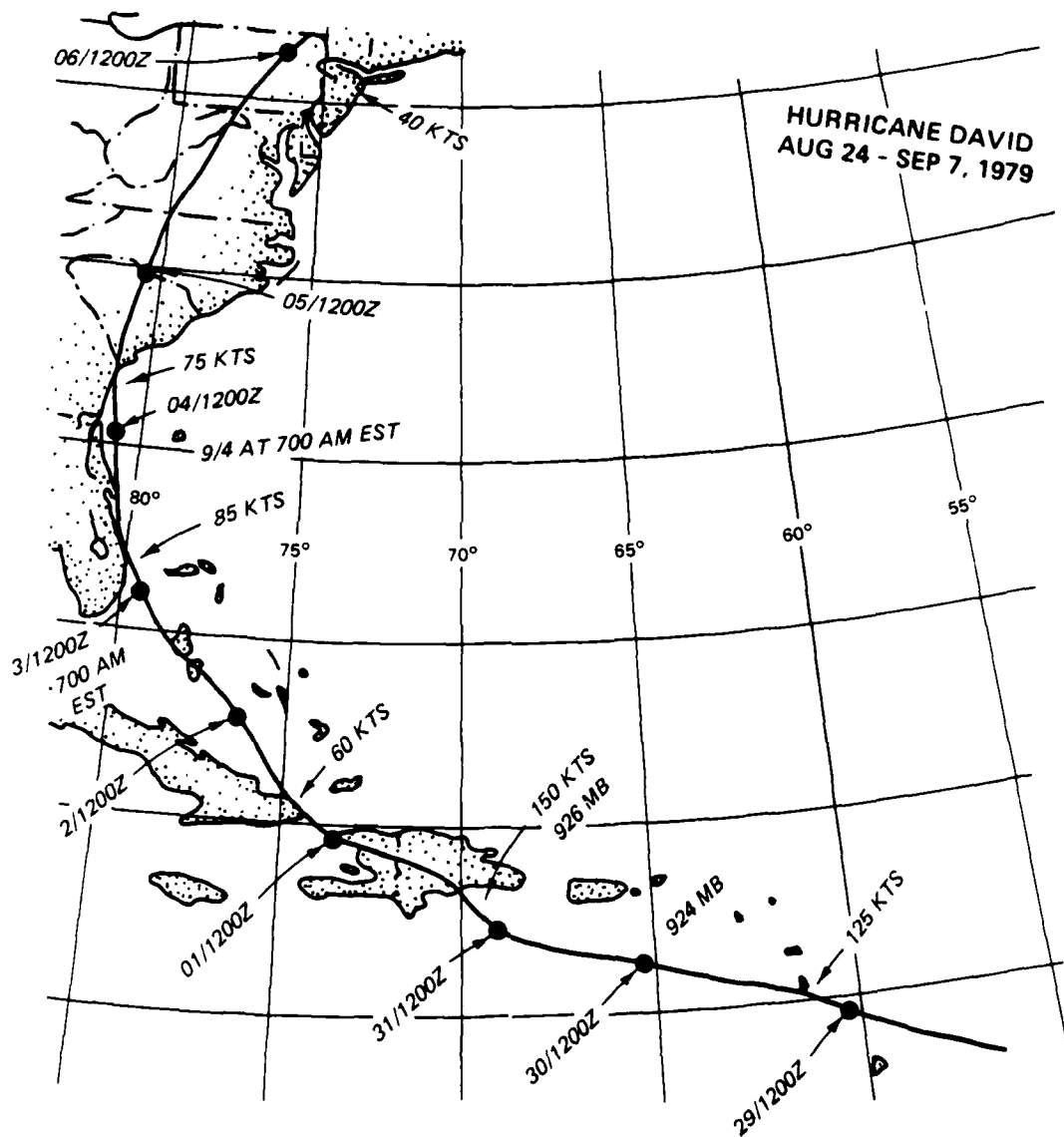


Figure VIII-1. Hurricane David Storm Track

Table VIII-1  
Hurricane David (Day 3 Hour 4 GMT) Position Data

<u>Time</u>	<u>Latitude (oN)</u>	<u>Longitude (oW)</u>
0.	25.	78.9
2.	25.3	79.1
8.	26.3	79.6
14.	27.2	80.2
20.	28.	80.5
26.	29.1	80.8
32.	30.2	80.9
36.	31.1	81.1

Table VIII-2  
September 1979 (Day 3 Hour 4 GMT) Snapshot Data

<u>Time</u>	<u>Inflow Angle (o)</u>	<u>Bearing of Locus of Maximum Winds (o)</u>	<u>Radius (nm)</u>	<u>Forward Speed (kts)</u>	<u>Far Field Pressure (mb)</u>	<u>Central Pressure (mb)</u>	<u>Storm Compass Bearing (o)</u>
14.	10.	69.	12.	10.	1013.	973.	323.

Reduction Factor of .865 used to compute 10 meter 10-minute average overwater winds

SPH hydrodynamic  
sub-model simulation results

256. A period of 30 hours starting at 0400 HRS GMT on 3 September 1979 was simulated using a time step of 300 seconds. Convective acceleration terms were considered in the middle of the lake. The previously presented SPH wind-field and Schloemer pressure profile were used to provide meteorological forcing. No inflows or rainfall were considered. The levee configuration including tree islands shown in Figure V-3 was considered. Simulated water levels with respect to an initial lake level of 14.48 msl (plot area) are compared with observed water level histories in Plates B-200 through B-203. Simulated water levels are in reasonable agreement with observed levels in overall shape. The simulated level at Port Mayaca, however, does not reach the level observed. This is due to lower wind loading than observed over the lake. As previously noted, for a 40 mb pressure depression one would not expect an 85 knot maximum sustained wind magnitude. It would appear an adjustment to the reported control pressure depression would be warranted. Simulated vertically integrated current histories are shown in Plates B-204 through B-210. Maximum current magnitudes are on the order of 1.0 fps thus facilitating a 300 second time step. The general current structure over the entire lake is presented in Plates B-211 through B-217. Simulated maximum significant wave height at Clewiston is approximately 1.7 feet. No measured wave data are available. No significant flooding occurred during Hurricane David, although Kreamer and Torrey Islands were slightly inundated and sections of the southern group to Tree Islands were overtopped and became submerged. No overtopping of the major levee system occurred.

## PART IX: DESIGN HURRICANES

### General outline

257. The development of both standard project and probable maximum hurricanes is presented for Lake Okeechobee in terms of both track and hurricane intensity parameters. A single standard project and probable maximum hurricane are simulated using the complete hurricane modeling package; i.e., the hurricane sub-model is exercised to provide input for the hydrodynamic model simulation. In the final sections of this part, the effect of levee breaching is demonstrated for a hypothetical failure near Okeechobee during the probable maximum hurricane.

### Development of design hurricane parameters

258. Schwerdt et al. [2] have developed meteorological criteria for the most severe hurricane reasonably characteristic of a region, Standard Project Hurricane (SPH), and for the hurricane that will produce the highest sustained wind that can probably occur at a specified coastal location, Probable Maximum Hurricane (PMH). A single limiting value for the meteorological parameters of peripheral pressure ( $P_w$ ) and central pressure ( $P_o$ ), while upper and lower limits for the radius to maximum winds ( $R$ ), forward speed ( $T$ ), and track direction ( $\theta$ ) were determined at 100 nautical mile increments as shown in Figure IX-1 along the Gulf and eastern coasts of the United States.

259. The central pressures adopted for the SPH and PMH are shown in Figures IX-2 and IX-3. A peripheral pressure ( $P_w$ ) of 29.77 in. (1008 mb) was adopted for the SPH, while a peripheral pressure of 30.12 in. (1020 mb) was adopted for the PMH. The adopted upper and lower limits of the radius to maximum winds are shown in Figures IX-4 and IX-5 for the SPH and PMH, respectively. Adopted SPH and PMH upper and lower limits of forward speed are shown in Figures IX-6 and IX-7, respectively. In interpreting the maximum allowable range of track direction for the SPH and PMH shown in Figures IX-8 and IX-9, respectively, the relations between direction and forward speed shown in Table IX-1 must be used. The track direction represents the angle from which the storm is approaching the coast measured clockwise from North; i.e., a meteorological definition is employed.

260. In developing SPH and PMH storms for Lake Okeechobee, the conditions at the appropriate coastal sections are extrapolated to the vicinity of

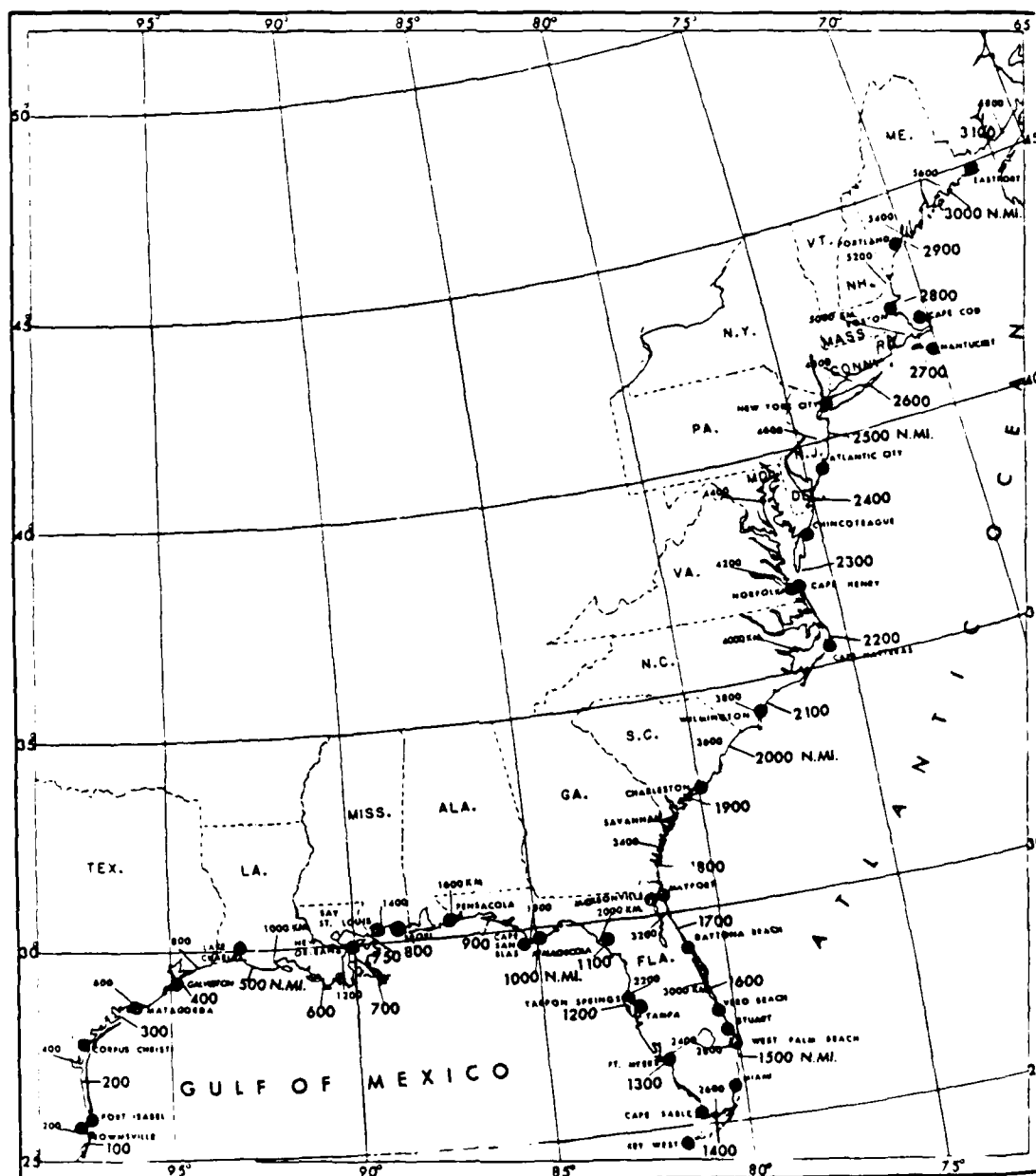


Figure IX-1. Locator map with coastal distance intervals marked in nautical miles and kilometers.



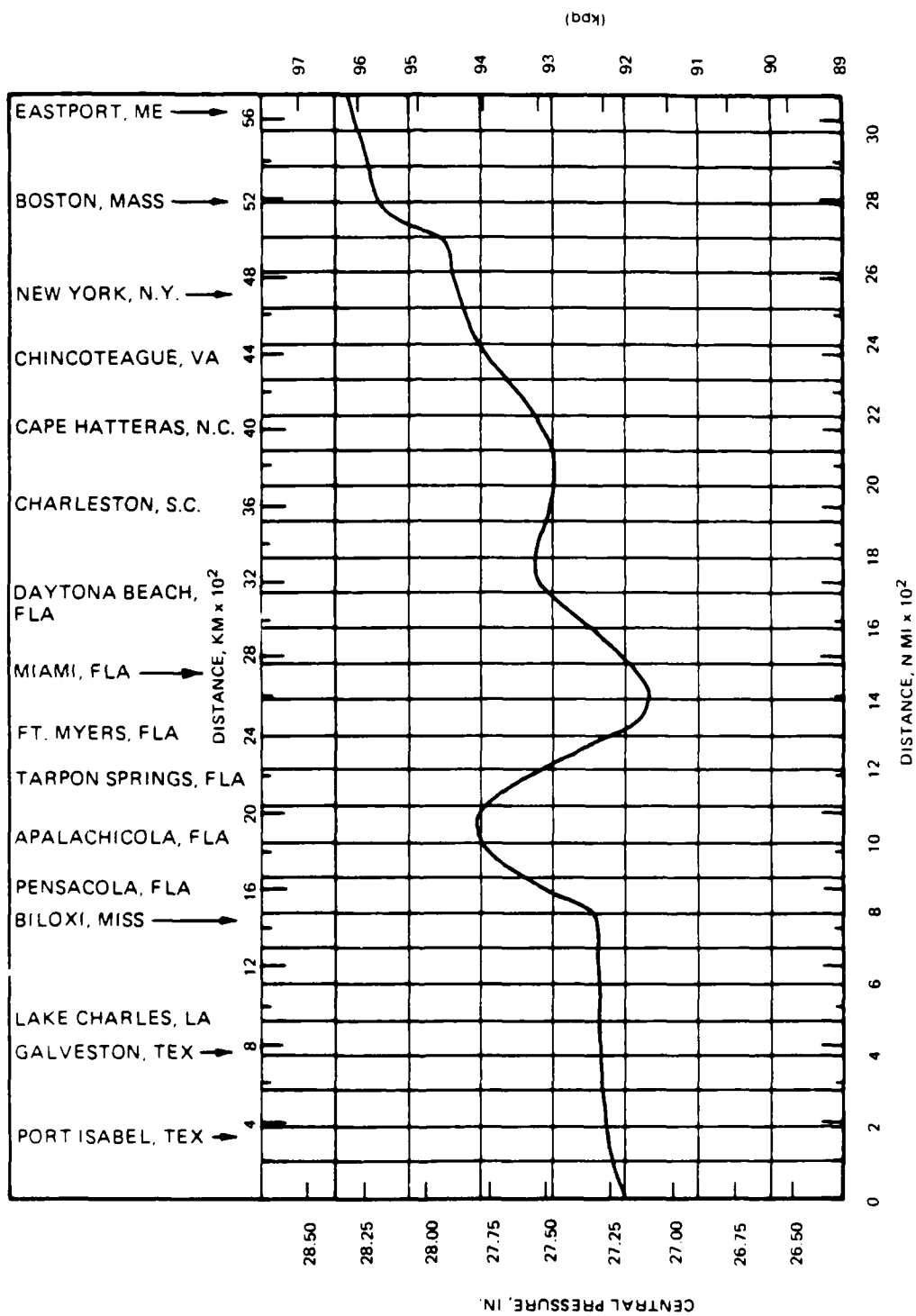


Figure IX-2.

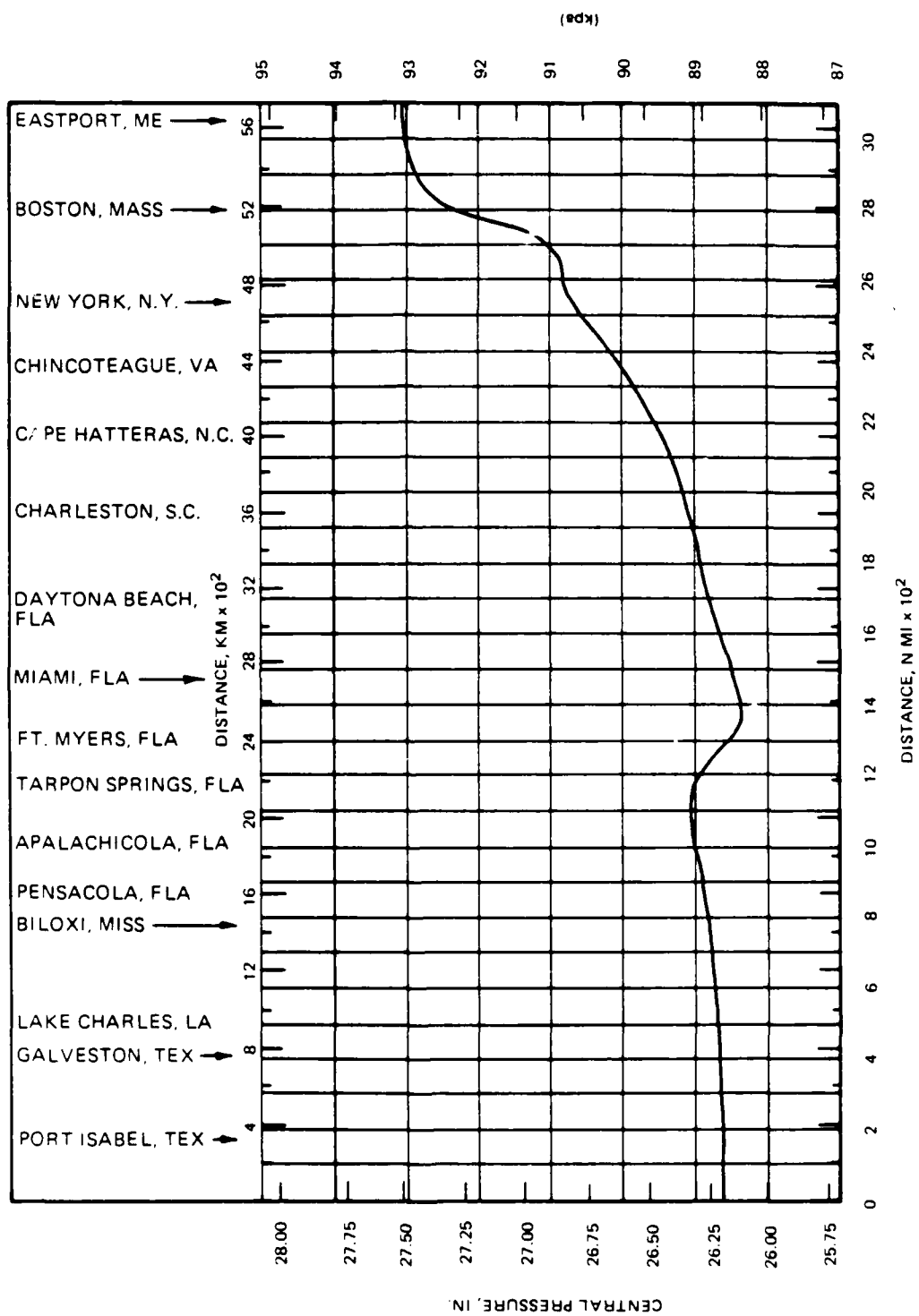


Figure IX-3.

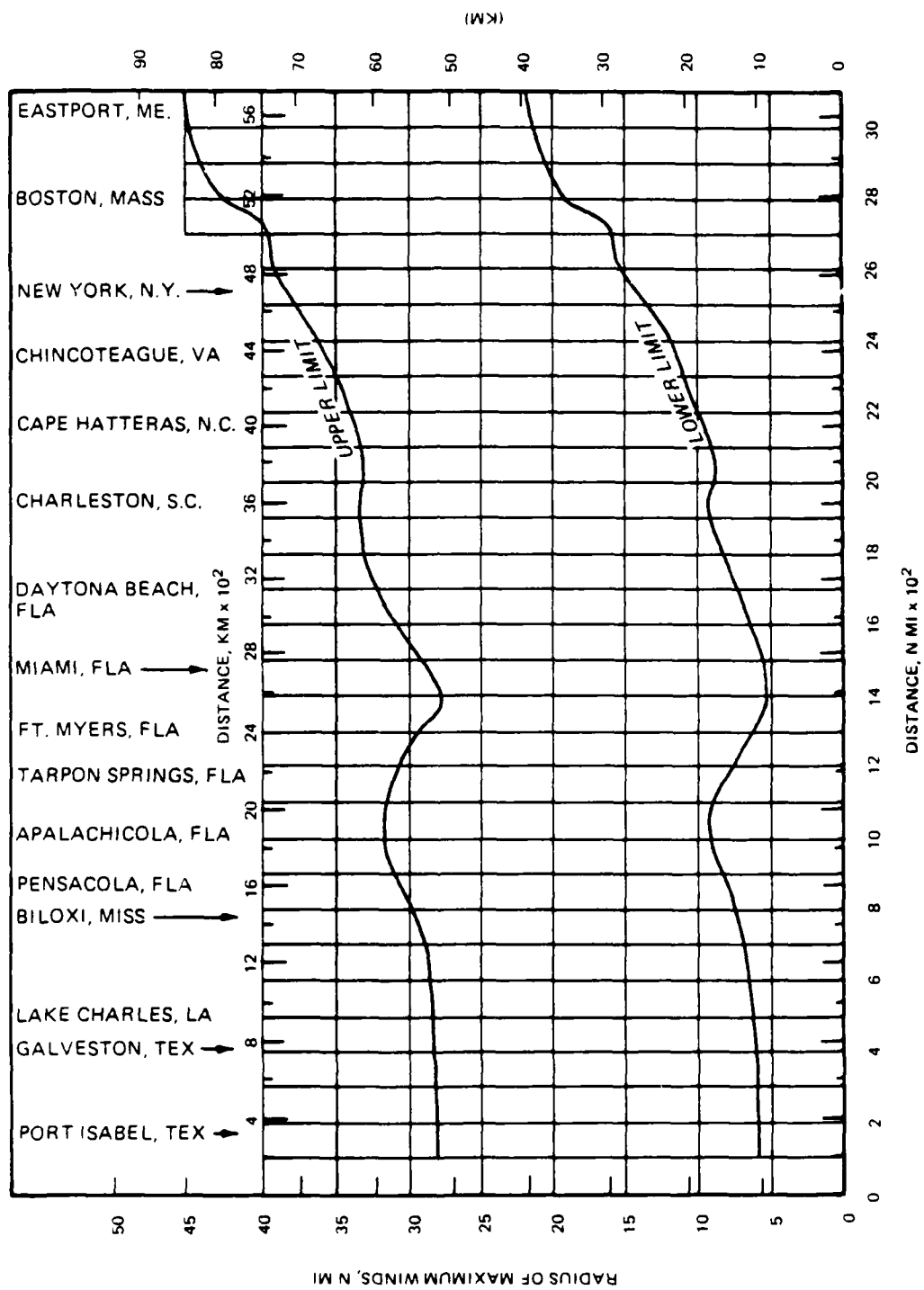


Figure IX-4.

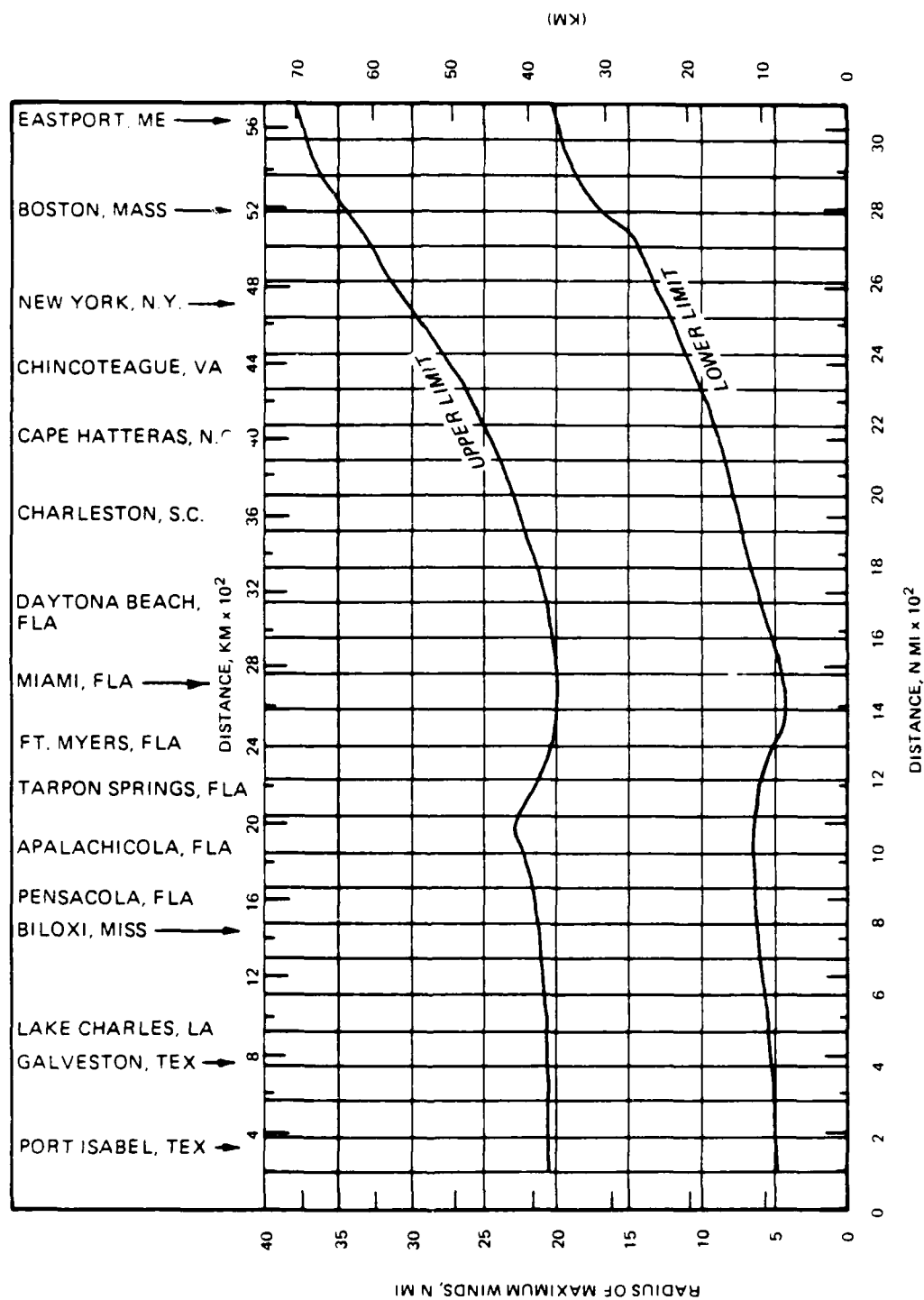


Figure IX-5.

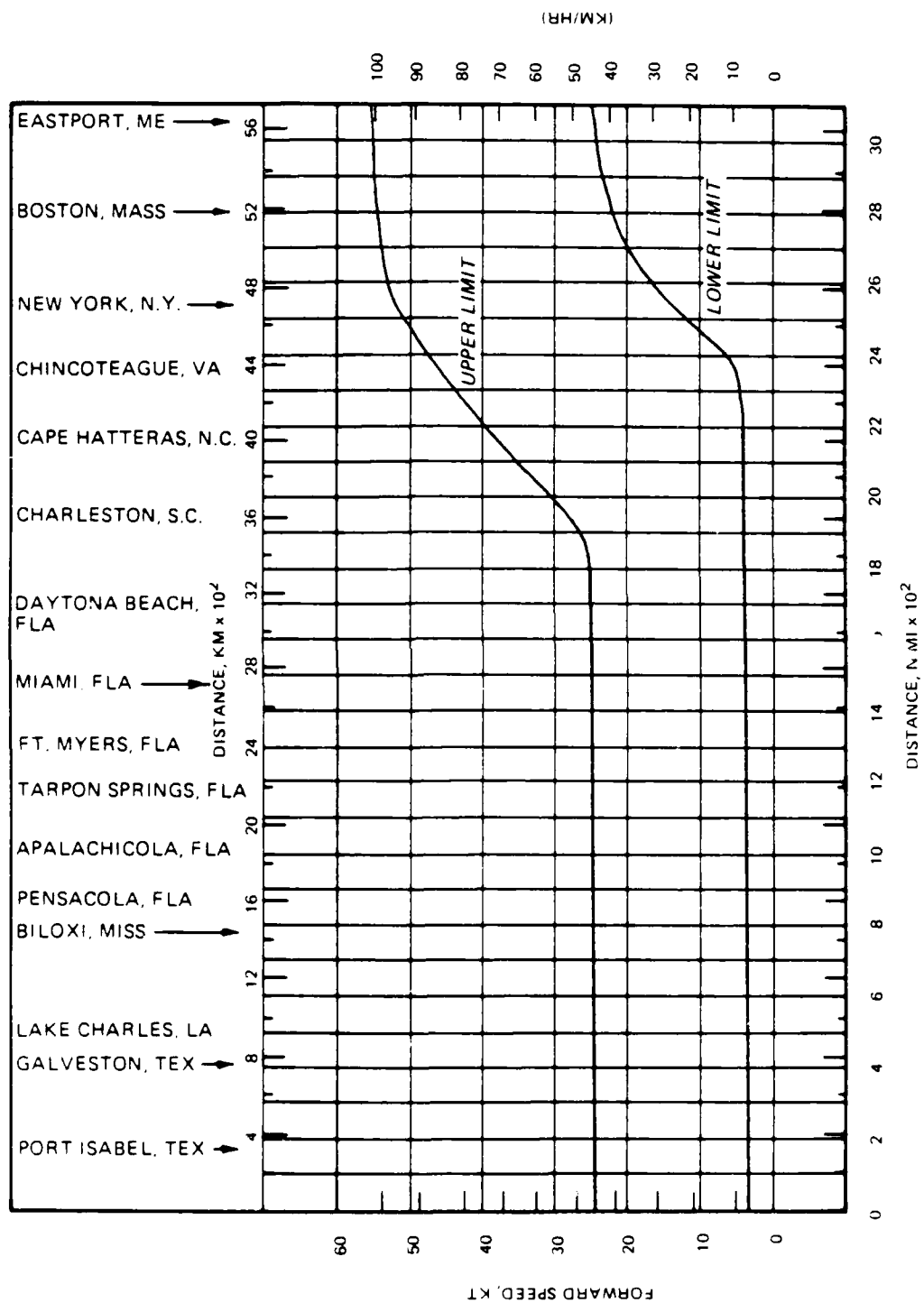


Figure IX-6.

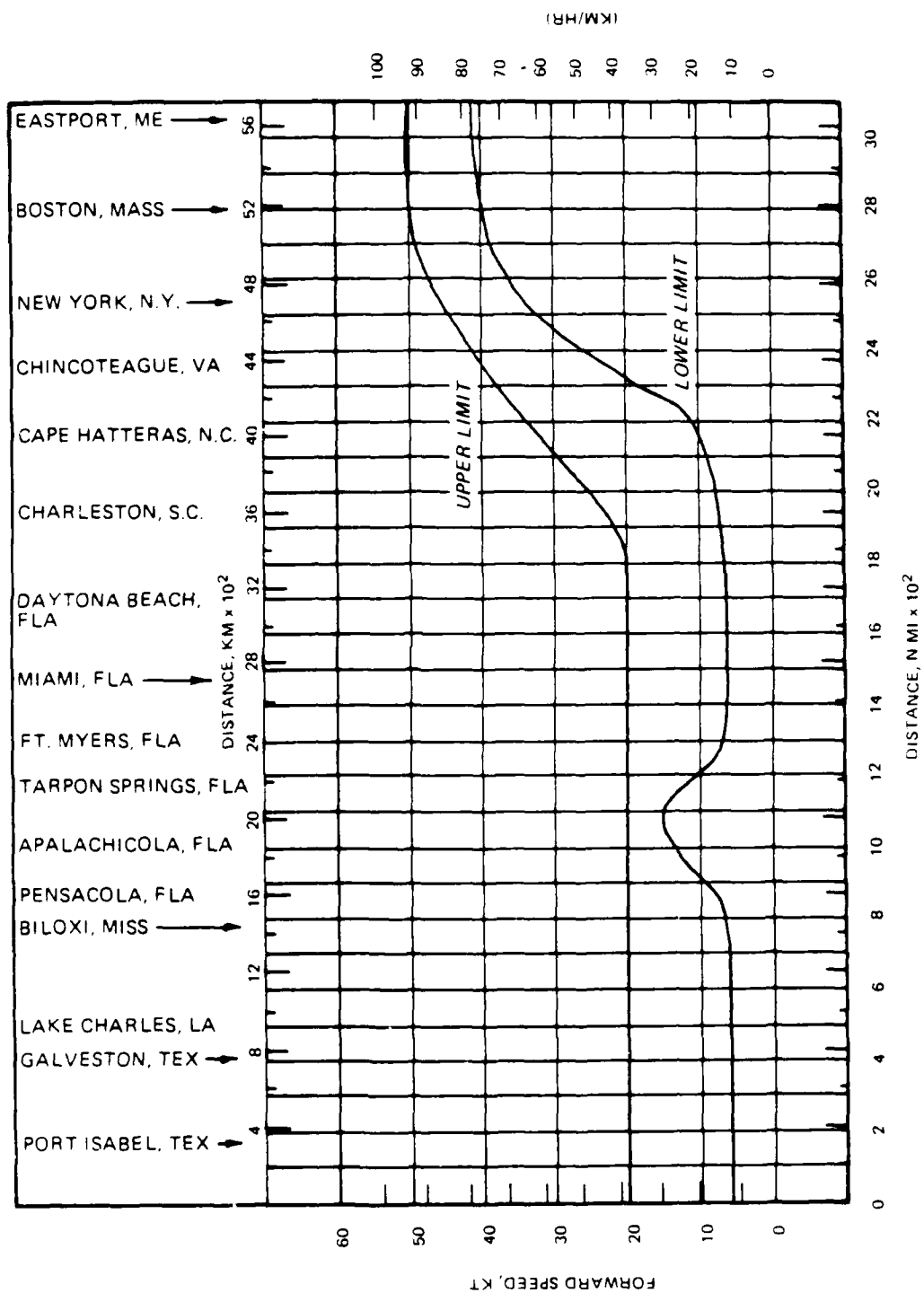


Figure IX-7.

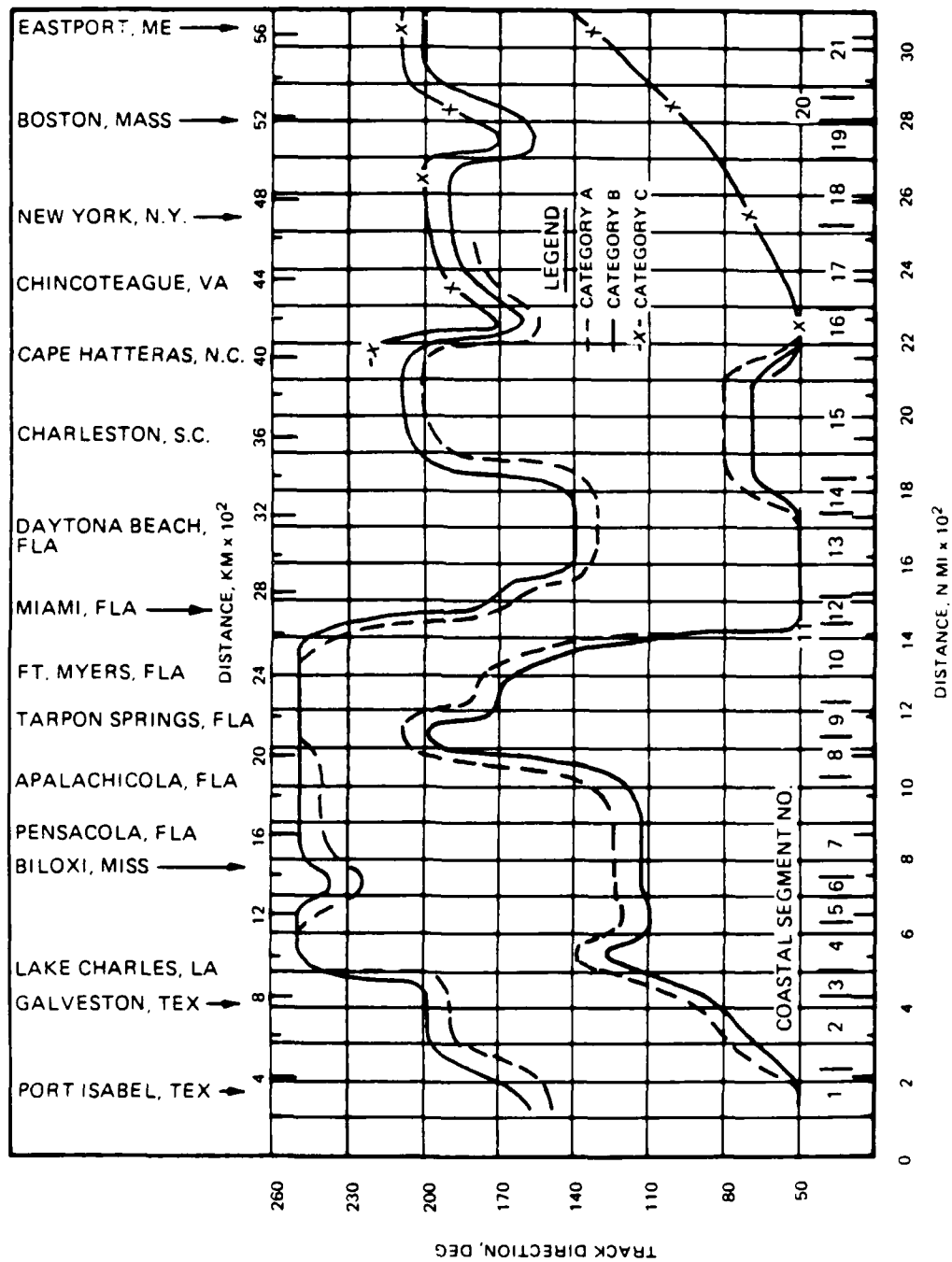


Figure IX-8.

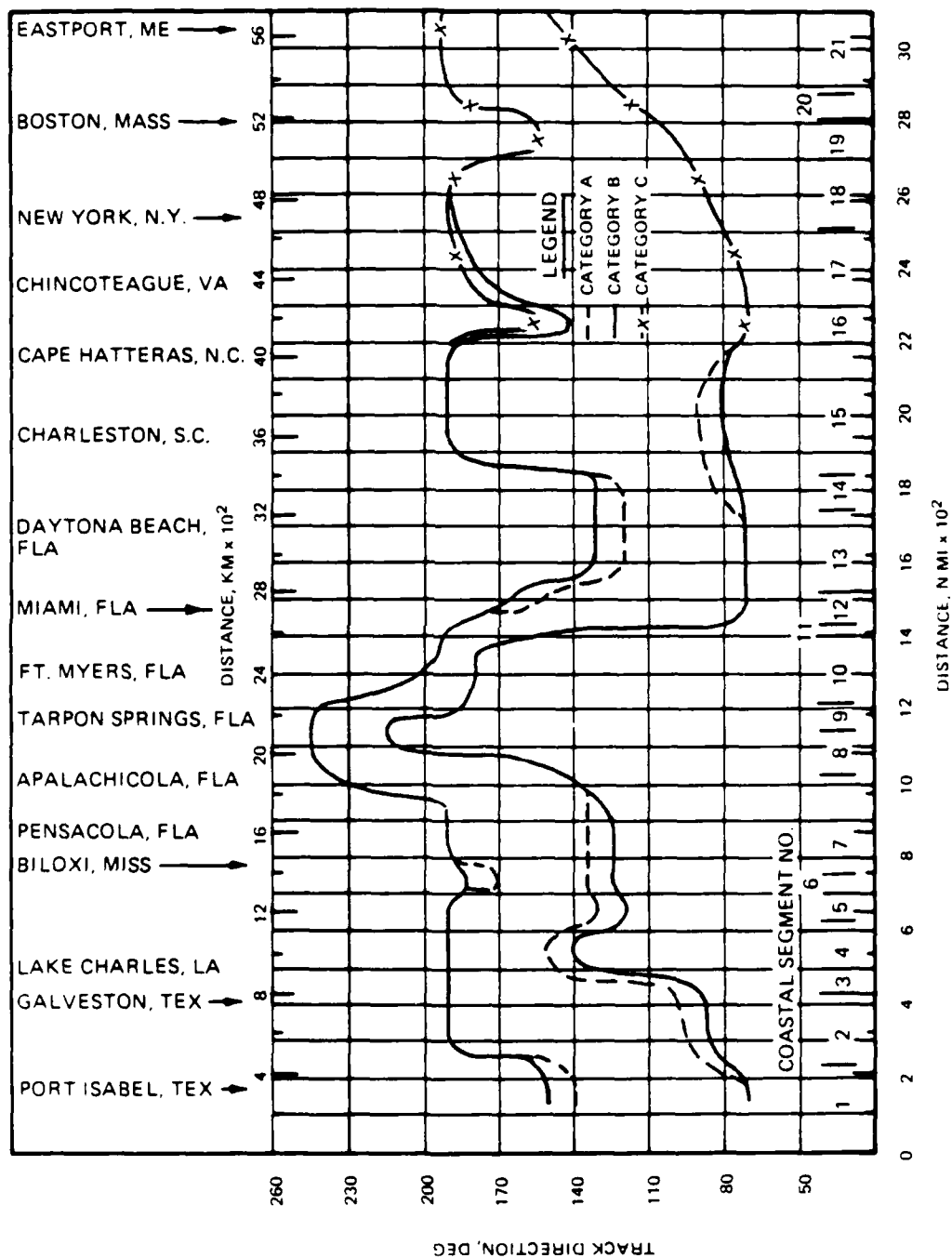


Figure IX-9.



Table IX-1

Relation Between Forward Speed (T) and Track Direction ( $\theta$ )

For the PMH

<u>Speed category</u>	<u>Forward speeds (T)</u>
A	$6 \text{ kt} \leq T \leq 10 \text{ kt}$ ( $11 \text{ km/hr} \leq T \leq 19 \text{ km/hr}$ )
B	$10 \text{ kt} < T \leq 36 \text{ kt}$ ( $19 \text{ km/hr} < T \leq 67 \text{ km/hr}$ )
C	$T > 36 \text{ kt}$ ( $T > 67 \text{ km/hr}$ )

For the SPH

<u>Speed category</u>	<u>Forward speeds (T)</u>
A	$4 \text{ kt} \leq T \leq 10 \text{ kt}$ ( $7 \text{ km/hr} \leq T \leq 19 \text{ km/hr}$ )
B	$10 \text{ kt} < T \leq 36 \text{ kt}$ ( $19 \text{ km/hr} < T \leq 67 \text{ km/hr}$ )
C	$T > 36 \text{ kt}$ ( $T > 67 \text{ km/hr}$ )

the lake. Design geometry and coastal design storm characteristics are presented prior to developing these general extrapolation procedures.

Design geometry

261. In order to specify the orientation of design hurricanes relative to the lake, it is necessary to specify certain geometrical relations. The latitude and longitude ordered pair ( $\lambda$ ,  $L$ ) of the center of the lake is specified in conjunction with a critical design radius,  $r$ . The critical design radius represents the approximate distance in nautical miles of the average hurricane radius to maximum winds known to have influenced the lake. From previous work  $r = 20 \text{ nm}$ ,  $\lambda = 26.92^\circ\text{N}$ ,  $L = 80.83^\circ\text{W}$ .

262. In general, it would appear necessary to consider storms passing through each point on the circle shown in Figure IX-10 from all compass directions. By consulting the limits of track direction for coastal segments for the SPH and PMH given by Schwerdt et al. [2], it is possible to eliminate certain angle bands.

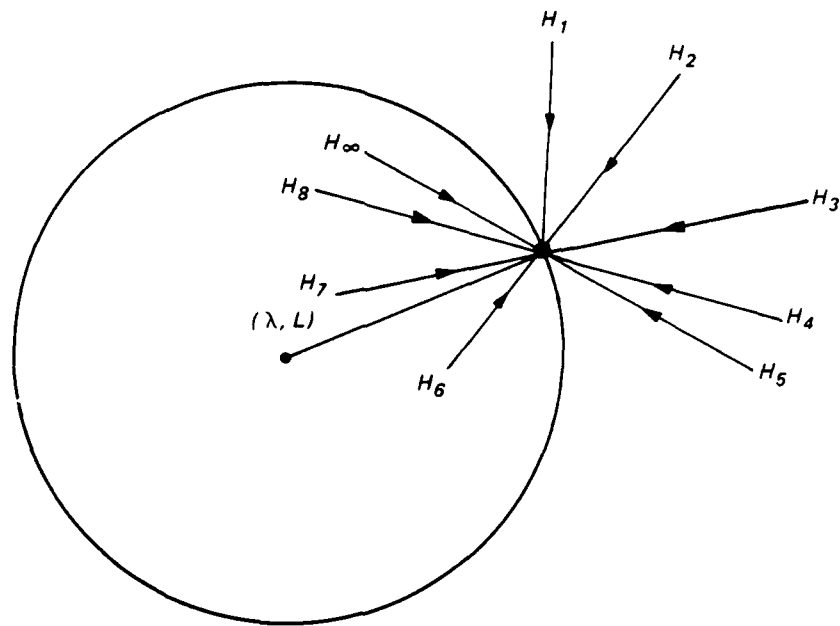


Figure IX-10. General Design Storm Geometry

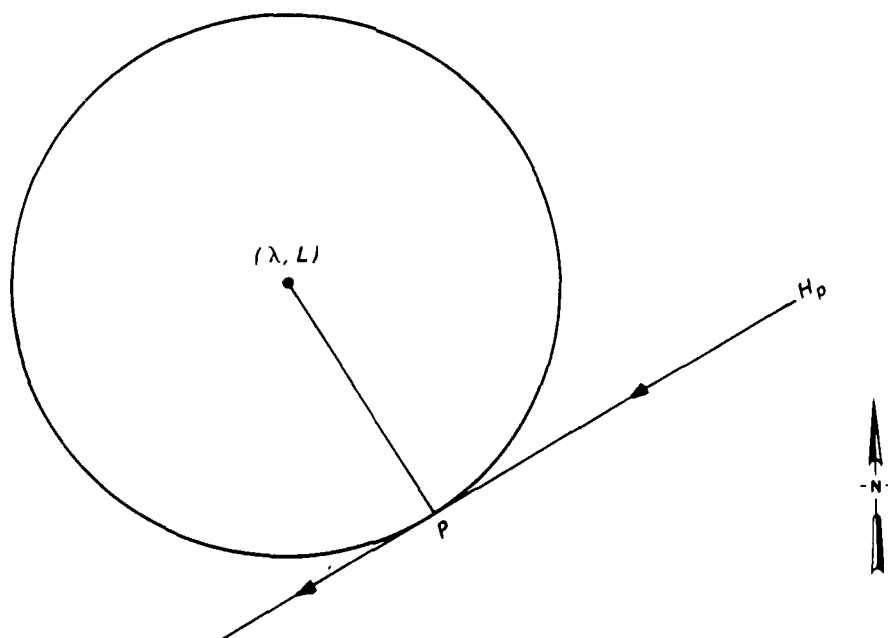


Figure IX-11. Critical Design Storm Geometry

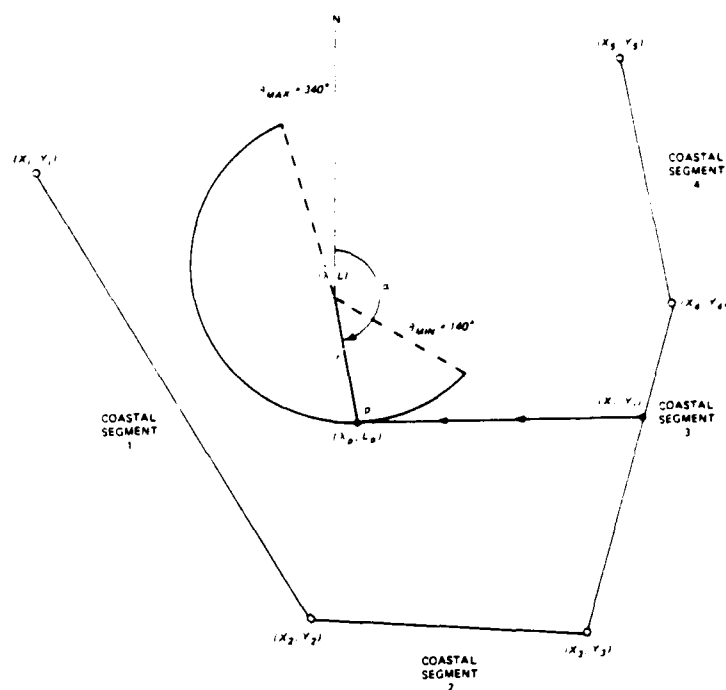


Figure IX-12. Coastal Segment Determination of Design Hurricanes

263. If one assumes that the most critical storm passes through the given point tangent to the circle at that point, it is possible to develop the design condition shown in Figure IX-11. For each point on the circle with critical design radius there is one critical storm direction. In addition, all points on the circle need not be considered based upon the limits of track direction. The limits on track direction define the locus of points on the circle, design circle sector, between 140-340° clockwise from North. Under this convention, the lake center is located always one critical design radius,  $r$ , to the right of the storm track. This orientation is assumed critical.

#### Coastal design storm characteristics

264. The coastal points shown in Table IX-2 encompass Lake Okeechobee as shown in Figure IX-1. The latitude and longitude coordinates of these points are as given in Table IX-2. The SPH and PMH design characteristics are shown in Tables IX-3 and IX-4, respectively for the coastal segments through which storms pass in influencing Lake Okeechobee.

#### General extrapolation procedures

265. Given the latitude and longitude ( $\lambda$ ,  $L$ ) of the center of the Lake, the critical design radius,  $r$ , and limits of the design circle sector angles  $\theta_{\min}$  and  $\theta_{\max}$  measured as compass bearings, one considers arbitrary points

Table IX-2  
Coastal Segment Points Location

<u>Point No.</u>	<u>Coastal Distance (nm)</u>	<u>Latitude (°N)</u>	<u>Longitude (°W)</u>
1	1200	28.	82.5
2	1300	26.5	81.88
3	1400	25.2	81.0
4	1500	26.5	80.1
5	1600	28.2	80.625

Table IX-3  
SPH Design Characteristics

Segment No.	Coastal Distance Range	P <sub>o</sub>	R		T		θ	
			L	U	L	U	L	U
1	1200-1300	27.42	7	30.5	4.	25.	170.	250.
2	1300-1400	27.19	5.5	29.			140.	250.
3	1400-1500	27.12	5.	28.5			50.	170.
4	1500-1600	27.25	5.5	30.	4.	25.	50.	155.
5	1400	17.08	5.	28.	4.	25.	110.	225.

P<sub>w</sub> = 29.77 in.

Table IX-4  
PMH Design Characteristics

Segment No.	Coastal Distance Range	P <sub>o</sub>	R		T		θ	
			L	U	L	U	L	U
1	1200-1300	26.2	5.5	21.	10.	20.	180.	215.
2	1300-1400	26.13	4.5	20.	6.5	20.	180.	190.
3	1400-1500	26.12	4.	20.	6.	20.	70.	170.
4	1500-1600	26.16	4.5	20.	6.	20.	70.	140.
5	1400	26.11	4.	20.	6.	20.	155.	190.

P<sub>w</sub> = 30.12 in.

from  $\theta_{\max}$  and  $\theta_{\min}$  spaced in increments of angle  $\Delta\theta$ . For an arbitrary point P, the latitude and longitude are calculated as follows:

$$\begin{aligned}\lambda_p &= \lambda + r \sin\alpha/60. \\ L_p &= L - r \cos\alpha/60./\cos\lambda_p \\ \alpha &= \theta_{\max} - p\Delta\theta = \theta_p\end{aligned}$$

where

- $\lambda_p \equiv$  Latitude of point P
- $\lambda \equiv$  Latitude of center of the lake
- $L_p \equiv$  Longitude of point P
- $L \equiv$  Longitude of center of the lake
- $\alpha \equiv$  Compass bearing of point P (clockwise from North)
- $r \equiv$  Design radius in nautical miles

(Note: 1' of arc on the earth corresponds to 1 nautical mile)

266. One next constructs the line passing through point 1 tangent to the circle of that point as shown in Figure IX-12. The general formula for the equation of this line in latitude and longitude space is given as follows:

$$y = m_D x + b_D$$

where

$$m_D = -\tan \alpha$$

$$b_D = L_p - m_D \lambda_p$$

One next considers each coastal segment  $i$ ,  $i = 1, \dots, 4$ , as shown in Figure IX-12. Each segment is represented as a straight line of the form given below.

$$y = m_i x + b_i$$

where

$$m_i = (y_{i+1} - y_i) / (x_{i+1} - x_i)$$

$$b_i = y_i - m_i x_i$$

The line representing the storm is next checked against each coastal segment  $i$  until an intersection with segment  $i$  is found. The procedures are outlined as follows:

1. If  $m_i = m_0$  the lines are parallel and do not intersect. Skip to segment  $i + 1$ .
2. For  $m_i \neq m_0$   $x_1 = b_1 - b_0 / m_1 - m_0$  compute:
3. If  $x_1 \leq x \leq x_{i+1}$ , the lines intersect. If  $x < x_1$  or  $x > x_{i+1}$  skip to segment  $i + 1$ .

4. If the lines intersect:

- a. Employ (print) the SPH and PMH design characteristics for coastal segment  $i$ .
- b. Compute  $y_i = m_i X_i + B_i$
- c. Compute the distance between the point of intersection  $I$  and point  $P$  as follows:

$$d = 60. \sqrt{(\lambda - X_i)^2 + [(L - Y_i) \cos X_i]^2}$$

- d. Next calculate the time since landfall that it takes the storm center to reach point  $P$ :

$$T_p = \frac{d}{T_i}$$

(Note  $T_p$  is in hrs, since  $d$  is in (nm) and  $T_i$  is in kts)

- e. Enter Table IX-5 and determine and print the reduction factor and  $T_p$ .
- f. Proceed to the next point  $P \equiv \theta_p + \Delta\theta$

Table IX-5

Adjustment Factors For Reducing Hurricane Wind Speeds  
When Center Is Overland (Category B)

<u>Hrs After</u> <u>Center Is Overland</u>	<u>Reduction</u> <u>Factor</u>
7.5	.90
15.0	.80
22.7	.70

Program DESIGN

267. The above algorithm is employed in Program DESIGN to develop design storm characteristics for the lake. A listing of program along with attendant job control language and input data is presented in Appendix E. Final design storm characteristics are presented for angle  $\alpha = 140^\circ$  in Table A-33.

Development of a  
Standard Project Hurricane

268. Based upon characteristics associated with coastal segment 1300-1400, a hurricane was specified as shown in Table A-34. The joint probability method storm track geometry described in Part III of the second report of this series was employed in the hurricane sub-model. A meteorological angle of  $90^\circ$  corresponding to a compass bearing of  $180^\circ$  was used to specify the track of a storm passing through the center of the lake. Nine hours of winds were developed using three snapshots in previous format as shown in Plates B-192 through B-197 by the parametric standard project hurricane formulation. The initial storm position is along the track at a distance from lake center equal to the maximum of three times the radius of maximum winds and 120 nautical miles. The final storm position is along the track at a distance from lake center of three times the radius of maximum winds in nautical miles. Snapshot windfield vector and corresponding isovel contours are presented in Plates B-218 through B-221 using previously described formats. Maximum winds exceed 100 knots. Observe in Plates B-222 and B-223 that the central pressure deficit has decreased from 2.58 in Hg to 2.01 in Hg due to the hurricane filling relationships in Table IX-5.

Standard project hurricane  
initial hydrodynamic simulation results

269. In order to study the hydrodynamic response of the lake to the standard project hurricane previously developed, a numerical simulation was performed with the lake at an initial level of 15.5 msl. Four hundred thirty time steps of 75 seconds duration were used to simulate 8.95 hours. No inflows or rainfall were considered. The present levee and tree island configuration shown in Figure V-3 was considered. In this initial simulation, windfield and pressure information were updated every 24 time steps corresponding to 0.5 hour. Simulated water level histories are presented with respect to 15.5 msl plot zero in Plates B-224 through B-230 for HGS-1 through HGS-6 and Port Mayaca, respectively. Peak water levels with respect to mean sea level and their associated time of occurrence are presented in Tables A-35 and A-36, respectively. Storm loadings are presented in Plates B-231 through B-244. Observe the stair step type description at half hour intervals. The current response due to the spatial distribution of overlake winds is portrayed in Plates B-245 through B-260 at times of 1, 2, 3, 4, 5, 6, 7, and



8.96 hours, respectively. During the first four hours of the storm, winds are directed toward the western side of the lake. The water surface is elevated at the west and lowered on the east side of the lake. Water tends to pile up against the southern tree islands from the shore side and some overtopping occurs from the shore side. For the northern band of tree islands, overtopping occurs from the lakeside. This pattern becomes completely reversed as the storm passes through the center of the lake and the winds shift toward the east. The role of the tree islands in the overall response of the lake is very complex. As may be noted in Plate B-230 at Port Mayaca the resurgence at time 7.8 and 8.4 hours may be due to long-wave reflection from the southeastern entrance of the tree islands. Maximum currents are on the order of 7.5 fps. The maximum significant wave height at Clewiston is 5.2 ft.

Standard project hurricane  
additional hydrodynamic simulations

270. Two additional hydrodynamic simulations were performed using all the conditions of the initial simulation. In simulation one, the wind and pressure fields were interpolated at a variable number of time steps based upon the location and size of the storm. These procedures are more fully developed in Part X. Water surface histories with respect to 15.5 msl plot zero and the corresponding wind/pressure histories are given in Plates B-261 through B-266 at Clewiston, Canal Point, and Okeechobee, respectively. In simulation two, the wind and pressure fields are interpolated every time step. Water surface histories and corresponding wind/pressure histories are given in Plates B-267 through B-272. Water surfaces histories for each additional simulation are equivalent to the initial simulation results. Computational time requirements are vastly different as shown in Table A-37.

271. It would appear the approach used in the initial simulation or in additional simulation one is considerably cheaper.

Development of a  
probable maximum hurricane

272. Based upon characteristics associated with coastal segment 1300-1400 nm, the hurricane developed in Table A-38 is developed. A meteorological angle of  $90^\circ$  corresponding to a compass bearing of  $180^\circ$  was used to specify the track of a storm passing a distance of one radius to maximum winds to the left of the lake center. Nine hours of winds were developed using three snapshots in previous format as shown in Plates B-273 through B-278 by

the parametric standard project hurricane formulation. The initial storm position is along the track at a distance of 120 nautical miles from the meteorological line. The final storm position is along the track at a distance from the meteorological line of three times the radius of maximum winds. Note maximum sustained windspeeds are greater than 130 knots.

Probable maximum hurricane  
initial hydrodynamic simulation results

273. In order to investigate the hydrodynamic response of the lake to a hurricane of probable maximum intensity, a numerical simulation was performed with the lake at an initial level of 24.5 msl corresponding to the standard project flood elevation. A 45 second time step was employed in simulating 8.5 hours. No inflows or rainfall were considered. The present levee and tree island configuration shown in Figure V-3 was considered. In this initial simulation, windfield and pressure information were updated every 40 time steps corresponding to 0.5 hour. Simulated water level histories with respect to 24.5 msl plot zero are presented in Plates 279-285 for HGS-1 through HGS-6 and Port Mayaca, respectively. Peak water levels with respect to mean sea level and their associated time of occurrence are presented in Tables IX-12 and IX-13, respectively. Storm loadings are presented in Plates B-286 through B-299 in a stair step manner at half hour intervals. The current response due to the spatial distribution of overlake winds is portrayed in Plates B-300 through B-317 times of 1, 2, 3, 4, 5, 6, 7, 8, and 8.5 hours, respectively. The response from hour 7 on is such that lake currents are opposite in direction to wind loading over the eastern half of the lake. This is apparently due to the fact that the wind loading is not sufficient to overcome the water surface elevation gradient developed during the previous hours of the storm. At an initial lake level of 24.5 msl all tree islands are initially submerged. As water tends to drawdown faster on the lake side of the southern tree islands, some sections are overtopped from the shore side during the early hours of the storm. Eventually after 4-5 hours all southern tree islands become exposed. Maximum lake currents are on the order to 12.3 fps. The maximum significant wave height at Okeechobee is 9.97 feet. At hour seven, the levee at Okeechobee is initially overtopped. The still water level elevation exceeds the levee height from hour 7 through hour 8. During this period, the overtopping contribution due to waves is in the range of 4-61 cubic feet per second per foot of levee.

#### Probable maximum hurricane levee breaching hydrodynamic simulation

174. The section of levee at Okeechobee was specified to be in a breached condition at hour 7 based upon the initial probable maximum hurricane results. This initial simulation was rerun with a levee breach at hour 7 of duration of six hours. The breach was specified near Okeechobee as shown in Figure V-3 as shown in Table A-41. The hydrodynamic response of the lake remained essentially unchanged as may be noted by comparing Table A-42 and A-43 with Table A-39 and A-40 respectively. The peak water level in cell (38, 3) at Okeechobee is reduced by .1 feet only. Representative breach conditions are shown in Table A-44 at hour 6.8875 (before the breach), at hour 7.15 (immediately after the breach), and at hour 8.025. Note water levels are sufficient to overtop both barriers prior to the initiation of the breach. Immediately after the breach, flow over section (38, 3) reaches over 500,000 cfs, while at section (39, 3) the flow is approximately 60,000 cfs. By hour 8.025, the water level at the northern end of the lake has lowered such that only section (38, 3) is overtopped at a rate of approximately 23,000 cfs. Beyond hour 8.1625, no overtopping occurs. Levee elevations, under the current model formulation, continue to be lowered at a uniform rate per time step, determined by subtracting the initial elevations in Table IX-4 from the final elevations and dividing the result by the duration of breach then multiplying by the time step length.

#### Joint probability method considerations

175. As developed in Report 2 in this series, approximately 600 combined hurricane sub-model hydrodynamic sub-model simulation pairs must be executed in a joint probability method design for present levee and hurricane site structures. In the previous sections of Part IX a variable wind/pressure field interpolation procedure was developed producing essentially the same results as the single time step procedures used in Parts VI-VIII during the calibration process but at substantially less cost. As an additional cost-saving procedure, it is recommended that a variable time step approach be investigated. This approach could be implemented in the same manner as the variable interpolation procedure; e.g., only when the hurricane is close to the lake is the time step reduced from a user specified baseline value (300 seconds). The entire concept of storm track is in the concept of the

joint probability method further investigated in this part.

276. In Part IX paragraph 269, a standard project hurricane was simulated employing the characteristics shown in Table A-34. Nine hours corresponding to 180 nautical miles of track starting at a position 120 nautical miles due south from lake center were considered. In examining Table A-36, for lake areas near HCS-3, there was some question as to whether or not peak water levels had been reached. The storm track algorithm was modified as shown in the relation below to allow for seiching resurgence effects.

$$T = [\max(120., 3R) + 20. + 3R]/V_f + 2.5 \quad (9.1)$$

where

$T$  = Total storm track simulation time (hrs)

$R$  = Storm radius (nm)

$V_f$  = Storm forward speed (kts)

The last term representing 2.5 hours represents the travel time of a long-wave from one side of the lake to the other. A generalized hurricane sub-model simulation was performed using the above refined track requirement as shown in Table A-45. Windfield information is developed at hours zero and on. It is the same developed previously in Plates B-218 and B-219 and Plates B-220 and B-221, respectively.

277. The wind information at hour eleven is shown in Plates B-318 and B-319, respectively, using previous formats. Observe the CPI has been reduced from the hour nine value of 2.01 to 1.89 in H<sub>2</sub> at hour eleven. A corresponding hydrodynamic model simulation was performed for a period of 10.5 hours. Maximum surge elevation (msl) and their corresponding times of occurrence are shown in Tables A-46 and A-47, respectively. In comparing these results with those shown previously in Tables A-35 and A-36, respectively, very little differences is noted even in the vicinity of HCS-3. However, if one observes Plates B-229 and the corresponding results shown in Plate B-320, it is necessary to simulate over nine hours in order to be sure a peak level has been reached at HCS-6. For this reason and to provide a margin of safety the track algorithm given in Equation (9.1) is recommended.

## PART X: STUDY RESULTS AND CONCLUSIONS

278. Salient study results are presented and the following conclusions are drawn:

- a. A generalized modeling system has been developed for determining seiche and hurricane induced water level fluctuations in Lake Okeechobee. The system consists of two major components: 1) a hurricane sub-model (Program LOGHM) and a attendant graphics software (Program HGRAPH), and 2) a hydrodynamic submodel description of a long-wave and short-wave phenomena (Program LAKE) complete with graphics (Procedure POST).
- b. The hurricane sub-model consists of a direct parametric approach as well as a planetary boundary layer formulation. Both approaches are completely developed in this report. Generalized hurricane track interpolation procedures have been developed for hindcasting/forecasting as well as joint probability method (straight line) storm tracks.
- c. The hydrodynamic sub-model long and short wave theory are completely developed in this report. Wave runup and overtopping as well as levee breeching are considered. Within the long-wave calculations sub-grid scale barriers and a moving boundary are treated.
- d. A global grid (64 x 48) of 3072 cells has been constructed for hydrodynamic sub-model calculations. SAJ personnel assisted in developing lake topography and levee profile data suitable for the global grid.
- e. The August 12-13, 1968 seiche and the August 20-21, 1964 seiche were used to calibrate and verify the long-wave bottom friction mechanics independent from wind surface loading. Simulated levels are in reasonable agreement with measured water surface elevations at most gaging stations.

Based upon simulations results, the bottom friction mechanics including canopy effects seem reasonable. In the seiche simulations, the initial lake surface elevation is accurately known at only a few stations. This makes the specification of the initial lake profile difficult. Due to the small amplitudes of the seiches (approximately .5 feet), the specification of the initial lake surface is very critical for simulating these events.

- f. The August 1949 hurricane was considered as the most critical event for surface wind loading calibration. Both the PBL and SPH approaches in the generalized hurricane sub-model were exercised. Although peak maximum sustained windspeeds were on the order of 3-8 knots lower in the PBL approach, the inner

structure (winds within a vicinity of 2 radii of maximum winds from the storm center) was quite different. Overlake simulated windspeeds were compared with measured winds at several locations around the lake. Simulated PBL and SPH windspeeds were in excellent agreement with measured results during the initial and final hours of the storm track. During the period the storm center was near or over the lake, PBL windspeeds were as much as 25 knots lower than SPH windspeeds at some gaging stations. SPH windspeeds were in reasonable agreement with observed windspeeds during the storm period. Simulated PBL wind directions were usually within 30 degrees of simulated SPH wind directions for the gaging stations considered. Simulated SPH wind directions agreed within 20-30 degrees of observed directions.

The hydrodynamic sub-model was used to simulate hurricane induced water levels for both windfield formulations. Simulated PBL induced water levels were lower than SPH induced water levels at all gaging stations. However, PBL generated levels appeared to be in closer agreement with observed levels in the southern portions of the lake, while SPH generated levels were in closer agreement in the eastern and northern portions of the lake. The maximum water level excursion at Okeechobee was approximately 14.5 feet. The PBL generated maximum water level excursion at Okeechobee was 10.0 feet (31% error), while the SPH generated maximum excursion at Okeechobee was 12.8 feet (12% error). Simulated significant wave heights were slightly larger for the SPH windfield than for the PBL windfield. SPH windfield generated significant wave heights were in reasonable agreement with measured results. Significant wave heights and periods are larger for the CW-167 curve approach than under the SPM methodology. Considering the CW-167 and SPM results to define a range, measured significant wave heights and periods fall within the range. Regions of inundation generated by the SPH windfield are in excellent agreement with observed regions. For the PBL simulations, regions of inundation are reduced considerably in areal extent.

Based upon the results produced for the August 1949 hurricane, it appears that the wind and bottom stress formulations are reasonable in the long wave calculations. In order to further reduce the maximum error between simulated and observed water levels, it is necessary to better define the inner structure of the hurricane windfield during passage over the lake. The SPH formulation is superior to the PBL formulation based upon hydrodynamic simulation results.

- g. The October 1950 storm although not of the intensity of the August 1949 hurricane passed directly over the lake. The SPH approach was employed to generate the windfield. Simulated far field windspeeds and directions are in good agreement with measured data. Simulated near field windspeeds at the time of lake passage are within 20 knots of observed data in all cases and at most stations are within 10 knots. SPH windfield

induced peak water levels produced by running the hydrodynamic sub-model with the SPH windfield as input are within 1.-1.5 feet of peak measured levels except at HGS-3. Very little measured wave data are available at shoreline stations. Simulated wave data are in agreement with the limited measured data.

Based upon the results produced for the October 1950 hurricane, the wind and bottom stress formulations in the long wave calculation are confirmed. Discrepancies between observed and simulated water level histories are due to differences between the observed and computed windfields. Short wave simulated data appear reasonable.

- h. The September 1979 hurricane (David) was considered in order to check the model under the present levee configuration. Hurricane David produced overlake winds on the order of 60 knots; i.e., winds were not of hurricane intensity over the lake unlike the August 1949 and October 1950 storms. The SPH approach was used to generate the windfield input to the hydrodynamic sub-model. Peak simulated overlake winds were 40 knots, approximately 20 knots less than observed values. In the vicinity of Lake Okeechobee, a measured central pressure depression of 40 mb is reported to have produced maximum sustained winds of 85 knots. Based upon normal pressure relationships for calculating maximum overwater winds, an 85 knot peak wind cannot be generated. The SPH windfield maximum was approximately 65 knots with overlake maximum windspeeds at 40 knots. As one might suspect, SPH generated water levels are lower than observed water levels for gage stations nearest the passage of the storm; i.e., Port Mayaca. No measured wave data are available.

It is difficult to draw any other conclusion based upon these results, than the fact that the hurricane sub-model input data must be consistent in order to produce reasonable windfield results. Peak simulated water levels are directly dependent on the hurricane sub-model windfield. In effect, a chain reaction occurs in which errors in one step of the process generate errors in the next step.

- i. In order to develop evacuation planning alternatives, a design hurricane methodology was developed in conjunction with the hurricane-hydrodynamic model pair. Standard Project Hurricanes and Probable Maximum Hurricanes are developed for Lake Okeechobee by formally extrapolating in Program DESIGN (Appendix E) design hurricane characteristics developed for Atlantic and Gulf Coast sections by Schwerdt et al. [2]. A general design storm radius concept is developed in order to specify design storms passing within an arbitrary distance from lake center.
- j. A Standard Project Hurricane passing directly on a line from South to North through the center of the lake was considered for an initial level of 15.5 msl. The SPH approach was used to generate the design windfield. Peak sustained winds

exceeded 100 knots on the lake. A hydrodynamic simulation was performed using the SPH generated design windfield. Since the initial lake level corresponded to the elevation of the tree islands, at alternate portions of the simulation sections of the tree islands were overtopped, exposed, and completely submerged. Hydrodynamic sub-model output formats were extended to include maximum and time of maximum water levels as well as corresponding depth fields. A variable interpolation interval scheme was developed in order to reduce computational cost in the hydrodynamic sub-model. Simulated peak water levels exceeded 10.0 ft above the 12.5 msl model datum. No overtopping of the levee system occurred.

- k. A Probable Maximum Hurricane passing a distance of one radius to maximum winds to the west of lake center on a direct South to North track was considered for an initial lake level of 24.5 msl corresponding to the Standard Project Flood. Wind speeds in excess of 120 knots are developed over the lake by the SPH windfield formulation. This storm represents the worst possible condition for Lake Okeechobee. Water level elevations of over 19 feet above the initial lake level are produced at HGS-6 during the hydrodynamic sub-model simulation. Maximum significant wave heights on the order of 10 feet are produced at HGS-6. The levee at HGS-6 is overtopped for a period of approximately one hour.

Based upon the simulation of this event, the complete hurricane-hydrodynamic model pair is capable of simulating all storm events associated with a joint probability analysis.

- l. The Probable Maximum Hurricane condition just reported was reconsidered for the specification of a levee breach at Okeechobee. The breach was specified to occur at hour seven and last for the next six hours as shown in Table IX-4. The hydrodynamic response of the lake remained essentially unchanged. The peak water level at Okeechobee was reduced by .1 feet.

This simulation demonstrated that levee breach flows may be calculated as input to a link-node drainage model for flood routing and emergency action planning.

- m. The specifications of the track for joint probability method application was refined to allow the travel of a long-wave across the entire lake length in order to study resurgence effects on peak water levels.



## REFERENCES

1. Graham, H. E. and Nunn, D. E. Meteorological Considerations Pertinent To Standard Project Hurricane, Atlantic and Gulf Coastal of the United States, VHRP No. 33, November, 1959.
2. Schwardt, R. et al. Criteria For Standard Project Hurricane And Probable Maximum Hurricane Wind Field, Gulf and East Coast United States, NOAA Technical Report NWS-23, November, 1979.
3. Professor R. O. Reid, Texas A&M University under contract DACW72-78-C-0033 with the Coastal Engineering Research Center, Fort Belvoir, Virginia, 1978.
4. Revised Standard Project Hurricane Criteria for the Atlantic and Gulf Coasts of the United States, (Preliminary) Memorandum HUR7-120, Hydro-meteorological Branch Office of Hydrology, National Weather Service, Silver Spring, Maryland, 1972.
5. Tetra Tech, Inc. Coastal Flooding Storm Surge Model Part I: Methodology (1977, 1978) Part 2: Codes and User's Guide (1978, 1979) Federal Emergency Management Agency Washington, DC.
6. Schloemer, R. W. "Analysis and Synthesis of Hurricane Wind Patterns Over Lake Okeechobee, Florida", Hydromet Rep. No. 31, Washington, DC, 1954.
7. Myers, V. A., 1954. Characteristics of United States Hurricanes Pertinent to Levee Design for the Lake Okeechobee, Florida. Hydro-meteorological Report No. 32, US Weather Bureau, Department of Commerce and US Army Corps of Engineers, Washington, DC, pp 106.
8. Memoranda HUR 7-97 and HUR 7-97A, "Interim Report - Meteorological Characteristics of the Probable Maximum Hurricane, Atlantic and Gulf Coasts of the United States," May 7, 1968, along with "Peripheral Pressures for Probable Maximum Hurricanes," December 3, 1968.
9. Nunez, E. and W. M. Gray, 1978. A Comparison Between West Indies Hurricanes and Pacific Typhoons. Conference papers, 11th Technical Conference on Hurricanes and Tropical Meteorology, American Meteorological Society, Boston, Mass., pp 528-534.
10. Jelensnianski, C. P., 1967. Numerical Computations of Storm Surges With Bottom Stress. Monthly Weather Review, Vol 95, No. 11, pp 740-756.
11. Chow, Shu-hsien, 1971. A Study of the Wind Field in the Planetary Boundary Layer of a Moving Tropical Cyclone, Masters Thesis, New York University, Department of Meteorology, New York, N.Y., pp 58.
12. Collins, J. I. and Viehman, M. J. "A Simplified Empirical Model for Hurricane Wind Fields", Offshore Technology Conference, Vol 1, Preprints, Houston, Texas, April, 1971.

13. Smagorinsky, J. 1963. General Circulation Experiments With the Primitive Equations: I. The Basic Experiment. Mon. Wea. Rev., 91, 99-161.
14. Cardone, V. J. et al. A Unified Program for the Specification of Hurricane Boundary Layer Winds Over Surfaces of Specified Roughness, Contract No. DACW39-78-C-0100, US Army Waterways Experiment Station, Vicksburg, MS, 1979.
15. Arya, S. P. S. 1977. Suggested Revisions To Certain Boundary Layer Parameterization Schemes Used in Atmospheric Circulation Models. Mon. Wea. Rev., (Vol 105, No. 2) 215-227.
16. Ayres, Frank. Plane and Spherical Trigonometry, Schaum Outline Series, McGraw-Hill Book Co., New York, 1954.
17. Lai, Chintu. 1977 (Oct). Computer Simulation of Two-Dimensional Unsteady Flows in Estuaries and Embayments by the Method of Characteristics, USGS, Water Resources Investigations 77-85.
18. van Dorn, William G. "Wind Stress on An Artificial Pond", Journal of Marine Research, [12, 3], 1953, pp 249-276.
19. Charnock, H., 1955: "Wind Stress On a Water Surface, Quarterly Journal of the Royal Meteorological Society, 81, pp 639.
20. Garratt, J. R., 1977: "Review of Drag Coefficients Over Oceans and Continents", Monthly Weather Review, Volume 105, July, pp 915-929.
21. Wu, Jin, 1980: "Wind-Stress Coefficients Over Sea Surface Near Neutral Conditions - A Revisit, Journal of Physical Oceanography, Vol 10, pp 727-740.
22. Wu, Jin, 1982: "Wind-Stress Coefficients Over Sea Surface From Breeze To Hurricane", Journal of Geophysical Research, Vol 87, No 12, pp 9704-9706.
23. Powell, Mark D., 1980: "Evaluation of Diagnostic Marine Boundary-Layer Models Applied of Hurricane", Monthly Weather Review, June, pp 757-766.
24. Rosenthal, S. I., 1971: "The Response of a Tropical Cyclone Model to Variations in Boundary Layer Parameters, Initial Conditions Lateral Boundary Conditions, and Domain Size", Monthly Weather Review, Volume 99, pp 767-777.
25. Prater, M. D., 1981, Wave Dynamics Division, Hydraulics Laboratory, Internal Memorandum, U.S. Army Waterways Experiment Station, Vicksburg, Mississippi.
26. Bretschneider, C. L., "Revisions in Wave Forecasting: Deep and Shallow Water", Proceedings of the Sixth Conference on Coastal Engineering, ASCE, Council on Wave Research, 1958.

27. U.S. Army Coastal Engineering Research Center, Shore Protection Manual, Volume 1, Third Edition, 1977.
28. Coastal Engineering Technical Note, CETN-I-6, Revised Method for Wave Forecasting in Shallow Water, Coastal Engineering Research Center, March 1981.
29. Coastal Engineering Technical Note, CETN-I-7, Revised Method for Wave Forecasting in Deep Water, Coastal Engineering Research Center, March 1981.
30. Coastal Engineering Technical Note, CETN-I-5, Method of Determining Adjusted Windspeed,  $U_a$ , for Wave Forecasting, Coastal Engineering Research Center, March 1981.
31. Project CW-167, Waves and Wind Tides in Shallow Lakes and Reservoirs: Summary Report, U.S. Army Corps of Engineers, Jacksonville, Fla., June 1955.
32. Stoa, Phillip N., Reanalysis of Wave Runup on Structures and Beaches, Technical Paper No. 78-2, U.S. Army Corps of Engineer, Coastal Engineering Research Center, Vicksburg, Ms., March 1978.
33. Weggel, J. R., "Wave Overtopping Equation", Proceedings of the 15th Coastal Engineering Conference, ASCE, Honolulu, Hawaii, 1976, pp 2737-2755.
34. Butler, H. Lee. "Evolution of a Numerical Model for Simulating Long-Period Wave Behavior in Ocean-Estuarine Systems" in Estuarine and Wetland Processes, Hamilton, P. and Macdonald, K. (eds.), Plenum Press, New York, 1980.
35. Leendertse, J. I. A Water Quality Model for Well-Mixed Estuaries and Coastal Seas: Volume I, Principles of Computation, Rand Memorandum RM-6230-RC, February 1970.
36. \_\_\_\_\_. A Water Quality Model for Well-Mixed Estuaries and Coastal Seas: Volume II, Principles of Computation, Rand Memorandum R-708-NYC, July 1971.
37. Butler, H. Lee and Prater, Mark D. New York District sponsored Fire Island to Montauk Point Reformulation Study, January 1983, Program Version.
38. Reid, Robert O. and Bodine, Bernice R. "Numerical Model for Storm Surges in Galveston Bay," Journal of the Waterways and Harbors Division, ASCE, WW 1, February 1968.
39. Chen, Michael H. et al. "A Numerical Surge Model with Moving-Boundary Treatment," presented at the National Symposium on Urban Stormwater Management in Coastal Areas, ASCE Hydraulics Division Specialty Conference, Blacksburg, Va., June 19-20, 1980.

END

4-87

DTIC